UNIVERSITY OF SOUTHAMPTON

The Geoacoustic Properties of Shallow, Gas-bearing Sediments

Michael David John Tuffin

Submitted for the degree of Doctor of Philosophy

School of Ocean and Earth Sciences

October 2001

University of Southampton - Faculty of Science – School of Ocean and Earth Science

Doctor of Philosophy

October 2001

The Geoacoustic Properties of Shallow, Gas-Bearing Sediments

by Michael David John Tuffin

Abstract

Gassy sediments have long been recognised on high-resolution seismic profiles. It is known that gassy sediments exhibit different velocity- and attenuation-frequency responses in comparison with their fully saturated counterparts. A detailed study was carried out on gassy sediments found in Dibden Bay, Southampton Water (U.K.), using two in situ acoustic techniques: surface-towed chirp (2 – 8 kHz) high resolution sub-bottom profiling and a Southampton Oceanography Centre designed seabed mini-boomer system (1 – 10 kHz). Chirp sub-bottom profiles revealed extensive acoustic turbidity at approximately 1 m below seafloor, providing initial evidence for the presence of gas. Two experiments were carried out with the mini-boomer: a refraction / transmission experiment and a 24 hour transmission monitoring experiment. The refraction experiment used a horizontal array of four hydrophones. The results showed that the sediments were non-dispersive, and had frequency dependent quality factor and frequency independent attenuation coefficients. Attenuation coefficients were approximately 4 dB/m, an order of magnitude higher than published data for fully saturated sediments. Consistently low group velocities were believed to be caused by a non-gassy surface layer acting as a waveguide. The 24-hour monitoring experiment used a vertical array of hydrophones to detect the gas horizon and measure any variation in the acoustic character of the sediment over a tidal cycle. The results show that the gas horizon lies between 0.8 and 1.2 m and that the frequency of maximum attenuation increases with increasing hydrostatic pressure. This can only be in response to the shrinking of the gas bubbles. Modelling of the monitoring data, using parameters derived from a series of laboratory tests on core samples and a fitted bubble size distribution, shows that pressure equilibrium of the bubbles with their surroundings cannot account for the size of the radius change alone, and that there must be a diffusive component. Modelling using bubble size distributions generated from X-ray CT scan data proved not to match the output of the in situ data. This is thought to be the result of the small number of bubbles measured, the limited resolution of the measurement technique and a lack of information about the bubbles in the vertical plane. However, the bubble distributions generated (fitted and X-ray CT derived) appear to follow similar power laws, although more work is required to confirm this.

Acknowledgements

First and foremost, I would like to acknowledge the help, support and enthusiasm of my supervisors, **Dr Angus Best**, **Dr Justin Dix** and **Dr Jon Bull**. In addition, I would like to thank **Associated British Ports (Southampton)** for granting access to the field site.

There are a number of people I'd like to thank for their help with the field experiments. For the mini-boomer experiments, I'd like to thank **Andy Harris**, **Simon Dean** and **Gary Robb**. For the coring session I'd especially like to thank **John Roberts** and **Geotek**, who developed the pressurised corer, **Sally Marine** and her diving team for agreeing to dive in Southampton Water during October, as well as **Gary Robb** and **Stephanie Arnott**. For the chirp surveying, I'd like to thank the crew of the Bill Conway.

All this field data generated a bit of lab work, so thanks to: **Rachel Cave** and **Laura Coles** for the chemistry bits; **Dave Gunn** and **John Roberts** (again) for help with the core logger; and, although it now plays little part in the final version, everyone at Civil Engineering who helped with the geotechnics, namely **Toby Hayward**, **Andy Cresswell**, **Martin Rust** and **Harvey Skinner**. Thanks to BOSCOR for providing storage and logging facilities.

Finally, thanks to the guys I have shared an office with at various times: **Simon Russell**, **Simon Dean**, **Phil Cole** and **Gary Robb**.

This project was funded by NERC Studentship GT04/98/272/ES in CASE partnership with the Challenger Division for Seafloor Processes, Southampton Oceanography Centre.

Table of Contents

Chapter 1. Introduction

Zones of poor acoustic penetration and high reflection/backscatter amplitudes are commonly observed in high-resolution seismic profiles, often at depths of less than 20 m beneath the seafloor. This 'acoustic turbidity' is caused by the presence of free gas bubbles, principally methane but including other gases such as hydrogen sulphide, carbon dioxide and ammonia, that result in high attenuation and low velocity of transmitted signals relative to those transmitted through fully water saturated sediments (Schubel, 1974). Such areas are widespread and one example is Dibden Bay, Southampton Water.

The presence of gas in shallow sediments is thought to be the result of the anaerobic decomposition of organic matter (Floodgate and Judd, 1992). It has been observed that in the upper regions of the sediment column, where the pore water is rich in sulphates, hydrogen sulphide is preferentially created as a result of the dominance of sulphate-reducing bacteria. Beneath this region, carbonate-reducing bacteria may compete for the organic substrate more efficiently and produce methane (Rice and Claypool, 1981).

Knowledge of gassy sediment properties is of interest to a number of offshore activities, including drilling operations and the siting of seafloor structures (Sills and Wheeler, 1992). Slope stability is an area of concern to offshore operators who are working increasingly in the deep waters of the continental slope (water depths 200 – 2000 m). Evidence for gassy sediments such as pockmarks (McQuillin and Fannin, 1979) and gas hydrates are commonly found adjacent to large, historical, submarine landslides (Mienert and Posewang, 1999), and, although the causes of submarine landslides are poorly understood at present, it is known that the presence of gas bubbles may lower the shear strength of a marine sediment (Whelan *et al.*, 1976; Wheerler, 1988b). Remote sensing of the seabed and sub-seabed using high-resolution acoustic methods promotes the possibility of inverting acoustic data for the geotechnical parameters needed in the above applications. However, a better understanding of acoustic propagation mechanisms in both fully saturated and gassy marine sediments is required to achieve this goal.

Gassy sediments can exhibit different velocity- and attenuation-frequency responses to their fully saturated counterparts and the aims of this project are fourfold:

(a) to characterise the acoustic response of gassy sediments found at Dibden Bay at both high (300 – 700 kHz) and low (600 – 3000 Hz) frequencies; (b) to measure the physical characteristics of the sediment and the bubble size distribution; (c) to examine the veracity of an acoustic model of gassy sediments by comparison with *in situ* acoustic data; and (d) to provide a framework for future work aimed at predicting bubble size distributions from acoustic measurements.

1.1 Thesis structure

In **Chapter 2**, the occurrence and formation of shallow gas are discussed, as well as methods by which it may be detected. Shallow gas appears on sub-bottom profiles as areas of acoustic turbidity and this term may be used to represent the physical (Taylor 1992) and seismic (Judd and Hovland, 1992) character of the gas. The various geomorphological features that may arise from the presence of gas (e.g., pockmarks), the formation mechanisms and controls, and mechanisms contributing to the accumulation and trapping of the gas are also discussed.

In order to study how the presence of gas affects the acoustic properties of a sediment, it is first necessary to understand the acoustic propagation mechanisms in fully saturated sediments. **Chapter 3**, therefore, is a discussion of the various factors that may affect the geoacoustic properties (i.e., sound speed and attenuation) of fully saturated sediments and how the presence of gas is understood to affect these properties.

The acoustic response of gassy sediments has been modelled by Anderson and Hampton (1980a, b), using the acoustic properties of bubbly water as a basis, and this model, and the background theory, is outlined in **Chapter 4**.

Chapters 5 describes the *in situ* acoustic methods and results. Dibden Bay is ideal for experimentation because it is exposed at low tide, enabling both marine and terrestrially based experiments to be completed. Chirp (2 – 8 kHz) sub-bottom profiles were collected over the site, revealing extensive acoustic turbidity. In addition, two terrestrially based *in situ* acoustic experiments were conducted using a mini-boomer source with four hydrophone receivers (Best *et al.*, 2001). The first was a refraction / transmission experiment with the hydrophones placed horizontally at 1 m intervals. Shots were fired at increasing distances from the array. The second was a twenty-four hour transmission experiment using a vertical array of hydrophones placed at depths to ensure that at least one hydrophone was above the gas horizon and at least one was

below the horizon, as inferred from the chirp sub-bottom profiling. Shots were fired at ten-minute intervals over two tidal cycles. The purpose of this experiment was to localise the depth of the gas horizon and to determine whether variable hydrostatic pressure affects the bubbles and, hence, the acoustic properties of the sediment.

Chapter 6 describes the laboratory tests conducted on core material retrieved from the site. These tests were conducted with the aims of: characterising the sedimentary units and their physical properties for input to the gassy sediment model; to verify the existence of bubbles at depth and to quantify the bubble size distribution with depth for input to the model; and to measure the high frequency (300 – 700 kHz) acoustic response of the gassy sediment. In total, two 150 mm square Kastenlot cores, one 3 m long and one 2 m long, and two 3 m pressurised cores were collected. The pressurised cores used specially designed end caps, inserted on the seabed by divers, to maintain the *in situ* hydrostatic pressure. The tests consisted of: grain-size analysis; inorganic and organic carbon analysis; shear strength; shear-wave velocity; compressional-wave velocity; compressional-wave attenuation; bubble size analysis (through the use of X-ray computed tomography); and density.

In **Chapter 7**, the twenty-four hour data was modelled using the Anderson and Hampton (1980a, b) model, with adjustments to calculate the effect of increasing hydrostatic pressure on the gas bubbles. It was decided to model only the pressure dependency of the bubbles, since insufficient chemical data were available to account for diffusive changes. The adjustment calculations used the Ideal Gas Law to calculate the new bubble size after an increase in hydrostatic pressure, with an additional step to calculate the new gas porosity for that radius.

Conclusions and recommendations for future work are given in **Chapter 8**.

Finally, there are a number of appendices: **Appendix A** contains all X-ray CT scan images and a diagram of their locations; **Appendix B** contains all the high frequency acoustic results; **Appendix C** describes a number of geotechnical tests that were attempted; and **Appendix D** contains published work.

Chapter 2. Occurrence and formation of gas in marine sediments

2.1 Introduction

Many shallow sediments are almost acoustically impenetrable to sub-bottom profiling systems (Figure 2.1). These areas have been termed 'acoustically turbid' (Schubel, 1974), a term descriptive of the appearance of the seismic profile. That phrase is now generally defined as 'an area of chaotic reflections, caused by the presence of something (commonly gas) within the sediments which scatters and/or absorbs the acoustic energy' (Judd and Hovland, 1992).

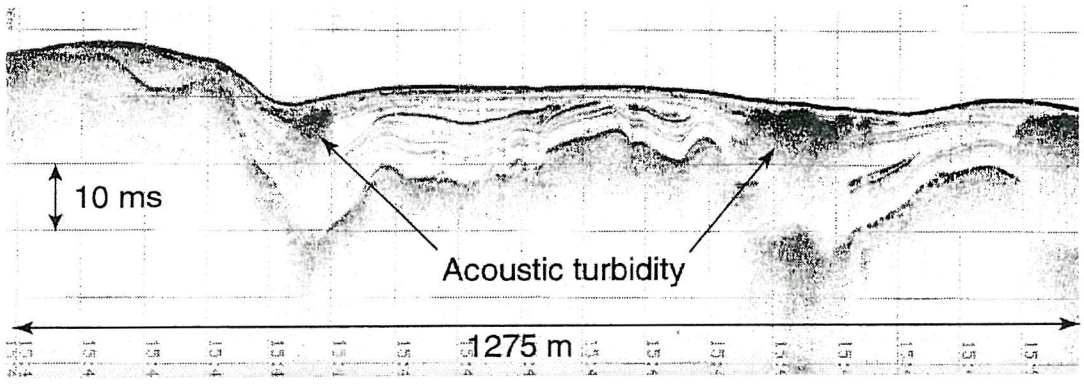

Figure 2.1. Chirp sub-bottom profile showing acoustic turbidity in Strangford Lough, Northern Ireland. From Lenham (2000).

Acoustic turbidity was investigated by Schubel (1974) in Chesapeake Bay. Cavities within cores retrieved from turbid areas, as well as gas venting during core retrieval, provided evidence for free gas within the sediments. There were no cavities in, or gas venting from, cores sampled from areas that were free of acoustic turbidity. Hence, an association between acoustic turbidity and the presence of free gas was made. Similar acoustically turbid zones have since been found in many areas around the world. These include Alaska (Cline and Holmes, 1977), the Bay of Fundy (Rashid and Vilks, 1977), the North Sea (McQuillin and Fannin, 1979), India (Siddiquie *et al.*, 1981), Eckernförde Bay (Whiticar, 1982), the Gulf of Mexico (Anderson and Bryant, 1990) and Hong Kong (Premchitt *et al.*, 1992).

Seismo-acoustic methods are not the only way of identifying the presence of free gas within a sediment. Other indicators include the presence of pockmarks (Hovland and Judd, 1988), seabed seeps of gas and the geochemical composition of the

water column (Deuser *et al.*, 1973) and sediment pore water (Emery and Hoggan, 1958; Bernard, 1979; Jones *et al.*, 1986). Evidence for gassy sediments have also been found in regions prone to slope failure, such as the Storegga Slide off the coast of Norway (Mienert and Posewang, 1999). While the causes of submarine landslides are poorly understood at present, it is certainly true that free gas may lower the shear strength of marine sediments (Whelan *et al.*, 1976; Wheeler, 1988b).

2.2 Seismic indicators

The term 'acoustic turbidity' was initially used by Schubel (1974) to describe an area of chaotic reflectors that caused a dark smear on the seismic record. This phenomenon was attributed to attenuation of the seismic wave. Adjacent reflectors often appear to be deflected downwards in what is known as a 'reflector pull-down' (Figure 2.2) due to the sharp decrease in compressional wave velocity found in gassy sediments. Such features have been found in many surveys (Carlson *et al.*, 1985; Premchitt *et al.*, 1992).

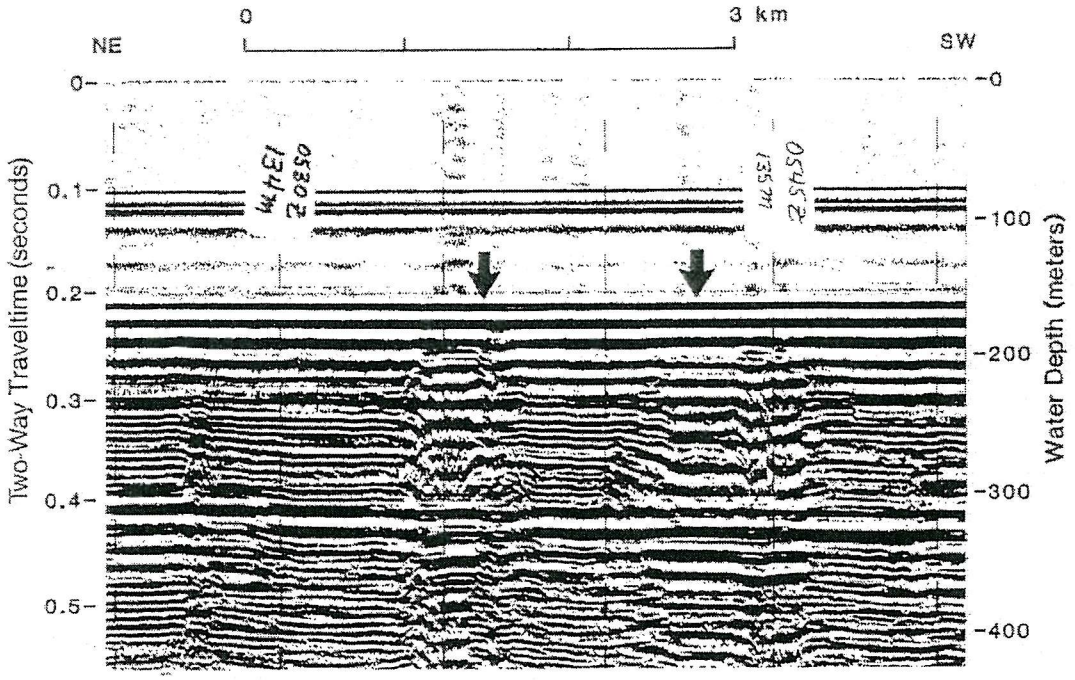

Figure 2.2. Airgun profile showing reflector pull-downs. From Carlson et al. (1985).

The generic term 'acoustic turbidity' may be subdivided to describe either the physical character (Taylor, 1992), how the gas actually exists in the sediment, or the seismic character (Hovland and Judd, 1988), how the gas appears on the seismic record. Taylor (1992) proposed the use of the term 'gas plume' to describe

accumulations that are small (< 50 m) in their lateral extent with distinct edges and examples may be seen in his data from the north-east Irish Sea (Figure 2.3). This is a similar description to that given for 'columnar disturbances' by Hovland and Judd (1988), who describe them as restricted patches in which no apparent reflections occur. It is thought that they could be formed by the disturbance of the regular mineral layering caused by the vertical migration of pore fluid (which may or may not be gas). This same formation process is considered by Taylor (1992) for gas. Another hypothesis proposed by Taylor (1992), as well as Judd and Hovland (1992), is that these plumes and columnar disturbances could be formed via a diapiric process where gas trapped by an impermeable layer may increase sufficiently in pressure to deform overlying strata, although significant pressures would have to be developed. Some evidence of this was found by Yuan *et al.* (1992) in the Irish Sea.

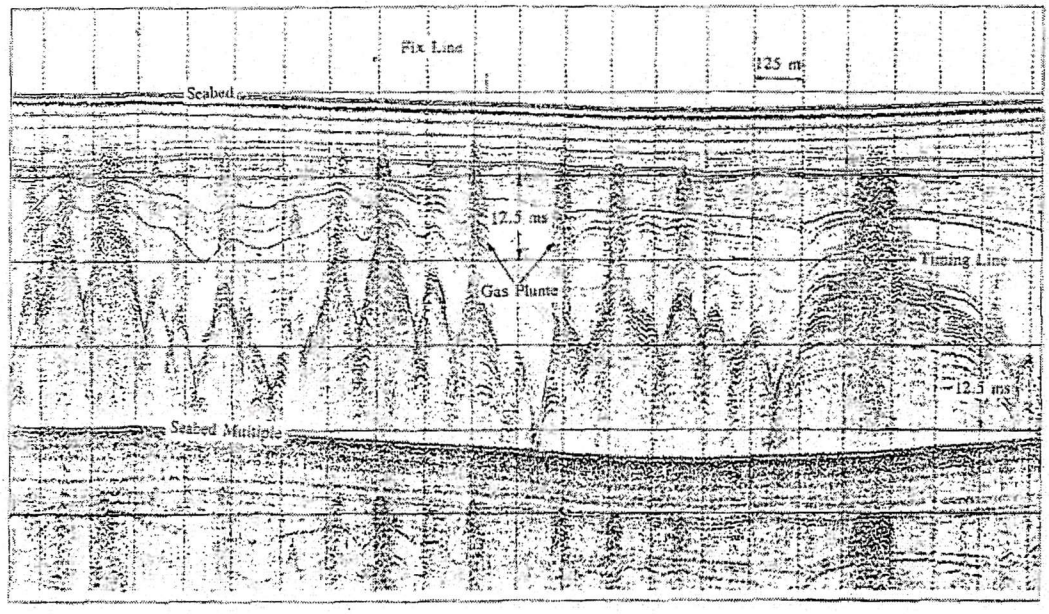

Figure 2.3. Uniboom sub-bottom profiler record showing gas plumes. From Taylor (1992).

For zones that extend between 100 m and 500 m, Taylor (1992) defines 'gas curtain' as a reflector of limited lateral extent having a high amplitude with sharp lateral boundaries extending vertically beneath the edge of the main reflector (Figure 2.4). These types of features are typically formed over infilled paleo-channels and the reflector may follow the attitude of the seabed. Features extending more than 500m are described as 'gas blankets' where large areas of the sub-bottom are acoustically turbid. The lack of a definite boundary associated with a gas blanket is interpreted by Taylor

(1992) as being the result of biogenic gas in just enough quantity to diffuse energy without forming a definite feature.

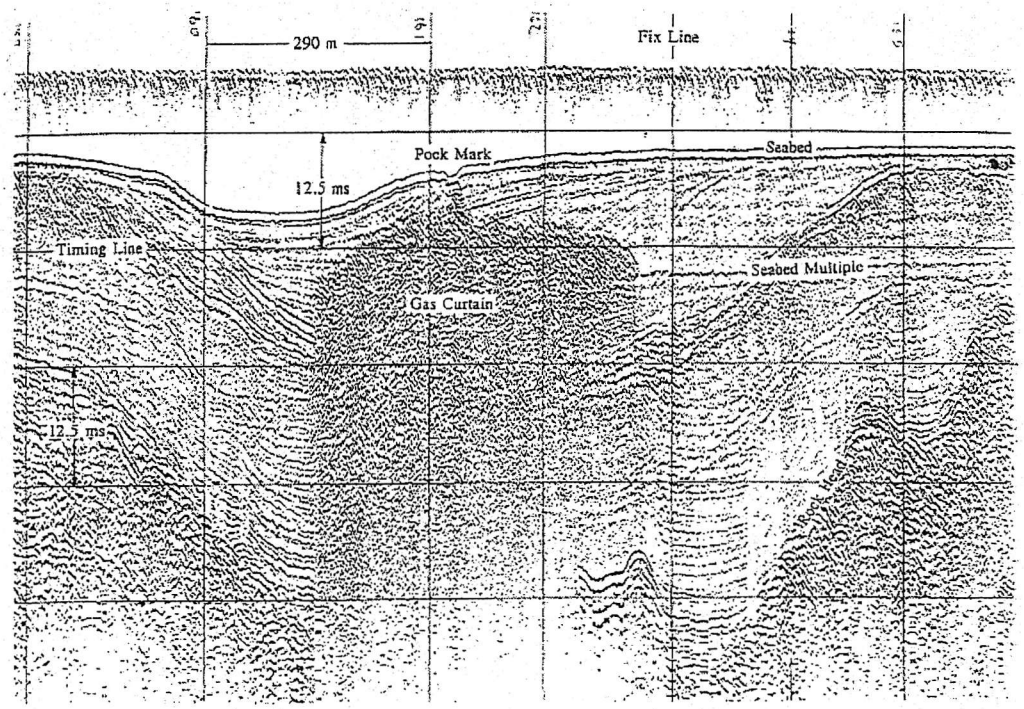

Figure 2.4. Uniboom sub-bottom profiler record showing a gas curtain. From Taylor (1992).

Other types of seismic signature include 'bright spots' and 'enhanced reflections' described by Hovland and Judd (1988). Bright spots are thought to be the result of the high acoustic contrast between gassy and non-gassy sediments, which causes a high amplitude, negative phase reflection, and are most often seen in deeper penetrating surveys. This reflection represents the top of a gas filled sediment. However, gas is not the only cause of such a signature as other materials, such as a layer of carbonate cement, that have a lower acoustic impedance compared to the overlying layer may produce a similar response. Enhanced reflections (Figure 2.5) are the shallow equivalent of bright spots and are described as 'coherent seismic reflections which have an increased amplitude for part of their extent' (Hovland and Judd, 1988). It is most likely that both of these features are the result of gas trapped within a layer of porous sediments because of their continuous nature and the relative ease with which the gas can migrate to a similar horizon in a porous layer. In areas of acoustic turbidity, where there is a more general disruption of the seismic record, it is thought that the gas is finely distributed throughout impervious sediments that prevent the gas from migrating to a common horizon (Judd and Hovland, 1992).

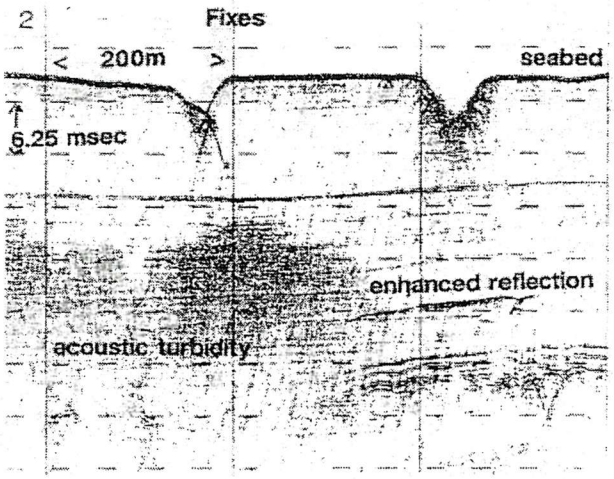

Figure 2.5. Deep-towed boomer record showing acoustic turbidity and enhanced reflections. From Judd and Hovland (1992).

The final feature that may appear on a seismic record is 'acoustic blanking' (Judd and Hovland, 1992) where an area may be devoid of reflections (Figure 2.6). This could again be due to fluid migration disturbing the sedimentary sequences or it may be due to the absorption of the energy by overlying gas charged sediments. As with bright spots, gas is not the only feature that may cause blanking – reflection of the majority of the energy by a strong acoustic impedance contrast between sediment layers will reduced the amount of penetrating energy and hence reduce the amplitude of any returns from beneath this interface. However, if multi-channel techniques are used with a streamer longer than the area of acoustic turbidity, deeper horizons may be seen at long offsets.

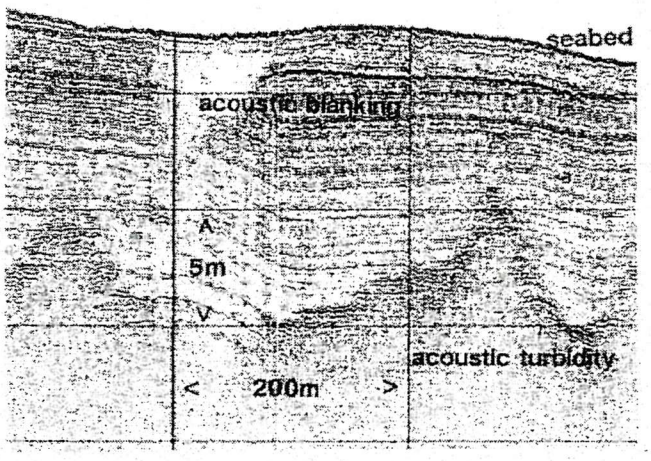

Figure 2.6. Deep-towed boomer record showing acoustic blanking. From Judd and Hovland (1992).

2.3 Geomorphological indicators

A pockmark is a depression in the seabed caused by the removal of sediments by escaping fluids (Judd and Hovland, 1992). They may be detected using side-scan sonar and sub-bottom profiling techniques (Figure 2.7). Pockmarks have been observed in many parts of the world including the North Sea (McQuillin and Fannin, 1979), Alaska and the Barents Sea (Hovland and Judd, 1988), the Gulf of Mexico (Anderson and Bryant, 1990), the Skagerrak (Hovland, 1991; Hempel *et al.*, 1994), and the Norwegian Channel (Max *et al.*, 1992). Pockmarks are often found in areas with gas, although some gassy areas have no pockmarks (Premchitt *et al.*, 1992; Siddiquie *et al.*, 1981). There are also areas that contain pockmarks, but no gas (Hovland and Judd, 1988). Pockmarks are typically between 10 – 50 m in diameter and about 1 – 15 m deep (Hovland and Judd, 1988), although larger ones, up to 500 m in diameter and 24 m deep, have been found (Hovland, 1991).

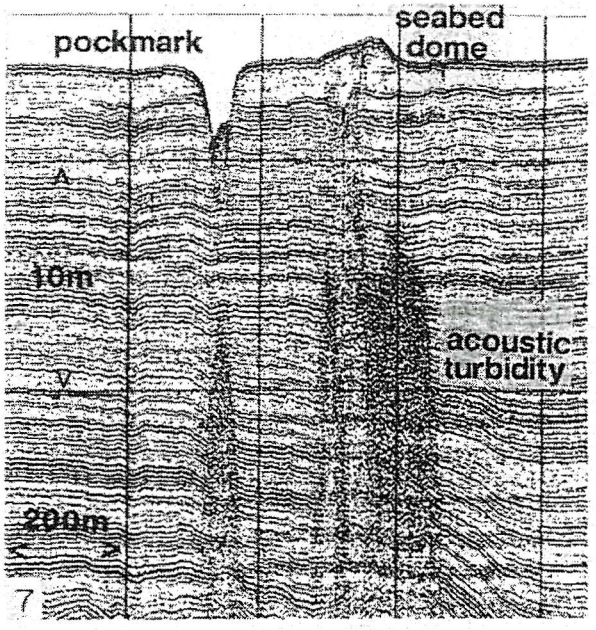

Figure 2.7. Pinger record showing a pockmark, a seabed dome and acoustic turbidity. From Judd and Hovland (1992).

The most likely mechanism for the formation of pockmarks is the expulsion of gas from the sediment. This may lift fine sediments into suspension in the overlying water column where they can be transported by seabed currents (McQuillin and Fannin, 1979). Hempel *et al.* (1994) studied a pockmarked area in the Skagerrak and proposed a relationship between the age of the pockmark and the number and strength of reflecting surfaces that may be seismically imaged directly below the pockmark.

Deep, coherent reflections directly beneath the pockmark indicate a newly formed pockmark because all the gas has been vented and there has been insufficient time for the recharging of gas in the structure subsequent to the initial release.

In areas of high concentrations of free gas, it is possible that the gas will migrate through the seabed and into the water column. There are two types of seepage, macro- and micro-seeps. Where the escaping fluids (liquid or gas) are visible, the seep termed is a macro-seep. A seep of dissolved gas is called a micro-seep (Judd and Hovland, 1992). Seeps may be detected visually as bubbles or shimmering water emanating from the seafloor or from the sea surface where they appear as slicks or 'boiling' areas of water (Figure 2.8). Seeps are also detected in echosounder and sub-bottom profiling records where they may be seen as strong vertical backscattering regions in the water column (Anderson and Bryant, 1990). Such seeps have been found in a number of areas around the world (e.g. Cline and Holmes, 1977; Kvenvolden *et al.*, 1979; Hovland and Sommerville, 1985; Hovland and Judd, 1988; Laier *et al.*, 1992).

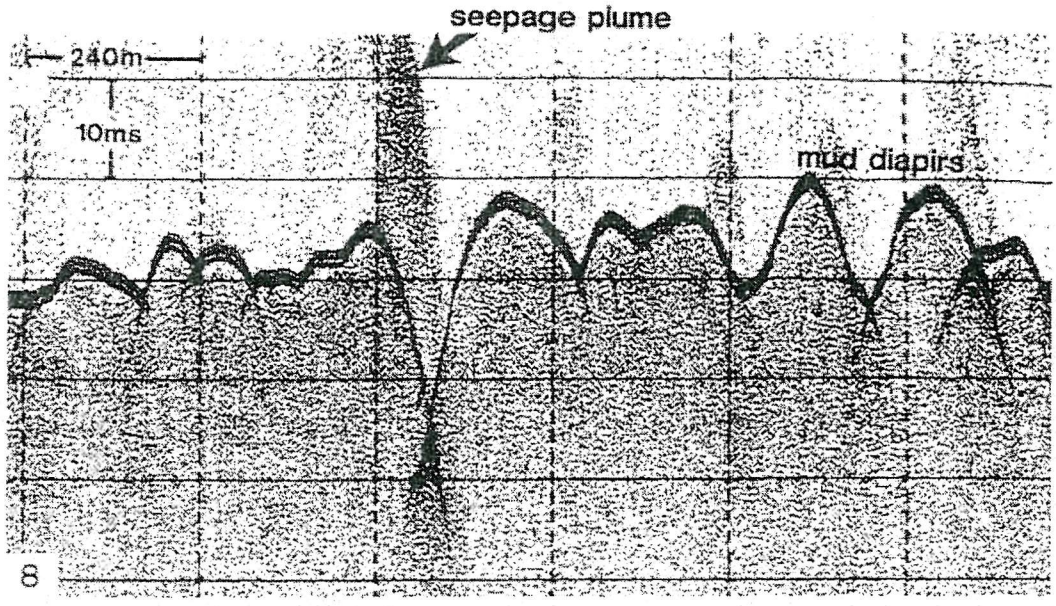

Figure 2.8. Deep-towed boomer record showing seepage plumes and mud diapirs. From Judd and Hovland (1992).

Other geomorphological features that indicate the presence of gas include seabed domes (Figure 2.7), the result of gas increasing the volume of the sediment (Hill *et al.*, 1992), and mud or clay diapirism (Hovland and Judd, 1988), where the gas has

made mud or clay layers more buoyant than the surrounding material causing it to dome upwards (Figure 2.8).

2.4 Geochemical evidence

The most convincing evidence for gas in sediments is when it can be sampled directly and analysed for its chemical composition. There are three methods: headspace analysis; *in situ* sampling at the seabed; and extraction during hydrocarbon exploration drilling.

'Sniffer' devices may be used to analyse any dissolved gases in the seawater by use of gas chromatography (Judd and Hovland, 1992). The presence of hydrocarbons could then be detected and, depending on the ratio of methane to higher hydrocarbons, the source of the hydrocarbon may be ascertained. If a core is taken, it is possible to extract the gas by placing a sample in a can containing distilled water with a headspace purged with helium. The can is then shaken up and the gas leaves the sediment for the headspace where it can be extracted and analysed by gas chromatography (e.g. Bernard, 1979; Carlson *et al.*, 1985). This method is similar to one used in hydrocarbon exploration. The drilling mud enters a tank having left the borehole and is stirred. The exsolved gases are collected and then pumped into a gas chromatograph for analysis (Judd and Hovland, 1992). Other tools have been developed, such as the BAT probe developed by the Norwegian Geotechnical Institute. It is inserted into the sediment to the required depth whereupon a series of needles sample the *in situ* pore water and/or gas which is stored in a container for later analysis (see Premchitt *et al.*, 1992). Mass spectrometer methods have also been used to analyse gas samples in the laboratory (Emery and Hoggan, 1958).

2.5 Shallow gas formation

There are several gases that are found in marine sediments with the most important being hydrogen sulphide and methane, of which methane is generated in the largest volumes (Floodgate and Judd, 1992). Light hydrocarbons (methane, ethane, propane, etc.) found in shallow sediments by Emery and Hoggan (1958) were concluded to have come from four possible sources: human contamination; leakage from deeper oil rich strata; survival of materials synthesised by plants; and the breakdown of organic matter by bacteria. However, leakage from a deeper oil rich strata (termed thermogenic gas) and bacterial formation (termed biogenic gas) are

believed to be the only significant sources of light hydrocarbons in sediment. Shallow gas has been described as gas 'formed close to the surface in marine sediments' (Smith and Floodgate, 1992). In some areas, gas is present within one metre of the seabed (Anderson *et al.*, 1998) and in others, the presence of gas may be detected throughout the sediment column. The depths of gas being considered in this work will be down to about 20 m.

2.5.1 Thermogenic gas formation

Organic material that is laid down and subsequently buried becomes altered by the heat and pressure encountered as the depth of burial becomes large - usually greater than 1000 m (Floodgate and Judd, 1992). Production of methane is generally associated with fine-grained sediments. When fine-grained sediments are deposited, the water current velocity must be low enough to allow the organic material to deposit. Once further deposition occurs, the depth of burial increases to a point where the pressure and temperature conditions are optimal for hydrocarbon generation and methane, along with higher order hydrocarbons, will begin to form. Further information on hydrocarbon formation may be found in Hunt (1979), Tissot and Welte (1984), and Floodgate and Judd (1992). Once formed, however, the gas can migrate towards the surface driven by its buoyancy. It can migrate through permeable strata or through faults and fissures. It can become trapped beneath impermeable sediments and appear on shallow seismic records.

2.5.2 Biogenic gas formation

Shallow gas within about 20 m of the seabed often has a biogenic source. In the presence of oxygen, aerobic decomposition of organic material will occur, producing carbon dioxide and water (Claypool and Kaplan, 1974). Oxygen will usually be depleted within a few millimetres of the sediment/water interface (Anderson and Hampton, 1980a), and below this level anaerobic decomposition will occur. There are two distinct zones of anaerobic decomposition: the sulphate-reducing zone and the carbonate-reducing (methane producing) zone (Figure 2.9). In each of the zones, a dominance of bacteria, or archaea, depends upon the prevailing environmental conditions. In the marine environment the sediment pore water will be rich in sulphates due to the presence of sulphates in the seawater. This concentration allows sulphate-reducing bacteria to compete efficiently for the organic substrate leading to hydrogen

sulphide production. Observations (e.g., Martens and Berner, 1977) show that the concentration of dissolved methane remains low until dissolved sulphate is removed. This suggests that methane production and sulphate reduction are mutually exclusive processes (e.g. Claypool and Kaplan, 1974; Martens and Berner, 1974), a hypothesis supported by the fact that few microbial organisms can exist in the presence of hydrogen sulphide.

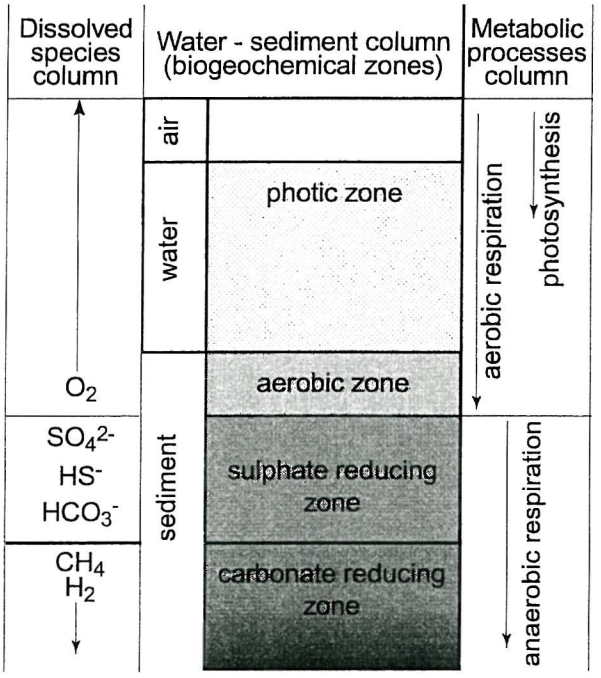

Figure 2.9. Diagrammatic cross section of a typical water/sediment column. From Rice and Claypool (1981).

However, the low concentrations of methane in the sulphate-reducing zone could indicate a balance between methane production and consumption (Figure 2.10), with physical processes acting to transport methane from one zone to the next. Barnes and Goldberg (1976) provided evidence for the active consumption of methane by the bacterial population existing within the sulphate-reducing zone in sediments from the Santa Barbara Basin. The rapid change in concentration of methane at the boundary between the sulphate reducing and carbonate reducing zone would only be possible if there was a sink of methane in the sulphate reducing zone. Barnes and Goldberg (1976) believe that acetate, produced by sulphate-reducing bacteria, is used as a substrate by the methanogenic bacteria that ferment it to produce methane and carbon dioxide. The methane produced is then predominantly oxidised to CO_2 by the sulphate reducing

bacteria. It is likely that this consumption of methane exerts some control over the overall distribution of methane in marine sediments (Bernard, 1979).

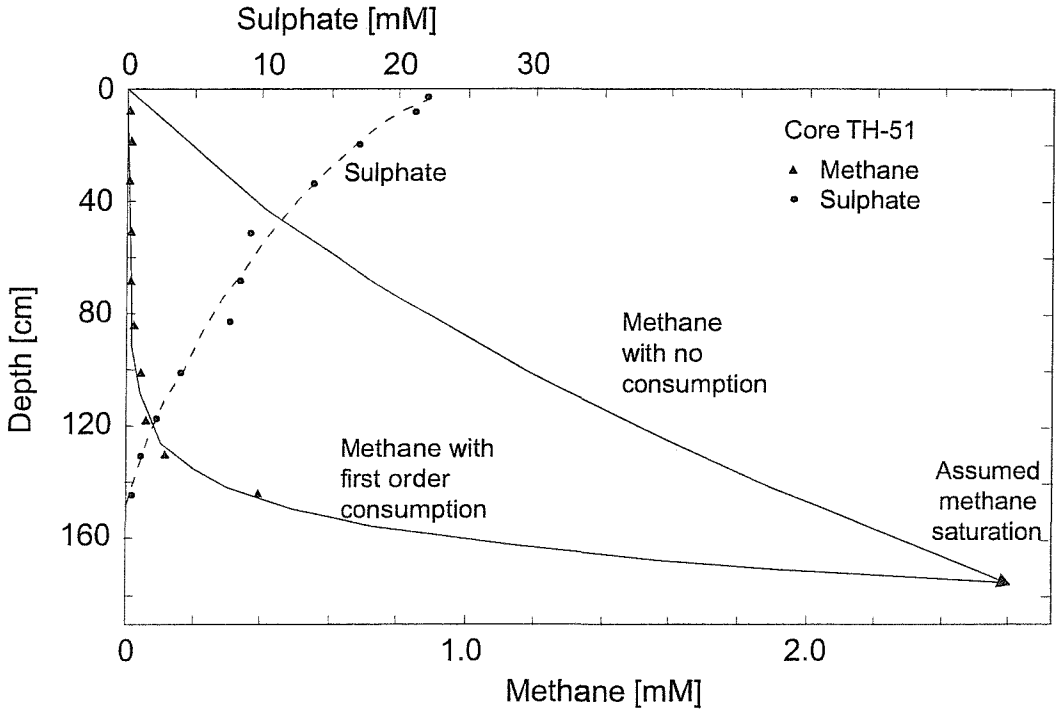

Figure 2.10. Methane and sulphate concentrations versus depth. Solid lines represent theoretical curves for no consumption and consumption. Dashed line is an exponential fit to the sulphate data. From Martens and Berner (1977).

The exact mechanism for methane production is largely unknown. However, acetate (which is a by-product of sulphate reduction) and CO_2 with H_2 appear to be the main substrates (Martens, 1982). This use of the by-products of the previous zone shows evidence of ecological succession.

There are a number of conditions that must be met before significant quantities of methane can be produced. Methanogenic archaea are strict anaerobes and they cannot function in the presence of any oxygen (Rice and Claypool, 1981). There must be a sulphate deficient environment, or the archaea will not compete effectively for the substrate since carbonate reduction is a less energetically efficient process than sulphate reduction (Rice and Claypool, 1981). Temperature also plays a part in production. Methanogenesis can occur over a wide range of temperatures, and 0 - 75 °C has been suggested (Rice and Claypool, 1981). Each species of bacteria will have a temperature range within which its production is most efficient. The archaea need sufficient space within which to function and significant compaction of the sediment will inhibit activity, although at shallow depths this is not a particular

problem. A significant rate of deposition is also required. Too slow and the organic matter will be decomposed in the aerobic and sulphate reducing zones. If the rate is too fast, however, the organic matter may be dilute with respect to the amount of mineral present and it may pass through the optimum zones of temperature and depth for methane generation (Rice, 1992). Microbial generation of methane is thought to be favourable at sedimentation rates between 0.2 and 1 mm/y (Clayton, 1992).

Once these conditions have been met, methane accumulation will begin and, assuming the local methane concentration exceeds the solubility and that the sediments are outside the gas hydrate stability zone, bubble will start to appear.

2.5.3 Biogenic or thermogenic gas?

Methane is the predominant gas produced by both thermogenic and biogenic mechanisms. The chemical and isotopic composition of the methane may be used to distinguish its source as either biogenic or thermogenic (Claypool and Kaplan, 1974). Thermal degradation of organic matter adds higher hydrocarbons to the gas and will increase the $\delta^{13}C$ value of the methane (Doose *et al.*, 1978) where:

$$\delta^{13}C = \left[\frac{\left({}^{13}C/{}^{12}C\right)_{sample} - \left({}^{13}C/{}^{13}C\right)_{standard}}{\left({}^{13}C/{}^{13}C\right)_{standard}} \right] \times 10^3 \text{ ‰} \qquad 2.1$$

The standard commonly used is the PDB-standard, or PeeDee Belemnite. This is the limestone used as the international reference standard for expressing carbon stable isotopic ratios. The carbon isotopic ratio of PDB is 0.0112372, and the carbon isotope ratios of other materials are expressed as parts per thousand relative to this value. A more negative value indicates a lower concentration of ^{13}C. Gases with a $\delta^{13}C$ value between -90‰ and -60‰ are generally believed to be of biogenic origin (Doose *et al.*, 1978) with higher stages of thermal alteration having values between -50 and -30 ‰ (Stahl, 1974).

Gas of biogenic origin will contain amounts of higher hydrocarbons (C_{2+}) in proportion with the temperature history, age of the sediments and organic matter content of the sediments from which the gas originates. If the ratio of the concentration of methane to higher hydrocarbons, i.e. C_1 / (C_{1-5}), is greater than 0.98 (Rice and Claypool, 1981) then the gas can be said to be biogenic. Low temperature thermal generation accounts for the volumes of higher hydrocarbons in biogenic gas.

2.6 Physical controls and geological associations

2.6.1 Accumulation and trapping of shallow gas

Upon generation, methane is initially dissolved in the interstitial water of the sediment along with lesser amounts of the other gases that are formed. Anderson and Hampton (1980a) noted that there are three possible outlets for the gas once the concentrations in the interstitial water begins to reach saturation point:

- The gases could diffusively exchange with overlying water
- They may combine with metal cations to become part of the sediment as authigenic minerals
- They can form bubbles and escape through buoyancy or become trapped within the sediment

It is believed that the diffusion rates between the sediment and the overlying seawater are too slow to provide an efficient pathway for the gas (Anderson and Hampton, 1980a). Mineralisation is an important mechanism in the removal of CO_2 and H_2S from solution, but this is not generally the case for shallow methane. Therefore, the main mechanism is to form bubbles. The concentration of methane at which the interstitial water becomes oversaturated, known as the point of oversaturation (POO), is dependent on a number of factors, the most important of which are pressure and temperature. Acoustic turbidity always occurs below the depth of the POO according to Abegg and Anderson (1997). Wever *et al.* (1998) noticed that there was an seasonal variation in the depth of acoustic turbidity in Eckernförde Bay of approximately half a metre to a metre. This variation lagged about three to four months behind the atmospheric temperature cycle. Convection helps the temperature of the water column to keep pace with that in the atmosphere, while heat propagates by conduction in the sediment. Conduction is a slower heat transfer mechanism resulting in a time lag observed in seasonal temperature changes in the sediment. The time lag is due to the lower thermal conductivity of the sediment compared to the overlying water. This depth variation must reflect a change in the solubility of the methane caused by the varying temperature of the sediment. It was seen that after the coldest atmospheric temperatures the depth to the acoustic turbidity was at a maximum and after the warmest atmospheric temperatures the depth was a minimum. The measured concentration of methane in the sediment volume, however, remained approximately

the same all year round, so the depth variability can only be the result of changing solubilities. It was thought that pressures exerted on the seabed by the atmosphere or tides could similarly affect the presence or absence of free gas. The effect of pressure on solubility is linear according to Henry's Law at the shallow depths being considered (Abegg and Anderson, 1997); increasing pressure causes an increase in solubility.

The mechanism of bubble formation once the POO has been exceeded is still uncertain. They could form either from small bubbles coalescing into larger bubbles or by growth from a number of nucleation points (Anderson and Hampton, 1980a). The pore water pressure will generally increase as methane is produced. The resultant pore fluid pressure is equal to the sum of the partial pressures of the gas and water phases (Rau and Chaney, 1988).

Three types of gas bubble (or void) were recognised by Anderson *et al.* (1998), (Figure 2.11). The bubbles may be smaller than the surrounding sediment particles and therefore contained entirely within the interstitial water (Type I); they may form a reservoir where the void is larger than the sediment particles but with the sediment structure remaining unaltered by the presence of gas (Type II); or they may be larger than the surrounding sediment particles, displacing the sediment to create a gassy cavity (Type III) (Wheeler, 1988a; Anderson *et al.*, 1998). The most common type of bubbles to occur in shallow, fine-grained sediments are Type III. These bubbles have been observed through core linings, in scanning electron microscope studies and in x-ray computed tomography (CT) experiments (Anderson and Hampton, 1980a; Gardner and Goringe, 1988; Anderson *et al.*, 1998).

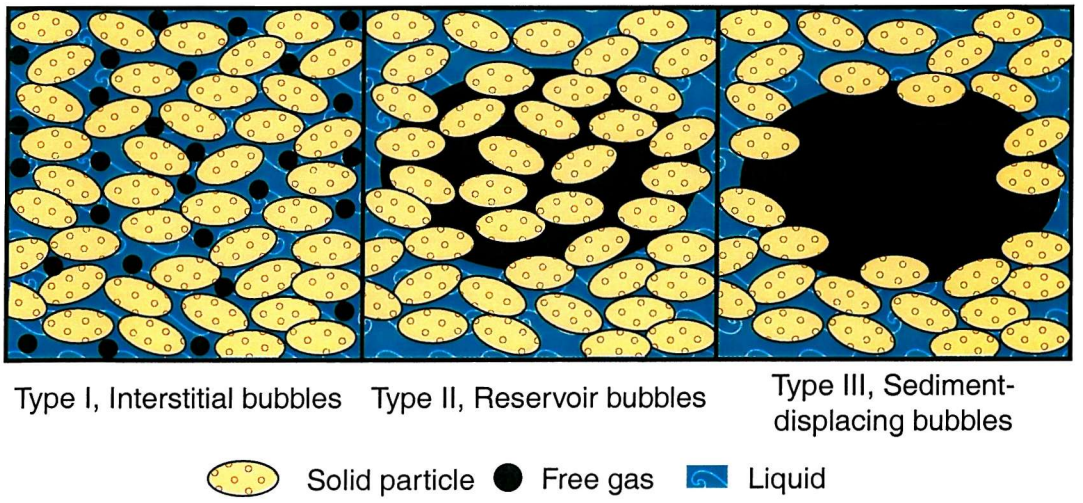

Figure 2.11. Types of bubbles found in sediments. From Anderson et al. (1998).

Other methods of bubble formation include the reduction of overlying hydrostatic pressure resulting in exsolution of methane from the sediment pore water. A reduction in hydrostatic pressure may be caused by a lowering of the sea level, uplift and/or erosion of the overlying sediments. These mechanisms for bubble formation are only likely to occur where methane has been in solution for a long enough period for the region to undergo such changes. Alternatively, the migration of gas bearing interstitial waters to an area of lower hydrostatic pressure may also result in gas bubble formation.

Large bubbles may move vertically under buoyancy by causing shearing in the sediment along failure planes around the cavity (Wheeler, 1990). Resistance of the sediment to shearing is proportional to the cross-sectional area of the sediment (i.e., the radius of the bubble squared) and depends on the undrained shear strength of the sediment. The buoyancy of the bubble is a function of its volume (the radius cubed), so the larger the bubble, the more likely it is to move buoyantly as long as it is above a critical radius, below which movement is not possible (Wheeler, 1990). An analysis by Wheeler (1990) showed that a bubble would have to have a radius of approximately 0.5m to begin moving in typical sediments through buoyancy alone, and he concludes that the only possibility for movement is transport through fissures in the sediment. In the absence of fissures, gas may only move in solution or as small bubbles that may move through the normal void spaces. Most evidence suggests that few bubbles have radii in excess of 10 mm (Anderson *et al.*, 1998; Gardner and Goringe, 1988). Deeper formations are often confined by the presence of a less permeable layer above. It is known that in areas where methane is present carbonate cements also exist (Rice and Claypool, 1981) and studies of these cements show that their chemical composition is characteristic of methane-derived carbonates (Whiticar and Faber, 1986). These cements can turn previously unconsolidated sediments into hard rock and they may act as a reservoir seal.

2.6.2 Geological and sedimentological associations

It is understood that the formation of methane requires organic material and that this material is only deposited in areas where the current speeds are low (see Section 2.5.2). Hence, gas formation is usually associated with the presence of clays and silts which, due to their size, are also deposited in areas of low current speeds. Anderson and Bryant (1989) remarked that there is evidence of an association of gas with infilled

paleo-fluvial systems. It is thought that when these systems were flooded by sea level rise, the channels were filled with sandy sediments that were subsequently overlain by estuarine deposits. A good example of this coincidence of buried channels with shallow gas is the Chesapeake Bay area (Hill *et al.*, 1992; Figure 2.12).

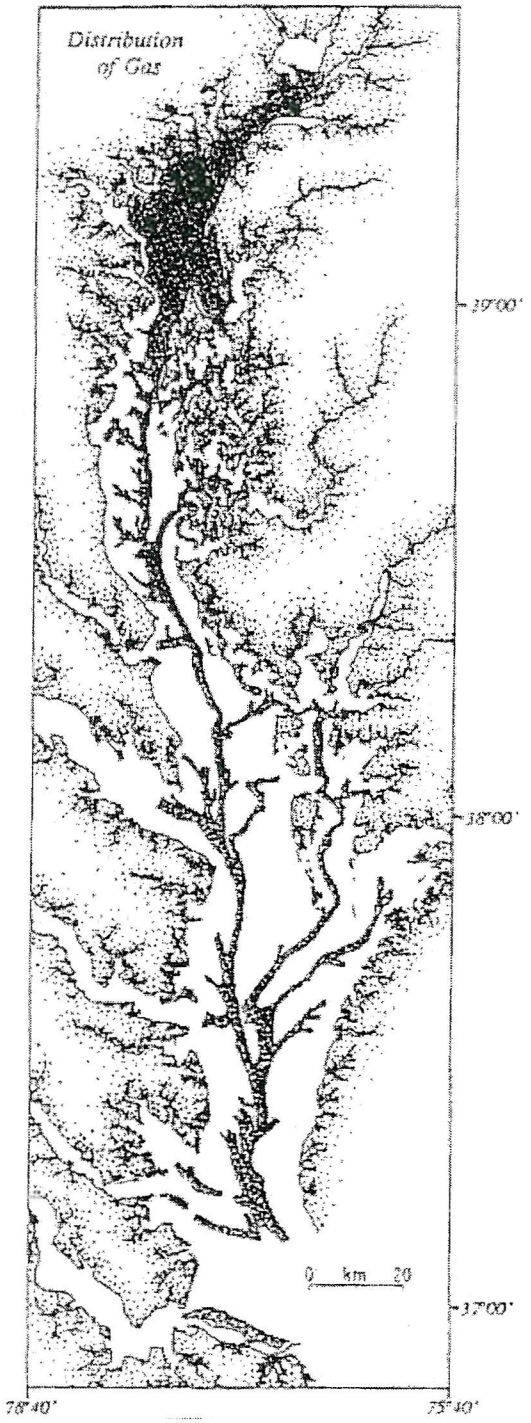

Figure 2.12. Gas distribution map in Chesapeake Bay. The stippled areas represent the gassy zones. From Hill et al. (1992)

It is evident that the amount of organic carbon above a minimum of 0.5% metabolizable organic carbon equivalent (Claypool and Kaplan, 1974) will not affect the volume of methane produced. Rashid and Vilks (1977) found that sediments containing small amounts of carbon were producing as much methane as those sediments relatively rich in carbon.

2.7 Summary

Free methane gas is found throughout the world in shallow, fine-grained marine sediments. It may be detected using acoustic and geochemical techniques and is often accompanied by seafloor features such as pockmarks and domes.

The gas may come from either thermogenic or biogenic sources, although the majority of gas in shallow sediments is biogenic, being generated by anaerobic, methanogenic bacteria. Bubble formation begins when the interstitial pore water becomes oversaturated with methane. The point of oversaturation is related to the solubility of methane in the water and, as such, may be affected by temperature and pressure.

Three types of bubbles have been recognised in sediments, with large, sediment-displacing bubbles being the most common (Type III bubbles). Bubbles with radii small compared to the mineral grains exist solely in the pore fluid and may move within the pore space of the sediment. Larger bubbles tend to move through cracks and fissures within the sediment as buoyancy forces alone are rarely, if ever, strong enough to move the bubble.

Methane production requires organic material in the sediment, which is deposited in areas of low current speed and may therefore be associated with fine-grained sediments.

Chapter 3. Geoacoustic properties of marine sediments

3.1 Introduction

The acoustic properties of water-saturated sediments are affected by a number of different factors related to the fabric of the sediment. In order to study how the presence of gas affects acoustic properties, it is necessary to consider the acoustic propagation mechanisms in fully water-saturated sediments.

For small strains ($< 10^{-6}$), such as those generated by a sound wave, saturated sediments behave elastically (Gassmann, 1951; Hamilton, 1971a), although to predict intrinsic attenuation losses, a linear viscoelastic, or nearly elastic, model should be used (Hamilton, 1971a). There are a number of parameters that affect the acoustic properties of a sediment, among which are: porosity, dynamic strain amplitude, overburden, grain size distribution, mechanical properties of individual mineral particles, degree of lithification (if any) and the overall structure of the sediment (Stoll, 1986).

Biot (1956a,b) developed a model to predict the velocity and attenuation characteristics of porous media. Various authors have modified Biot's original model to express the elastic parameters in forms that could be measured in marine sediments (e.g., Geertsma and Smit, 1961; Stoll and Bryan, 1970; Hovem and Ingram, 1979). Stoll (1980) further developed the model to account for intrinsic frame losses by introducing complex elastic moduli, because the original Biot model only accounts for global fluid flow losses and underestimated attenuation. The saturating fluid is assumed compressible and able to flow relative to the solid, allowing frictional and viscous forces to be considered. The Biot-Stoll model was developed by considering the relationships between the fluid pressure and dilatation as well as stress-strain characteristics and the dynamics of the system. Analysis of the model predicts the existence of three types of wave – one rotational, and two dilatational. Biot (1956a, b) notes that the rotational wave is slightly dispersive (i.e., velocity of the wave is frequency dependent) and has an absorption coefficient proportional to the frequency squared. Of the two types of dilatational waves, known as waves of the first and second kind, only one is significant for this study. Waves of the first kind have practically negligible dispersion and the absorption coefficient is proportional to the square of the frequency. Waves of the second kind are highly attenuated and propagate more in the nature of a diffusive process and will not be considered within the scope of this study.

The model predicts that for compressional waves (waves of the first kind) losses in the skeletal frame are dominant at low frequencies and that viscous losses due to the relative motion of the fluid with respect to the solid phase are dominant at higher frequencies (Stoll, 1974). Stoll (1986) later pointed out that attenuation at low frequencies may be dominated by viscous losses provided there is sufficient mobility of the fluid relative to the skeletal frame. When there is no relative motion between the sediment frame and the pore fluid, Biot's (1956a,b) model reduces to that of Gassmann (1951). The major parameters of the Biot-Stoll model describe the sediment skeletal structure and the mobility of the pore fluid (Stoll, 1980). Other researchers have used an experimental approach to determining the geoacoustic properties of sediments, most notably Hamilton (1970, 1971a,b, 1972).

Although all the attenuation mechanisms in marine sediments are not fully understood, the Biot-Stoll model, and that of Gassmann (1951), can be used to describe most sediments by parameter fitting. For the purpose of this study, it is assumed that the expressions are valid for water-saturated marine sediments. This basic understanding of the mechanisms at work in fully saturated sediments allows us to begin to address the problem of free gas. Free gas in sediments has been detected for some time (see Chapter 2), but it was not until the 1980s that more quantitative work began to be done on the acoustic and geotechnical properties of the sediment (e.g., Anderson and Hampton, 1980a, b; Wheeler, 1988a, b).

What follows is a description of some of the research done on the geoacoustic properties of sediments, and some of the effects that free gas can have on those properties.

3.2 Saturated sediments

3.2.1 Elastic properties

Hamilton investigated sediments from three different environments: the continental terrace (shelf and slope), the abyssal plain (turbidite) and the abyssal plain (pelagic). He proposed a number of empirical relationships between the geotechnical and acoustic properties of the sediments and compiled a series of reports (Hamilton, 1970, 1971a,b, 1972). The geotechnical properties considered include: porosity, density, bulk modulus (reciprocal of compressibility), dynamic shear modulus (or rigidity) and mean grain size.

The influence of geotechnical elastic parameters on acoustic properties may be derived from the 1-D wave equation for the velocity of a compressional-wave, V_p:

$$V_p = \left(\frac{K + 4/3\, G}{\rho} \right)^{1/2}, \qquad 3.1$$

where K is the bulk modulus of the sediment; G is the dynamic shear modulus of the sediment; and ρ is the density. If the sediment lacks rigidity (i.e., $G = 0$) then this equation reduces to Wood's (1955) equation and the sediment acts as a fluid. Evaluating the elastic moduli (K and G) is best done using the compressional- and shear-wave velocities of the sediment, but in the absence of such measurements, it is possible to compute these values from the volume contributions of the individual components of the sediment. Hamilton (1971a) made comparisons between a true bulk modulus, measured using compressional- and shear-wave velocity, and a calculated aggregate of the bulk moduli of the water and solid phases of the sediment alone. The results (Figure 3.1) indicate that the measured values are in excess of the aggregate, computed value. The difference is a structural, or frame, component of the sediment bulk modulus and the presence of rigidity affecting the compressional-wave velocity.

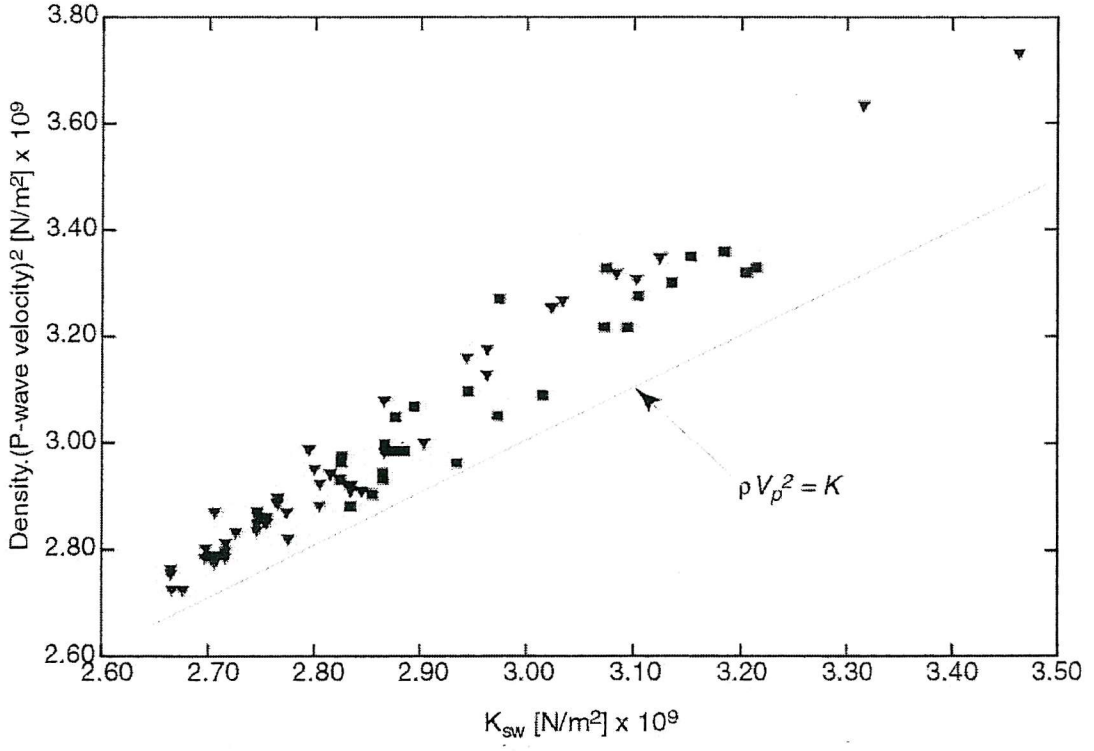

Figure 3.1. Bulk modulus calculated without a frame bulk modulus component versus density × (compressional-wave velocity)^2. Measured values from three different environments are plotted (abyssal hill, squares; abyssal plain, triangles) for

comparison. From Hamilton (1971a).

Packing of particles gives rise to an inherent structural elasticity and rigidity that is largely independent of the mineral grain properties. Packing of non-cohesive particles is responsible for the dynamic shear modulus (rigidity) of sediments such as sands. Clays have additional physicochemical forces acting between the particles that provide further resistance to shear; these forces are collectively known as cohesion.

Gassmann (1951) developed a method of deriving the bulk modulus, K, for saturated rocks from wave velocities measured on dry samples:

$$K = K_s \frac{K_f + Q_g}{K_s + Q_g}, \qquad 3.2$$

$$Q_g = \frac{K_w (K_s - K_f)}{n(K_s - K_w)}, \qquad 3.3$$

where K_s, K_f, K_w are the bulk moduli of the mineral grains, of the frame and of the pore water, respectively; and n is the porosity. Porosity, the ratio of the volume of the voids to the total sediment volume, is dependent on a number of factors, most importantly the size, shape, mineralogy and packing of the sediment grains. Sands assume positions among other grains under gravity and water flow effects and typically have porosities in the range 35% - 50% (Hamilton, 1970a). Sands are distinct from clays in that they are held together with the friction derived from grain to grain contacts and particle angularity (e.g., Figure 3.2). The structure of higher porosity silts and clays, however, is dominated by physicochemical forces.

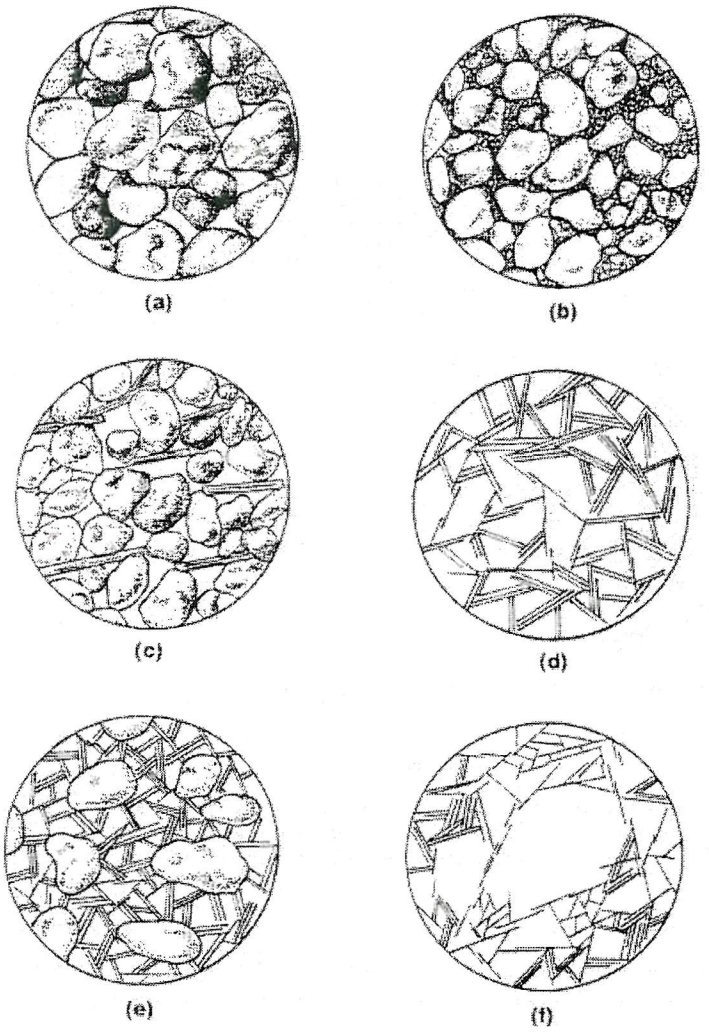

Figure 3.2. Common sediment structures: (a) single-grained structure, (b) mixed-grained structure, (c) bridging effect of platy minerals, (d) card-house structure of marine clay, (e) card-house structure of freshwater clay (dispersed), (f) card-house structure of marine silty clay. From Hamilton (1987).

The dynamic shear modulus of a sediment, G, is related to its structure and to various factors relating to interparticle movements under shear stresses. These include intergranular contacts and interlocking due to angularity. In coarse sands, there are few intergranular contacts, meaning that G will be comparatively low. As the grain size decreases, the porosity of the sand increases and, hence, the number of grain-to-grain contacts increases. This results in an increase in the dynamic shear modulus. At a certain porosity, there will be a maximum value of G where interlocking of the grains and the number of intergranular contacts are at a maximum. As the porosity increases further, more and more silt and clay material is present. This reduces the number of sand grains in contact with one another and cohesion generated by interparticle

physicochemical forces begin to dominate. Generally, in silts and clays, the cohesion (and, therefore, rigidity) decreases as porosity increases (Figure 3.3).

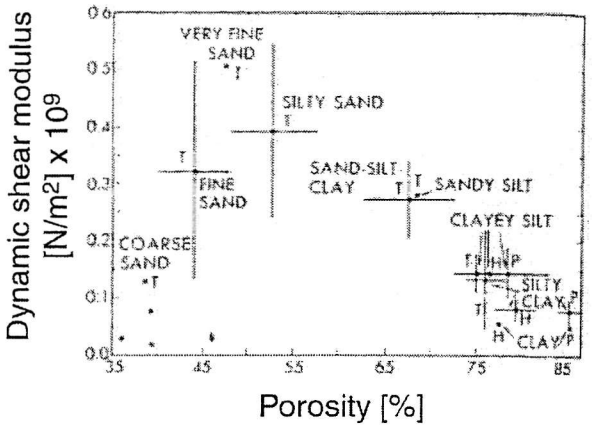

Figure 3.3. Sediment porosity versus dynamic shear modulus. From Hamilton (1971a).

In silts and clays, the particles may not be in contact with one another, and they interact through adsorbed water. Shear stresses are resisted through cohesion. Particles that touch may become cemented, or lithified, through pressure point solution and redeposition. Clay structure also has an influence on the geotechnical and elastic properties of the sediment. Different arrangements of particles will have different strength interparticle forces and the number of interparticle contacts may vary (Figure 3.4). In addition, different clay minerals have different strength interparticle forces.

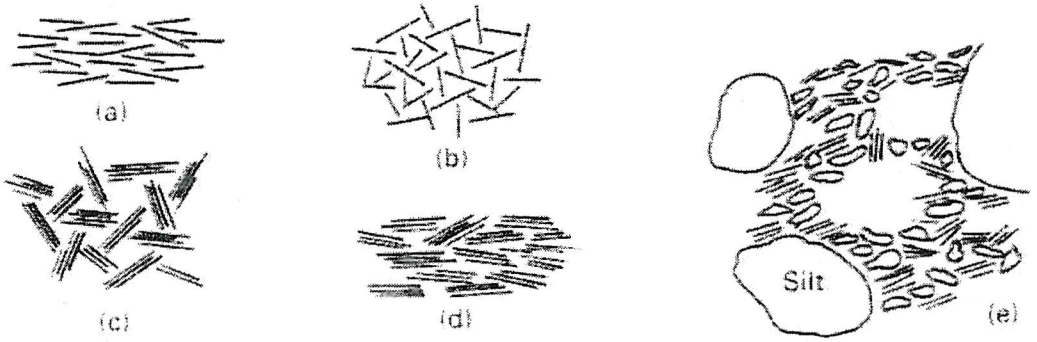

Figure 3.4. Clay structures: (a) dispersed, (b) flocculated, (c) bookhouse, (d) turbostratic, (e) example of a natural clay. From Craig (1992).

3.2.2 Attenuation

As discussed by Hamilton (1972), the main causes of intrinsic attenuation are thought to be viscous losses in the pore fluid and losses due to solid friction. However, many researchers now believe that solid friction is not important at low acoustic strains

($< 10^{-6}$). Winkler *et al.* (1979) measured the attenuation in rocks at different strains and confining pressures. They found that losses due to grain boundary friction were only important at low confining pressures and at strains greater than about 10^{-6}. In addition, Tittmann (1977) measured values of quality factor, Q (inversely proportional to attenuation), above 3000 in lunar rocks in an ultra-high vacuum apparatus. Measurements on the same sample in air gave a Q value of approximately 60. This dramatic drop in Q was thought to be due to the presence of adsorbed water in the rock. Although the exact mechanisms of attenuation in rocks are unknown, these two studies seem to indicate that most of the losses are due to pore fluid. However, viscous losses occur in two ways: global movement of the fluid relative to the sediment frame (which requires a permeable, porous frame), and local fluid motion at intergranular contacts (Stoll, 1980). However, measured values of attenuation include losses due to wavefront spreading, reflection, refraction, energy conversions and scattering as well as losses due to intrinsic mechanisms, and must, therefore, be considered an overestimate (McCann and McCann, 1985). In most sediments, Rayleigh scattering will only occur when the insonifying frequency reaches at least several hundred kilohertz, if not megahertz (Hamilton, 1972), when the wavelength is of a similar size to the grain diameter. The results of many authors work (e.g. Kibblewhite, 1989; Bowles, 1997) show that attenuation varies linearly with frequency:

$$\alpha = k.f^{n'}, \qquad 3.4$$

where k is a constant; and n' is the exponent of frequency. While n' is generally accepted to be approximately equal to one in the majority of sediments (Hamilton, 1972 and Figure 3.5), k varies according to a number of factors including sediment structure; porosity; grain size, shape and angularity; the number of interparticle contacts; and physicochemical forces (if any). These factors are similar to those that affect the dynamic shear modulus of the sediment.

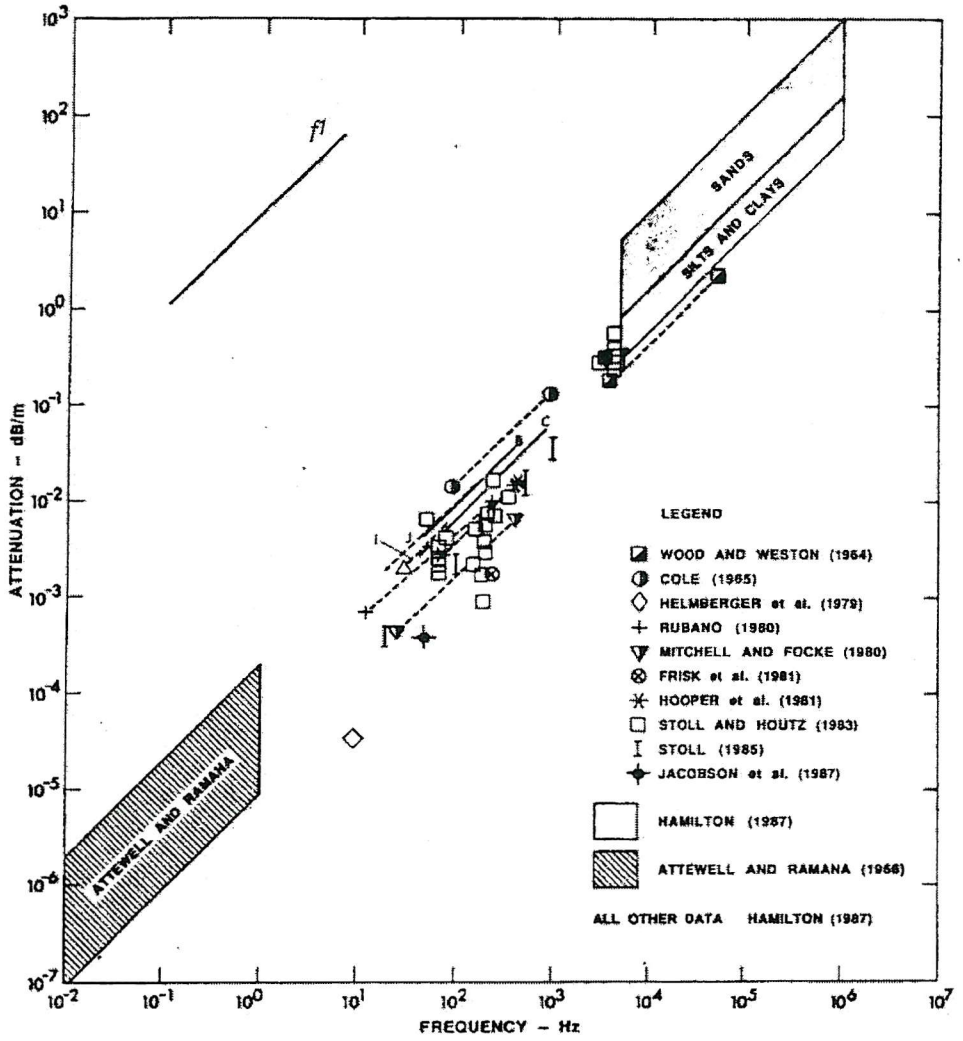

Figure 3.5. Compressional-wave attenuation versus frequency in silts and clays. From Kibblewhite (1989).

The high permeability of sands (compared with clays) means that viscous losses due to fluid motion relative to the sediment frame should dominate. A study of viscous attenuation (Hovem and Ingram, 1979) shows that the important parameters for viscous losses are the permeability, the grain size and the porosity, all of which are inter-related. Measured values of viscous attenuation compare well to theoretical values predicted by the Biot-Stoll model (Hovem and Ingram, 1979; Figure 3.6). It was found that at low frequencies the attenuation was related to f^2 and at higher frequencies the attenuation was related to $f^{1/2}$, although the relationship was close to f^1 in the frequency range (10 – 100 kHz) in which measurements are generally made (Hovem and Ingram, 1979; McCann and McCann, 1985; Figure 3.6). As frequency increases, the wavelength will reach a similar order of magnitude to that of the mineral grains and

Rayleigh scattering will occur and attenuation is related to f^4 (Busby and Richardson, 1957).

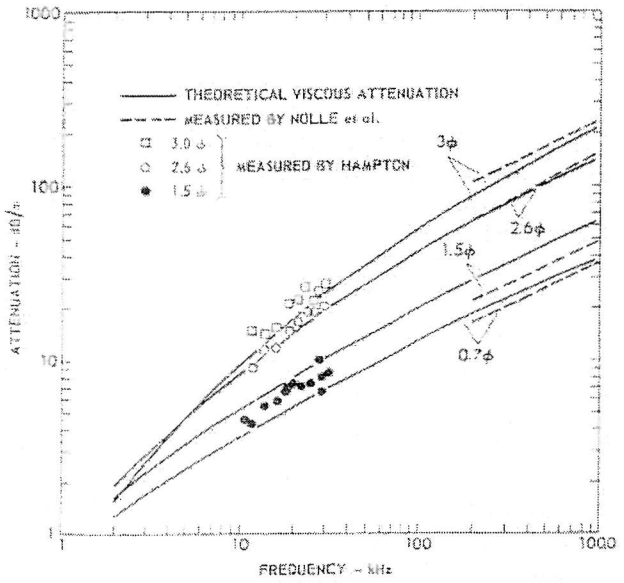

Figure 3.6. Attenuation in saturated sands versus frequency. From Hovem and Ingram (1979).

In silts and clays, or where permeability is low, viscous losses are dominated by local fluid motion at intergranular contacts, which is similar to "squeeze film" motion in lubrication theory (Stoll, 1980 and Figure 3.7).

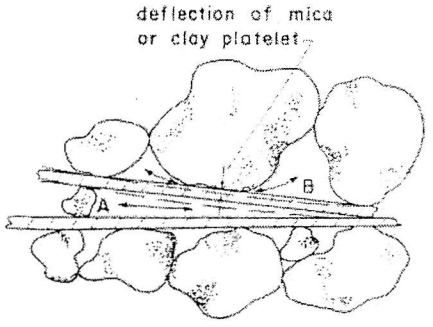

Figure 3.7. Schematic of sediment showing regions A and B where "squeeze film" motion of fluid occurs. From Stoll (1985).

When frame losses dominate (at low frequencies, for example), intergranular friction and grain angularity are the most important mechanisms, influencing the attenuation in the same way that they influence rigidity (see Section 3.1.1). Hamilton (1972) demonstrated this by plotting porosity against the constant of attenuation, k, (Figure 3.8). The shape of this graph is similar to that seen in Figure 3.3, a plot of

porosity versus dynamic shear modulus. Where grain angularity and number of intergranular contacts are at a maximum, the constant of attenuation, k, is at a maximum, meaning that the attenuation is at a maximum. As silt and clay size material becomes more common in the sediment, the number of intergranular contacts and the strength of the interparticle forces decrease with increasing porosity and the constant of attenuation decreases.

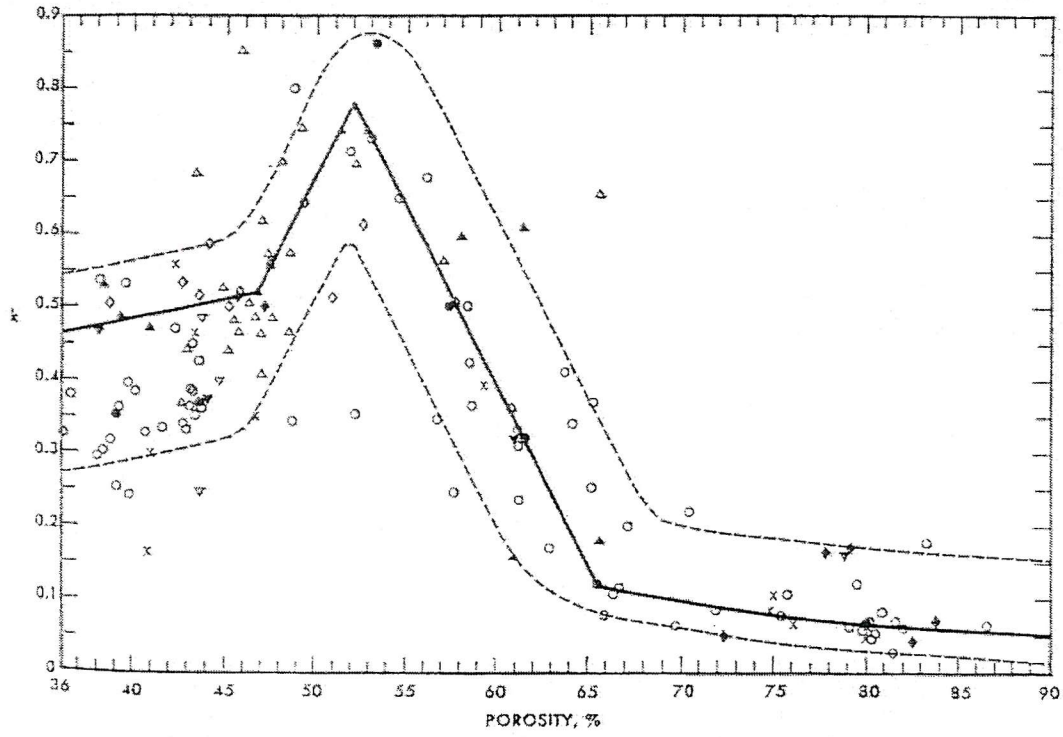

Figure 3.8. Porosity versus constant of compressional-wave attenuation, k, measured at 14 kHz. From Hamilton (1972).

3.2.3 Velocity

Equation 3.1 indicates that compressional-wave velocity is dependent on the density, bulk modulus and dynamic shear modulus of the sediment in question. In addition, the shear-wave velocity of a sediment, V_s, can be calculated from the 1-D wave equation:

$$V_s = \left(\frac{G}{\rho}\right)^{1/2}, \qquad 3.5$$

As with attenuation, factors which affect ρ, G and K will affect the wave velocity (both shear and compressional). Shumway (1958) measured the dependence of

compressional-wave velocity on temperature for both sediment and water. Results show that the variation of compressional-wave velocity in sediment with temperature follows the same profile as that measured in water (Figure 3.9).

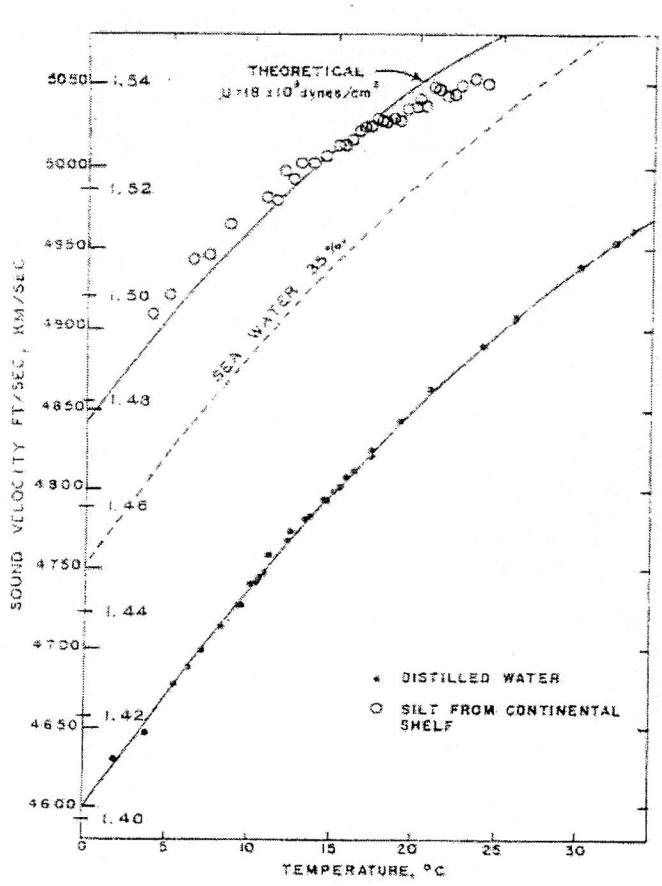

Figure 3.9. Compressional-wave velocity versus temperature in a continental shelf silt, seawater and distilled water. From Shumway (1958)

This variation is thought to be the result of the relatively large changes in bulk modulus (reciprocal of compressibility) of the water, compared to those of the mineral grains (Figure 3.10), imposed by the change in temperature. From these curves it is possible to infer that the frame bulk moduli and the dynamic shear modulus are comparatively unaffected by temperature.

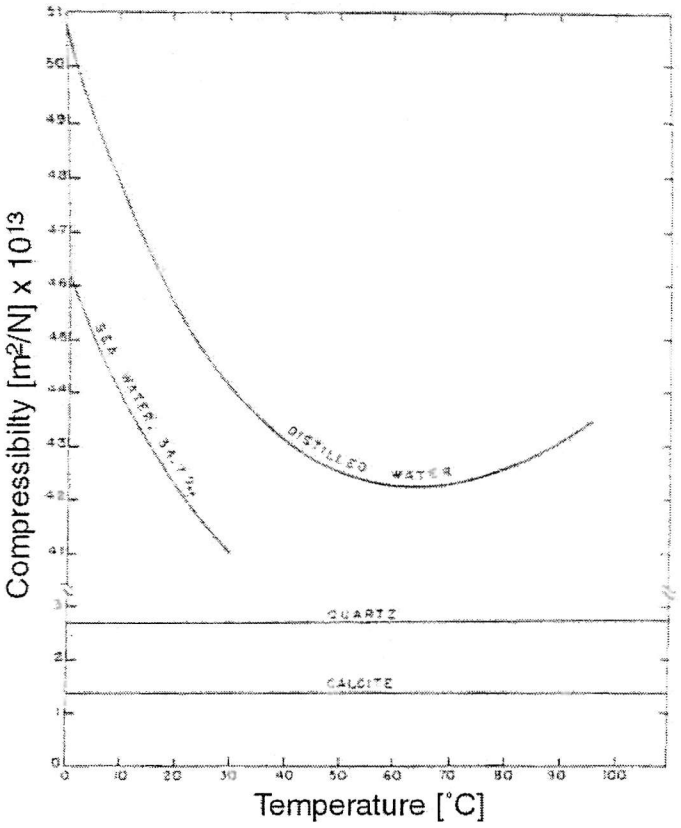

Figure 3.10. Compressibility versus temperature for distilled water, seawater, quartz and calcite. From Shumway (1958).

Overburden (or confining) pressure also has an effect on velocity. In the field of Soil Mechanics, the total overburden is the sum of: effective pressure, formed by the pressure of buoyed weight of the mineral grains and borne by the sediment frame, and pore water pressure (e.g., Craig, 1992). An increase in effective pressure will result in a decrease in porosity as a result of frame compression. With reduced porosity there will be less water per unit volume in the sediment, so the significant contribution of the highly compressible water (compare grain bulk modulus and water bulk modulus values at a constant temperature in Figure 3.10) to the total bulk modulus will be reduced, resulting in a higher net bulk modulus. In addition, the frame bulk modulus increases with decreasing porosity according to Gassmann's (1951) formulation (Hamilton, 1971a). Finally, increased pore water pressure and effective pressure will increase the bulk modulus of the pore water and the mineral grains (Hamilton, 1979) with the result that compressional-wave velocity is increased.

Reductions in porosity, other than those resulting from increased effective stress, also affect the rigidity and density of the sediment (Section 3.2.1). Mineral

grains are closer together, resulting in more inter-granular contacts and interlocking in the case of sands, increasing the sliding and rolling friction. In silts and clays, this results in higher cohesion. The net result is an increase in the dynamic shear modulus of the sediment. The increase in density in small compared to the increases in the elastic moduli, resulting in a net increase in compressional and shear-wave velocity (Hamilton, 1979).

Kolsky's (1956) experiments on stress pulses in viscoelastic solids provided evidence for a frequency-dependent velocity. Velocity dispersion in sediments is thought to be the result of energy losses due to the movement of fluid relative to the sediment frame (Biot, 1956a, b). Futterman (1962) later demonstrated that where attenuation is linearly proportional to frequency, velocity dispersion of the sound wave is implied by the principle of causality. However, Hamilton (1972) concluded that dispersion was negligible, citing a number of reports. Later measurements made by Wang and Nur (1990), and subsequently by Best and McCann (1995), on rock samples with differing pore fluid viscosity show velocity dispersion larger than that predicted by Biot theory in rocks with high viscosity pore fluid. It was concluded that the high dispersions were caused by a local fluid loss mechanism not accounted for in Biot theory, suggesting that dispersion may occur in non-cohesive sediments.

3.3 Gassy sediments

The presence of bubbles, of whatever type, will affect the overall geotechnical and acoustic properties of the sediment. Various models have been proposed to predict the effects of different types of gas bubble on these properties.

From a qualitative perspective, it is possible to predict some of the geotechnical and acoustic properties of the gassy sediment. For example, the presence of large bubbles (Type III) (see Section 2.6.1) will reduce the number of intergranular contacts and the density of the sediment, and thus affect the attenuation, shear strength and dynamic shear modulus. Reducing the dynamic shear modulus, in addition to reducing the net bulk modulus and the bulk density, results in a decrease in the sediment compressional- and shear-wave velocities. Alternatively, the presence of very small bubbles (Type I), existing in the pore spaces of the sediment, will affect only the compressibility of the pore fluid. What follows is a general description of the geotechnical and acoustic properties of such sediments.

3.3.1 Geotechnical and elastic properties

The presence of bubbles and their effects on the elastic moduli affect the shear strength of the sediment. As previously mentioned, gassy sediments may affect slope stability and Whelan *et al.* (1976) found the expected increase in shear strength with depth of burial was minimised when gas was present. Following a series of triaxial tests on gassy sediments, Wheeler (1988b) found that the undrained shear strength could be increased or decreased by the presence of gas. Increases were caused by bubble flooding and shrinking. The largest losses in shear strength were found to occur at low values of effective stress (close to the seabed) and at high values of total stress (i.e., pore water pressure and effective stress) (deepwater situations).

Gas pressure, u_g, is a significant parameter in modelling the effects of large, Type III bubbles and may be related to the pore pressure, u_w, the radius of curvature of the meniscus, R, and the value of surface tension, T:

$$u_g \approx u_w + \frac{2T}{R}, \qquad 3.6$$

Wheeler *et al.* (1990) placed limits on the value of the radius of curvature of the meniscus. The smallest radius of curvature cannot be less than a critical value, R_c, which is defined as the radius of curvature that just bridges the gaps between individual sediment particles. This lower bound is of the order of the pore throat size and would correspond to a situation where the gas pressure, u_g, is greater than the pore water pressure, u_w. The other extreme is where the pore water pressure is approximately equal to the gas pressure, and the radius of curvature is simply the radius of the bubble cavity, a (Figure3.11).

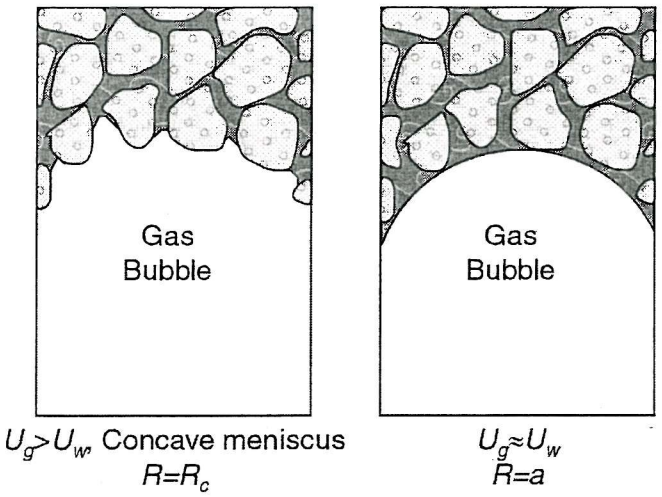

Figure 3.11. Bubble menisci curvatures. From Wheeler et al. *(1990).*

The pressure of gas inside the bubble may then be defined as:

$$u_w + \frac{2T}{a} \leq u_g \leq u_w + \frac{2T}{R_c}, \qquad 3.7$$

The difference between u_g and u_w (i.e., the surface tension component or gas overpressure) can vary greatly. Wheeler *et al.* (1990) assumed values for T (0.073 N/m, the value for air-water interfaces), a (0.4 mm) and R_c (0.5 μm, the size of a typical clay particle), and calculated that the difference can range from about 1 kPa to 300 kPa. If the difference between u_g and u_w falls below $2T/a$ then the bubble cavity will begin to flood. If the difference exceeds the value of $2T/R_c$ then the bubble will expand into the surrounding sediment. However, due to the fine-grained nature of many gassy sediments and the resulting high value of $2T/R_c$, cavity expansion and contraction will normally occur before flooding or movement of gas into the sediment matrix (Sills and Wheeler, 1992).

In sediments of a larger particle size (such as sands), the maximum and minimum radii of curvature are of the same order of magnitude (Sills and Wheeler, 1992), causing a small surface tension range resulting in the bubble moving into an adjacent water filled void or flooding, rather than cavity expansion or contraction, with changes in pressure. This mobility of bubbles in larger grained sediments means that bubbles may become trapped by an overlying layer of silt or clay material.

Gas bubbles move in fine-grained sediments either as small bubbles (Type I) through the normal void spaces of the sediment under buoyancy or pore water flow, or as large bubbles (Type III) (see Section 2.6.1).

3.3.2 Elastic modelling

The elastic properties of the sediment depend on the type of bubbles present. Three types of bubble have been described (Section 2.6.1; Figure 2.11) and each type of bubble will exert different influences on the sediment elastic moduli. There are various models described in the literature that may be used to predict the elastic moduli of gassy sediments for the three types of gas bubbles.

3.3.2.1 Type I bubble model

Type I bubbles are smaller than the surrounding sediment and hence fit within the normal pore spaces. They may be free floating, adhered to one or more particle walls or embedded in the roughness of the particles (Anderson *et al.*, 1998). They are

often too small to see and it is not possible to detect them using X-ray CT as this method has a minimum resolution of about 0.42mm (Anderson *et al.*, 1998). Due to their existence within the pore water of the sediment, they affect only the compressibility of the pore water (Wheeler, 1988a). Modelling of the sediment elastic moduli is relatively simple because it is only necessary to adjust the compressibility of the water to allow for the gas. Additionally, small bubbles will have no effect on the dynamic shear modulus (also known as the rigidity modulus) because fluids are unable to sustain any shear stresses and any shear stress travelling through the sediment will be transmitted by the solid phase of the sediment. Anderson and Hampton (1980a, b) formulated an expression based on Gassmann's (1951) expression (Equations 3.2 and 3.3) where the bulk modulus of the pore water, K_w, in the calculation of the parameter Q is substituted for a bulk modulus, K_{wg}, that accounts for the compressibility of the gas, K_g:

$$K_{wg} = \frac{K_w K_g}{\frac{n_g}{n} K_w + \left(1 - \frac{n_g}{n}\right) K_g}, \qquad 3.8$$

where n is the porosity; and n_g is the gas porosity (gas volume / total sediment volume). If this Type I model were to be used in the investigation of Type III bubbles, the effects of large cavities must be accounted for in the formulation of the bulk modulus of the frame, since any large cavity would ultimately make the frame more compressible. In addition, any effect of the cavities on the dynamic shear modulus must be considered. These factors are not accounted for in Anderson and Hampton (1980a, b) and this model may, therefore, only be used in the modelling of Type I bubble systems.

3.3.2.2 Type II bubble model

Type II bubbles have been observed in some cores and their effects on the elastic moduli have been modelled by Domenico (1977). His results are based on those of Geertsma (1961) whose work was an extension of Biot's (1956a, b) equations for a fluid-saturated porous solid and are essentially the same as those obtained by Gassmann (1951). The model assumes that the fluid compressibility is the weighted-by-volume average of the gas and liquid (brine) compressibilities and that the bulk compressibility is a weighted-by-volume average of the fluid compressibility and the grain compressibility. This implies an even distribution of liquid and gas throughout

the sediment pore space and takes no account of the sediment frame compressibility effects (if any). This type of bubble is often very small, perhaps only just larger than the sediment particles and they affect the fluid bulk modulus in much the same way Type I bubbles. As a result are this type of model is unsuitable for modelling gas found in fine-grained sediments.

3.3.2.3 Type III bubble model

Wheeler (1988a) developed a conceptual model for sediments containing large, Type III gas bubbles. Due to their size, each bubble is surrounded by many mineral particles and the outer edge of the bubble is in contact with these mineral particles and the interstitial water. He proposed that, rather than considering the gassy sediment as a three-phase sediment, the mineral and water phases are combined to form a single phase of saturated sediment, the properties of which may be measured (Figure 3.12).

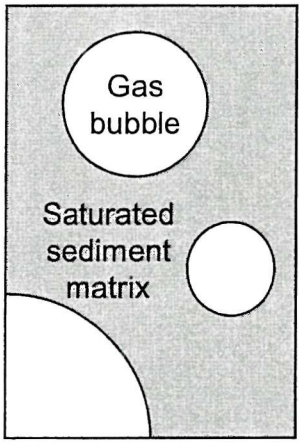

Figure 3.12. Continuum model of sediment containing Type III bubbles. From Wheeler (1988a).

Wheeler and Gardner (1989) used this model to produce theoretical expressions for the dynamic shear and bulk moduli by assuming the saturated sediment matrix acts as a simple elastic material because sediments react elastically (in terms of velocity, not attenuation) to the strains generated by the passage of an acoustic signal. This theory is based on work by Hill (1965) who considered the elastic behaviour of a composite material comprising a volume fraction, n_g, of spherical inclusions in a matrix described by the moduli K_{inc} and G_{inc} for the inclusions, and K_{mat} and G_{mat} for the matrix. A set of equations were derived by Hill (1965) to predict the composite moduli, K_{comp} and G_{comp}:

$$\frac{n_g}{(K_{comp}-K_{mat})}+\frac{(1-n_g)}{(K_{comp}-K_{inc})}=\frac{\alpha}{K_{comp}}, \qquad 3.9$$

$$\frac{n_g}{(G_{comp}-G_{mat})}+\frac{(1-n_g)}{(G_{comp}-G_{inc})}=\frac{\beta}{G_{comp}}, \qquad 3.10$$

$$\text{where } \alpha=3-5\beta=\frac{K_{comp}}{K_{comp}+\frac{4}{3}G_{comp}}, \qquad 3.11$$

Wheeler and Gardner (1989) rearranged Hill's (1965) equations to produce a quartic equation for G_{comp}:

$$\frac{n_g K_{inc}}{K_{inc}+\frac{4}{3}G_{comp}}+\frac{(1-n_g)K_{mat}}{K_{mat}+\frac{4}{3}G_{comp}}+\frac{5n_g G_{mat}}{G_{comp}-G_{mat}}+\frac{5(1-n_g)G_{inc}}{G_{comp}-G_{inc}}+2=0, \qquad 3.12$$

By replacing Hill's (1965) moduli with those for gassy sediments such that:

$$K_{inc}=K_g,\ G_{inc}=0,\ K_{mat}=K_m,\ G_{mat}=G_m,\ K_{comp}=K,\ G_{comp}=G, \qquad 3.13$$

and substituting Conditions 3.13 into Equation 3.12, an expression for G, the gassy sediment dynamic shear modulus, and then K, the gassy sediment bulk modulus, may be found:

$$\frac{n_g K_g}{K_g+\frac{4}{3}G}+\frac{(1-n_g)K_m}{K_m+\frac{4}{3}G}+\frac{5n_g G_m}{G-G_m}+2=0, \qquad 3.14$$

$$K=\frac{4G(5n_g G_m-2(G_m-G))}{3(3(G_m-G)-5n_g G_m)}, \qquad 3.15$$

Notice that in this system of equations there is no requirement to know variables such as the bulk modulus of the interstitial water, the frame bulk modulus or the bulk modulus of the sediment particles. This is because they are accounted for in the saturated sediment matrix bulk modulus with may be directly measured using geotechnical or acoustic testing techniques on fully saturated sediments or obtained from the literature (e.g., Hamilton, 1971a).

3.3.3 Attenuation

Attenuation coefficients measured in gassy sediments are significantly higher than those measured in saturated sediments. Wood and Weston's (1964) experiments on laboratory mud, from which they saw gas escaping, showed attenuations of 1740 dB/m at 8 kHz and 2395 dB/m at 14 kHz. Edrington and Calloway (1984) measured the constant of attenuation, k (Equation 3.4), in gassy sediments found in the Gulf of Mexico. Their results indicated a value of 1.4 dB / kHz.m, which they state as being an

order of magnitude greater than values seen in saturated sediments. Measurements of quality factor, Q, by Wood *et al.* (2000) also indicate high attenuation with Q being inversely related to attenuation:

$$A(t) = A_0\left[1-\frac{\pi f t}{Qn}\right]^n, \qquad 3.16$$

where $A(t)$ is the amplitude of a signal of frequency f; after travelling for a length of time t, and a number of cycles n, through a medium with a quality factor Q, and with a starting amplitude of A_0 (Wood *et al.*, 2000). Values of Q less than 90, some as low as 6, were measured in areas associated with free gas, compared to saturated sediment values ranging from 90 to 600. Gardner (2000) measured attenuation in a laboratory prepared gassy sediment. The sample was produced using the zeolite technique described by Nageswaran (1983) and gas fraction and bubble size distribution were measured using scanning electron microscope techniques. Attenuation coefficients of 6000 dB/m were reported for the highest frequencies (~100 kHz). Samples with very little, or no, gas present show attenuation coefficients of 100 dB/m at 700 kHz. This value is comparable to data for a fully saturated soil (Hamilton, 1972; Figure 3.5).

The widely accepted explanation for these extremely high attenuation coefficients is that they are the result of bubble scattering and resonance, such as with bubbles in water (Anderson and Hampton, 1980a, b). Bubbles of gas in water vibrate when excited by acoustic energy. If the insonifying frequency is of the correct frequency, the bubble will resonate. The resonant frequency, f_0, is adequately defined by Minnaert's (1933) equation:

$$f_0 = \frac{1}{2\pi r_0}\left(\frac{3\gamma P_0}{\rho_w}\right)^{1/2}, \qquad 3.17$$

where r_0 is the bubble radius; γ is the ratio of the specific heats of the gas (the ratio of the specific heat at constant pressure to the specific heat at constant volume); P_0 is the ambient hydrostatic pressure; and ρ_w is the water density. Resonance of the bubble causes its scattering cross section to be at a maximum, and, hence, the effective attenuation is at a maximum.

3.3.4 Velocity

Compressional-wave velocity in gassy sediments is generally lower than that found in saturated sediments, sometimes by an order of magnitude. Edrington and Calloway (1984) measured a compressional-wave velocity of approximately 800 m/s in soft clays found in the Gulf of Mexico. Tinkle *et al.* (1988) routinely measured velocities less than approximately 300 m/s in the gassy sediments of the Mississippi Delta, the lowest measurement being approximately 115 m/s.

In water, the compressional-wave velocity of bubbly water is less than that of bubble-free water below resonance. Above resonance, the compressional-wave velocity is the same as that in bubble-free water (Anderson and Hampton, 1980a, b; Chapter 4). A similar phenomenon is thought to occur in sediments. A decrease in the compressional wave velocity is related to bubble size and insonifying frequency. When the insonifying frequency is below the resonant frequency the compressional-wave velocity is determined by the bulk sediment properties (Figure 3.13). The high compressibility of the gas (compressibility is inverse bulk modulus) compared to the surrounding saturated sediment matrix means that the net bulk modulus and dynamic shear modulus decrease, resulting in a net reduction of compressional-wave velocity. If the insonifying frequency is greater than the resonant frequency of the bubble, the compressional-wave velocity is determined by the surrounding saturated sediment matrix (Sills *et al.*, 1991). As the insonifying frequency approaches the resonant zone, compressional-wave velocity decreases from its below resonance value and then increases rapidly as the insonifying frequency passes through the resonant zone before finally dropping to that found above resonance (i.e., the velocity expected of gas-free sediments).

Anderson and Hampton (1980a, b) developed a model predicting the acoustic properties of gassy sediments based on the theory of the acoustics of bubbly water, and a synopsis of this model is given in detail in Chapter 4.

3.4 Summary

From the discussion, it can be seen that attenuation is due to two main mechanisms: frictional losses due to grain sliding and rolling, and viscous losses. Viscous losses may be further subdivided into: losses due to global fluid motion relative to the sediment frame and losses due to local fluid motion – "squeeze film". In

general, for non-gassy sediments attenuation is linearly proportional to the frequency (Hamilton, 1972), although this may vary between a square dependency at low frequencies to a square root dependency at high frequencies (Hovem and Ingram, 1979). These mechanisms are affected by porosity (which is related to overburden pressure and the grain size distribution), and by permeability and viscosity.

Compressional-wave velocity is dependent on the bulk modulus and the dynamic shear modulus of the sediment. The bulk modulus is calculated as a composite of the bulk moduli of the sediment grains, the pore fluid and the frame, as described by Gassmann (1951). The shear modulus is a function of intergranular contacts, grain angularity and cohesion.

If the gas manifests itself in small, Type I bubbles, then it affects only the compressibility of the pore fluid. The bulk modulus may be calculated by substituting the bulk modulus of the water for a value accounting for the increased compressibility of the gas. However, most bubbles are of the large, Type III variety and they also affect the frame bulk modulus and the dynamic shear modulus.

Bubbles affect the acoustics of the sediment by resonating, and the resonant frequency is dependent mainly on the radius of the bubble. At resonance, the scattering cross-section of the bubble is at a maximum, and so is the attenuation. At frequencies below resonance, the wavelength is much greater than the radius of the bubble and the compressional-wave velocity is determined by the net bulk modulus of the gassy sediment, which is much lower than in the saturated sediment. Hence, the compressional-wave velocity is reduced. Above resonance the wavelength is of the same order of magnitude as the bubble radius and the waves are unaffected by the gas (Sills *et al.*, 1991), except where scattering occurs.

Chapter 4. Acoustic modelling of gassy sediments

4.1 Introduction

Prior to the work of Anderson and Hampton (1980a, b), the majority of research into gassy sediments was focused on confirmation of the presence of gas acoustically and on the biogeochemical systems producing the gas (Chapter 2). Anderson and Hampton (1980a, b) attempted to provide a basic framework for predicting the acoustic properties of gassy sediment, in terms of the compressional-wave velocity and attenuation, and their model is discussed in this chapter. It has been used by Wilkens and Richardson (1998) to predict the velocity and attenuation characteristics of gassy sediments found in Eckernförde Bay, and Gardner (2000) confirmed some of the predictions of the model by experiment. It was decided, therefore, to use this model to predict the velocity and attenuation characteristics of the gassy sediments in Dibden Bay.

The acoustic properties of gassy sediments are dominated by bubble resonance and scattering, in a similar way to the acoustic properties of bubbly water, and Anderson and Hampton (1980a, b) formulated their model based on the theory of acoustic propagation in bubbly water.

4.2 Acoustic propagation in bubbly water

In order to understand acoustic propagation in bubbly water, it is necessary to appreciate the mechanics of bubble motion. It is known that bubbles in water resonate when excited by an insonifying frequency equal to the bubble resonant frequency, and that this resonance affects both the attenuation and velocity characteristics of the water. In the system, the water acts as a vibrating mass, with the gas bubble supplying the restoring force. The resonant frequency, f_0, of bubbles, of radius r_0, may be calculated using Minnaert's (1933) equation (Equation 3.17). However, this expression assumes an adiabatic equation of state for the gas in the bubble. Devin (1959), while investigating the damping of pulsating bubbles, proposed that expansion and contraction occurred polytropically (i.e., pressure and volume change in such a way that the specific heat remains constant). Therefore, a polytropic coefficient, A, must be inserted into Minnaert's (1933) expression:

$$f_0 = \frac{1}{2\pi r_0}\left(\frac{3\gamma P_0}{A\rho_w}\right)^{1/2}, \quad 4.1$$

$$A = (1+B^2)\left[1+\frac{3(\gamma-1)}{X}\left(\frac{\sinh X-\sin X}{\cosh X-\cos X}\right)\right], \quad 4.2$$

$$B = 3(\gamma-1)\left(\frac{X(\sinh X+\sin X)-2(\cosh X-\cos X)}{X^2(\cosh X-\cos X)+3X(\gamma-1)(\sinh X-\sin X)}\right), \quad 4.3$$

$$X = r_0\sqrt{\frac{2\omega\rho_g s_p}{C_g}} \quad 4.4$$

where P_0 is the ambient hydrostatic pressure; γ is the ratio of the specific heats of the gas; ρ_w and ρ_g are the densities of the water and gas, respectively; ω is the angular frequency; s_p is the specific heat at constant pressure of the gas; and C_g is the thermal conductivity of the gas.

The oscillation of bubbles in water is subject to damping. Devin (1959) concluded that bubble damping at resonance occurred through three mechanisms:

- thermal damping, d_t - the work done compressing the bubble is more than the work done by the bubble in expanding and the difference is discharged as heat into the surrounding liquid.
- radiation damping, d_r - a pulsating bubble loses energy by generating sound waves.
- viscous damping, d_v - viscous forces acting at the bubble boundary exert an excess pressure resulting in the dissipation of energy.

The total damping of the bubble, d, is the sum of these.

Eller (1970) extended the work of Devin (1959) and produced expressions for each component for both at resonance and off resonance:

$$d_t = B \quad 4.5$$

$$d_r = \frac{\rho_w r_0^3 \omega^3 A}{3\gamma P_0 c_0} \quad 4.6$$

$$d_v = \frac{4\omega\mu A}{3\gamma P_0} \quad 4.7$$

where μ is the viscosity of the gas-free liquid; and c_0 is the compressional-wave velocity in bubble-free water.

Silberman (1957) proposed an expression to calculate the compressional-wave velocity in bubbly water, c, for a distribution of bubbles of radius r:

$$\left(\frac{c_0}{c}\right)^2 = \frac{1+a_w X_*}{2}\left\{1 \pm \left[1+\left(\frac{a_w Y_*}{1+a_w X_*}\right)^2\right]^{1/2}\right\} \qquad 4.8$$

$$X_* = \frac{v_g\left(1-f_*^2\right)}{\left(1-f_*^2\right)^2 + d_*^2} \qquad 4.9$$

$$Y_* = \frac{v_g d_*}{\left(1-f_*^2\right)^2 + d_*^2} \qquad 4.10$$

$$a_w = \frac{K_w}{\gamma P_0} \qquad 4.11$$

$$f_* = \frac{f}{f_0} \qquad 4.12$$

$$d_* = d f_*^2 \qquad 4.13$$

where v_g is the volume concentration of bubbles; K_w is the bulk modulus of the water; f is the insonifying frequency; and d is the damping factor obtained from Spitzer (1943). If there is a range of bubble sizes present, described as m individual radii, then Silberman (1957) proposes that X_* and Y_* are replaced by X_M and Y_M:

$$X_M = \sum_{i=1}^{m} \frac{v_i\left(1-f_{*i}^2\right)}{\left(1-f_{*i}^2\right)^2 + d_{*i}^2} \qquad 4.14$$

$$Y_M = \sum_{i=1}^{m} \frac{v_i d_{*i}}{\left(1-f_{*i}^2\right)^2 + d_{*i}^2} \qquad 4.15$$

where v_i is the volume concentration for bubble radius r_i etc.

The theoretical compressional-wave velocity through a screen of single sized bubbles is shown in Figure 4.1, assuming small v_g.

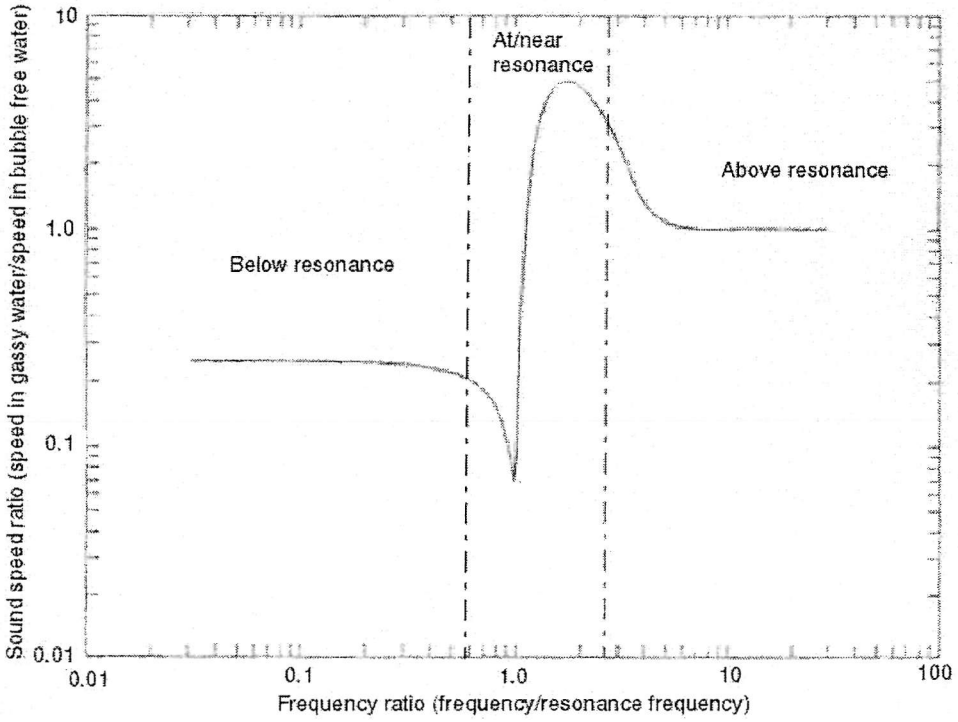

Figure 4.1. Sound speed ratio (c / c_0) versus frequency ratio (f / f_0) for bubbly water with a single bubble size. From Anderson and Hampton (1980a).

If the insonifying frequency is below the resonant frequency of the bubble, the acoustic wavelength is longer than the bubble radius and the compressional-wave velocity is determined from the bulk acoustical properties of the water. The presence of the gas bubbles decreases both the bulk modulus and density of the water, and the compressional-wave velocity is below that of bubble-free water.

At or near resonance, the changes in pressure and volume within the bubble begin to differ in phase and the mixture is highly dispersive. Slightly above resonant frequency, the acoustic wavelength is of an equivalent, or smaller, size to the bubble and the bubble then acts as a discrete scatterer of energy. The phase difference of the pressure and volume changes makes it possible for the mixture to have a greater bulk modulus than that of bubble-free water, and the compressional-wave velocity is greater than that seen in bubble-free water.

At higher frequencies still, the velocity approaches that of bubble-free water. The acoustic wavelength is small enough that the average parameters of the mixture do not describe the path that the wave takes, and the wave propagates at the same speed as in pure water.

This theoretical behaviour has been confirmed by experiment. Laird and Kendig (1952) measured the compressional-wave velocity of water containing 0.045 percent air by volume in single sized bubbles. They found that, at low frequencies, the velocity was approximately one-third the value for bubble-free water and, at high frequencies, the phase velocity approached the value of that found in bubble-free water. Similar results were recorded by Fox *et al.* (1955), with phase velocity varying from 500 m/s to approximately 2300 m/s (Figure 4.2).

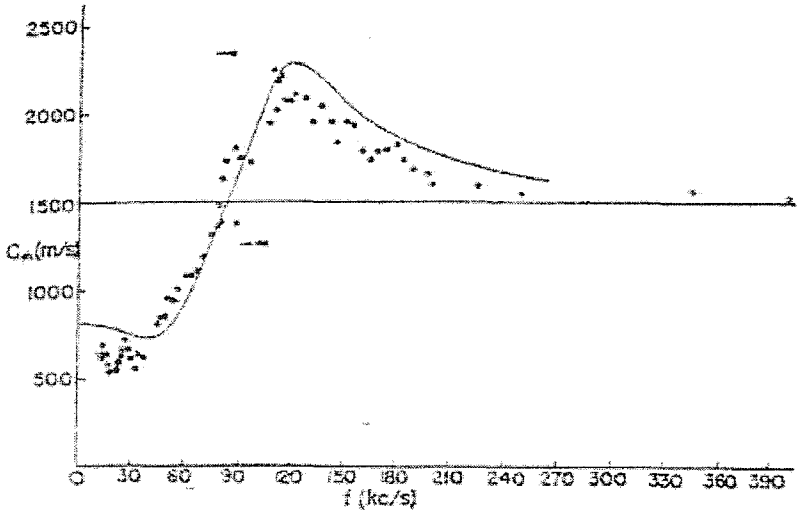

Figure 4.2. Phase velocity versus frequency measurements in bubbly water. From Fox et al. *(1955).*

Attenuation in bubbly water is dominated by scattering, with energy being radiated omnidirectionally. The scattering cross section of a bubble is maximum at resonance (Figure 4.3).

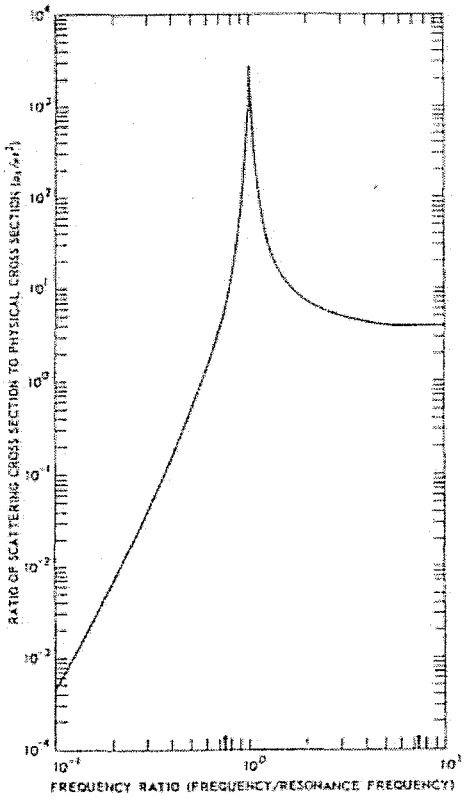

Figure 4.3. Normalised scattering cross section versus frequency ratio for water with a single bubble size. From Anderson and Hampton (1980a).

Laird and Kendig (1952) measured the compressional-wave attenuation in bubbly water containing 0.045 percent air by volume and found values as high as 790 dB/m at 10 kHz. Fox *et al.* (1955) recorded a peak attenuation of 3000 dB/m at approximately 70 kHz at resonance (Figure 4.4). The frequency observed is close to that for resonance in their phase velocity results (Figure 4.2).

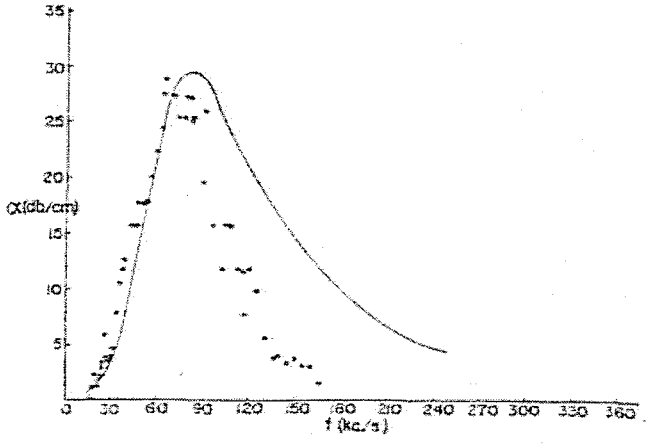

Figure 4.4. Attenuation measurements versus frequency in bubbly water. From Fox et al. *(1955).*

Silberman (1957) also proposed an expression for the attenuation of bubbly water, α:

$$\alpha = \frac{\pi f}{c_0} \cdot \frac{c}{c_0} \cdot a_w Y_* \qquad 4.16$$

In the same manner as for the compressional-wave velocity, the attenuation due to a distribution of bubbles may be calculated by substituting Y_* for Y_M. Measurements made in a standing wave tube by Silberman (1957) appear to confirm this result (Figure 4.5).

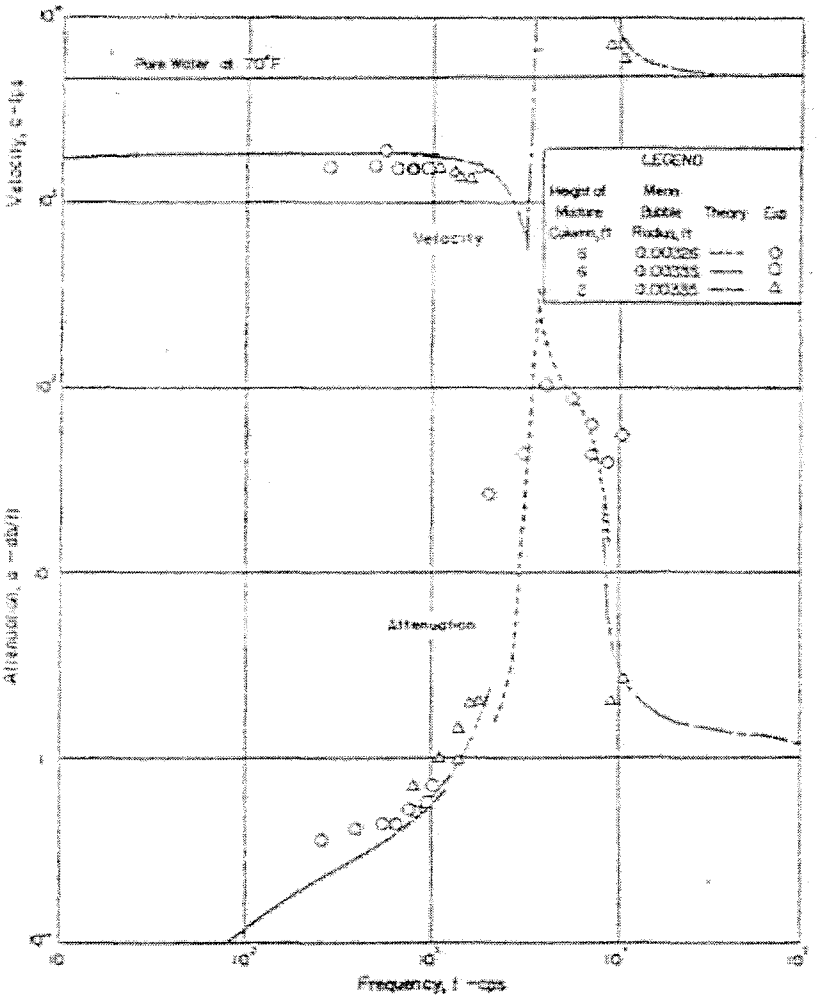

Figure 4.5. Phase velocity and attenuation coefficient in bubbly water, theory and measurements, $v_g = 3.77 \times 10^{-4}$, $r \approx 1$ *mm (0.0035 ft). From Silberman (1957).*

4.3 The acoustics of bubbles in sediments

Unlike water, sediments have rigidity, and bubble resonant frequency and damping is affected. As in water, the surrounding sediment acts as the vibrating mass,

and the restoring force is provided by the gas bubble and by the elasticity of the surrounding material. Meyer *et al.* (1958) found that the resonant frequency, f_0, of an empty spherical cavity, of radius r_0, in rubber could be described by:

$$f_0 = \frac{1}{2\pi r_0}\left(\frac{4G}{\rho_s}\right)^{1/2} \qquad 4.17$$

where G is the dynamic shear modulus of the material, and ρ_s is the density of the material. However, this expression does not account for the response of the gas inside the cavity, as described by Equation 4.1. Inserting this term results in the resonant frequency equation presented by Anderson and Hampton (1980b):

$$f_0 = \frac{1}{2\pi r_0}\left(\frac{3\gamma P_0}{A\rho_s} + \frac{4G}{\rho_s}\right)^{1/2} \qquad 4.18$$

It can be seen from the expression that if the solid component loses all rigidity (i.e. the dynamic shear modulus = 0) then the resonant frequency becomes that for a bubble in water (Equation 4.1). If the sediment becomes very rigid (i.e., the dynamic shear modulus becomes very large), then the resonant frequency becomes that predicted by Meyer *et al.* (1958).

Bubble motion in sediment is damped by similar mechanisms to those for bubbles in water. Instead of viscous losses due to surrounding fluid motion, however, there will be frictional losses due to motion of the surrounding sediment. Thermal losses due to the expansion and contraction of the gas bubble will remain the same. Weston (1967) investigated the propagation of sound in the presence of bladder fish and noted that the radiation damping at resonance could be predicted by the equation:

$$d_r = k_0 r_0 \qquad 4.19$$

$$k_0 = \frac{\omega_0}{c_0} \qquad 4.20$$

$$\omega_0 = 2\pi f_0 \qquad 4.21$$

Anderson and Hampton (1980a) state that to account for radiation losses off resonance the expression must be modified, such that:

$$d_r = kr\left(\frac{\omega_0}{\omega}\right)^2 \qquad 4.22$$

where k is the wavenumber at frequency f. It can be seen that at resonance (i.e., $f = f_0$) Equation 4.22 is the same as Equation 4.19. They state that this is equivalent to

the radiation damping for bubbles in water (Equation 4.6), if the resonant frequency is calculated using Equation 4.1. This is not the case however, since rearranging Equation 4.1 gives:

$$\frac{A\rho_w}{3\gamma P_0} = \frac{1}{\omega_0^2 r_0^2}$$

Substituting into Equation 4.6 gives:

$$d_r = \frac{r_0^3 \omega^3}{c_0} \cdot \frac{1}{\omega_0^2 r_0^2} = \frac{r_0 \omega}{c_0} \cdot \left(\frac{\omega}{\omega_0}\right)^2$$

Since:

$$k = \frac{\omega}{c_0},$$

$$d_r = kr\left(\frac{\omega}{\omega_0}\right)^2$$

Hence, the (ω_0/ω) term in Equation 4.22 stated by Anderson and Hampton (1980a) is in error. It was later concluded by Anderson (pers. comm.) that there is, in fact, no special off-resonance frequency dependence of the radiation damping term, with the only frequency dependence being derived from the frequency dependence of k. The radiation damping term is, therefore:

$$d_r = kr \qquad 4.23$$

Weston (1967), after Andreeva (1964), calculates damping due to fish tissue (or any other surrounding medium):

$$d_f = \frac{4G'}{\rho_s \omega_0^2 r_0^2} \qquad 4.24$$

where G' is the imaginary component of the complex shear modulus, $G_* = G + iG'$, of the surrounding material (in this case, fish tissue). This expression is used by Anderson and Hampton (1980b) to account for damping due to frictional losses.

In order to calculate the gassy sediment sound speed, Anderson and Hampton (1980b) adjust Equation 4.8:

$$\left(\frac{c_0}{c}\right)^2 = \frac{1 + a_s X_*}{2}\left\{1 \pm \left[1 + \left(\frac{a_s Y_*}{1 + a_s X_*}\right)^2\right]^{1/2}\right\} \qquad 4.26$$

$$a_s = \frac{K_{sat}}{\gamma P_0 + 4/3\, G} \qquad 4.27$$

where K_{sat} is the bulk modulus of the saturated sediment. In the parameters X_* and Y_*, the volume concentration of bubbles is replaced by gas porosity, n_g. Gas porosity is the ratio of gas volume to the total sediment volume. The main difference between this expression and Silberman's (1957) is the adaptation of the parameter a_s to account for sediment structure. Anderson and Hampton (1980b) give little explanation into the physical meaning of this adjustment, but a later explanation by Anderson (pers. comm.) indicates that this is to account for the tendency of the cavity wall to resist deformation.

In support of the theory, Anderson and Hampton (1980b) cite a number of authors. Jones *et al.* (1964) reported negative seafloor reflection coefficients in Lake Travis, Texas, below 3.2 kHz, indicating either a lower sediment compressional wave velocity than the overlying water, a lower density than the overlying water, or both. Muir (1972) detected compressional wave velocities within 1% of the overlying water compressional-wave velocity in the same lake at 40 kHz.

Attenuation is calculated in much the same way as compressional-wave velocity. The parameter a_w in Equation 4.16 is simply replaced by the parameter a_s (Equation 4.27), thus:

$$\alpha = \frac{\pi f}{c_0} \cdot \frac{c}{c_0} \cdot a_s Y_* \qquad 4.28$$

Typical results of the model (Equations 4.26 and 4.28), using values from Table 1, may be seen in Figure 4.6. Saturated sediment bulk modulus was calculated using Equations 3.2 and 3.3. Saturated sediment compressional wave velocity was calculated using Equation 3.1.

Sediment porosity	0.61 *
Saturated sediment density, ρ_{sat}	1475 kg.m^{-3} *
Mineral bulk modulus, K_m	3.6×10^{10} N.m^{-2} †
Frame bulk modulus, K_f	1.389×10^{8} N.m^{-2} ‡
Interstitial water bulk modulus, K_w ($= \rho V_w^2$)	2.24×10^{9} N.m^{-2}
Dynamic shear modulus, G	2.813×10^{5} N.m^{-2} †
Imaginary part of shear modulus, G'	1×10^{4} N.m^{-2} *
Bubble radius, r	$0.01\text{-}10 \times 10^{-3}$ m
Gas porosity, n_g	0.0001, 0.001, 0.01
Gas density, ρ_g	0.717 kg.m^{-3} at STP ¥
Specific heat at constant pressure of gas, S_p	2.19 J.kg^{-1}.°C^{-1} ¥
Thermal conductivity of gas, C_g	3.11×10^{-2} J.s^{-1}.m^{-1}.°C^{-1} ¥
Ratio of the specific heats of the gas, γ	1.31 ¥

† Value from Wilkens and Richardson (1998) * Estimated values
‡ Calculated from results in Hamilton (1971a) ¥ From Kaye and Laby (1995)

Table 4.1. Parameters used in model.

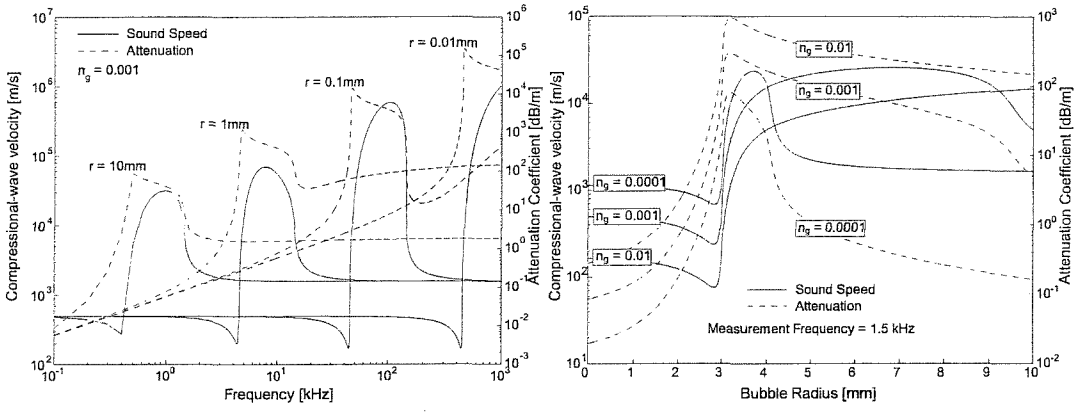

(a) (b)

Figure 4.6. Model results of sound speed and attenuation in a fine-grained, gassy sediment for (a) constant bubble radius and gas porosity versus measurement frequency and (b) constant measurement frequency and gas porosity versus bubble radius.

The results displayed illustrate the dependence of resonant frequency on both gas porosity and bubble radius. Larger bubble radii have lower resonant frequencies than smaller radii bubbles (Figure 4.6b). For a single insonifying frequency, there is a single bubble radius at which resonance occurs (Figure 4.6b), depending on the properties of the surrounding material.

4.4 Summary

Anderson and Hampton (1980a, b) base their model on the theories of bubble resonance in water. Recent results (Gardner, 2000) suggest that the model predicts the

acoustic response of gassy sediment both above and below resonance, although predictions in the resonant range of the bubbles are still in question. Bubble resonance is dependent on the bubble radius, and properties of the gas and the surrounding media. Three damping mechanisms exist: thermal, frictional and radiation. The scattering cross section of bubbles is maximum at resonance, causing maximum effective attenuation.

The effect of the presence of gas bubbles on the compressional wave velocity is dependent on the insonifying frequency. If the insonifying frequency is below the bubble resonant frequency, the compressional wave velocity is determined by the bulk properties of the gassy sediment. Phase differences in the pressure and volume changes near resonance mean that the gassy sediment may have a greater bulk modulus than that of a saturated sediment, causing an increase in compressional-wave velocity. High above resonance, the gassy sediment compressional-wave velocity approaches that of gas-free sediment.

Chapter 5. *In situ* acoustic experiments

5.1 Introduction

In this chapter, the main field site, Dibden Bay, is described, as well as the *in situ* acoustic methodology and results. These methods include chirp high-resolution reflection profiling and two experiments using a mini-boomer acoustic source: a refraction/transmission experiment and a 24-hour acoustic monitoring experiment.

5.2 Dibden Bay

Dibden Bay is situated on an area of land reclaimed during the twentieth century on the western side of Southampton Water facing Ocean Dock (Figure 5.1; Figure 5.2). The reclamation overlies a layer of Holocene deposits, built up between the end of the last ice age and the beginning of the 20th century, which is known to contain layers of peaty material that outcrop in the side of the main shipping channel (Wessex Archaeology, 2000). Southampton Water is the drowned lower portions of the rivers Test and Itchen and is a partially stratified estuary 10km long and 2km wide (Flood, 1981). It has a complicated tidal regime and the tidal range can reach 5m at Southampton (Dyer, 1980). The tidal curve for the estuary shows a young flood stand and a double high water feature (Figure 5.3), with the second high water about two hours after the first (Webber 1980). The Dibden Bay area of Southampton Water is intertidal, enabling both marine and terrestrially based experiments to be conducted.

The site is generally composed of soft mud, with some regions covered with a layer of shells. Boreholes and an auger core (Figure 5.4) show good potential for the production of methane (see Section 2.5). In the top 3m of sediment there are three distinct layers of highly organic material: 0.2 – 0.4m, 1.35m and below 2.3m. The sediment is dark grey in colour, indicating the anoxic conditions required by methanogenic archaea. The odour of hydrogen sulphide, the product of sulphate-reducing bacteria, may be detected at the site, another indicator of the anoxic conditions in the sediment.

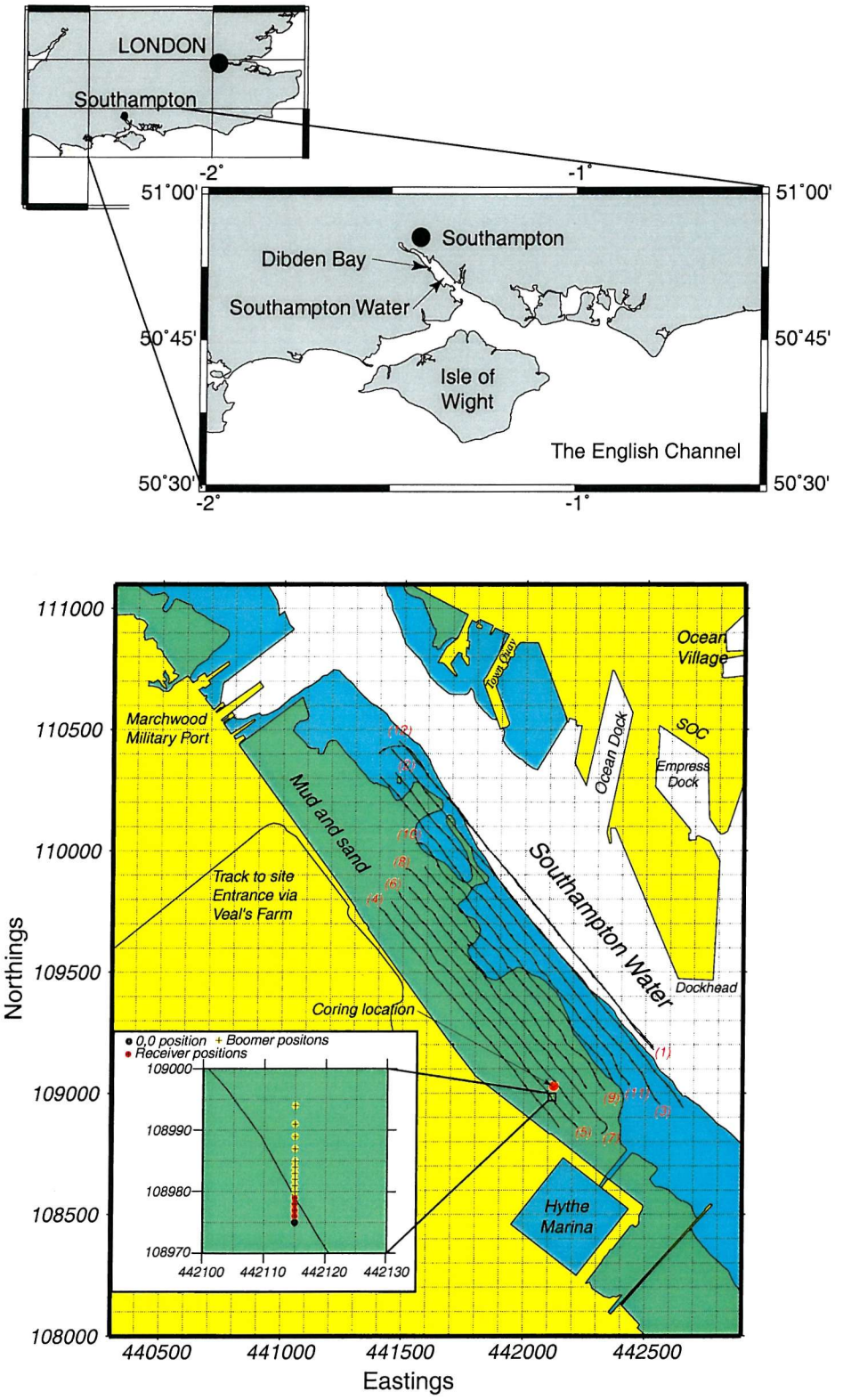

Figure 5.1. The location of Dibden Bay showing chirp sub-bottom profiling lines, mini-boomer transmission experiment location and orientation, and coring location. Yellow areas represent permanently dry regions, green areas represent the intertidal zone, blue areas represent permanently submerged regions and white areas represent the main shipping channel.

Figure 5.2. Photograph of the site at low tide.

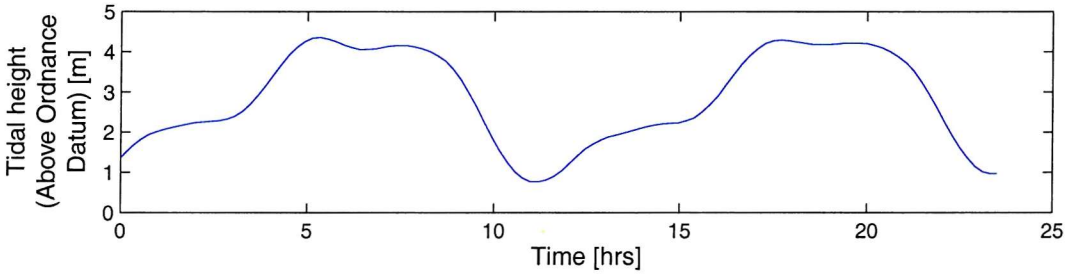

Figure 5.3. Tidal curve at Dockhead, Southampton Water, 24th to 25th March 2000.

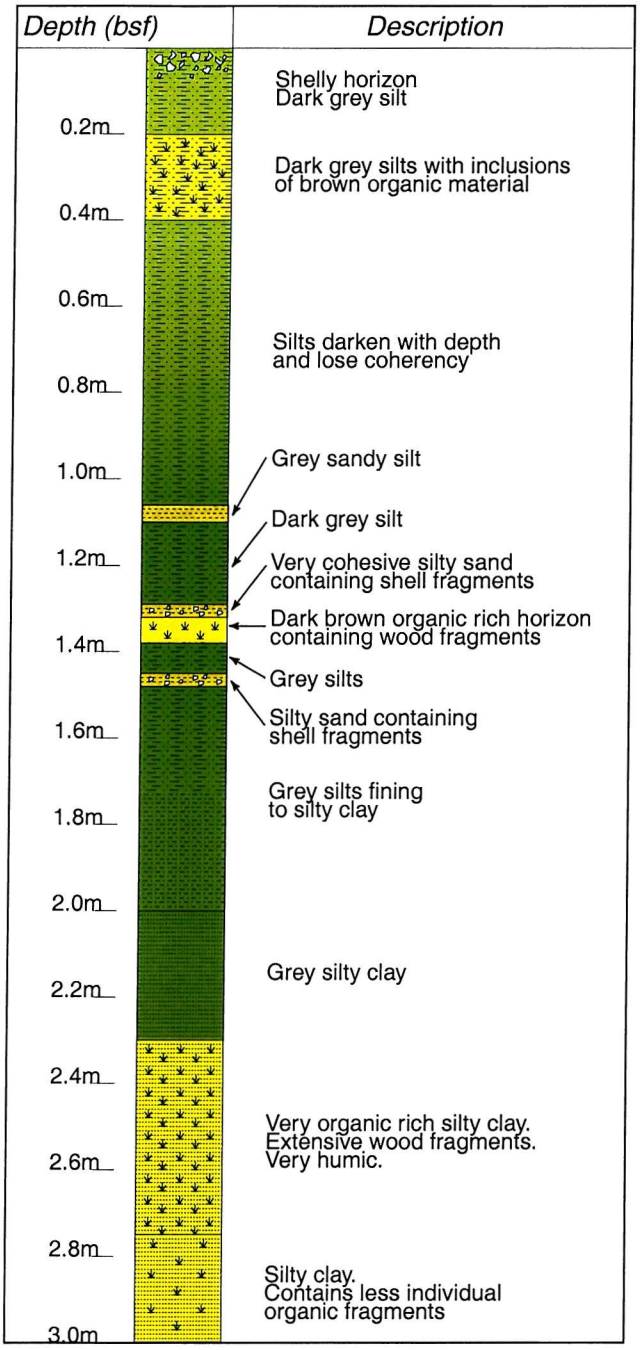

Figure 5.4. Sediment column profile at the mini-boomer site.

5.3 Chirp Sub-bottom profiling

Sub-bottom profiles were collected at Dibden Bay in January 1999 using a GeoAcoustics GeoChirp sub-bottom profiling system mounted on a catamaran (Figure 5.5). A number of survey lines were shot parallel to shore, as indicated in Figure 5.1. The system generates a 2 - 8 kHz sweep, with a dominant frequency of 5 kHz and a

band width of 2 octaves, which lasts 32 ms and has a sampling frequency of 25 kHz (Figure 5.6). The signal is transmitted by an array of 4 transducers with a beam angle of 45° (Quinn, 1997). A short, 8 element, single channel, 0.5 – 15 kHz hydrophone streamer is used to record normal incidence reflections.

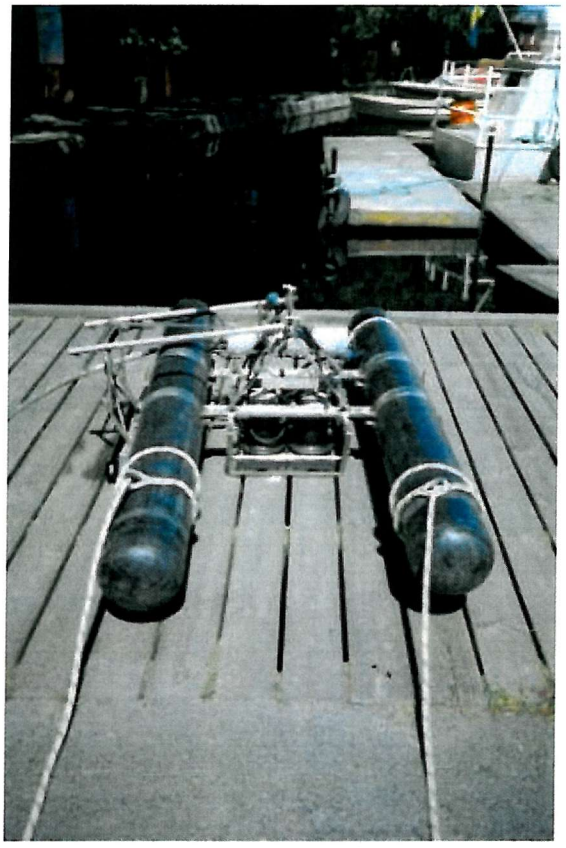

Figure 5.5. The chirp sub-bottom profiler mounted on a catamaran. From Lenham (2000).

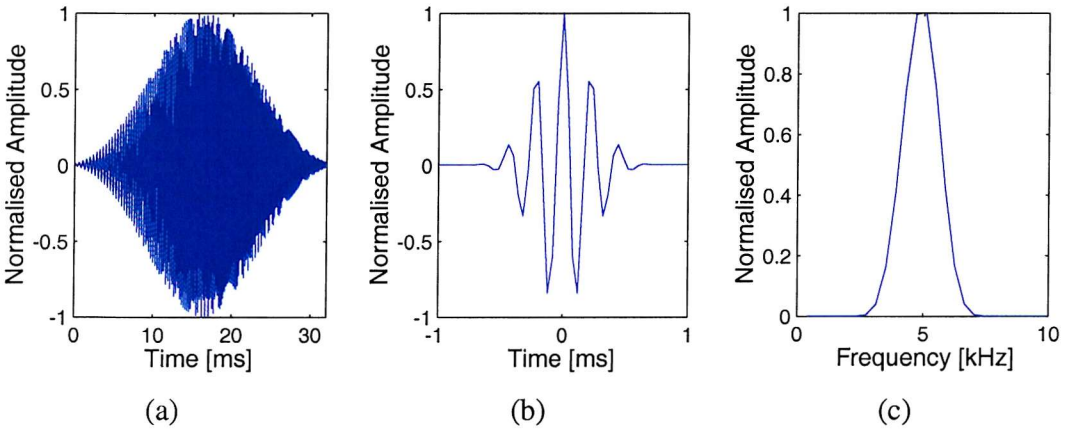

Figure 5.6. (a) The chirp pulse, (b) the zero phase Klauder wavelet – the autocorrelation of the chirp pulse and (c) the power spectrum

The data are recorded digitally in both correlated and uncorrelated format and may be subsequently processed in proprietary seismic processing software (e.g. ProMAX). Further information on the processing of chirp data may be found in Quinn (1997), Quinn *et al.* (1998) and Lenham (2000).

5.4 Chirp profiling results

Chirp sub-bottom reflection profiles show very little penetration of energy into the sediment. Acoustic turbidity dominates the profiles across the entire survey area with the exception of small isolated areas (Robb, 2000). A typical section may be seen in Figure 5.7.

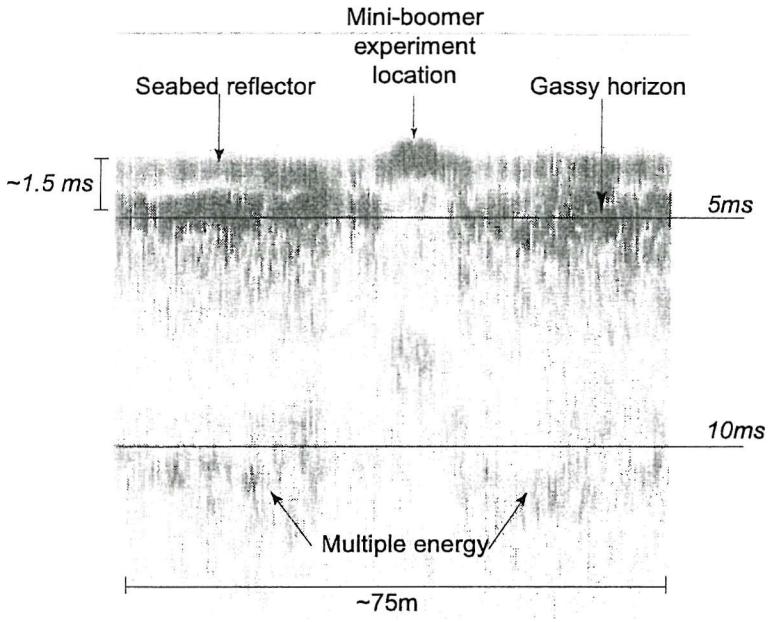

Figure 5.7. A typical correlated, unprocessed sub-bottom profile from Dibden Bay.

This section is from the south-western end of line 5, close to shore. The seabed reflector may be seen, followed by a second reflector arriving approximately 1.5 ms two way travel time (TWTT) later. The second horizon, interpreted as representing the onset of free gas (see Section 2.2), typically arrives between 1 and 2 ms TWTT throughout the survey area, corresponding to a depth in the sediment of approximately 0.75 – 1.5 m, assuming a compressional-wave velocity of 1480 m/s in the sediment (Shumway, 1960). The dome structure in the centre of the section corresponds to a surficial shell layer. The presence of the shell layer strengthened the sediment enough to support terrestrially based experiments, and as a result was chosen as the site for further study. The lack of a second reflector beneath this shell layer may be explained

by the highly reflective nature of the shell bed, which prevents energy penetrating and reflecting from deeper horizons. However, it is assumed that the gas horizon extends beneath this region because of the ubiquitousness of the gas horizon and evidence of anoxic conditions and organic material from the auger core (Figure 5.4).

5.5 Mini-boomer acoustic source

The mini-boomer, a Southampton Oceanography Centre designed acoustic source, uses a high voltage inverter to drive a magneto propulsive plate 20 cm in diameter and an array of four hydrophones (Figure 5.8). Tests by Best *et al.* (2001) have shown that it produces a repeatable signal (Figure 5.9), a spherical radiation pattern, a spectral content between 0 – 11 kHz notched at about 2.5 kHz (Figure 5.10) and the source level is estimated to be 215 dB re. 1 μPa @ 1m. Maximum strains of approximately 10^{-5} are induced, so non-linear effects may be ignored. The hydrophones show a flat frequency response up to 10 kHz (Best *et al.*, 2001).

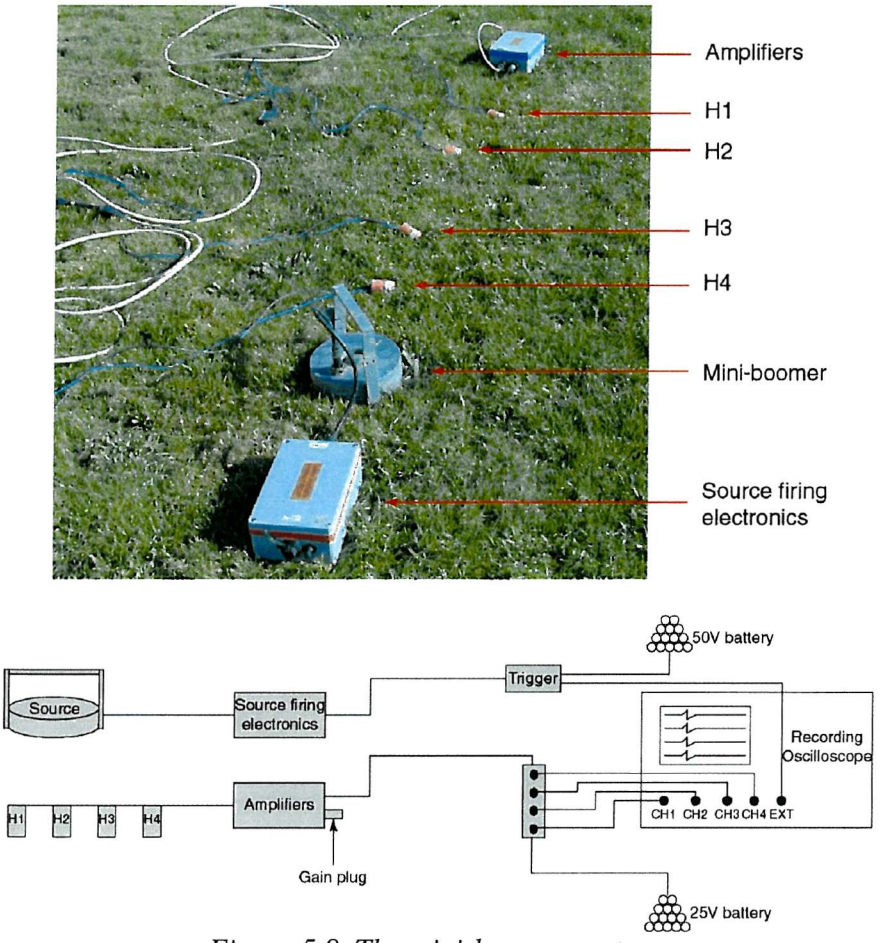

Figure 5.8. The mini-boomer system.

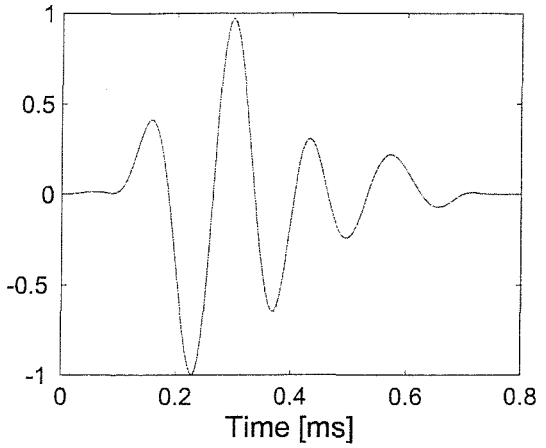

Figure 5.9. Self-normalised mini-boomer pulse recorded in water. Adapted from Best et al. *(2001).*

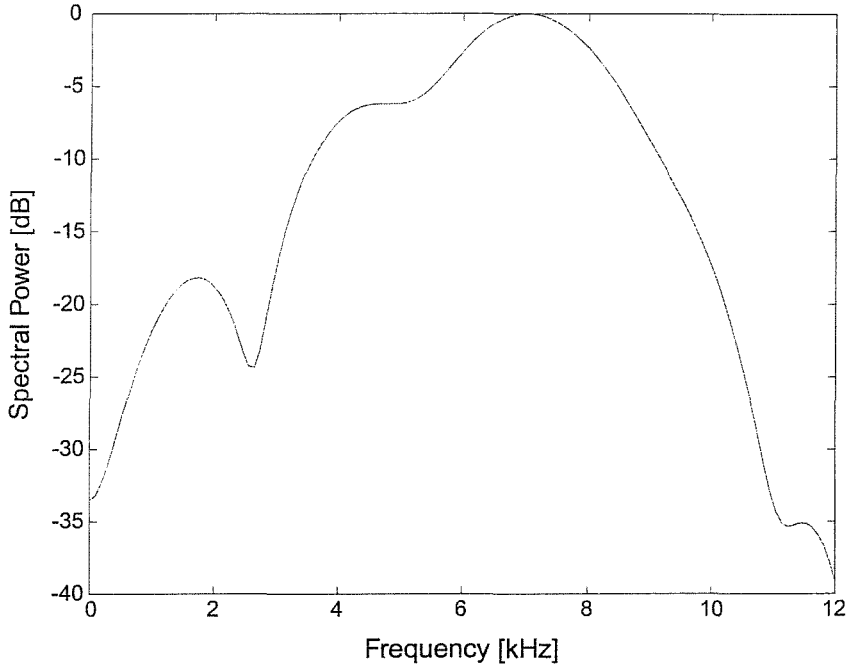

Figure 5.10. The power spectrum of the mini-boomer derived from transmission experiments in water.

An exchangeable plug on the hydrophone amplifiers allowed simple adjustment of the gain applied to each hydrophone before recording. Two experiments were carried out using the mini-boomer: a refraction / transmission experiment and a 24 hour transmission monitoring experiment

5.6 Data processing

The mini-boomer data for both experiments were processed using the filter correlation method described by Courtney and Mayer (1993). This technique involves filtering the selected data and a reference signal into a series of frequency bands, each of 100 Hz, from a minimum central frequency of 100 Hz, to a maximum central frequency of 3 kHz. Frequencies less than 600 Hz and higher than 3 kHz were ignored as the spectral power of the signal at the closest source-receiver offset in the refraction / transmission experiment, 1 m, were more than 60 dB down on the source signal (Figure 5.11).

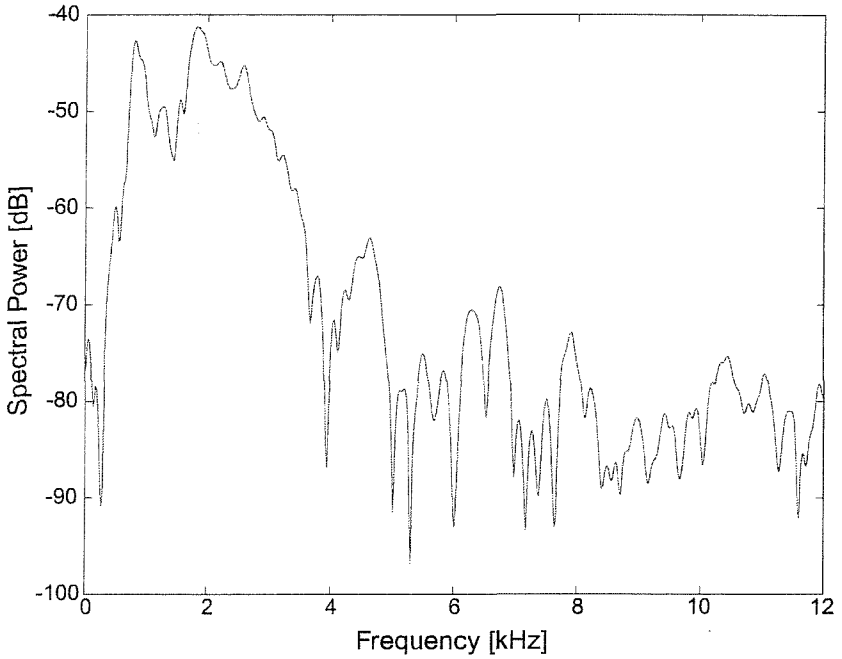

Figure 5.11. The mini-boomer power spectrum, relative to that in water, when fired through sediments at Dibden Bay at a horizontal offset of 1 m.

The attenuation coefficient for the frequency band under consideration, of central frequency f, is then calculated using a log spectral ratio method. Assuming that the attenuation of the signal is exponential and that spherical spreading applies, the frequency-dependent amplitude of the reference time series, $A_{ref}(f)$, and signal time series, $A_{sig}(f)$, with respect to the initial frequency-dependent signal amplitude, $A_o(f)$, are:

$$A_{ref}(f) = \frac{1}{x_{ref}} . A_0(f) . e^{-\alpha(f).x_{ref}}, \qquad 5.1$$

$$A_{sig}(f) = \frac{1}{x_{sig}} . A_0(f) . e^{-\alpha(f).x_{sig}}, \quad 5.2$$

where x_{ref} and x_{sig} are the source-receiver separations for the reference and signal time series, respectively; and $\alpha(f)$ is the frequency-dependent attenuation coefficient of the sediment in nepers / m. The signal amplitudes were calculated as the root-mean-square (RMS) energies of the time series. In the refraction / transmission experiment the signals were windowed from 1 ms prior to the first arrival for a period of 2.5 ms in order to isolate the first arrival pulses. The frequency-dependent attenuation coefficient in dB / m, $a(f)$, can then be calculated by taking the ratio of the reference time series to the signal time series such that:

$$\frac{A_{ref}(f)}{A_{sig}(f)} = \frac{x_{sig}}{x_{ref}} . e^{\alpha(f).(x_{sig} - x_{ref})}, \quad 5.3$$

$$\alpha(f) = \frac{1}{\delta x} \ln \left| \frac{A_{ref}(f)}{A_{sig}(f)} . \frac{x_{ref}}{x_{sig}} \right|, \quad 5.4$$

$$a(f) = 8.686 . \alpha(f), \quad 5.5$$

where δx equals $x_{sig} - x_{ref}$.

A cross-correlation between the filtered signal and the filtered reference is calculated and the frequency-dependent time delay, $\delta t(f)$, that corresponds to the cross correlation maximum is used to calculate the phase velocity of that frequency band (Equation 5.6):

$$c(f) = \frac{x_{sig} - x_{ref}}{(T_{sig} - T_{ref}) + \delta t(f)}, \quad 5.6$$

where T_{ref} and T_{sig} are the start times of the windowed reference and signal time series, respectively.

Finally, quality factor, $Q(f)$, and group velocity, V_g, were calculated for the refraction / transmission experiment using Equations 5.7 and 5.8:

$$Q(f) = \frac{\pi . f}{\alpha(f) . c(f)}, \quad 5.7$$

$$V_g = \frac{x_{sig}}{t_{sig}} \quad 5.8$$

Where x_{sig} is the source receiver separation; and t_{sig} is the first arrival time of the pulse.

5.7 Refraction / transmission experiment

The experiment was carried out on the edge of, and extending beyond, the shell bed located at the south-western end of the survey area, as indicated in Figure 5.1. The four hydrophones were placed into the sediment to a depth of 60 cm at 1 m intervals in a northerly direction, with a 40 dB gain applied to each. At an offset of 1 m for the first hydrophone, the mini-boomer was buried in the sediment to a depth of approximately 30 cm, below the depth of the surficial shell layer. A weight was placed on top of the device to improve the coupling. Three shots were fired and the source was then moved progressively further away to the north. During processing, the recorded signals were stacked. The positions of the shots relative to the hydrophones are illustrated in Figure 5.12.

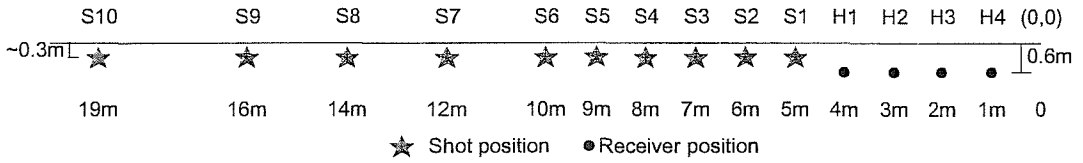

Figure 5.12. The mini-boomer refraction / transmission experiment layout.

A self-normalised common receiver gather, for receiver 1, may be seen in Figure 5.13. Normalisation was accomplished by dividing each trace by its own absolute maximum, resulting in a time series varying between –1 and +1.

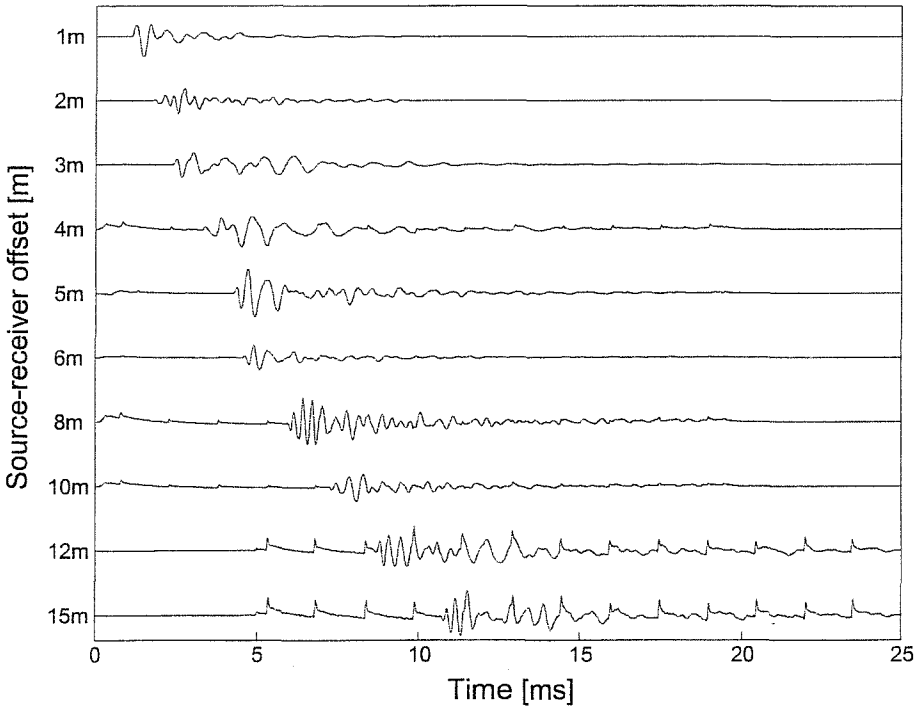

Figure 5.13. Common receiver gather – receiver 1.

At short offsets the signal to noise ratio is quite high. At longer offsets, such as the 12 m and 15 m offset, this decreases and regular spikes, occurring at 1.5ms intervals, are seen. These spikes are due to electrical interference noise within the system. At the shortest offset, the first arrival pulse is well defined and is followed by some reverberations. Evidence of a phase change in the signal may be seen by comparing this signal to others at longer offsets (e.g., 6 m). Second arrivals, either refracted or reflected, may be seen in most receivers, most notably on the fifth offset. Similar characteristics were found in the other three common receiver gathers.

5.7.1 Group velocity

Group velocities for each shot / receiver combination, calculated from first arrival times of all shots, are shown in Figure 5.14.

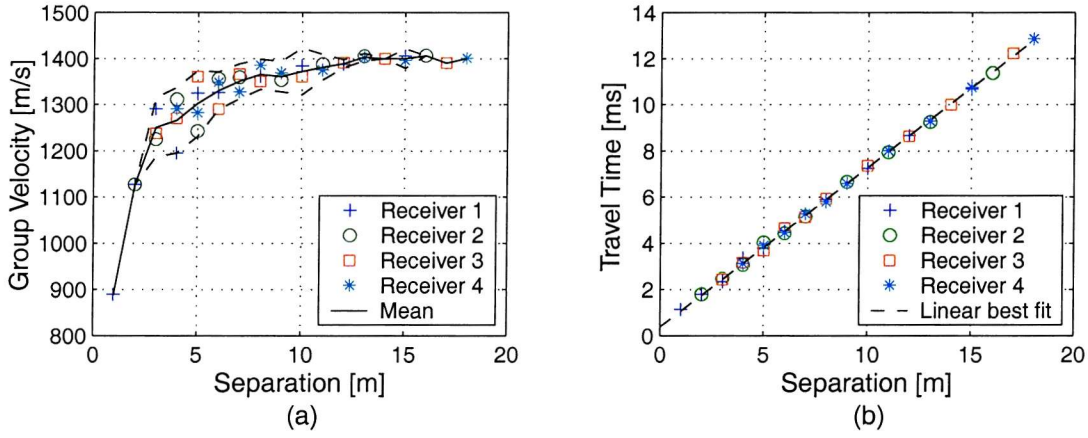

Figure 5.14. (a) Group velocity versus offset. Individual data are plotted as well as the mean within 95% confidence intervals. (b) Travel time versus offset. Individual data are plotted as well as a linear best fit.

At the shortest offsets, group velocity appears to be very low, with the shortest offset having a group velocity of 901 m/s. As offset increases, group velocity approaches 1400 m/s, the maximum being 1431 m/s (Receiver 4, 13 m offset). It can clearly be seen that the travel time versus offset plot does not pass through the origin of the graph, indicating that there could be a small trigger delay. This raises doubts about the validity of the group velocity data.

5.7.2 Phase velocity

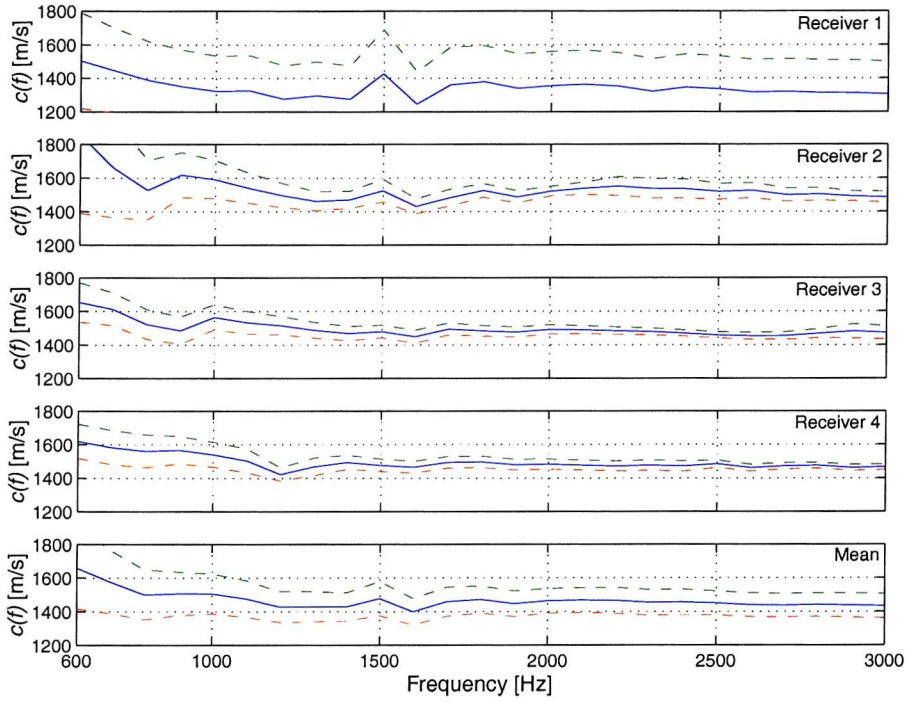

Figure 5.15. Phase velocity calculated for each receiver from all offsets and the global mean plotted with 95 % confidence intervals.

Between 600 and 1500 Hz, the phase velocity decreases from the peaks around 500 Hz to the more constant values found above 1500 Hz. Above 1500 Hz, the mean phase velocity for receiver 1 is 1339 m/s. This value is lower than the three receivers, which have mean values of 1510 m/s, 1473 m/s and 1474 m/s for receivers 2, 3 and 4 respectively. Receivers 1, 2 and 3 appear to have a small peak in phase velocity at approximately 1500 Hz, while the peak for receiver 4 occurs at 1400 Hz. The mean values were calculated simply as the mean of receivers 1 to 4. The same calculation was made for attenuation and quality factor.

5.7.3 Attenuation

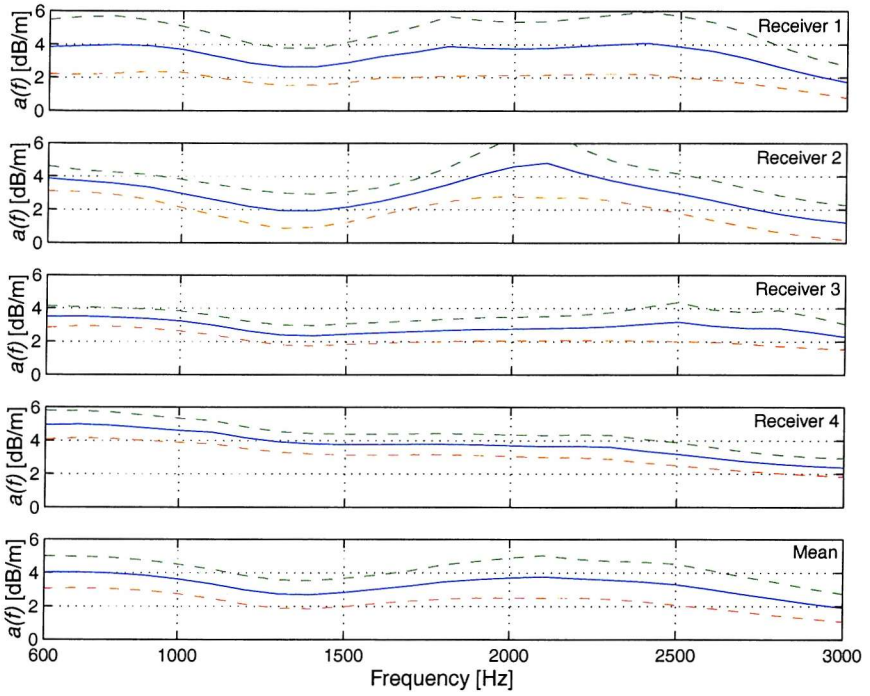

Figure 5.16. Attenuation coefficients calculated for each receiver from all offsets and the global mean plotted with 95 % confidence intervals.

There is a plateau between 600 Hz and 1000 Hz. Receiver 1 has a fairly constant attenuation of 4 dB/m in this range; receiver 2 varies from 4 dB/m at 500 Hz to 3 dB/m at 1000 Hz; receiver 3 has a value of approximately 3.5 dB/m; and receiver 4 has the highest attenuation in this frequency range, varying from 4.5 dB/m to about 5 dB/m.

Receiver 1 shows an additional plateau of approximately 4 dB/m between 1800 Hz and 2400 Hz. Receiver 2 shows a peak in of 4.8 dB/m at 2100 Hz, while the peak in receiver 3, at 2500 Hz, is just 3.2 dB/m. Finally, receiver 4 shows neither a plateau nor a peak at these high frequencies, but at 2300 Hz there is a significant decrease in the slope of the attenuation profile. These sediments clearly do not conform to the theory that attenuation is proportional to the first power of frequency (Section 3.2.2; Equation 3.4).

5.7.4 Quality factor

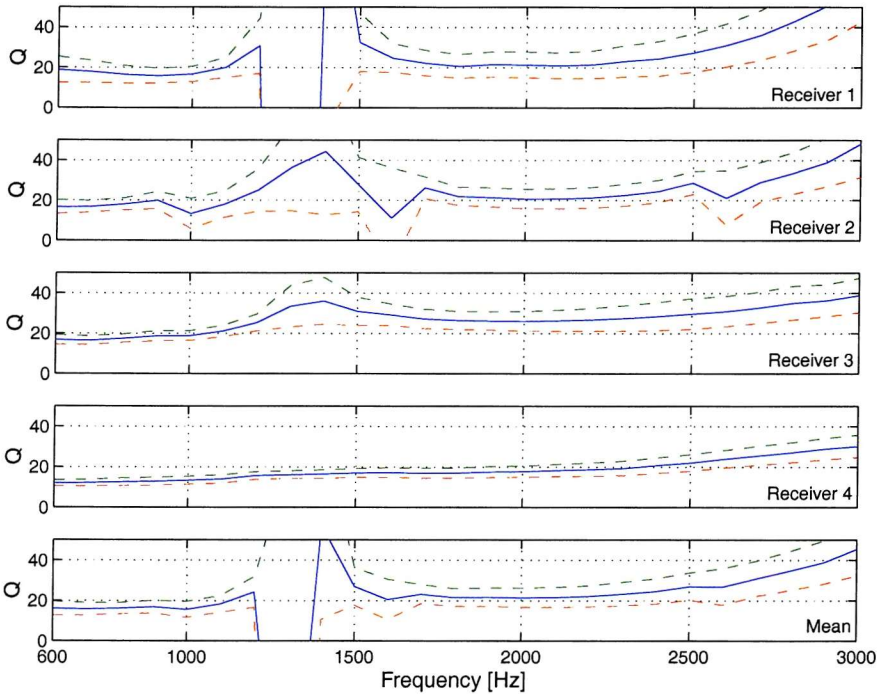

Figure 5.17. Quality factor calculated for each receiver from all offsets and the global mean plotted with 95 % confidence intervals.

Quality factor, calculated at each individual frequency using Equation 5.7, steadily increases throughout the frequency range, with the exception of instabilities around 1500 Hz. In between these instabilities, the values for all receivers are similar. Between 600 Hz and 1200 Hz the mean quality factors are 19.1, 18.1, 19.2, and 13.0 for receivers 1, 2, 3 and 4, respectively. The low value seen on receiver 4 indicates more highly attenuating sediment. For the frequency range 1700 – 2800 Hz, the mean quality factors are 26.0, 24.3, 28.5 and 20.2 for receivers 1, 2, 3 and 4, respectively. Again, quality factor on receiver 4 is lower than the other three.

5.8 Twenty-four hour transmission monitoring experiment

In situ transmission measurements were obtained during March 2000 using the mini-boomer system with a vertical array of hydrophones over a period of twenty-four hours. As discussed in Section 2.6.1, it is thought that changes in pressure may affect the solubility of the gas and change the bubble radii (Wever *et al.*, 1998). It was hoped that by using a vertical array the depth of the free gas horizon could be localised, and that changes to the gas horizon imposed by the variation in water depth might be measured. The hydrophones were placed at strategic depths such that there was at least

one above the gas horizon and one below as inferred from the chirp reflection profiles (Figure 5.18). The shallowest, at 0.3 m, was placed in the first layer containing organic material. The next was placed above the predicted depth of the gas at 0.8m. The final two receivers were placed at 1.2 m and 1.8 m, below the depth where the gas horizon is thought to occur. Variable gains were applied to each hydrophone before recording: receiver 1 had 30 dB applied, followed by 40 dB, 50 dB and 60 dB for receiver 4. Shots were fired at ten-minute intervals over a twenty-four hour period – approximately two tidal cycles.

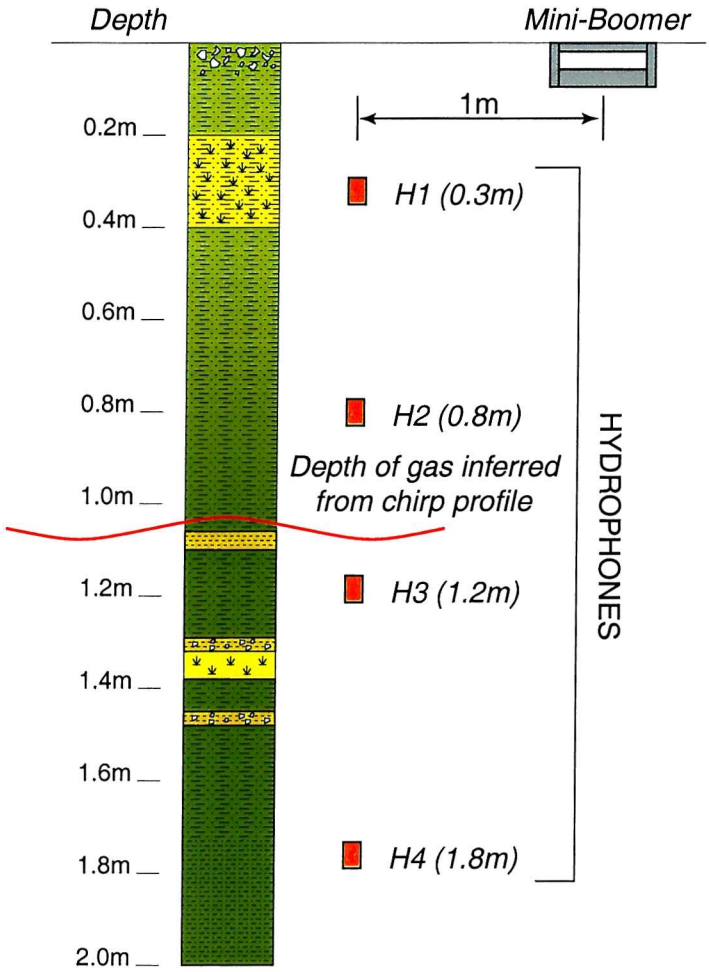

Figure 5.18. The 24-hour transmission experiment layout.

Two shot gathers, the first from the beginning of the experiment, the second at the point of greatest water depth, are shown in Figure 5.19.

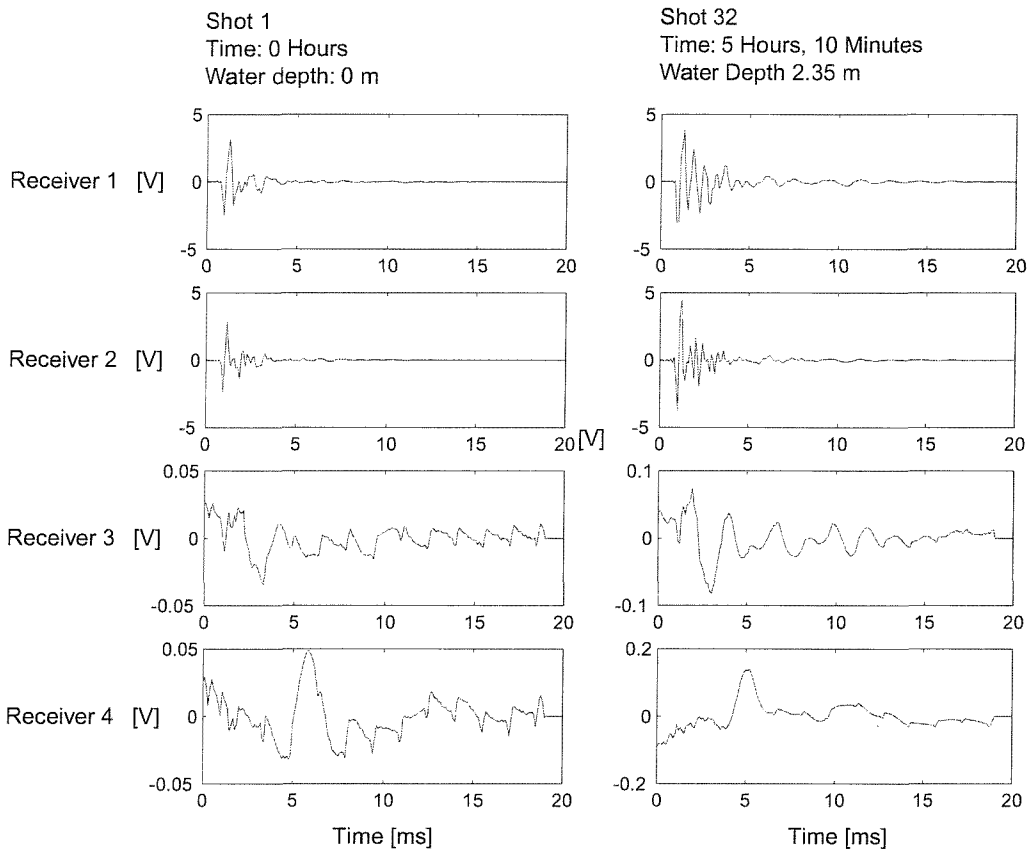

Figure 5.19. Shot gathers at the lowest and highest water depths during the experiment. Applied gains have been removed and signal amplitudes are in volts. Note the change in scales in receivers 3 and 4 between each shot.

A deterioration in the signal to noise ratio (SNR) with increasing depth of receiver is evident in both shot gathers. The noisy spikes occurring at approximately 1.5 ms intervals on receivers 3 and 4, similar to those seen at long offsets in the refraction / transmission experiment (Section 5.7, Figure 5.13), are thought to be the results of electrical interference noise within the system. There is a clear drop in signal amplitude between receivers 2 and 3 in both gathers, indicating the presence of a highly attenuating zone between the two. There is little difference in amplitude of the signals recorded on receivers 1 and 2. An improvement in SNR with increasing tidal height is evident from receivers 3 and 4 in both shot gathers. The signals show less influence from the electrical noise with deeper water, and the highest voltage recorded for each hydrophone is in excess of those seen for shallow water, indicating lower attenuation of the signal. Data recorded on receiver 4 were seen to have an exponential slope superimposed. Efforts to remove this slope were made, but the attempt was ultimately unsuccessful. However, the greatest change in the received signal occurred

between receivers 2 and 3 (compare signal amplitudes in Figure 5.19), and, as a result, the majority of the investigation was centred around these two.

5.8.1 Phase velocity

5.8.1.1 Receivers 1 (reference) and 2 (attenuated signal) (Figure 5.20):

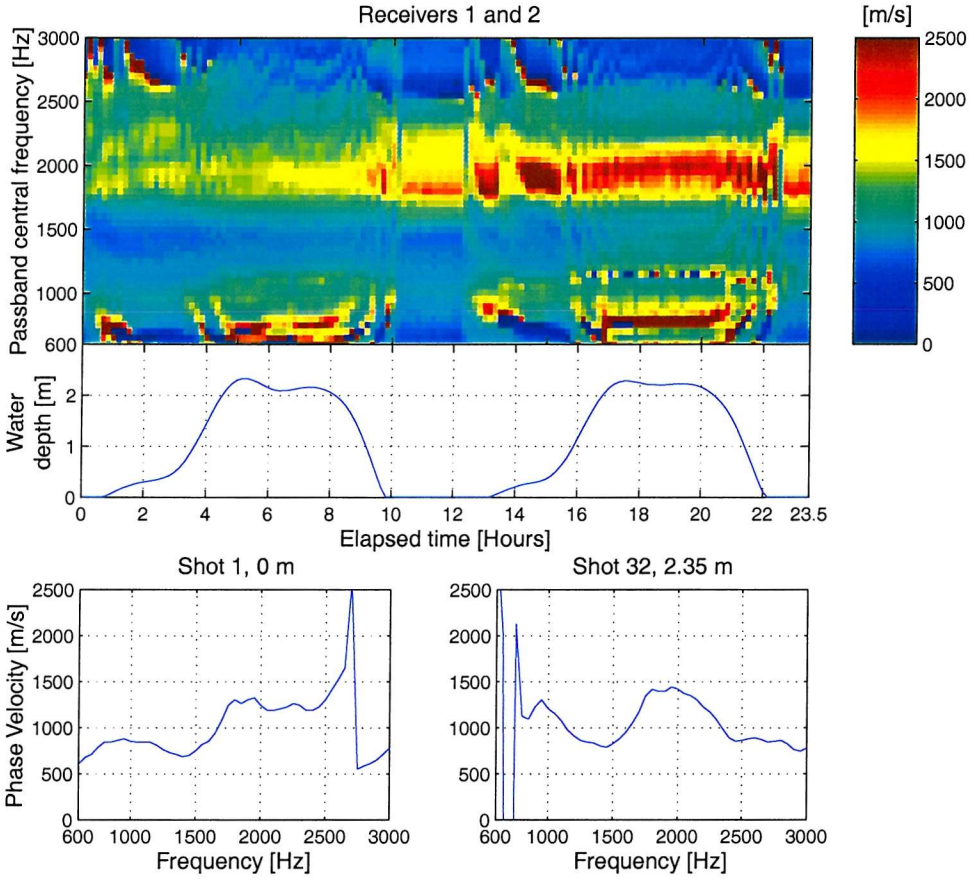

Figure 5.20. Phase velocity [m/s] for receivers 1 and 2 plotted with water depth and profiles at the lowest and highest tide.

The phase velocity profile (Figure 5.20) shows values ranging typically between 500 and 1500 m/s with the exception of three distinct areas. At times of increased water depth, phase velocity increases dramatically in the frequency range 600 to 1000 Hz. Between 1700 and 2000 Hz, at all water depths, there is a distinct peak in phase velocity. Above 2000 Hz in the high hydrostatic regime, the phase velocity decreases to approximately 850 m/s by 2450 Hz, while at low water depths, the phase velocity begins to increase at 2450 Hz to a maximum of 2600 m/s at 2700 Hz, before finally decreasing to 500 m/s.

5.8.1.2 Receivers 1 (reference) and 3 (attenuated signal) (Figure 5.21):

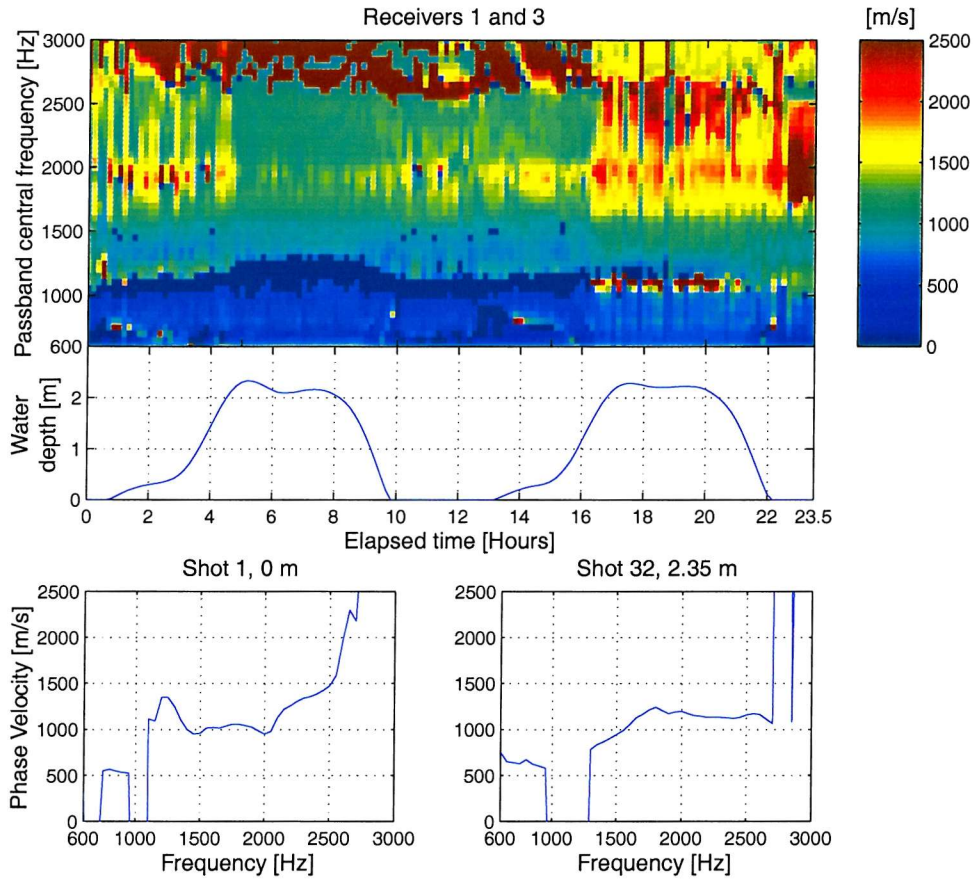

Figure 5.21. Phase velocity [m/s] for receivers 1 and 3 plotted with water depth and profiles at the lowest and highest tide.

Below 1000 Hz, the phase velocity varies between 520 and 560 m/s where a value is registered, at low tide. At high tide, the velocity increases to between 750 m/s (600 Hz) and 580 m/s (950 Hz). Low velocity regions, possibly the result of very high attenuation preventing the calculation of an accurate cross-correlation, are seen between 950 and 1100 Hz at low hydrostatic pressures, extending up to 1300 Hz at higher hydrostatic pressure.

A peak in phase velocity, of approximately 1350 m/s, is seen between 1200 and 1250 Hz at low tide, before decreasing to 1000 m/s. At 2000 Hz the phase velocity then steadily increases until 2700Hz when the increase is dramatic. At high tide, a peak of 1250 m/s is seen at 1800 Hz. Above 1800 Hz, the phase velocity drops to 1130 m/s until 2700 Hz when it increases off the scale, similar to the profile at low tide.

5.8.1.3 Receivers 2 (reference) and 3 (attenuated signal) (Figure 5.22):

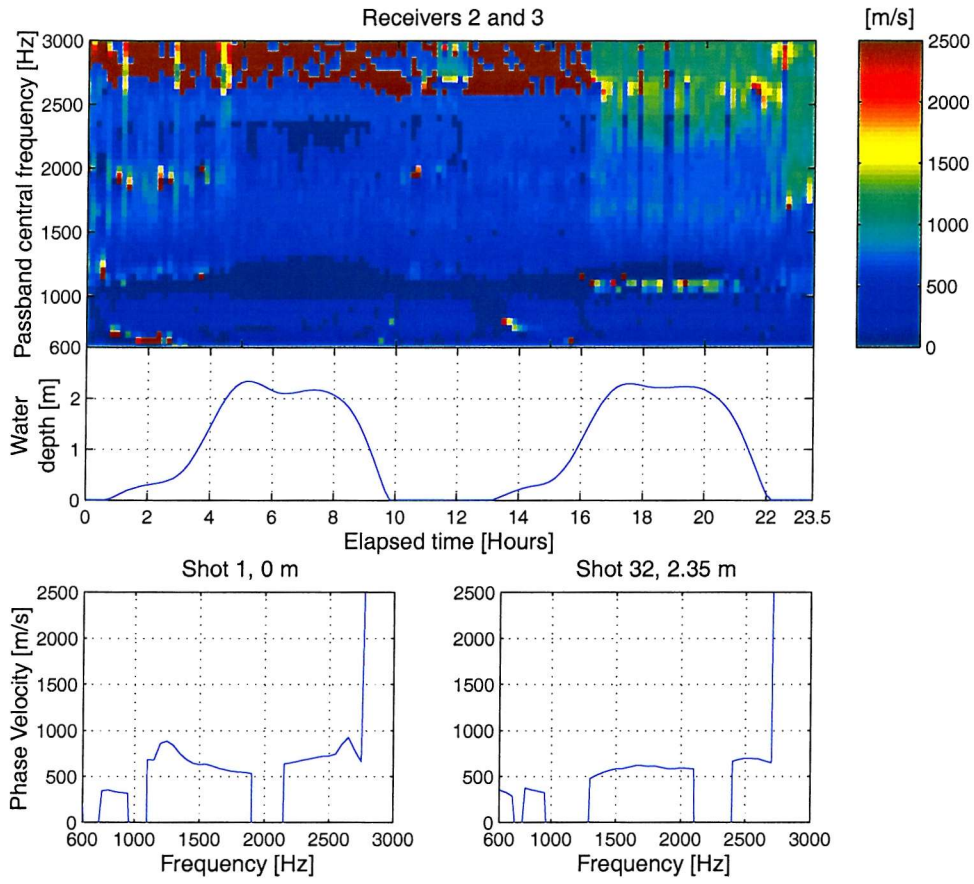

Figure 5.22. Phase velocity [m/s] for receivers 2 and 3 plotted with water depth and profiles at the lowest and highest tide.

The phase velocity profile is very similar to that seen in the previous section with the exception that the velocities are lower. In the region below 1000 Hz the velocity is between 320 m/s and 340 m/s at low tide, and between 320 m/s and 370 m/s at high tide. In general, the profile shows velocities typically less than 900 m/s (at 1250 Hz). There is a substantial drop in velocity around 2000 Hz at low tide, a feature which is repeated at high tide, only centred around 2250 Hz.

5.8.2 Attenuation

5.8.2.1 Receivers 1 (reference) and 2 (attenuated signal) (Figure 5.23):

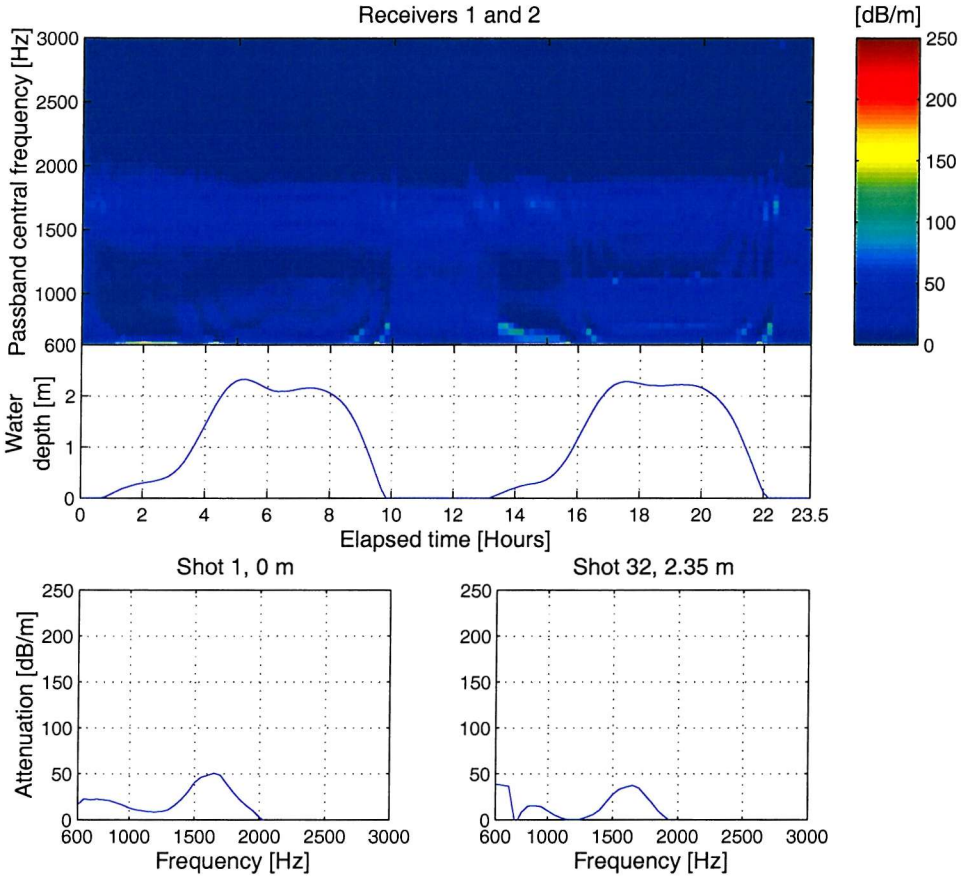

Figure 5.23. Attenuation coefficients [dB/m] for receivers 1 and 2 plotted with water depth and profiles at the lowest and highest tide.

The attenuation profiles show low attenuation, compared to the other receiver pairings, in the majority of frequency range – always less than 55 dB/m. At low frequencies (less than 1000 Hz), there is clear evidence of a tidal variation of attenuation. There is a small peak in attenuation between 700 and 800 Hz at low tide reaching 22 dB/m, while at high tide attenuation reaches 55 dB/m at 500 Hz. Between 1000 and 2000 Hz, there is another peak occurring at 1650 Hz at both high (37 dB/m) and low (50 dB/m) tides. Above 2000 Hz, the attenuation coefficients become negative, indicating an increase in signal amplitude at these frequencies. This increase in high frequency amplitude is evident in Figure 5.19. The signal recorded on receiver 2 clearly appears 'spikier' and must contain more high frequencies than the signal recorded on receiver 1. A simple investigation of the relative spectral power of the two

signals indicates that above 2000 Hz, the signal recorded on receiver 2 is stronger than that recorded on receiver 1 (Figure 5.24). This could indicate that energy is being re-radiated at a frequency greater than 2 kHz as a result of bubble resonance.

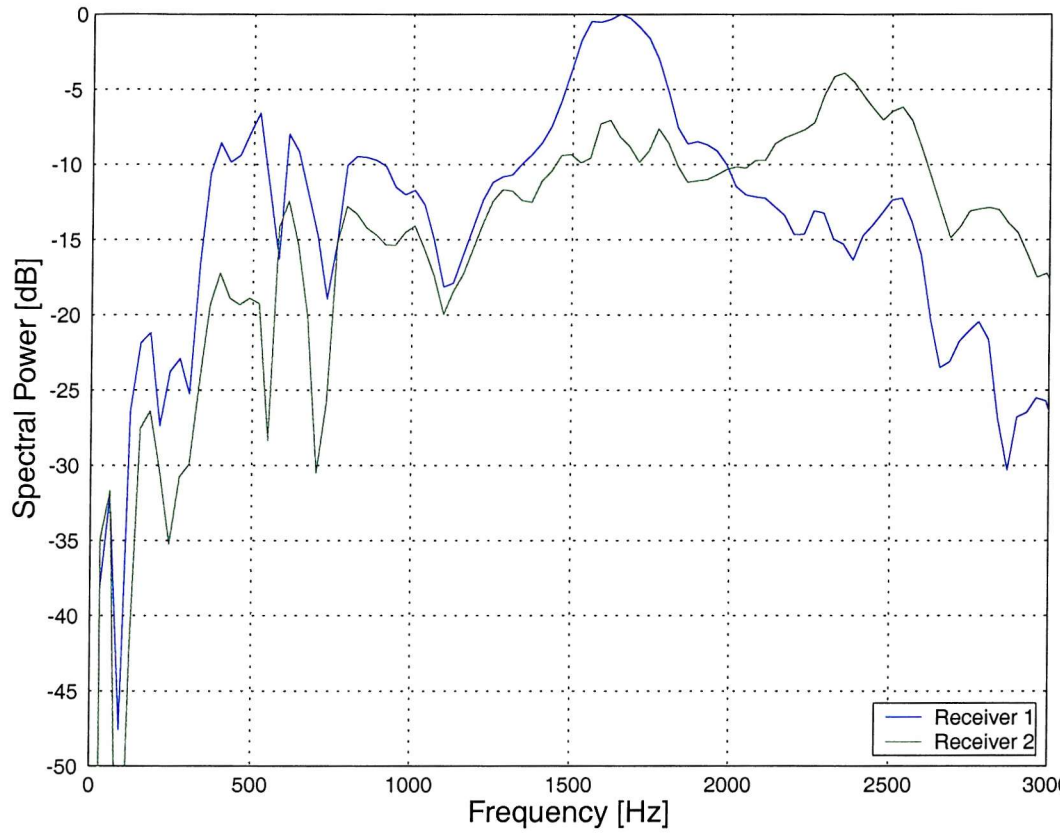

Figure 5.24. The spectral power (relative to the maximum amplitude recorded on receiver 1) of shot 32 on receivers 1 and 2.

5.8.2.2 Receivers 1 (reference) and 3 (attenuated signal) (Figure 5.25):

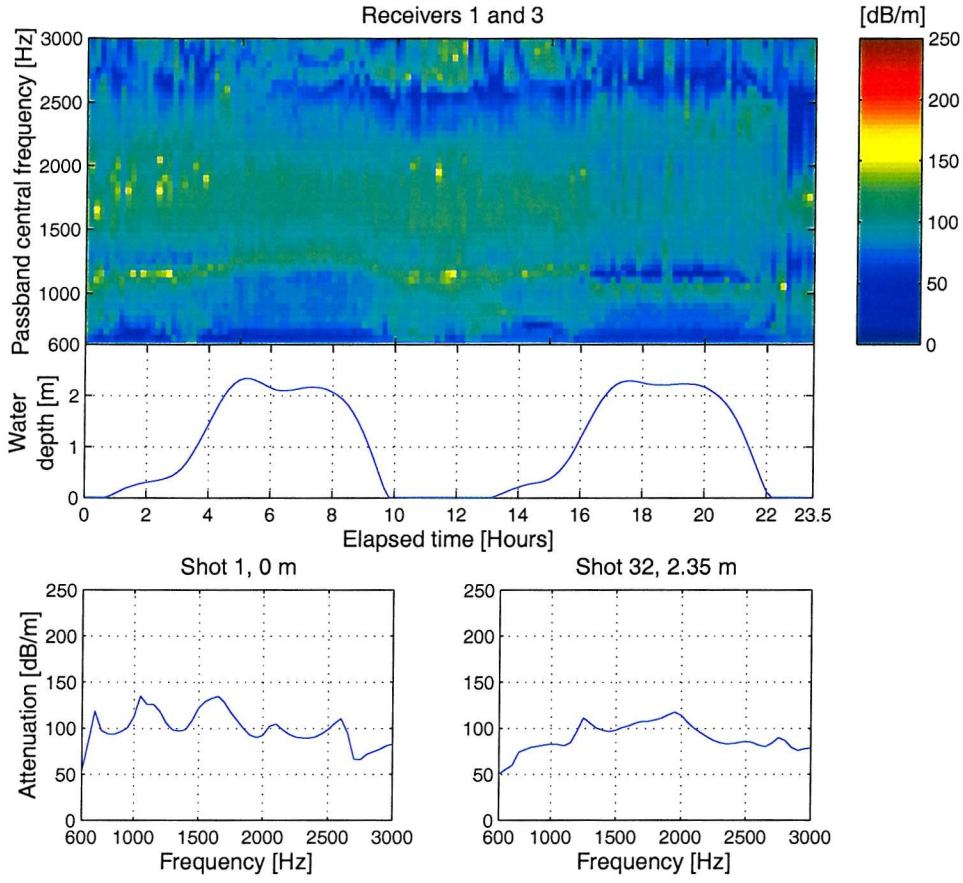

Figure 5.25. Attenuation coefficients [dB/m] for receivers 1 and 3 plotted with water depth and profiles at the lowest and highest tide.

Attenuation coefficients reach 100 to 150 dB/m for much of the time. As frequency increases, there are a number attenuation peaks at low tide: 118 dB/m at 700 Hz; 134 dB/m at 1050 Hz; 134 dB/m at 1650 Hz; 104 dB/m at 2100 Hz; and 110 dB/m at 2600 Hz. It is interesting to note that the low tide profile between 900 and 1300 Hz resembles the modelled attenuation profile of a gassy sediment (Section 4.3; Figure 5.26).

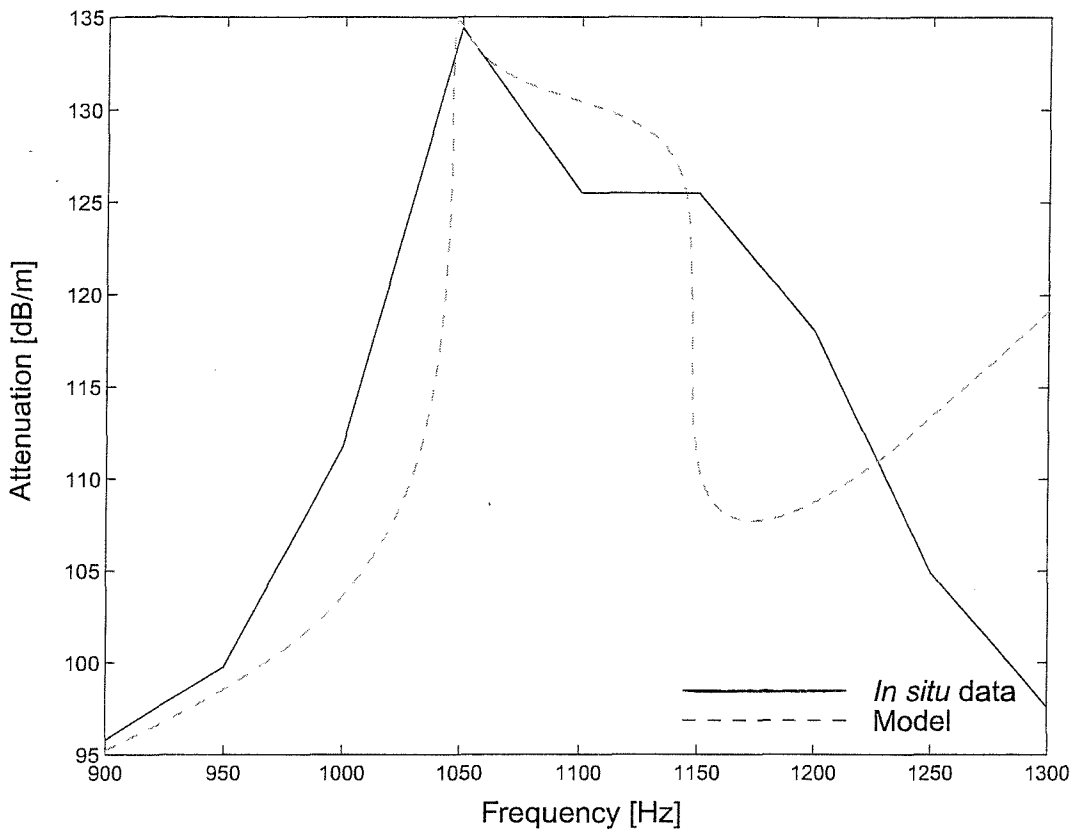

Figure 5.26. Comparison of the attenuation profiles of the sediment for receivers 1 and 3 at low tide and a typical model result. Note that the model result is adapted from Figure 4.6a, is not to scale and is shown only for comparison purposes.

As the tide increases, these peaks become less well defined and the profile becomes smoother. Two peaks may be seen: 110 dB/m at 1250 Hz; and 117 dB/m at 1950 Hz. Throughout the entire experiment, there is a clear band of high attenuation coefficients, occurring between 1000 and 1300 Hz. The frequency at which the maximum attenuation coefficients occur increases at the same point the water depth increases, and then decreases as the water depth decreases, indicating some kind of pressure dependency of attenuation.

5.8.2.3 Receivers 2 (reference) and 3 (attenuated signal) (Figure 5.27):

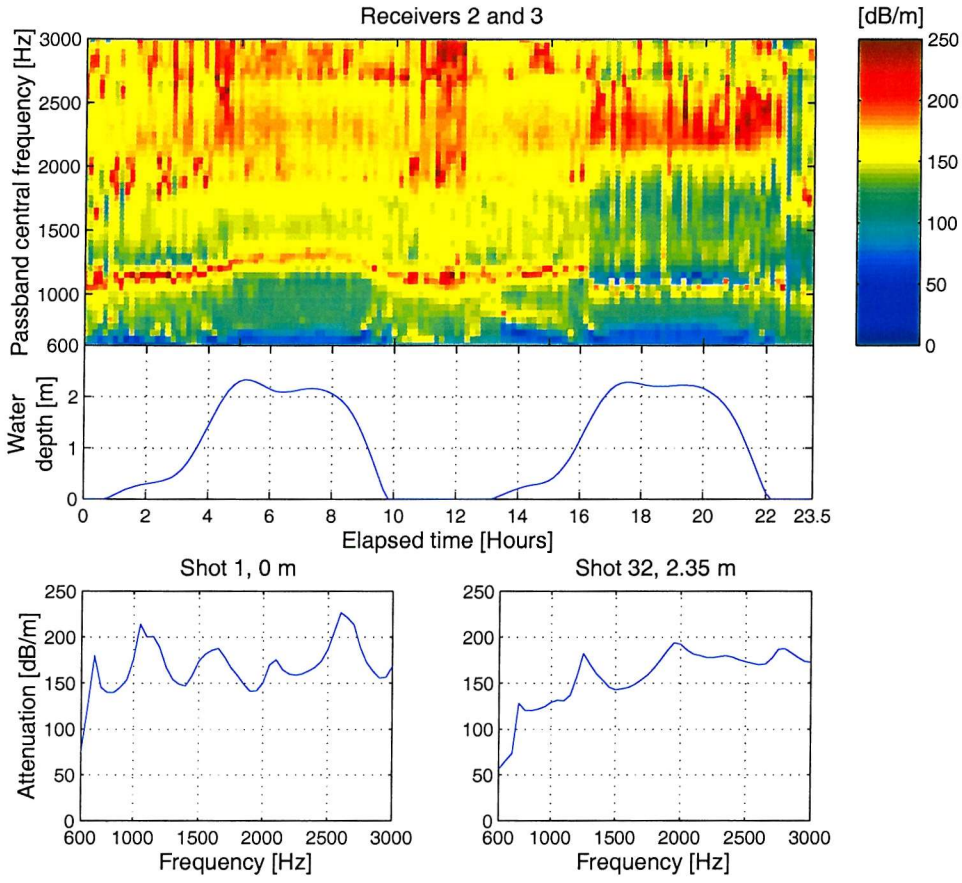

Figure 5.27. Attenuation coefficients [dB/m] for receivers 2 and 3 plotted with water depth and profiles at the lowest and highest tide.

The profile for this receiver pair is very similar to that seen in Section 5.8.2.2. The main difference is in the magnitude of the attenuation coefficients. At low tide the peak attenuation coefficients are: 180 dB/m at 700 Hz; 214 dB/m at 1050 Hz; 188 dB/m at 1650 Hz; 175 dB/m at 2100 Hz; and 227 dB/m at 2600 Hz. These attenuation coefficients are in excess of those seen between receivers 1 and 3 implying that the majority of the attenuation is occurring between receivers 2 and 3. The attenuation per metre is, therefore, higher. At high tide, there are peaks in the same position as those found for receivers 1 and 3, and, again, they are higher. Again, there is a clear band of high attenuation between 1000 and 1300 Hz, and the frequency at which this band occurs clearly increases with increasing water depth.

5.9 Discussion

It is clear from the outset that Dibden Bay is a suitable environment for methane production. The presence of organic material in the sediment column is a requirement for the production of gas, and it was found that there are several distinct layers of highly organic material in the auger core. In addition, the sediments are dark grey, almost black, in colour, which is an indication of the anoxic conditions required by the microbes to produce methane.

Positive evidence for the presence of free gas is provided by the presence of acoustic turbidity on the chirp sub-bottom profiling results (Chapter 2). The acoustic turbidity, which extends across almost the entire site, is estimated to be between 0.75 m and 1.5 m below the seabed. There is evidence that sulphate may be completely reduced anywhere between 10 cm (Hill *et al.*, 1992) and 2 m (Rice and Clayool, 1981), so this depth is consistent with the hypothesis that methane is not produced in large quantities until sulphate is depleted (Martens and Berner, 1974).

5.9.1 Refraction / transmission experiment

The refraction / transmission experiment shows a variable group velocity with offset, with the shortest offsets having the lowest velocity. The lowest velocity is of a similar value to that found in soft, gassy clays found in the Gulf of Mexico by Edrington and Calloway (1984). At longer offsets, the velocity approaches 1400 m/s. This value is still low compared to other sediments, such as those found in Lough Hyne by Best *et al.* (2001). An explanation could be that the surficial shell layer acts as a waveguide, with the energy travelling as a head wave, although these waves are more rapidly attenuated than spherical waves (Figure 5.28). This could, however, account for the higher than expected attenuation coefficients measured during this experiment. Those signals at short offsets could have their first arrivals associated with the direct path through the low velocity layer (dashed lines), and those signals at longer offsets could have their first arrivals associated with a path diverted through the shell layer (solid lines).

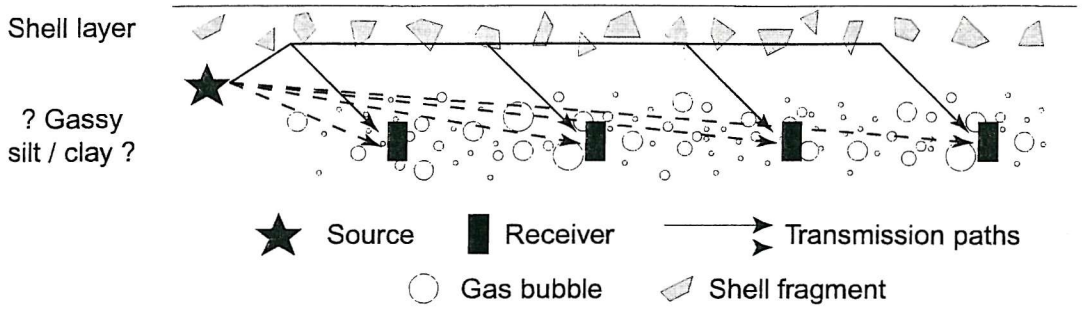

Figure 5.28. Potential travel paths for the refraction / transmission experiments.

It has been traditionally observed that most marine sediments follow a linear dependence of attenuation on frequency (Section 3.2.2), and that dispersion, although present and implied through its causal relationship with attenuation, is negligible (Section 3.2.3). Yet the evidence presented here is clearly contradictory. Phase velocity, while unstable at low velocity, does appear largely constant, but attenuation shows a non-linear dependence on frequency. Q has a trend of increasing with frequency and, while many authors report a constant quality factor (e.g. Toksoz *et al.*, 1979; Kjartansson, 1979), there is evidence that Q may be frequency dependent (e.g. Brennan, 1980; Malagnini, 1996). These results are also described in Tuffin *et al.*(2000). Comparison with data published by Kibblewhite (1989) and Bowles (1997), both of whom present compilations of data from a number of studies, shows that the attenuation coefficients found in Dibden Bay (ignoring their non-linearity) are significantly higher than those found in a number of other studies. Typical values quoted for the type of sediment found in Dibden Bay (i.e. silty clay / mud), and for a similar frequency range, are in the region of 10^{-2} to 10^{-1} dB/m compared to values as high as 5 dB/m in Dibden Bay.

Attenuation is thought to be largely dominated by local, viscous fluid flow rather than intergranular friction and global fluid motion (Section 3.2.2), but this alone cannot account for the degree to which the observed attenuation coefficients are in excess of those in similar sediments. Evidence from the auger core and the chirp reflection profiling indicates the presence of free gas, probably methane. It is known that free gas causes significant increases in attenuation (Section 3.3.3), even in small amounts, and that bubbles resonate at a specific frequency depending on their radius and a number of environmental parameters. The elevated and distinctly non-linear nature of the attenuation coefficients could be a direct result of gas bubbles, with the broad peaks seen in the 500 – 1000 Hz region and around 2000 Hz the result of bubble

resonance. However, these attenuation coefficients are very low compared to those measured in the 24 hour experiment and it is possible that these measurements indicate the water-saturated sediment properties of the surface shell layer and the organic layer beneath it.

5.9.2 Twenty-four hour transmission experiment

In the twenty-four hour experiment, it is clear from the common shot gathers presented in Figure 5.19 that there is a significant change in the recorded signal between receiver two, at 0.8 m depth, and receiver three, at 1.2 m depth. This is also reported in Tuffin *et al.* (2001). This change in signal character is most likely due to the presence of free gas in larger amounts than encountered in the refraction / transmission experiment. The depth of this assumed free gas horizon matches that predicted from the chirp reflection profiling. Indeed, at the mini-boomer site, the TWTT of the gas horizon is approximately 1.5 ms. Using a compressional-wave velocity of 1400 m/s (the value to which the refraction / transmission data trends at long offsets), this time corresponds to a depth of 1.05 m, or 1.11 m when the velocity is taken to be 1480 m/s (Shumway, 1960). This depth happens to coincide with a slightly sandier layer observed in the auger core (Figure 5.4). It is possible that the gas is accumulating in significant quantities in this layer, or that it is migrating there from a deeper source. The overlying sediments may either prevent fluid moving upward or may be regions of significant sulphate production, where methane is metabolised by any sulphate reducing bacteria present (Section 2.5.2).

Phase velocity is variable across the whole frequency range, and generally lower than expected for similar, gas-free sediment types. Attenuation is high across the frequency range, probably due to bubble scattering and resonance. The model presented by Anderson and Hampton (1980a,b) (Chapter 4; Figure 4.6) predicts that below resonance, the phase velocity of a gassy sediment will be very much lower than that of a fully saturated sediment. Although there are instabilities in the data, a result of the high attenuation of the signal, the phase velocity is generally very low, especially when comparing receivers 2 and 3. Attenuation coefficients are very high – up to 250 dB/m in certain parts of the spectrum – and there are two distinct peaks, occurring at 700 Hz and 1050 Hz when receiver 3 is processed as the attenuated signal. These could correspond to a bubble resonance peak, as could the sharp increase in phase velocity above 2500 Hz. In addition, the frequencies at which these peaks occur are seen to

increase with increasing water depth. Since the only environmental change that has occurred is the increase in water depth, it can be concluded that hydrostatic pressure has an effect on free gas. The Anderson and Hampton model (Figure 4.6) predicts that, for the same environmental conditions, an increase in resonant frequency is the result of a decrease in bubble radius. This implies that the change in hydrostatic pressure causes the bubbles to vary in size.

5.10 Summary

Three *in situ* acoustic experiments were carried out: a chirp high-resolution reflection survey; a refraction / transmission experiment using a mini-boomer acoustic source; and a twenty-four hour transmission monitoring experiment using a mini-boomer acoustic source and a vertical array of hydrophones.

The chirp reflection profiling showed, almost exclusively, acoustic turbidity, the cause of which is accepted to be the presence of free gas. The depth to the free gas horizon was calculated to be approximately 1 m.

The refraction / transmission experiment showed a dependence of compressional-wave group velocity on offset, possibly as a result of a waveguide effect caused by the presence of a surficial shell layer. There was some evidence of dispersion, the attenuation-frequency relationship was not linear and there was evidence of a frequency-dependent Q. It is possible that the non-linear nature of the attenuation profile is due, in some part, to the presence of free gas.

The twenty-four hour transmission monitoring experiment revealed that, between 0.8 and 1.2 m, free gas exists in the sediment. Very high attenuations and low phase velocities were measured in this region, and there was evidence for a dependence of attenuation not only on frequency, but also on ambient hydrostatic pressure, something not previously observed. The frequency at which a peak of attenuation occurred increased in response to an increase in water depth. It is hypothesised that this peak in attenuation is related to a resonance effect associated with a particular dominant bubble radius, and that the increase in frequency at which this attenuation peak occurs at elevated ambient hydrostatic pressure is due to a decrease in the radius of the bubble.

Chapter 6. Laboratory experiments

6.1 Introduction

In this chapter the sample retrieval and laboratory methods used in this thesis, and the results obtained, are described and discussed. The aims of the laboratory analyses were: to characterise the sedimentary units and their physical properties for input to the gassy sediment model; to verify the existence of bubbles at depth and to quantify the bubble size distribution for input to the model; and to measure the high frequency (300 – 700 kHz) response of the gassy sediment for possible comparison with modelling results. Tests were carried out on material extracted from the site in a series of cores. These laboratory tests include: grain size analysis; carbon analysis; shear strength; shear wave velocity; compressional wave velocity; compressional wave attenuation; bubble size analysis (through the use of X-ray computed tomography); and gamma ray density.

6.2 Sampling techniques

A barge, equipped with a crane and 'spud' legs, was used to collect core samples from the site during October 2000 for testing in the laboratory. Two 150 mm square Kastenlot cores were collected (Figure 6.1), one 3 m long and one 2 m long. In addition, two pressurised cores (Figure 6.2), each 3 m long with an internal diameter of 10 cm, were collected. The pressurised cores used specially designed end caps (Figure 6.3), which were sealed by divers on the seabed, to maintain the *in situ* hydrostatic pressure conditions within the cores. All tests on the pressurised cores were performed on the same core to enable a degree of consistency to be kept between measurements.

Figure 6.1. The Kastenlot core on deck before deployment.

Figure 6.2. Deployment of the pressurised coring system.

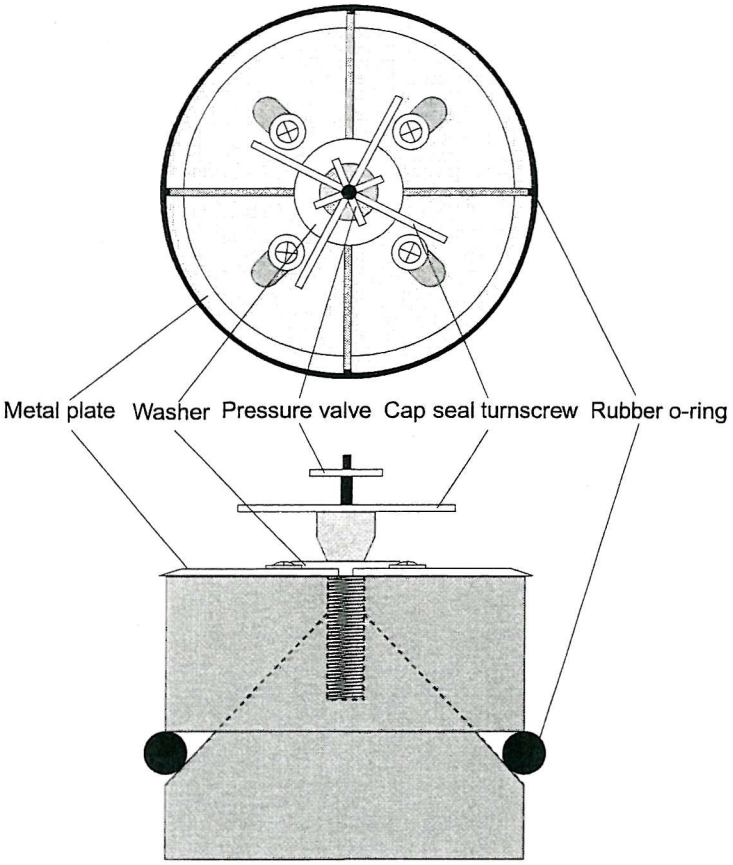

Figure 6.3. Pressurised core end-cap schematic. Turning the screw forces the plastic washer outwards, which in turn pushes the sharpened metal plates outwards. These plates cut into the core barrel and prevent any movement of the cap up or down the core barrel. While this occurs a large rubber o-ring is compressed to make an airtight seal between the cap and the barrel. A valve is also fitted to enable the pressure to be monitored or changed.

6.3 Laboratory methods

6.3.1 Grain size analysis

The long Kastenlot core was sub-sampled at ten centimetre intervals down the core for grain size analysis. The samples were wet sieved into the following fractions: > 500 μm, 250-500 μm, 125-250 μm, 63-125 μm, < 63 μm. Analysis below 63 μm was completed using a Micromeritics SediGraph 5100 Particle Size Analysis System, using sodium hexametasulphate (Calgon) as the dispersant. The system measures particle size using X-ray absorption (e.g., Stein, 1985).

6.3.2 Marine sediment core logger (MSCL)

The 3 m Kastenlot core was sub-sampled by means of inserting a plastic channel, with a square cross-section, into the core and cutting away the surrounding sediment. Both this sub-sample and the pressurised core were logged using SOC's marine sediment core logger (MSCL) (Gunn and Best, 1998) (Figure 6.4). The MSCL has sensors to measure compressional-wave velocity using a 500 kHz source, gamma ray density and magnetic susceptibility at 1 cm intervals down the core. The parameters of interest to this study were compressional-wave velocity and gamma density.

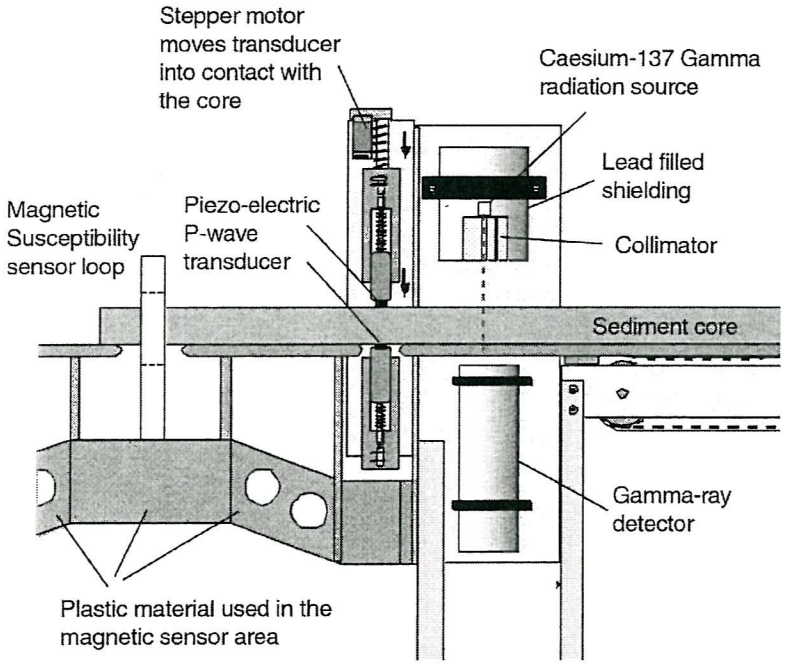

Figure 6.4. SOC's MSCL showing compressional-wave gamma density susceptibility sensors. From Best and Gunn (1999).

Compressional-wave velocity calibration was carried out using a water-filled core. The total measured compressional-wave travel time is the sum of the travel time through the sediment, and the travel time offset. The travel time offset is the sum of the travel time in the liner, the travel time from the transducer to the outside of the core and the picking error (the software picks the second zero crossing of the received signal) (Figure 6.5). By measuring the total travel time through a water core and measuring the internal diameter, it is possible to calculate the travel time offset.

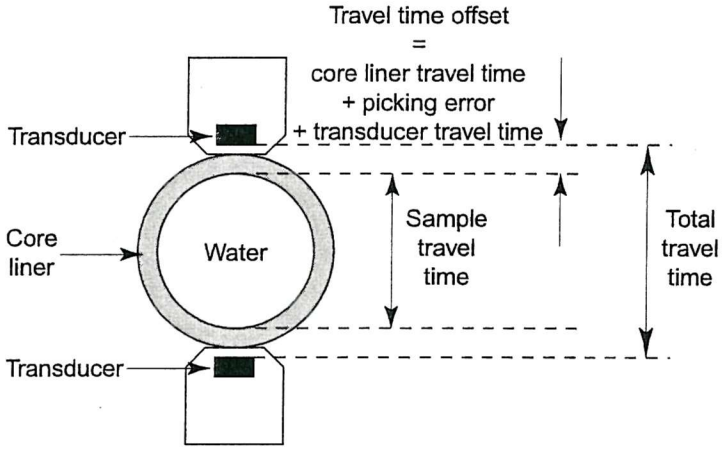

Figure 6.5. Calibrating compressional-wave velocity.

Density calibration was carried out using a stepped aluminium calibration block (Figure 6.6) placed in a water-filled core, as described by Best and Gunn (1999).

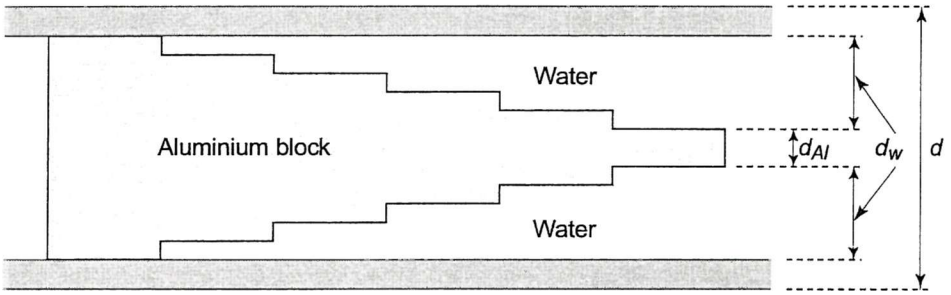

Figure 6.6. The stepped aluminium calibration block.

The density of a material, ρ, in g/cm^3, of sample thickness d, measured in cm, is related to the measured gamma-ray intensity, I, measured in counts per second, by the equation:

$$\rho = \frac{1}{\mu d} \ln \left| \frac{I_0}{I} \right| \qquad 6.1$$

where I is the measured intensity; I_0 is the source intensity; and μ is the Compton mass attenuation coefficient of the material. The average density in the calibration core, ρ_{ave}, can be calculated using:

$$\rho_{ave} = \frac{d_{Al}}{d} \rho_{Al} + \frac{d_w}{d} \rho_w \qquad 6.2$$

where d is the outside core diameter; d_{Al} and d_w are the thicknesses of the aluminium and water, respectively (Figure 6.6); and ρ_{Al} and ρ_w are the densities of the aluminium and water, respectively. Plotting the natural log of measured intensity versus (ρ_{ave} × thickness) gives a calibration curve that can be described by a 2nd order

polynomial equation. This equation may then be used to calculate sediment density from measured intensity values.

Porosity, n, was then calculated using:

$$n = \frac{\rho - \rho_m}{\rho_w - \rho_m} \qquad 6.3$$

where ρ, ρ_m, ρ_w are the bulk density of the material, the density of the mineral grains and the density of the pore water, respectively. The density of the mineral grains was assumed to be 2590 kg/m^3 (Wilkens and Richardson, 1998), although this figure does vary between mineral types. The density of the pore water was taken to be 1030 kg/m^3 (Kaye and Laby, 1995)

The same methods were used to calibrate the Kastenlot core sub-sample. However, flat slabs of aluminium, of known thickness, were placed into the channel to calibrate the gamma-ray density, rather than a stepped circular insert.

6.3.3 Carbon analysis

Dry samples were crushed and analysed for both carbonate and total carbon content using carbon coulometry (Engleman *et al.*, 1985). A coulometer automatically measures the absolute mass amount of carbon dioxide resulting from the combustion or acidification of a sample. Inorganic carbon is measured by acidification, and total carbon is measured by combustion. Organic carbon content is calculated as the difference between total carbon and inorganic carbon.

6.3.4 Shear wave analysis

Shear velocity was measured down the core by inserting bender elements (Shirley and Hampton, 1978) into the core material (Figure 6.7).

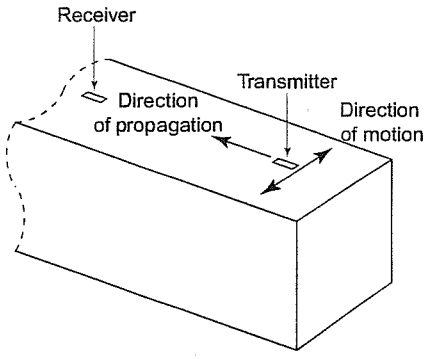

Figure 6.7. Shear-wave measurement.

A transmitting element, driven with a 50 Volt spike, was placed into the sediment with a receiver placed 10 cm down the core. A pulse was fired and the receiver was then moved a further 10 cm down the core. The transmitter was moved a further 10 cm down the core and the process repeated. First arrival times were picked and group velocity was subsequently calculated using Equation 5.8. An estimate of shear wave frequency was made by measuring the period of the received wave and was found to be approximately 160 Hz.

6.3.5 Shear vane testing

The longer of the Kastenlot cores was tested for shear strength using a shear vane device (e.g., Craig, 1992) at 10 cm intervals down the core. The shear vane is a simple device and is suitable for determining the *in situ* undrained shear strength of saturated clays. The type of instrument used – a miniature vane – consists of eight plastic vanes attached to a calibrated gauge via a spring of known properties (Figure 6.8). The vanes are pushed into the surface of the sediment and the device is slowly twisted. The maximum shear stress sustained by the sample is shown on the gauge.

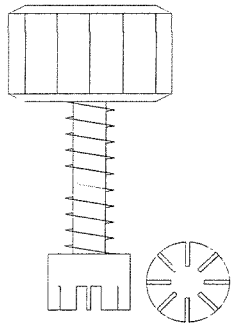

Figure 6.8. The miniature shear vane

6.3.6 Bulk modulus calculation

The bulk modulus of the sample was calculated in two ways. The first method, which is thought to give the best values for elastic moduli (Hamilton, 1971a), uses the 1-D wave equation (Equation 3.1). The dynamic shear modulus was calculated using shear wave velocity and density measurements (Equation 3.5). Dynamic shear modulus values were calculated for the pressurised core using the shear wave velocity measured in the Kastenlot core and the density measured for the pressurised core. Compressional-wave velocity measurements were then used to calculate the bulk

modulus of the sediment. The second method involved the calculation of the bulk modulus using Gassmann's (1951) equations (Equations 3.2 and 3.3), with the bulk modulus of the frame, K_f x 10^8 N/m^2, being calculated using Hamilton's (1971a) regression equation for silt clays:

$$\log(K_f) = 3.73580 - 4.25075n \qquad 6.4$$

where n is the porosity. A value of 54.4 GN/m^2 was assumed for the bulk modulus of the mineral grains (clayey silt, San Diego Trough; Hamilton, 1971a). The bulk modulus of the pore water was calculated from the 1-D wave equation for water (i.e. $G = 0$), assuming a compressional-wave velocity of 1489.8 m/s (the value at 10 °C and a salinity of 35 ‰; Kaye and Laby, 1995) and a density of 1030 kg/m^3 (Kaye and Laby, 1995).

Attempts were made at measuring the frame bulk modulus by means of isotropic compression, but the values were inappropriate due to the high strains produced in compression. See Appendix C for further information.

6.3.7 Pressurised core testing

The pressurised core was logged using the MSCL at 1 cm intervals (see previous section). The parameters of interest were compressional-wave velocity and gamma density. Compressional-wave transmission measurements were then made at 5 cm intervals down the core using a broadband (300 – 700 kHz) source, enabling transmitted signals to be recorded and analysed for phase velocity and attenuation. The source was placed in contact with the core using a specially designed collar to provide a constant coupling force. In addition, measurements were made at 1 cm intervals in the regions where detailed X-ray CT scans (see next section) had been made, with the intention of matching acoustic properties to known bubble size distributions.

The transmission data were processed for compressional-wave attenuation and phase velocity using a direct computation method. The reference data were measured on a core of the same dimensions containing distilled water (Figure 6.9).

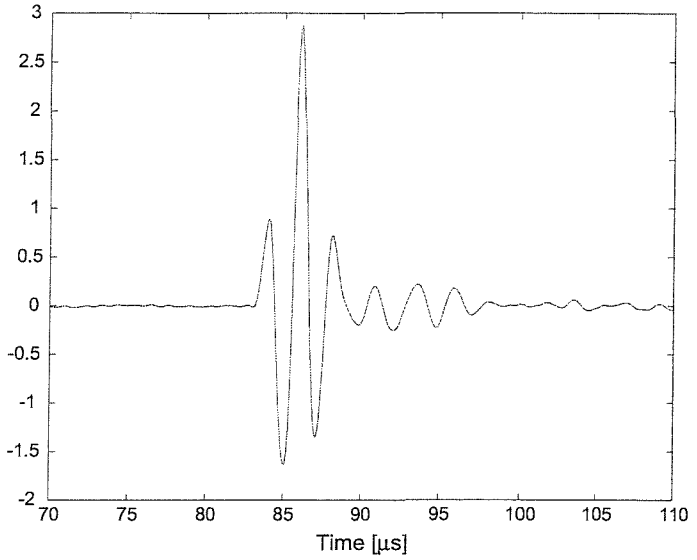

Figure 6.9. The broadband pulse transmitted through the reference water core.

The attenuation coefficient, *a(f)*, was calculated using:

$$a(f) = \frac{8.686}{x_{\text{int}}} \ln \left| \frac{A_w(f)}{A_s(f)} \right| + \alpha_w f^2 x_{\text{int}} \qquad 6.5$$

where x_{int} is the internal diameter of the core; $A_w(f)$ and $A_s(f)$ are the spectral amplitudes of the water and sediment signals, respectively (geometric effects cancel out); α_w is the compressional wave attenuation in distilled water (36×10^{-15} N / m.Hz^2 at 10 °C; Kaye and Laby, 1995); and f is the frequency.

Phase velocity, *c(f)*, was calculated using:

$$c(f) = \frac{x_{\text{int}}}{\left(T_s - \frac{\phi_s}{2\pi f} \right) - \left(T_W - \frac{\phi_W}{2\pi f} \right) + \frac{x_{\text{int}}}{V_w}} \qquad 6.6$$

where T_s and T_w are the window start times of the sediment and water signals, respectively; ϕ_s and ϕ_w are the phase spectra of the water and sediment signals, respectively; and V_w is the velocity of sound in distilled water (assumed to be 1447.3 m/s at 10 °C; Kaye and Laby, 1995).

6.3.8 X-ray Computed Tomography (CT)

X-ray CT scanners have been used for a number of years in medicine. More recently, they have been used for non-destructive analysis of cores (Orsi *et al.*, 1994). The technique allows three-dimensional images of the internal structure of a core to be generated with little effort. The technique has been used to analyse the gassy sediments

found in Eckernförde Bay (Anderson *et al.*, 1998) and generate bubble size distributions. It should be noted that only Type III bubbles can be observed by this method. Types I and II are below the resolution limits of this technique.

X-ray CT scans were collected at six depths on the core, each 58 mm long, with the intention of calculating a bubble size distribution for the core in terms of an equivalent spherical radius (ESR) and associated gas porosity. Twelve slices from each of the detailed scans were printed. The full set of slices may be seen in Appendix A. Unfortunately the positions of the scans were not under the control of the author and, as a result, no scans were collected in the regions between hydrophones 2 and 3 (i.e. 0.8 m to 1.2 m).

Each image was analysed and any isolated regions that had relative density less than that of water were assumed to be filled with gas (since X-ray attenuation is proportional to density, low density areas will appear overexposed, and therefore black, on the negative). These regions were then measured using a Vernier calliper to an accuracy of 0.1 mm. Non-circular regions were treated as elliptical objects, with one short and one long axis. Due to the resolution limits of the X-Ray apparatus and the manner in which densities are calculated, the smallest dimension measured was 0.6 mm. The printed slices were not consecutive, or at regular intervals, and as a result it is extremely difficult to measure a vertical dimension for each of the cavities, although some may be traced through the scans. Therefore, three methods were used to estimate the vertical dimension and thus calculate the ESR, assume that; the longest horizontal dimension is the same as the vertical dimension (LD method); the shortest dimension is the same as the vertical dimension (SD method); and the bubbles are not spherical, but are 1 mm high elliptical prisms (2-D method), since scans were collected at 1 mm intervals down the core. Volumes of the ellipsoids and elliptical prisms were calculated and an ESR was calculated. Gas porosity was calculated as the ratio of the volume of gas to the volume of the scan.

6.4 Laboratory results

6.4.1 Grain size analysis

The analysis results, presented in Figure 6.10, clearly show that the majority of the material throughout the sediment column consists of material mainly less than 63 μm (i.e. silt and clay sized material). There are, however a number of depths at which there is significant sand content (i.e. greater than 63 μm). The top 50 cm of the sediment column has significant quantities of material between 63 and 125 μm. This is due in part to large amounts of shell fragments (see Section 5.2 and Figure 5.4), most notably at 10 cm in depth. At 70 cm there is a very definite peak for material between 63 and 125 μm (fine sand) that was not observed in the auger core. This is repeated at 100 and 110 cm. The latter two peaks could be due in part to a small layer of sandier material found in the auger core at these depths. At 120 and 130 cm there are peaks in the greater than 500 μm size. These could be the result of a second layer of shell fragments, which was found at approximately 130 cm in the auger core. From 140 to 180 cm, the material has a significant proportion of clay (< 2 μm), ranging from 32.4 % to 39.5 % mass frequency.

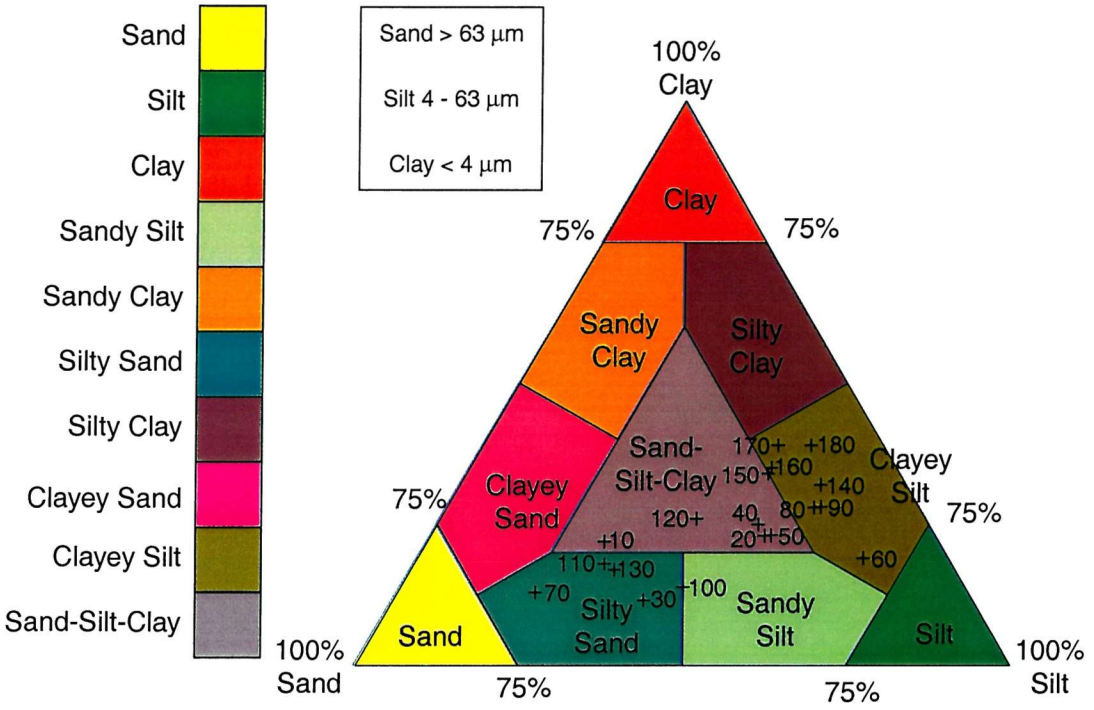

Figure 6.10. (a) Ternary diagram of grain size analysis, based on Shepard (1954).

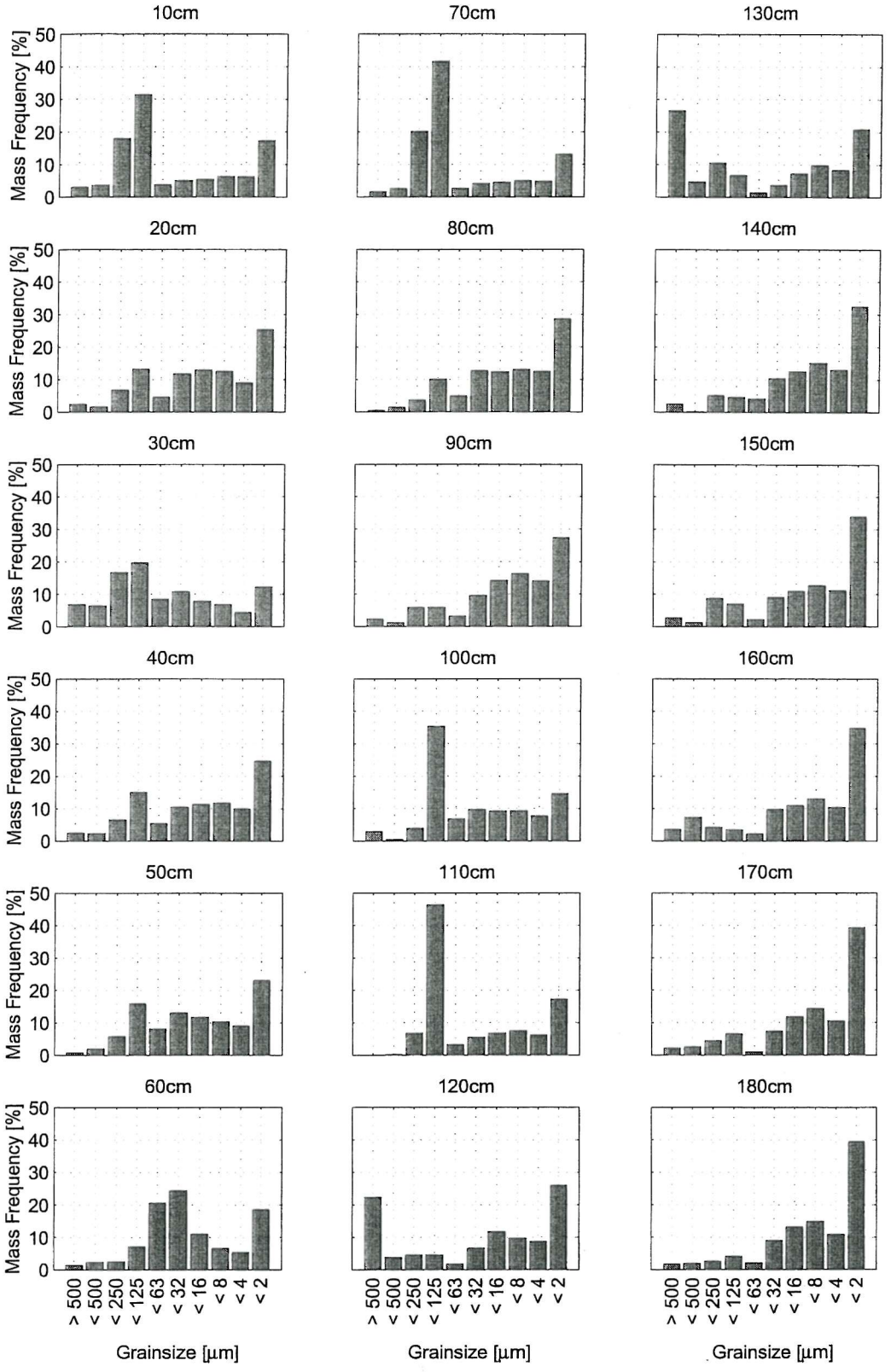

Figure 6.10. (b) Grain size analysis results by sample.

6.4.2 MSCL data, carbon analyses and shear measurements

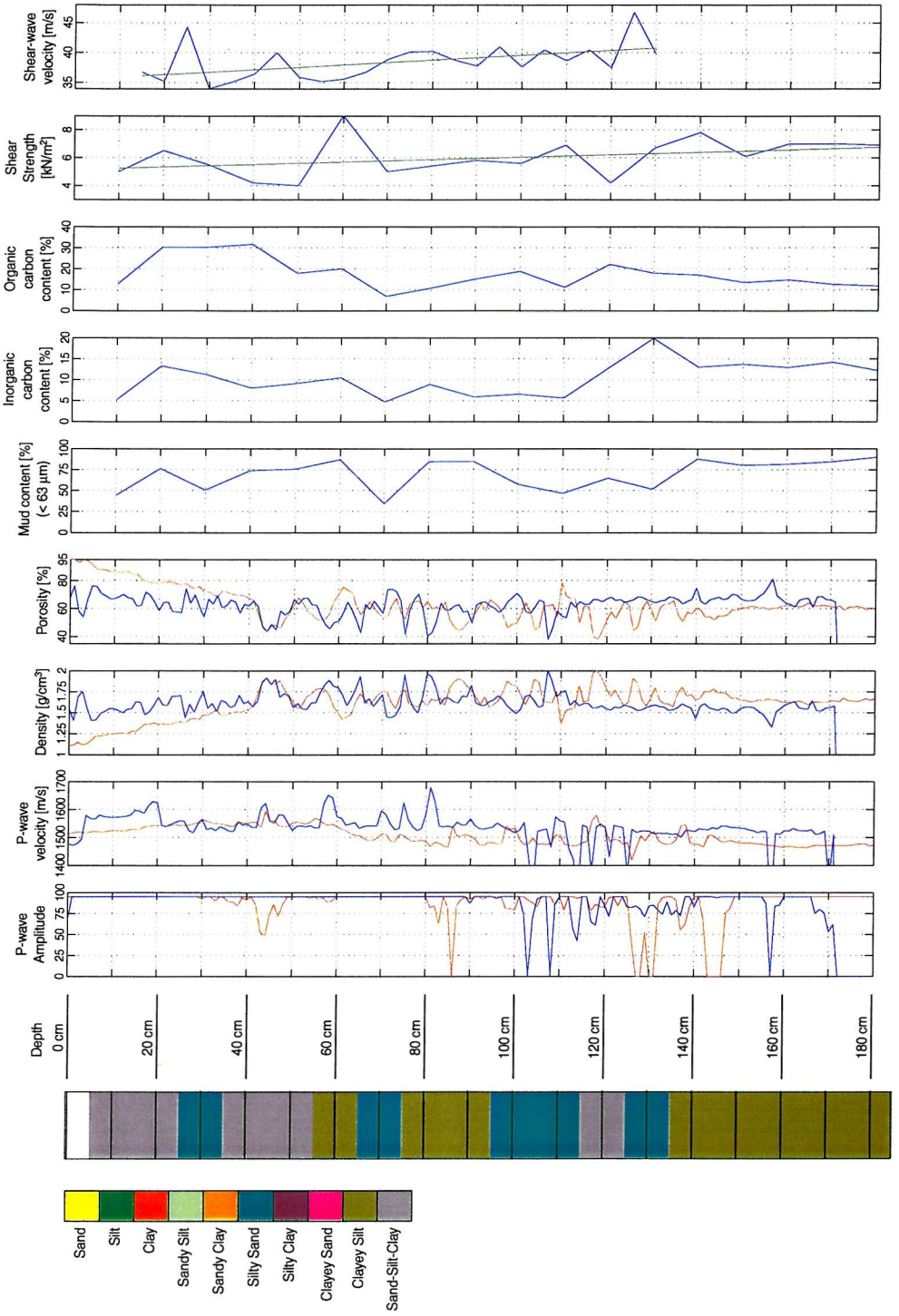

Figure 6.11. MSCL core log data for the pressurised core (red line) and the Kastenlot core (blue line), calculated porosity, mud content (< 63 µm fraction), inorganic and organic carbon content, shear strength (Kastenlot core only; green line is best-fit) and shear-wave velocity (Kastenlot core only; green line is best fit) plotted alongside the grain-size analysis results. MSCL data presented are gamma-ray density, compressional-wave velocity and signal amplitude. High signal amplitude (i.e., close to 100) is an indication of a reliable result.

It should be noted that the cores suffer from compression during the retrieval process. The two different types of core (Kastenlot and pressurised) will each experience different amounts of compression. In addition, the pressurised core contained a certain amount of water at the top. In order to compare results, the data obtained for the pressurised core was depth corrected by matching the double peak in density in the Kastenlot core at approximately 45 cm to a similar peak found in the pressurised core.

Measurements of compressional-wave velocity are broadly in agreement with data presented by Shumway (1960). He reported that coarse silt, with a porosity of 63 %, had a compressional-wave velocity of 1510 m/s, values close to the means obtained from the MSCL data (Table 6.1). The compressional-wave velocity of the pressurised core is generally less than that measured in the Kastenlot core, most obviously deeper than 55 cm, and the trend is for slightly decreasing velocity with increasing depth. Indeed, below 140 cm the velocity of the pressurised core is consistently 50 m/s lower than that measured in the Kastenlot core. Excluding the high velocity layer near the surface (0 - 20 cm), the Kastenlot core compressional-wave velocity is generally constant with depth, with a series of peaks between 55 and 85 cm depth. There are a series of troughs in the compressional-wave velocity deeper than 100 cm, but these coincide with regions of low signal amplitude, indicating poor transmission. Density and porosity values for the two cores are consistent with one another. However, shallower than 40 cm, the pressurised core steadily decreases in density (increases in porosity). This is due to slumping of the core material inside the barrel.

Parameter	Mean ± 95 % CI	Range of values
Compressional-wave velocity:		
Pressurised core	1508 ± 4.9 m/s	1594 – 1418 m/s
Kastenlot core	1535 ± 8.3 m/s	1679 – 1243 m/s
Density:		
Pressurised core	1.582 ± 0.025 g/cm^3	2.002 – 1.105 g/cm^3
Kastenlot core	1.612 ± 0.017 g/cm^3	2.004 – 1.325 g/cm^3
Porosity:		
Pressurised core	63.2 ± 1.8 %	95.2 – 37.7 %
Kastenlot core	62.7 ± 1.1 %	81.1 – 37.6 %
Shear wave velocity:		
Kastenlot core	38.5 ± 1.3 m/s	34.0 – 46.8 m/s

Table 6.1. MSCL mean velocity and porosity values with 95 % confidence intervals and range of values.

Mud content is generally high (greater than 75 %) throughout the sediment with the exception of three zones: 30 cm, 70 cm and 90 to 140 cm. These correspond to the layers of silty sand, one of which is thought to contain peaty material (30 cm, high organic carbon content, evidence of wood fragments in auger core, Figure 5.4), and another that contains shell fragments (130 cm, high inorganic carbon content. Trendlines have been plotted with the shear velocity and strength data, indicating a steady increase in both parameters with depth.

Upon detailed examination, it may be seen that in the first 10 cm of the Kastenlot core, there is a peak in density reaching 1.75 g/cm^3 at 3cm, coinciding with the surficial shell layer. In this region, and up to 20 cm depth where the sediment is sand-silt-clay, the density of the pressurised core appears low due to slumping of the sediment within the core barrel. Between 3 and 20 cm the compressional-wave velocity steadily increases from 1580 m/s to 1628 m/s and the trend for the density is to also increase from 1.4 g/cm^3 to 1.68 g/cm^3. In this range, each of the mud content, organic and inorganic carbon contents and shear strengths also increase. The shear-wave velocity graph appears at first to not match the profile of the shear strength. However, when core compression is taken into consideration (shear wave velocity was measured on the shorter of the two Kastenlot cores, while shear strength was measured on the longer), the peak at 25 cm could be taken to represent the same change in material property that is represented by the peaks in the other measurements. Alternatively it could be proposed that, because the shear strength measurements only test the intact surface of the core they do not account for any cracking / cavities in the sediment, unlike the shear-wave measurements, which travel through the body of the core.

At 20 cm, there is a sharp decline in compressional-wave velocity measured on the Kastenlot core that corresponds well with the change from a shelly material to one containing much organic material. This organic layer is thought to extend from approximately 20 to 40 cm, and this is represented by low, reasonably constant compressional-wave velocities of approximately 1450 m/s, which suddenly rises to 1620m/s at 44 cm. At this point, the compressional-wave velocity measured in the pressurised core also increases, as does the density measured on both cores. This organic layer is marked by a drop in mud content, possibly due to large fragments of organic material. The organic carbon content, however, remains high at 30 %, as may be expected. Shear strength decreases in this region from 6.5 kN/m^2 to 4.2 kN/m^2. Shear wave velocity also decreases from 44 m/s to 36.5 m/s if it is assumed that the

peak at 25 cm matches the shear strength peak at 20 cm. Below this organic layer, the organic carbon content reduces while inorganic carbon and mud contents increase slightly.

At 55 to 60 cm there appears to be a higher velocity layer in the Kastenlot core data. This is matched by an increase in density in both sets of MSCL density data and also by a sharp increase in the shear strength. Accounting for core compression, it is probable that the peak followed by a trough in the shear wave velocity, between 45 and 60 cm, is a result of the same factors that cause a similar profile in the shear strength between 60 and 80 cm. It is then possible to conclude that there is also a peak shear wave velocity at 60 cm. This feature was not noted in the examination of the auger core, but the grain size data shows an increase in the very coarse (32 to 63 μm) and coarse (16 to 32 μm) silt fractions and the sediment may be classified as clayey silt.

Between 60 and 80 cm the compressional-wave velocity of the pressurised core is consistently lower by approximately 50 m/s than that measured on the Kastenlot core, possibly as result of open cracks or bubbles. However, much of the structure, such as the peaks at 70 and 75 cm, is reproduced. These two peaks reach 1595 m/s and 1625 m/s for the Kastenlot core and 1510 m/s and 1510 m/s for the pressurised core. These velocity peaks are matched by peaks in density in both cores. A third peak in velocity, reaching 1680 m/s, is seen in the Kastenlot core at 80 cm and is matched by a peak in density, although no evidence was seen in the pressurised core data. Mud content and both inorganic and organic carbon contents seem to decrease in this region, and it is at 70 cm where there is a sharp increase in the fraction of sand-sized material (> 63 μm), with the sediment being classified as silty sand. However, mud content and both carbon contents both increase towards 80 cm as the sediment becomes clayey silt once more.

At 100 to 110 cm, there is a large increase in sand size material associated with the thin sandy layer found in the auger core, and the grain size data show both of these samples to be silty sand. The large increase in the greater than 500 μm fraction in the region of the second shelly layer (from 120 to 130 cm) is matched by a steady increase in inorganic carbon content (i.e. calcium carbonate). It is likely that the sudden decrease in shear strength is a result of shell material preventing cohesion between clay particles.

6.4.3 Bulk modulus calculation

Presented in Figure 6.12 are plots of dynamic shear modulus, acoustically derived bulk modulus and computed bulk modulus. Mean computed bulk modulus is the 5th point mean of the raw computed data. This means that at every 5th point (i.e., 5 cm in depth) a value is assigned that is the mean of the values at that depth and the two values on each side. In this way, the data are decimated to match the sampling interval of the acoustically derived data. All comparisons between the two datasets (computed and acoustically derived) will be based on this decimated dataset.

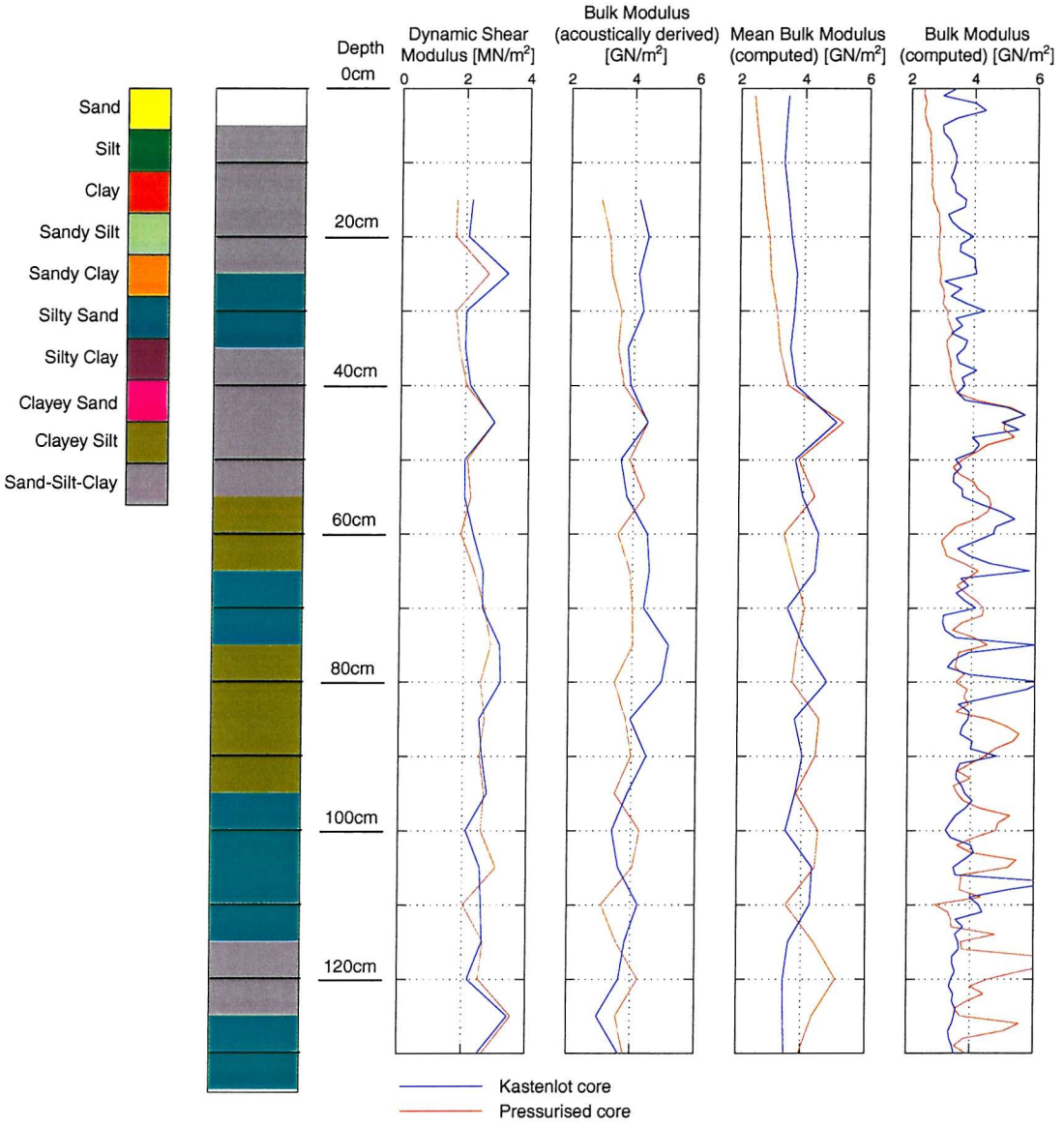

Figure 6.12. Acoustically derived and computed (mean and raw) values of bulk modulus plotted against depth.

Down the core, the shapes of the two bulk modulus profiles (acoustically derived and mean computed) are rather similar. There are a number of peaks in the supposedly more accurate acoustic data that are reproduced in the computed data. For example, the peaks at 45 cm, 80 cm, 90 cm and 110 cm are present in both (computed and acoustically derived) pressurised datasets. It is interesting to note, however, that at some points the mean computed values are higher than the acoustically derived values for both cores, while at other points the opposite is true. Good examples are seen in the pressurised data at 45 cm, where both computed values are higher, and at 70 cm, where the computed value for the Kastenlot core is lower. It is possible to see that at depths greater than 40 cm, the computed values tend to be greater than their acoustically derived counterparts for the pressurised core data. This fact is particularly noticeable at 45 cm and 85 cm. However, for the Kastenlot core, the acoustically derived data appears to be greater than the computed data. The acoustically derived data is noticeably lower than the Kastenlot core data between 60 cm and 100 cm, reflecting the compressional wave velocity profile from the MSCL (Section 6.4.2), Mean values of the shear modulus and bulk modulus (both methods), with 95 % confidence intervals, are displayed in Table 6.2. The data are all within one standard deviation of each other, although it is interesting to note that the acoustically derived pressurised core bulk moduli are consistently lower than those measured in the Kastenlot. This could be the result of gas bubbles increasing the overall compressibility of the sediment (i.e. decreasing the bulk modulus).

Parameter	Mean (95 % CI)	Range
Dynamic shear modulus:		
Pressurised core	2.42 ± 0.20 MN/m^2	$3.55 - 1.69$ MN/m^2
Kastenlot core	2.52 ± 0.18 MN/m^2	$3.44 - 2.00$ MN/m^2
Bulk modulus (acoustic):		
Pressurised core	3.75 ± 0.17 GN/m^2	$4.46 - 2.97$ GN/m^2
Kastenlot core	4.07 ± 0.21 GN/m^2	$5.14 - 2.96$ GN/m^2
Bulk modulus (computed)		
Pressurised core	3.90 ± 0.28 GN/m^2	$5.22 - 2.75$ GN/m^2
Kastenlot core	3.89 ± 0.18 GN/m^2	$5.01 - 3.45$ GN/m^2

Table 6.2. Mean values for the elastic moduli of the sediment with 95 % confidence intervals.

6.4.4 Pressurised core broadband transmission data

Broadband results are shown in Figures 6.13 and 6.14. Plots of all broadband data (signal, attenuation profile and phase velocity) may be seen in Appendix B.

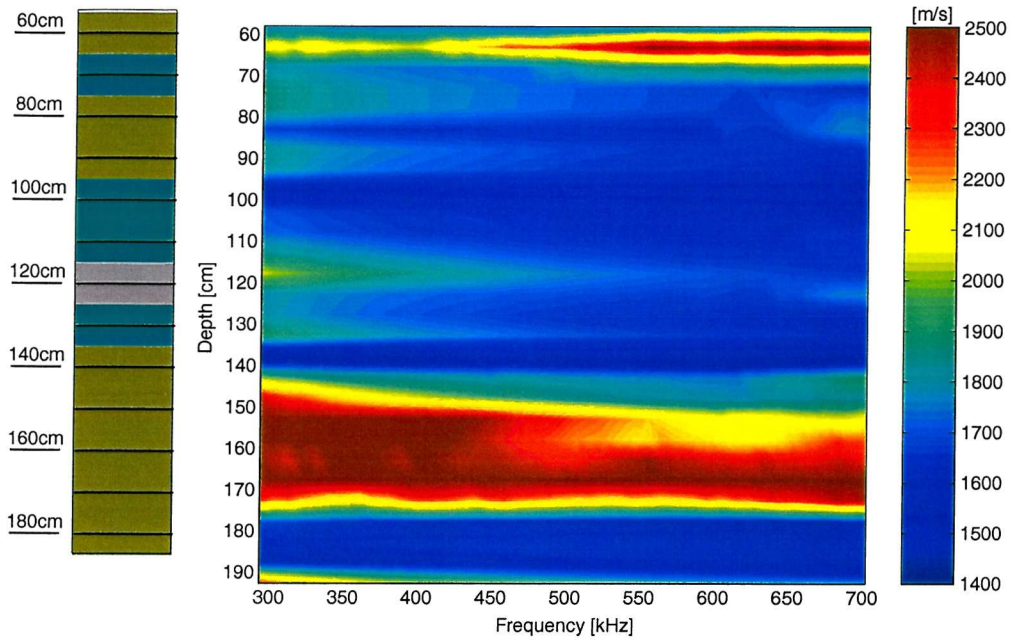

Figure 6.13. Phase velocity [m/s] for the broadband transmission experiments, plotted alongside the grain size analysis results for comparison.

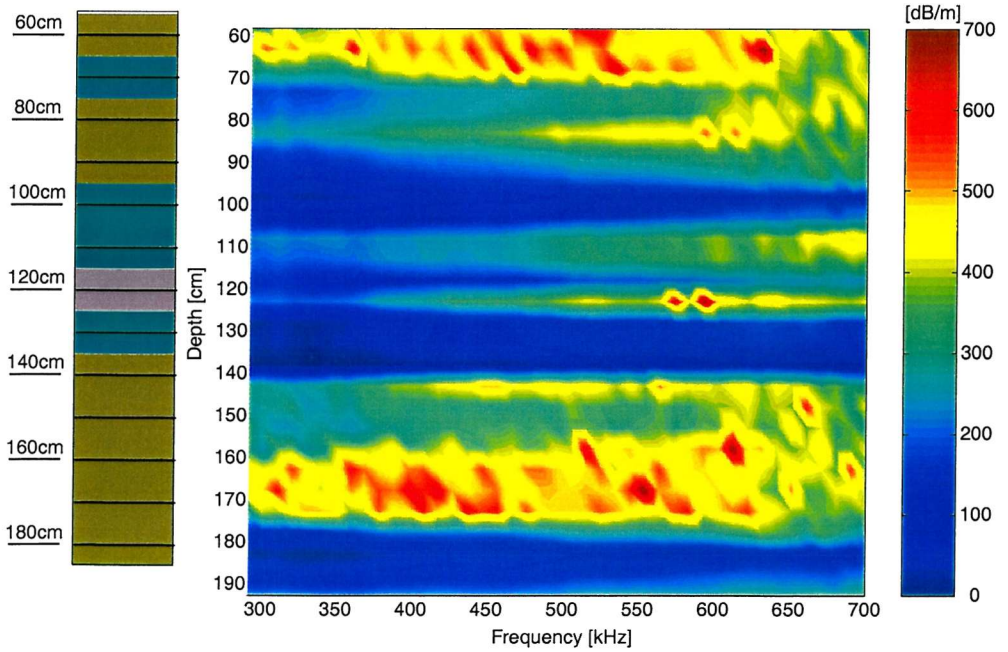

Figure 6.14. Attenuation coefficients [dB/m] for the broadband transmission experiments, plotted alonside the grain size analysis results for comparison.

The most striking features in these plots are the bands of high attenuation and phase velocity shallower than 70 cm and between 140 cm and 180 cm – all regions of clayey silt or sand-silt-clay material. In these regions, the phase velocity reaches, and in some cases exceeds, 2500 m/s, and attenuation coefficients reach 700 dB/m. High phase velocity is possibly a result of very poor signal to noise ratio. Attenuation coefficients of various types of fully saturated silt clays and clays have been measured at between 40 dB/m (at 400 kHz) and 90 dB/m (at 500 kHz) (Bowles, 1997), values that are consistent with those presented by Kibblewhite (1989), but considerably lower than those encountered here. Much of the rest of the broadband data shows linearly increasing attenuation coefficients, from approximately 200 dB/m at 300 kHz to 400 dB/m at 700 kHz.

Values of exponent of frequency (*n'* in Equation 3.4) were found by measuring the gradient of a straight line fitted to of log-log plots of attenuation (in nepers) versus frequency. The coefficient of correlation (R^2) was calculated to give a measure of the goodness of fit. The results show that, while the majority of exponents of frequency (*n'* in Equation 3.4) are clustered around unity, some reach as high as 3.8 (Figure 6.15).

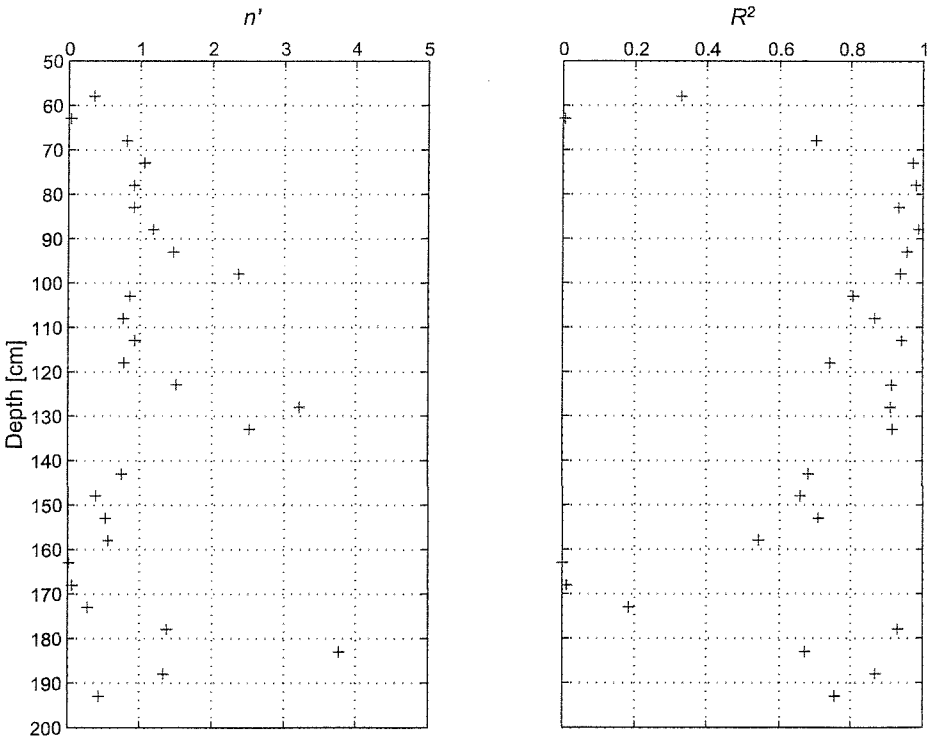

Figure 6.15. Exponent of frequency, n', and associated R^2 values versus depth.

The exponent of frequency is usually expected to be close to one (Hamilton, 1972), unless Rayleigh scattering is occurring, when it is expected to be close to four (Busby and Richardson, 1957). The mean exponent of frequency is 1.08 ± 0.37 (95 % confidence interval), indicating that the data generally conforms to Hamilton's (1972) conclusion that *n'* is close to unity. However, there are a number of regions where this is not the case. At 98 cm, 128 cm, 133 cm and 183 cm values of exponent *n'* are greater than 2, and at 98 cm, 128 cm and 133 cm, the coefficients of correlation are greater than 0.90, indicating a good fit to the data. Grain size analysis results show that these regions (100cm and 130 cm) are areas where the sediment is silty-sand. It should be noted that, at 128 cm and 133 cm, there is evidence from the X-ray CT scans of a large number of free gas bubbles (Scan 13) and that the free gas horizon is thought to exist at approximately 1m (Section 5.4, Section 5.8). At 183 cm, R^2 is 0.67, indicating an unreliable fit.

Phase velocity outside of the high velocity regions is generally between 1400 m/s and 1700 m/s, although some of the data show velocities around 2000 m/s at low frequency before dropping to below 1700 m/s, usually by 400 kHz.

6.4.5 X-ray Computed Tomography

Example scans are shown in Figure 6.16.

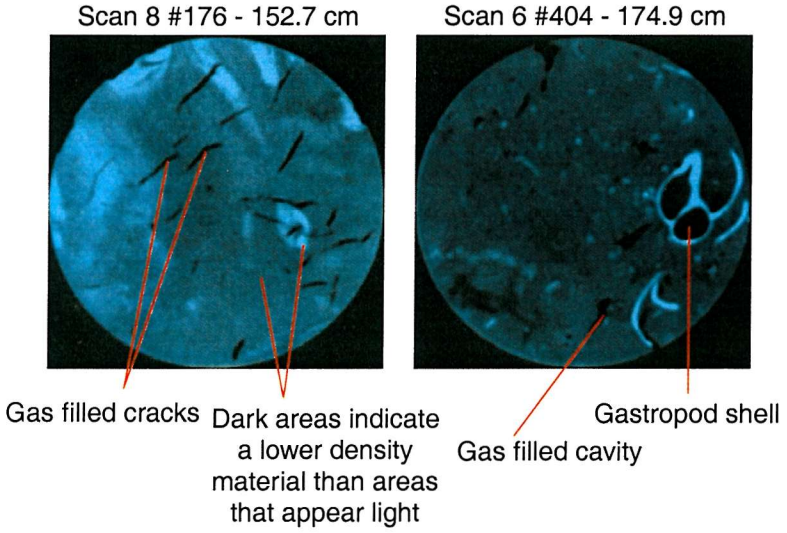

Figure 6.16. Sample CT scans.

Size (equivalent spherical radius, ESR) and depth distribution of the bubbles is shown in Figure 6.17a. Bubble size distribution is displayed in Figure 6.17b. The data appeared to follow a power law distribution and the discrete frequency method detailed

by Pickering *et al.* (1995) was used to measure the parameters of the power law. As described by Pickering *et al.*, the data were binned into interval of equal size such that each bin contained at least one sample. The number in each interval was plotted against the interval midpoint using log scales, ignoring the intervals and any intervals with fewer than two data points (Pickering *et al.*, 1995). A line of best fit was then calculated using a robust least squares method (Press *et al.*, 1992). It should be noted, as described in Pickering *et al.* (1995) that the gradient of the fitted line will be the slope of the distribution + 1.

The methods used to calculate the ESR (Section 6.3.8) will have an effect on the size distribution. Using the LD method increases the number of bubbles over 10 mm ESR, while the 2-D method produces a distribution of bubbles entirely below 10 mm ESR. Although the scans are all below the depth of receivers 2 and 3 in the twenty-four hour experiment (Section 5.8), the data will be assumed to be representative of the whole gassy zone.

Scan 15 has a comparatively small number of bubbles, all of which fall either below 5 mm ESR (2-D method) or 10 mm ESR (LD method). Scan 13 has the greatest concentration of small bubbles and it is interesting to note that this scan straddles the boundary between a highly organic layer and a sandier layer with shell material. This is the zone where high values of exponent n were measured (Section 6.4.4). Scans 11 and 8 have few spherical, or near-spherical, cavities in them, and much of their contribution to the gas porosity is made of cracks. As a result, they have a large proportion of their bubbles greater than 5 mm ESR, especially using the LD method. Scan 5 has a number of large, near-spherical bubbles, as well as a number of smaller bubbles. Finally, scan 6 has a number of inclusions of various geometries, as well as a number of gastropod and bivalve shells, some of which are still intact, that contain void spaces.

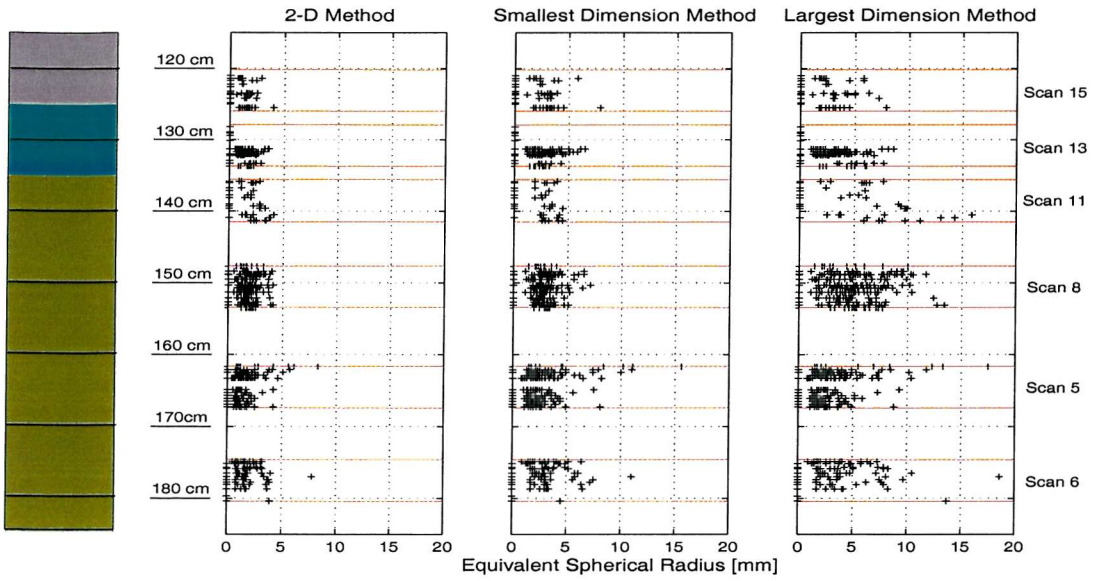

Figure 6.17. (a) Bubble size and depth distribution for each of the three methods used to determine equivalent radii.

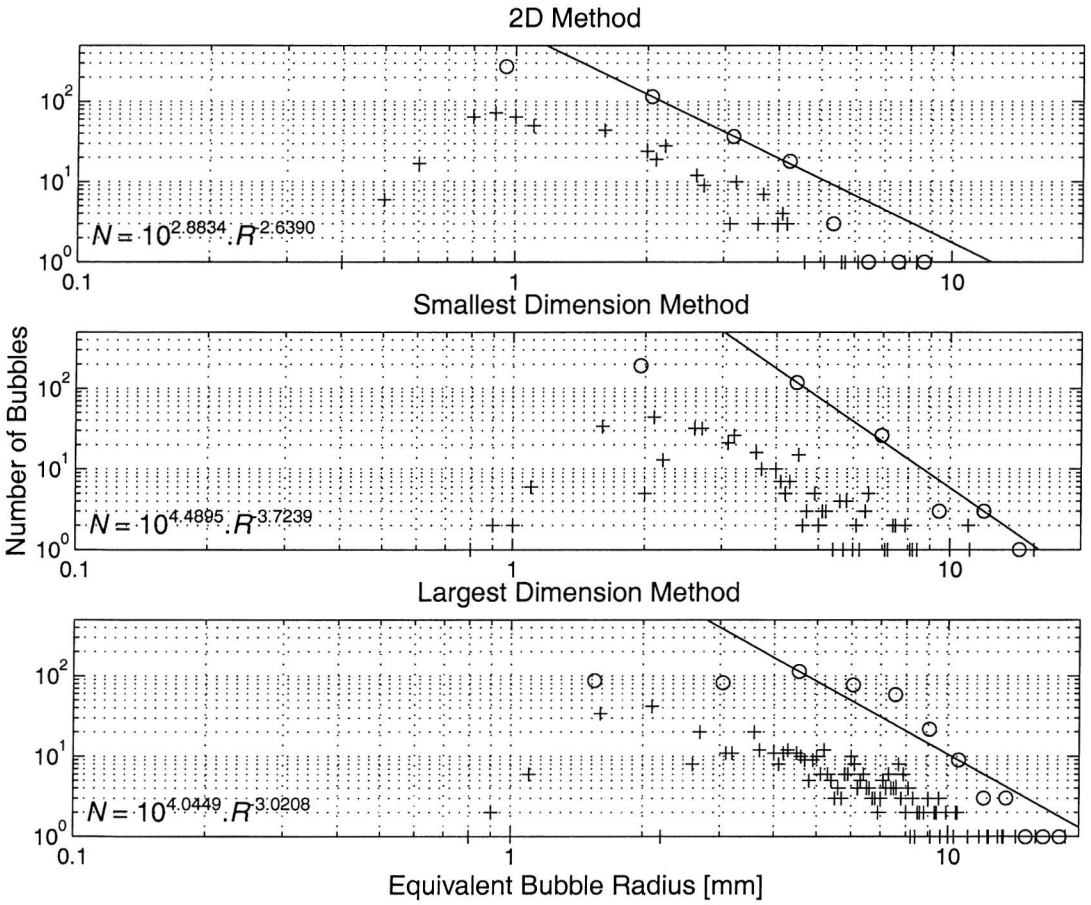

Figure 6.17. (b) Bubble size distribution for each of the three methods used to calculate equivalent spherical radius. The '+' symbols represent the actual bubbles and the 'o' symbols represent the binned data to which the line was fitted.

Although the data (Figure 6.17b) indicates that there is a radius at which a maximum number of bubbles occurs, this is most likely due to the resolution of the measurement techniques (X-ray CT scanning and manual measurement of the X-ray films) since bubbles with radii as small as 0.1 mm have been observed (Gardner and Goringe, 1988). In bubble clouds in water, it is known that the number of bubbles of a certain radius increases as the radius decreases to a certain point, after which the number of bubbles decreases with decreasing radius (Farmer and Vagle, 1989). As discussed in Section 3.3.1, decreasing bubble radius leads to an increase in the surface tension, causing the internal pressure of the bubbles to increase (Equation 3.6). This will eventually lead to the bubble being driven into solution and it is thought that the limiting radius for a bubble is 10 μm (Anderson and Hampton, 1980a), far less than the smallest radius that may be measured in these experiments. Data presented by Anderson *et al.* (1998) indicate a similar tail off in bubble numbers as the resolution of the machine used to measure them is approached. It may be concluded, then, that the tail off in bubble numbers is due to the resolution of the measurement techniques and that the number of bubbles present will continue to increase with decreasing radius at a similar rate to that seen above the observable maximum.

Figure 6.18 shows scan slices and associated broadband transmission data recorded close to the centre of each scanned region.

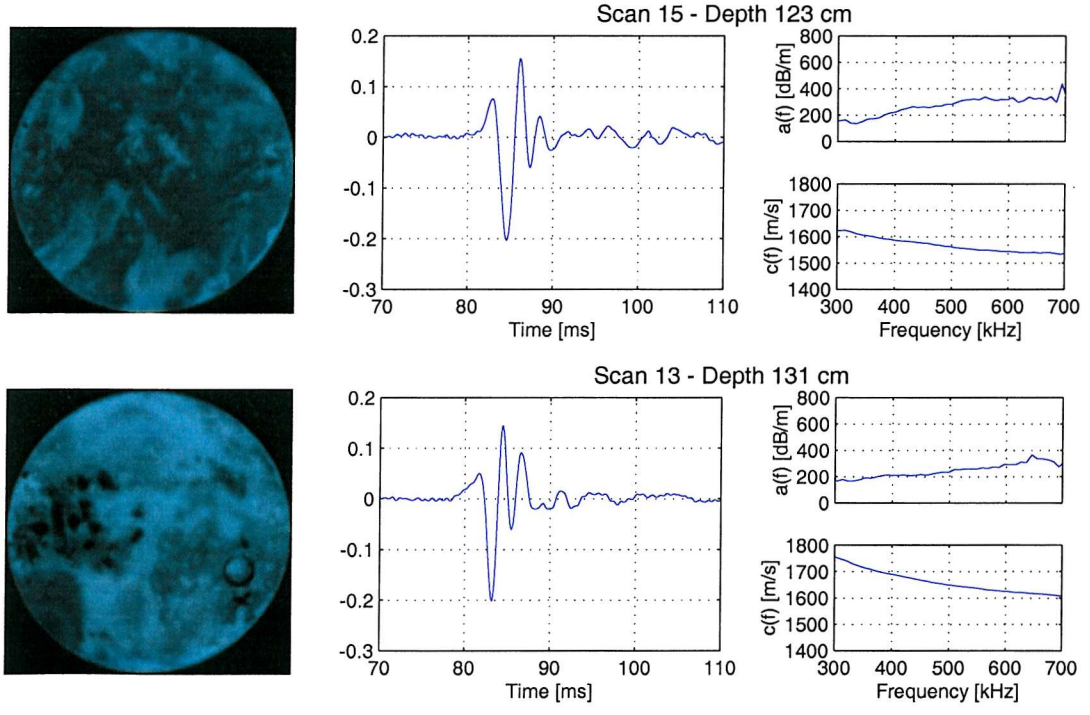

Figure 6.18 continues over page.

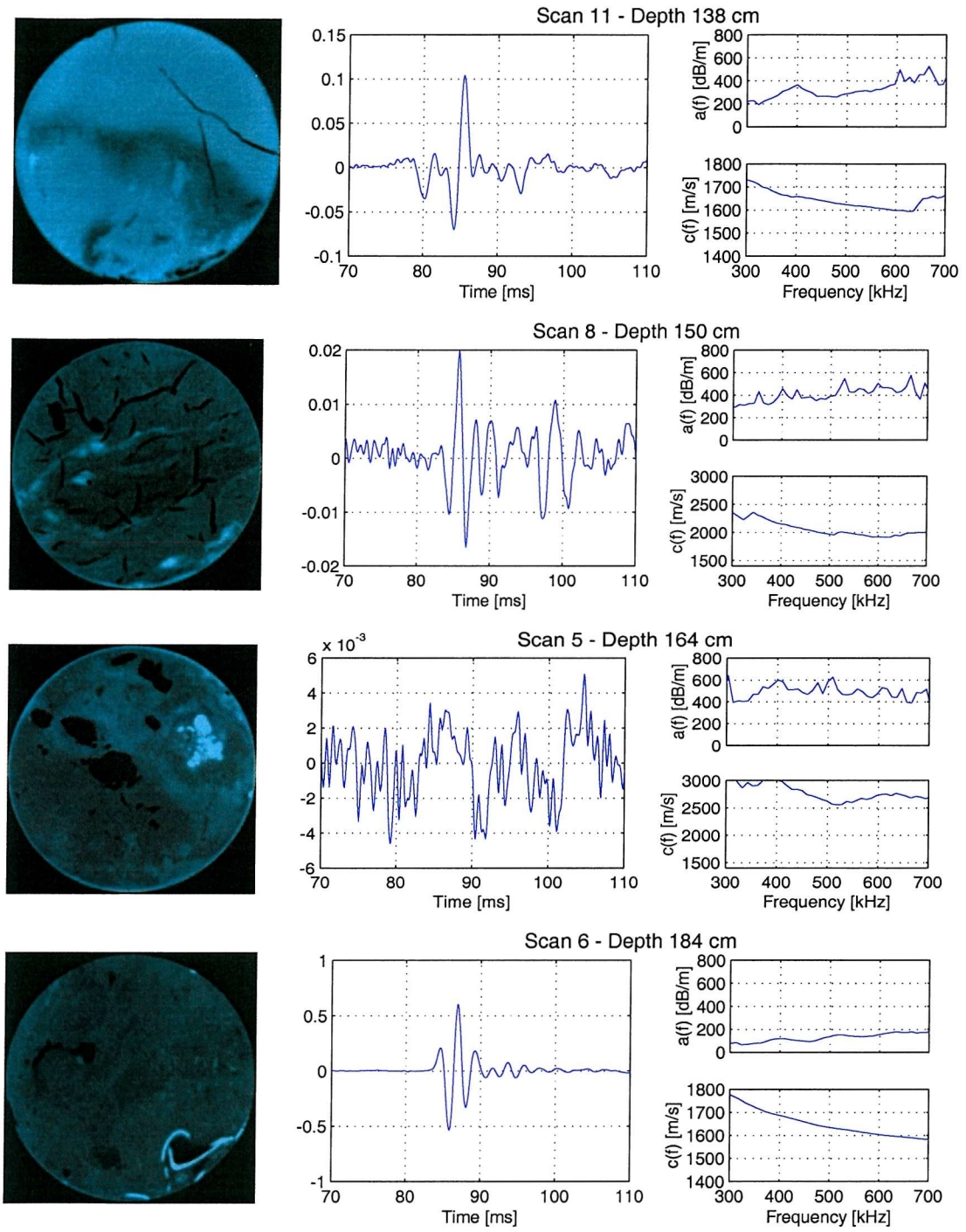

Figure 6.18. X-Ray CT scans and associated broadband transmission data: signal, attenuation a(f) and phase velocity c(f).

These selected acoustic data, obtained and processed in the manner described in Section 6.3.7, show a trend of steadily increasing attenuation across the frequency range (300 – 700 kHz) generally between 200 and 400 dB/m, with the exception of the data at 150 cm (Scan 8) and 164 cm (Scan 5). This is consistent with the data in the previous section, where there was a band of highly attenuating sediments between 140

and 180 cm. Phase velocity has a similar profile for all depths, again with the exception of Scans 5 and 8, decreasing from approximately 1700 m/s to 1600 m/s with increasing frequency.

Scans 5 and 8 show high attenuation, generally above 400 dB/m. The trend on Scan 8 is for attenuation to increase with frequency, while Scan 5 shows no obvious relationship between frequency and attenuation. CT images show that Scan 8 has significant cracking and Scan 5 has large bubbles and a significant amount of large grained material. Both features could be responsible for the high attenuation coefficients measured. However, the large number of bubbles observed in Scan 13 do not appear to increase attenuation, perhaps because they are not resonating.

In order to determine if bubble resonance is occurring, a resonant bubble radius was calculated for the frequency range of the two experiments using Equation 4.18 (rearranged to find r). Physical parameters used for the model were derived from the mean values of the results described in Section 6.4.2, and are listed in Table 6.3. Additional parameters may be found in Table 4.1. Results are shown in Figure 6.19.

Frequency range	0.1 – 1000 kHz
Sediment density	1692 kg/m^3
Gas density	0.717 kg/m^3
Depth	0.725 m
Dynamic shear modulus	2.52 MN/m^2

Table 6.3. Values of physical parameters used to calculate resonant bubble radius

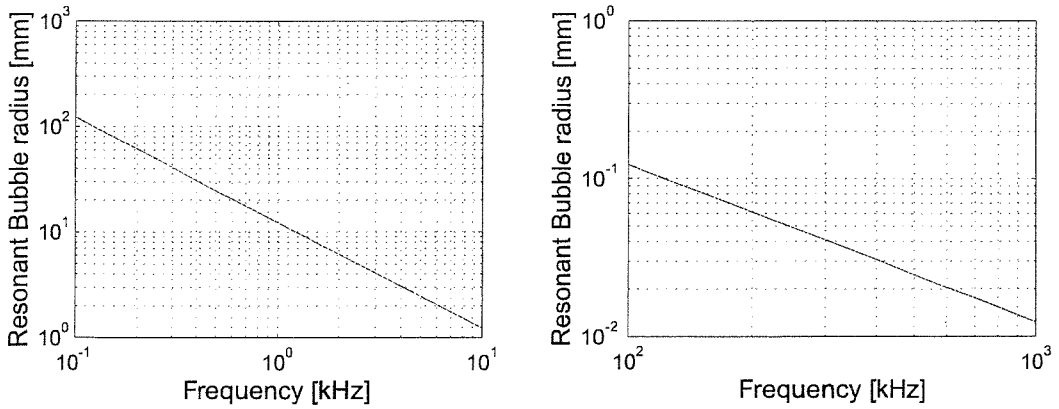

Figure 6.19. Resonant bubble sizes for the frequency ranges used in the in situ *and laboratory acoustic experiments, (a) 0.1 – 10 kHz and (b) 100 – 1000 kHz*

At 300 kHz, a resonant bubble in the conditions found in Dibden Bay would have a radius of 0.04 mm, far below the resolution of the CT scanner. This would indicate that either Rayleigh scattering is occurring or the bubbles are increasing the attenuation off-resonance.

At the lower frequency range of the mini-boomer (Figure 6.19a), the model predicts a resonant bubble would have a radius between 123 mm (at 100 Hz) and 4.1 mm (at 3 kHz). Results from the CT scans indicate that there are bubbles of sufficient size in the sediment to resonate at these frequencies, causing the high attenuation coefficients measured in the twenty-four hour experiment.

6.5 Discussion

The main purpose of this chapter was to establish a set of parameters for input to the model, to investigate the high frequency (300 – 700 kHz) acoustic response of the sediment and to investigate the bubble size distribution.

In many ways, the sediment is typical of fully saturated sediments of a similar composition. Compressional-wave velocity measurements from the MSCL are in close agreement with data presented by Shumway (1960), whose results indicate that a coarse silt (much of the sediment in this study has been classified as clayey silt, with layers of silty-sand and sand-silt-clay material), with a porosity of 63 %, has a compressional-wave velocity of 1510 m/s. This is very close to the value obtained for the pressurised core (1508 m/s), while the velocity measured in the Kastenlot core is higher by about 25 m/s (1535 m/s). However, this could be the result of the sediment partially drying after sub-sampling. Shear wave velocity values (mean 38.5 m/s) appear low compared to other data (Bowles, 1997), with values quoted for mud, measured at 100 Hz, approximately 50 % higher than those measured in Dibden Bay. However, the silty clay sediments from Eckernförde Bay, which are known to contain gas, have shear wave velocities consistently lower than 20 m/s (Wilkens and Richardson, 1998). Evidence from the CT scans shows that there are large cavities in the sediment. Therefore, according to the model of Wheeler and Gardner (1989), the dynamic shear modulus of the sediment can be expected to be lower than a similar, fully saturated sediment. Note that any fluid, either liquid or gas, may be present in the cavity to produce such an effect.

The bulk modulus of the sediment, both acoustically derived (Kastenlot core: 4.07 GN/m^2; pressurised core: 3.75 GN/m^2) and computed (Kastenlot core:

3.89 GN/m^2; pressurised core: 3.90 GN/m^2) from the individual components, is in agreement with the work of Hamilton (1971a). His results indicate that continental shelf sediments, with a porosity of 60 %, have a bulk modulus of approximately 3.95 GN/m^2.

Down through the sediment column, zones that are known, from the evidence of the auger core (Figure 5.4), to contain significant amounts of organic matter (e.g., 20 to 40 cm) have a noticeable increase in the organic carbon content (from 15 % to 30 %). Similarly, zones with a known increase in content of shell material (such as 130 cm, silty-sand) have a marked increase in the inorganic carbon content, reaching 20 %. Changes in stratigraphy are also matched by changes in velocity and density. A good example is the highly organic layer between 20 and 40 cm where there is a sudden drop in velocity. The sediment changes from a sand-silt-clay composition to silty-sand and back.

The high frequency acoustic response of the sediment is typified by attenuation coefficients increasing from 200 dB/m at 300 kHz to 400 dB/m at 700 kHz, although some are lower. For the most part, attenuation is proportional to the first power of frequency, and regions where there is good signal to noise ratio (i.e. outside the zones of high attenuation highlighted in Section 6.4.4), the coefficient of correlation is high, generally above 0.9, indicating a good fit to the data. Attenuation coefficients in this range could be considered slightly high for silts and clays (Kibblewhite, 1989). However, it should be noted that poorly sorted sediments in Lough Hyne, tested using the same experimental configuration, have attenuation coefficients of 500 dB/m at 400 kHz and 750 dB/m at 700 kHz (Best *et al.*, 2001).

A number of zones in the sediment column are different from the general character. Below 60 cm the compressional-wave velocity measured on the pressurised core is consistently lower than that measured on the Kastenlot core, ignoring areas of low signal amplitude. It is possible that this reduction in compressional-wave velocity is the result of bubble resonance. However, as mentioned in Section 6.4.5, resonant bubbles are less than 40 μm at this frequency and if the bubble size distribution is similar to those encountered in water (Section 6.4.5), it is possible that there will only be a few bubbles of this size present. Evidence suggests that bubbles smaller than 10 μm are forced into solution very quickly (Anderson and Hampton, 1980a), so

perhaps bubbles smaller than 40 μm may also eventually dissolve, making resonance unlikely.

There are zones in the sediment column where the attenuation is not proportional to the first power of frequency. Surprisingly, they are not in the region where the gas horizon was inferred from the *in situ* acoustic evidence (i.e., between 0.8 m and 1.2 m). These regions (shallower than 70 cm and between 140 cm and 180 cm) typically have low R^2 values when calculating the exponent of frequency, indicating that they are not related to frequency in the manner expected. Rather, they appear to have consistently high attenuation across the frequency range. For example, data measured at 163 cm has attenuation coefficients that vary between 400 dB/m and 600 dB/m with no discernable relationship with frequency. Scan 5, which covers the region 161.7 cm to 167.5 cm, shows a large amount of coarse-grained material and a number of large, almost spherical bubbles and Scan 6 (174.7cm to 180.5 cm) shows evidence of bivalve and gastropod shells. It is possible that this mix of very coarse material and clay material (often comprising up to 40 % of the sediment) is causing scattering to occur. Other evidence from the X-ray CT data shows that deeper than 140 cm there is significant cracking of the sediment. This is most effectively demonstrated in Scan 8 (147.7 cm to 153.5 cm). It is possible that these cracks were caused by the coring process. However, their limited vertical extent and central positioning in the core would suggest that they are natural features of the sediment. They could be the result of gas bubble growth or migration and it has been observed that bubbles grown in a gel often form penny shaped cavities (Boudreau, *pers. comm.*). Evidence from X-ray CT scans indicates that one of the long axes of these penny shaped bubbles is in the vertical direction (Abegg and Anderson, 1997).

Other data, such as those at 98 cm, 128 cm, 133 cm and 183 cm, have high values of n', approaching four. Attenuation proportional to the fourth power of frequency is an indication of Rayleigh scattering. Rayleigh scattering occurs where the grain size approaches the acoustic wavelength. At 500 kHz and a compressional-wave velocity of 1550 m/s, the wavelength is 3.1 mm. At 130 cm in the grain size analysis data, and on the auger core, there is a layer of coarser sediment with approximately 27 % of the material in excess of 500 μm, accompanied by a sharp increase in inorganic carbon content, an indication of carbonate shell material.

However, evidence from Scan 13 (127.9 cm to 133.7 cm) shows that there are a large number of small, free gas bubbles in this region. In the region were the gas horizon is thought to exist from the *in situ* acoustic experiments (80 cm to 120 cm; Section 5.8), at 98 cm, the exponent of frequency reaches 2.4 and the correlation coefficient is 0.94, indicating a good fit for the data. The sediment here is also slightly coarser than above or below, being silty-sand rather than clayey silt or sand-silt-clay. Similar values are seen for the measurements at 128 cm and 133cm. This value for the exponent is between the expected value for non-scattering, fully saturated sediment and that for Rayleigh scattering, and it is possible that this is due to the gas bubbles.

6.6 Summary

A summary log is displayed in Figure 6.20. A number of laboratory experiments were carried out to determine: the grain size distribution; the compressional-wave velocity; the shear-wave velocity; the bulk density; the organic and inorganic carbon content; and the shear strength. In addition, the bulk modulus of the sediment was calculated and a pressurised core was imaged using X-ray computed tomography. A complete table of the final values used in the Anderson and Hampton model is displayed in Chapter 7.

Increases in inorganic carbon are matched with increases in coarse-grained material coincident with shell layers. Increases in organic carbon are coincident with known layers of peaty material. Compressional-wave velocity and porosity are consistent with published data (Shumway, 1960). Acoustically derived and computed values of bulk modulus were in close agreement and consistent with published data (Hamilton, 1971a).

The broadband compressional-wave data highlighted a number of interesting features. Much of the sediment column conforms to the first power dependency of attenuation on frequency. However, there are two zones where the attenuation is consistently high and shows no discernable relationship with frequency. X-ray CT scans in these areas show the presence of large amounts of coarse-grained, shell material, as well as significant cracking of the material. These cracks could be a side effect of the coring procedure or they could be the result of the growth or migration of gas bubbles.

Other regions, outside the two zones mention previously, show attenuation depending on powers of frequency much greater than unity. At these frequencies,

Rayleigh scattering is possible, but X-ray CT scan evidence indicates the presence of a large number of small bubbles at one of the depths that this occurs. The frequencies used here are too high for these bubbles to be resonating, but they may be the cause of the elevated values of exponent *n'*.

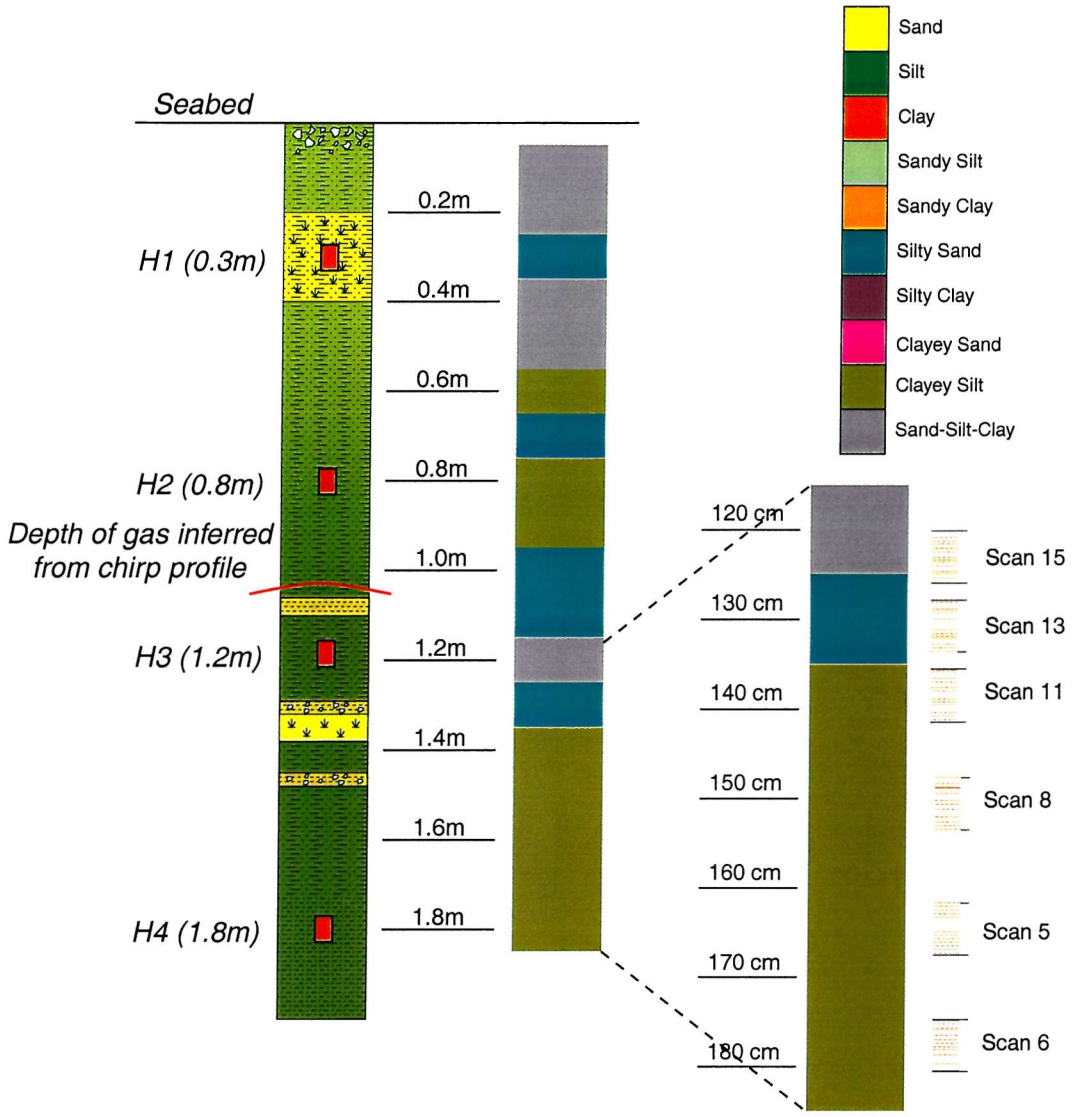

Figure 6.20. Summary log showing: location of hydrophones in 24-hour experiment (Note. This is based on the auger core and the colours have no particular relevance in terms of grain size); a log based on sediment classification; a log of CT scan locations; and a key of sediment classifications for the grain size analysis data.

Chapter 7. Modelling the gassy sediments in Dibden Bay

7.1 Introduction

In this chapter, the Anderson and Hampton model, described in Chapter 4, will be used to calculate theoretical attenuation coefficients and compressional-wave velocities over two tidal cycles using parameters measured in Chapter 6 and the water depths measured from the twenty-four hour *in situ* experiment. The model will be adjusted to account for the effect of varying hydrostatic pressure on bubble radius and gas porosity. Initially a bubble distribution will be fitted so that the model output will match the *in situ* acoustic data for receivers 2 and 3 (Figures 5.22 and 5.27) at low tide, enabling an assessment of the model modifications. Subsequently, a bubble size distribution, adapted from the results of the X-ray CT data, will be applied. Attenuation coefficients calculated by the model do not account for the sediment's intrinsic attenuation, only that produced by the bubble-sediment system. However, the mean intrinsic attenuation of the sediment, measured in the refraction / transmission experiment (Section 5.7), is approximately 4 dB/m. This is only a small fraction (approximately 1.5 %) of the maximum attenuation range of the gassy sediment, so it was decided to omit this component of attenuation.

7.2 The effects of hydrostatic pressure on free gas

The results of the twenty-four hour transmission monitoring experiment indicate that as hydrostatic pressure increases with the rising tide, the bubble radius decreases, since the resonant frequency of the system was seen to increase. It is known that, for the same environmental conditions, only a reduction in bubble size can result in a change in resonant frequency (Section 4.3). The tidal range during the experiment at Dibden Bay was 0 – 2.35 m. This represents, assuming a depth of 1 m to the gas horizon, an increase in hydrostatic pressure from approximately 10 kN/m^2 to 34 kN/m^2 over a 12 hour period, assuming a water density of 1030 kg/m^3 (Kaye and Laby, 1995). Two mechanisms by which a bubble may shrink under changing hydrostatic pressure were considered: pressure equilibrium and diffusion.

7.2.1 Pressure equilibrium

Direct measurement of the pressure inside a gas bubble is not practical, so an estimate must be made by considering the conditions in the surrounding saturated sediment matrix. Limits on the internal pressure of a gas bubble were proposed by Wheeler *et al.* (1990) (Section 3.3.1; Equation 3.7) who concluded that the internal pressure of a bubble was equal to the pore water pressure plus a surface tension term determined by the radius of curvature of the menisci.

Wang *et al.* (1998) provide a detailed model to calculate the ocean tide pore pressure variation, p, in a gassy environment:

$$p = \sigma_B \left[\gamma + (1-\gamma) e^{-i(1+i)\pi z/q} \right] \qquad 7.1.$$

$$\gamma = \frac{1}{1 + n\left(K' + K_{w+g}\right)} \qquad 7.2.$$

$$K' = \frac{3(1-\upsilon)}{1+\upsilon} K \qquad 7.3.$$

$$q = \sqrt{\pi \eta F} \qquad 7.4.$$

$$\eta = \frac{\kappa}{\mu S} \qquad 7.5.$$

Where z is depth; σ_B is the tidally induced surface loading; γ is the loading efficiency; n is the porosity; K' is the confined bulk modulus; ν is the Poisson's ration of the matrix frame; K is the unconfined bulk modulus; K_{w+g} is the bulk modulus of the gas bearing water; μ is the dynamical viscosity of the pore fluid; κ is the sediment permeability; S is the kinematic storage coefficient; and F is the tidal period. The physical sense of the parameter q is the depth of penetration of the pressure changes. For clays the value of q is a few metres (Wang *et al.*, 1998). The material at Dibden Bay is silty clay with a porosity of 63 % (see Chapter 6), and it may be assumed that the permeability is similar to, if not larger than, the value quoted for clay (above), making it clear that the induced pore pressure variation will penetrate to the depth of the gas horizon, identified as being between 0.8 m and 1.2 m from the *in situ* experiments. It was decided, therefore, to assume a pore pressure at the depth of interest equal to the hydrostatic pressure, a common assumption in the field of Soil Mechanics (Craig, 1992).

Surface tension effects are often small compared to the pore pressure, depending on the bubble radius. If it is assumed that the pore water pressure is approximately equal to the gas pressure, the radius of curvature of the meniscus is equal to the radius of the cavity. For a bubble radius of 0.1 mm and a surface tension coefficient of 0.073 N/m (the value for an air/water mixture), surface tension amounts to 1460 N/m^2; for a bubble radius of 1 mm, the surface tension amounts to 146 N/m^2. Evidence suggests that bubble radii in Dibden Bay (Section 6.4.5) and elsewhere (Gardner and Goringe, 1988; Anderson *et al.*, 1998) are in excess of 0.1 mm. In addition, the resonant bubble radius in the frequency of interest in the twenty-four hour transmission monitoring experiment (0 to 3 kHz) is greater than 1 mm (Section 6.4.5, Figure 6.19). It was decided, therefore, to ignore surface tension effects as being insignificant.

If the bubble exists in equilibrium with its surroundings, there must be an increase in the internal pressure of the bubble to match any increase in the pore water pressure. In the absence of any mass transfer into the bubble, there is a decrease in bubble volume, and hence bubble radius. This change in bubble radius will result in a change in the resonant frequency of the system. Assuming the gas conforms to the Ideal Gas Law and there is no temperature change within the sediment during the adjustment, the final bubble radius, r_F, may be calculated from:

$$r_F^3 = \frac{P_I}{P_F} . r_I^3 \qquad 7.6.$$

where r_I is the initial bubble radius; and P_I, P_F are the initial and final pressures, respectively. A decrease in hydrostatic pressure will result in an increase in bubble radius using the same argument.

Each time the bubble radius changes there will be an associated change in the gas porosity, n_g. For example, in a sediment containing 10 mm radius bubbles at a gas porosity of 0.001, for every 1 m^3 of sediment there is 0.001 m^3 of gas. Each bubble contains 4188.8 mm^3 of gas, so there must be 239 bubbles in that cube of sediment. If the bubble radius decreases by 1 mm, the total volume of gas becomes 0.00073 m^3, reducing the gas porosity to 0.00073, a change of 27 %. Therefore, for each change in bubble radius a new gas porosity, based on the new total volume of all the bubbles, will be calculated.

7.2.2 Gas diffusion

Although solubility is affected by changes in pressure according to Henry's Law (Abegg and Anderson, 1997), the mechanism by which the gas transfers from the bubble to the pore water is diffusion, and it is diffusion that will characterise the change in bubble size (Boudreau, pers. comm.). The following model for predicting the radius $R(t)$ of a growing bubble was proposed by Boudreau *et al.* (2001):

$$R(t)=\left[\frac{nD}{2c_g}\left\{\frac{SR_1^{\,2}}{3D}+(c_1-c_0)\right\}t+R_0^{\,2}\right]^{1/2} \qquad 7.7.$$

where n is the porosity; D is the tortuosity-corrected diffusivity; c_g is the concentration of gas in the bubble; S is the local rate of methanogenesis; R_1 is the separation distance between bubbles ($R_1 \gg R$); c_1 is the ambient concentration of the gas; c_0 is the pore water concentration of the gas at R and is a function of c_g; t is the time; R_0 is the initial radius of the bubble. Consider a gas bubble at equilibrium with the surrounding water-saturated sediment. A small reduction in bubble volume, such as that caused by an increase in hydrostatic pressure, will lead to a small increase in c_g (small enough that $c_0 \leq c_1$); diffusion will act to slow down the rate of bubble growth. However, a large reduction in bubble volume (and associated increase in c_g) will lead to sediment undersaturation ($c_0 > c_1$) that may outweigh the local rate of gas production (methanogenesis); this will result in a net reduction in bubble volume and radius. If there is insufficient undersaturation the bubble will continue to grow, albeit at a slower rate.

With sufficient chemical data, it should be possible to use this model to calculate the effect of increasing c_g on the radius of the bubble, but, in the absence of the chemical data required, it has been decided to assume that there is no net change of the bubble radius due to diffusion. This mechanism has, therefore, been excluded. However, its importance may be inferred from the time it takes for the diffusive process to occur. The timescale, t, for a diffusive adjustment over a length L is given by Einstein's relation:

$$t=\frac{L^2}{2D} \qquad 7.8$$

In the case of a bubble in a sediment, L is thought to be of the order of the bubble radius and D is of the order 10^{-5} cm^2/s (Boudreau *et al.*, 2001). Bubbles have been measured between 1 mm and 10 mm in radius, corresponding to timescales

between approximately 8 minutes and 14 hours, respectively. This would indicate that some bubbles might undergo significant diffusion during the period of a tide, assuming saturation conditions were conducive (see above).

7.3 Model implementation

Sound speed ratio and attenuation may be calculated from the equations derived in Chapter 4.

The model was implemented as follows:

- Input initial environmental parameters
- Input bubble radii and associated gas porosity data
- Check tidal height and calculate ambient hydrostatic pressure
- Adjust bubble radius and gas porosity for new ambient hydrostatic pressure
- Calculate parameters X_* and Y_* for that bubble radius and gas fraction over twenty-four hour period
- Repeat until X_* and Y_* have been calculated for all bubble radii over the twenty-four hour period
- Calculate sound speed ratio and attenuation based on the sum of X_* and Y_* (i.e., X_M and Y_M) for each water depth

Table 7.1 lists the parameters, and their values, required by the model.

Water depth	0 – 2.35 m †
Sediment depth	1 m †
Water density, ρ_w	1030 kg/m^3 ‡
Saturated compressional-wave velocity, c_0	1535 m/s †
Sediment density, ρ_s	1612 kg/m^3 †
Saturated sediment bulk modulus, K_{sat}	3.89 GN/m^2 †
Dynamic shear modulus, G	2.52 MN/m^2 †
Quality factor, Q	20.5 †
Imaginary shear modulus, G'	123 kN/m^2 †
Porosity	62.7 % †
Gas density, ρ_g	0.717 kg/m^3 at STP ‡
Specific heat at constant pressure of gas, S_p	2.19 J kg^{-1} °C^{-1} ‡
Thermal conductivity of gas, C_g	3.11×10^{-2} J s^{-1} m^{-1} °C^{-1} ‡
Ratio of specific heats of gas, γ	1.31 ‡
Insonifying frequency range, f	600 – 3000 Hz †

Table 7.1. Values of parameters input to the model. †Denotes values determined in this study, ‡ denotes standard values (Kaye and Laby, 1995).

7.4 Fitted distribution

Initially, a bubble size distribution was matched to the *in situ* acoustic data by comparing the resultant attenuation coefficients to those measured on shot 1 of the twenty-four hour experiment (Figure 5.27). The frequency and magnitude of the various peaks (numbered peaks 1 to 5, left to right) seen in the attenuation profiles (shots 1 and 32) were measured (Table 7.2).

	Shot 1, Time 0 hrs, Depth 0 m		Shot 32, Time 5:10 hrs, Depth 2.35m	
	Frequency [Hz]	Attenuation [dB/m]	Frequency [Hz]	Attenuation [dB/m]
Peak 1	700	180	750	128
Peak 2	1050	214	1250	182
Peak 3	1650	188	1950	194
Peak 4	2100	175	2350	180
Peak 5	2600	227	2800	187

Table 7.2. Frequency and magnitude data for attenuation profiles of shots 1 and 32

A series of attenuation coefficients over the frequency range (600 Hz to 3000 Hz) were calculated using a range of bubble radii with an arbitrarily determined gas porosity. The radius at which the frequency of maximum attenuation occurs was found, and those matching the peaks found in the *in situ* data (Table 7.2) were recorded. A range of gas porosities were then applied, and those that gave an attenuation coefficient matching the *in situ* data were also recorded. The results are shown in Table 7.3 and Figure 7.1.

	Shot 1, Time 0 hrs, Depth 0 m		Shot 32, Time 5:10 hrs, Depth 2.35m	
	Radius [mm]	Gas porosity	Radius [mm]	Gas porosity
Peak 1	19.49	0.0163	18.20	0.0072
Peak 2	13.04	0.0110	10.97	0.0058
Peak 3	8.33	0.0039	7.06	0.0031
Peak 4	6.56	0.0023	5.87	0.0020
Peak 5	5.31	0.0026	4.93	0.0016

Table 7.3. Resonant bubble radii and gas porosity for single bubbles

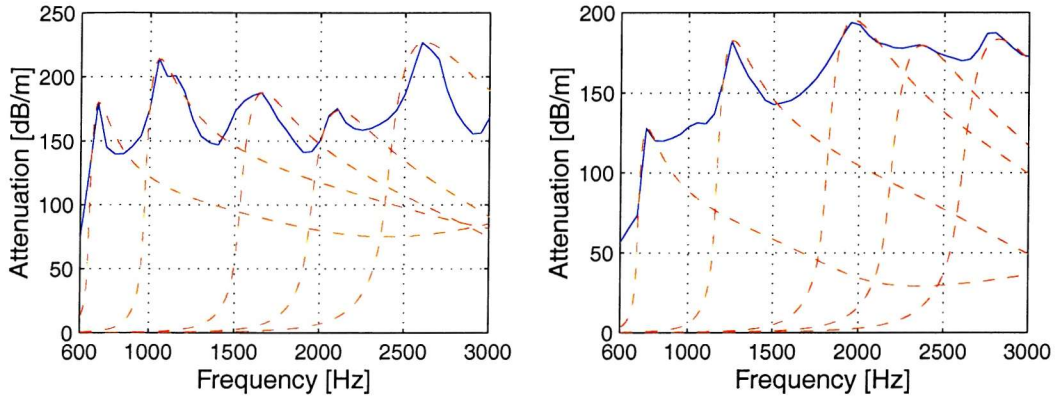

Figure 7.1. In situ attenuation profiles (blue lines) and model attenuations for single bubbles (dashed red lines) (Table 7.3) for (a) shot 1 and (b) shot 32.

Simply inserting these values into the model as a distribution will not work, however. Interactions between the different bubble radii occur, changing the attenuation profile. For example, an increase in gas fraction at one radius can reduce the attenuation coefficient at a lower radius. In Figure 7.2, increasing the gas porosity of the high frequency resonant bubble has the effect of reducing the attenuation due to the low frequency resonant bubble by approximately 45 dB/m.

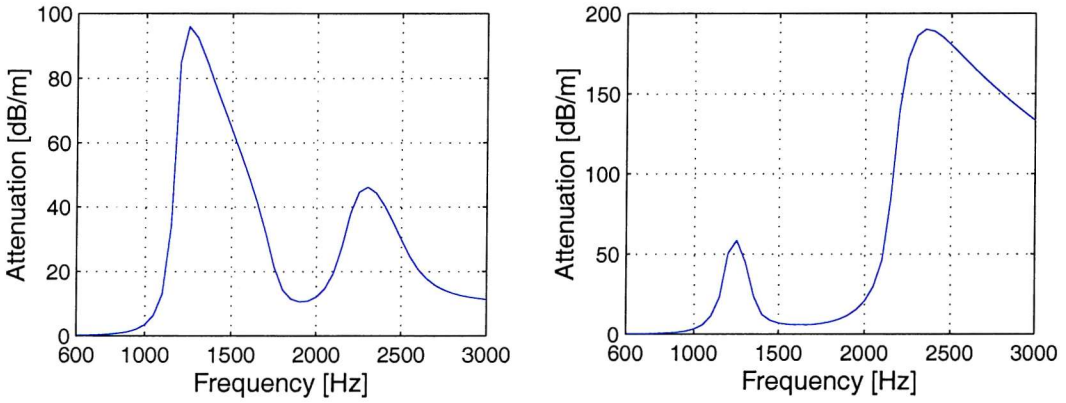

Figure 7.2. Attenuation profiles for a two-bubble system. In both cases the gas porosity of the low frequency resonant bubble is 0.002 and the gas porosity of the high frequency resonant bubble increases from 0.0002 (a) to 0.002 (b).

.

A range of bubble radii from 0.5 mm to 20.8 mm was selected, since, as demonstrated above, bubbles resonating at high frequencies affect the attenuation at lower frequencies, and a series of gas porosities was estimated, based on those calculated above (Table 7.3). By trial and error, based on the starting point of the first

attenuation peak measured in Table 7.3, the bubble size distribution was refined and the resulting attenuation and phase velocity profiles were calculated.

7.4.1 Bubble size distribution

The final bubble size distribution is shown in Figure 7.3.

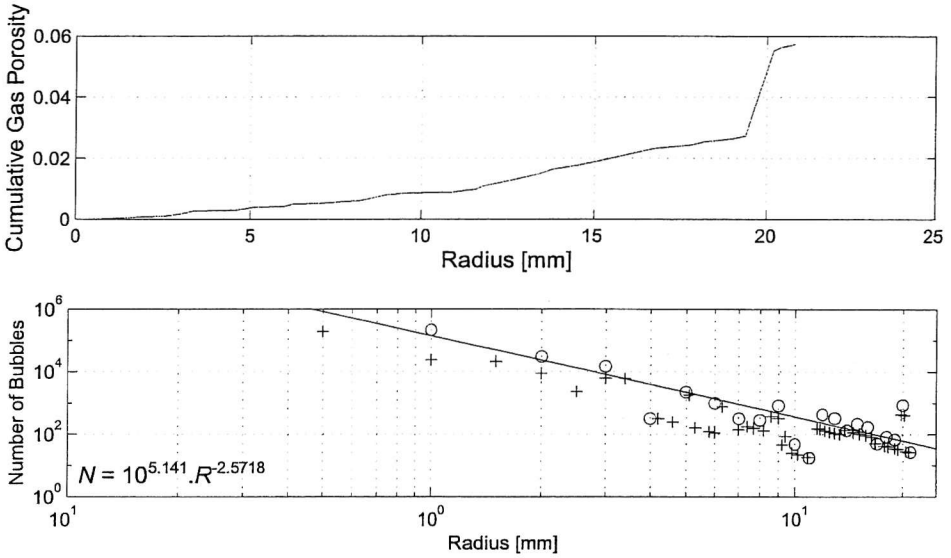

Figure 7.3. (a) Cumulative gas porosity versus bubble radius and (b) bubble distribution based on a 1 m^3 volume of sediment. The '+' symbols represent the actual bubbles and the 'o' symbols represent the binned data to which the line was fitted.

The bubble distribution (Figure 7.3b), although calculated for an imaginary $1m^3$ volume of sediment, may be compared to the distribution calculated from the X-ray CT data by analysing the exponent of radius of the line of best fit, calculated by binning the data in the same way as described previously (Section 6.4.5). A similar exponent would indicate a similar distribution since the constant of proportionality merely reflects the absolute number present, a figure dependent on the volume of sediment for which the number present is calculated. The histogram for the fitted bubble size is based upon a 1 m^3 volume of sediment, while the X-ray CT data are not, hence the difference in numbers of bubbles present. Table 7.4 shows the exponents of radius (in mm) of the fitted data and the X-ray CT data:

Distribution	Exponent
Fitted model	-2.5718
2-D method	-2.6390
SD method	-3.7239
LD method	-3.0208

Table 7.4. Comparison of exponent of radius in mm between fitted and measured distributions.

Clearly the exponent of the fitted data is similar to that of the 2-D method, although the other two methods are considerably different. This could be a consequence of the method used to measure the bubble radii, the small sample sizes or the method used to calculate the power-law distribution.

7.4.2 Attenuation coefficients

The attenuation coefficient results, compared to the *in situ* twenty-four hour data for receivers 2 and 3, are shown in Figure 7.4.

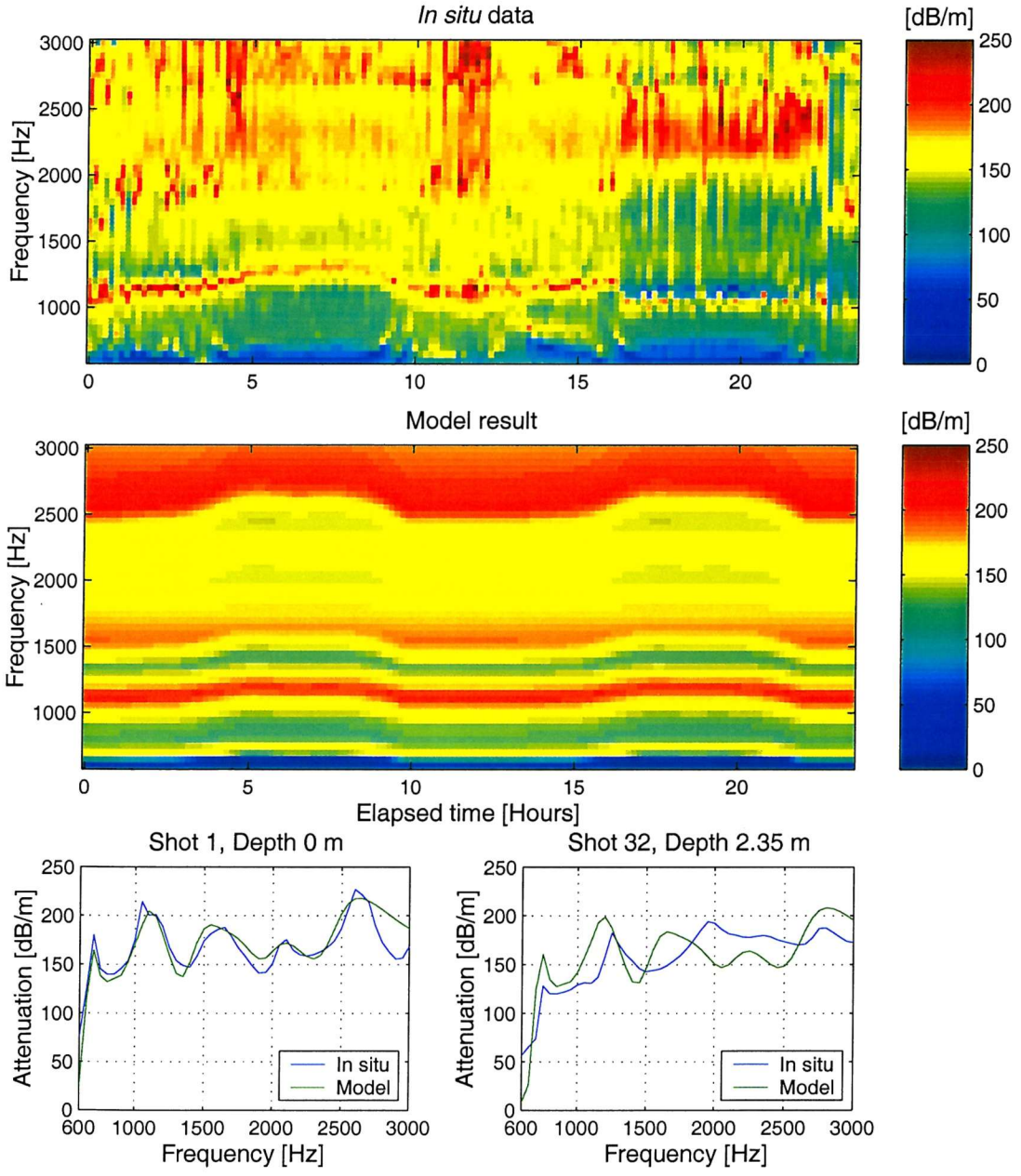

Figure 7.4. Attenuation profiles for both the in situ and model data.

The model correctly predicts a variation of frequency of maximum attenuation with hydrostatic pressure, and the magnitude of the attenuation coefficients are broadly in agreement with those measured *in situ*. However, it is clear that the model does not accurately reflect amplitude of the changes to the bubble radii. At high tide, the frequency of peak 1 is predicted adequately, while the magnitude is not. At peak 2, neither the frequency nor magnitude is predicted. Peaks 3 and 4 underestimate the change in frequency. The magnitude of the attenuation in these peaks increases at high tide, a response also not predicted by the model. Finally, the frequency of peak 5 is reasonably well predicted, while the magnitude is not. A summary is given in Table 7.5.

	Shot 1, Time 0 hrs, Depth 0 m		Shot 32, Time 5:10 hrs, Depth 2.35m	
	Frequency [Hz]	Attenuation [dB/m]	Frequency [Hz]	Attenuation [dB/m]
Peak 1	700	164	750	160
Peak 2	1100	205	1200	199
Peak 3	1550	190	1650	183
Peak 4	2100	172	2250	164
Peak 5	2650	218	2800	208

Table 7.5. Frequency and magnitude data for fitted model attenuation profiles of shots 1 and 32

7.4.3 Phase velocity

Phase velocity results, compared to the *in situ* twenty four hour data for receivers 2 and 3, are shown in Figure 7.5.

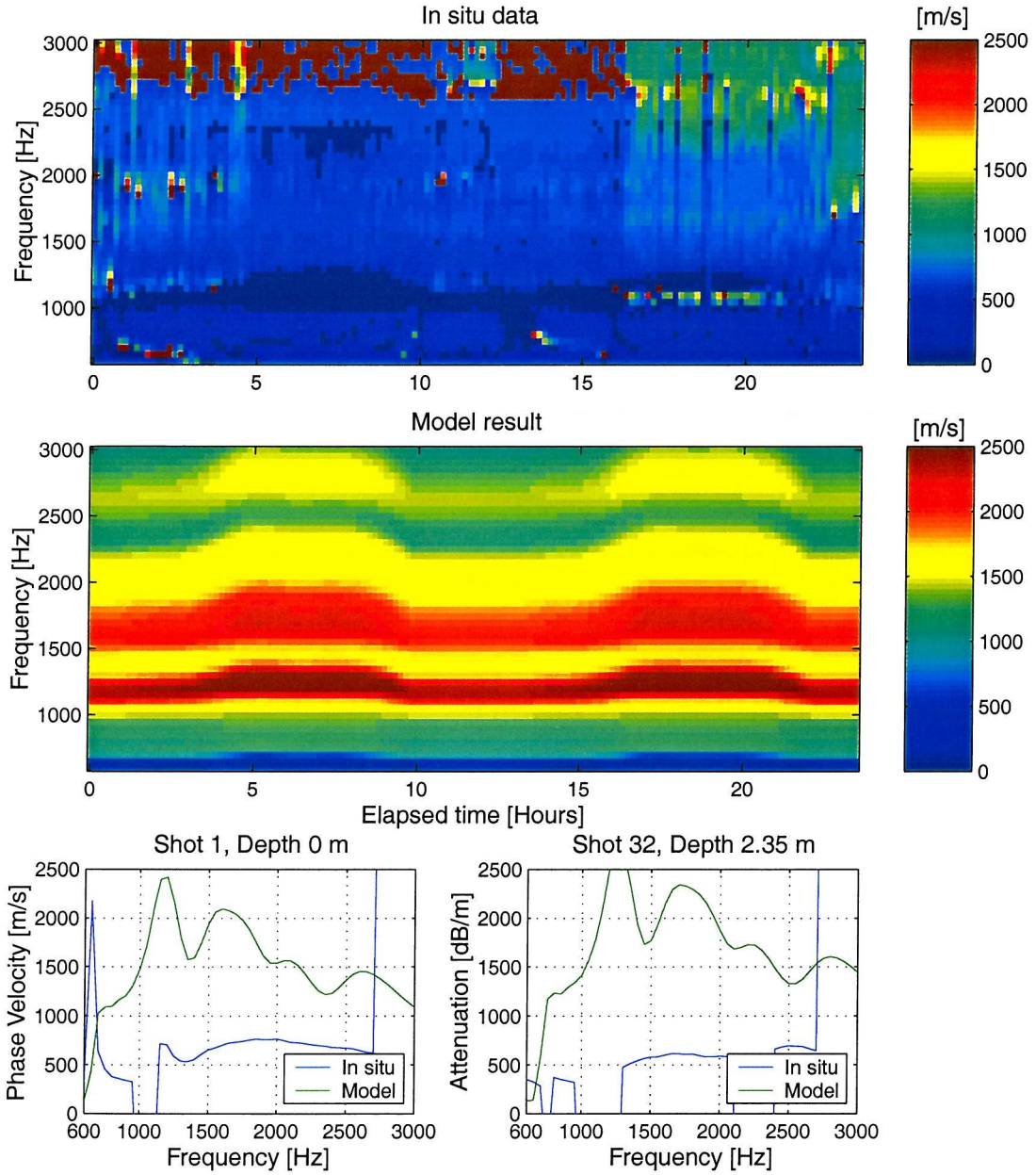

Figure 7.5. Phase velocity profiles for both the in situ and model data.

The model does not accurately predict the phase velocity of the sediment, but if it is assumed that the 'drop outs' of phase velocity (e.g. at 1000 Hz) are indications of extremely high attenuation, and therefore resonance, the model phase velocity is reacting in the manner expected of the model: initially there is a sharp increase in velocity followed by a decrease towards a more 'normal' value (i.e. the fully saturated

value). This is clearly demonstrated in the profile of shot 1 at 1000 Hz. However, rather than the model being inaccurate it is possible that the *in situ* data are incorrect due to the high attenuation of the transmitted signal between receivers 2 and 3. Poor signal to noise ratio will impair the cross-correlation required to calculate the phase velocity in the filter correlation technique (Section 5.6), with the consequence that a correlation may be made between signal and noise rather than signal and signal.

7.5 X-ray CT distribution

7.5.1 Bubble size distribution

The X-ray CT data provides an opportunity for accurate acoustic modelling of the sediment. However, deficiencies in the data prevent an actual bubble distribution for depths of the *in situ* data being generated. CT scans were conducted below the depth receiver 3 in the twenty-four hour experiment, and recorded slices are not at regular intervals. It is therefore necessary to assume that the scans are representative of the general character of the sediment column. As a whole, the scans cover a depth of 34.8 cm, close to the distance between receivers 2 and 3 in the twenty-four hour experiment. It was decided, therefore, to amalgamate the scans as if they represented a single, continuous column at the depth of interest. The distributions were corrected for the 'roll-off' in the number of bubbles present at low radii (below 2 mm) by using the robust least squares fit.

7.5.2 Attenuation coefficients

The calculated attenuation coefficients for the three distributions (2-D, SD and LD methods) are shown in Figure 7.6.

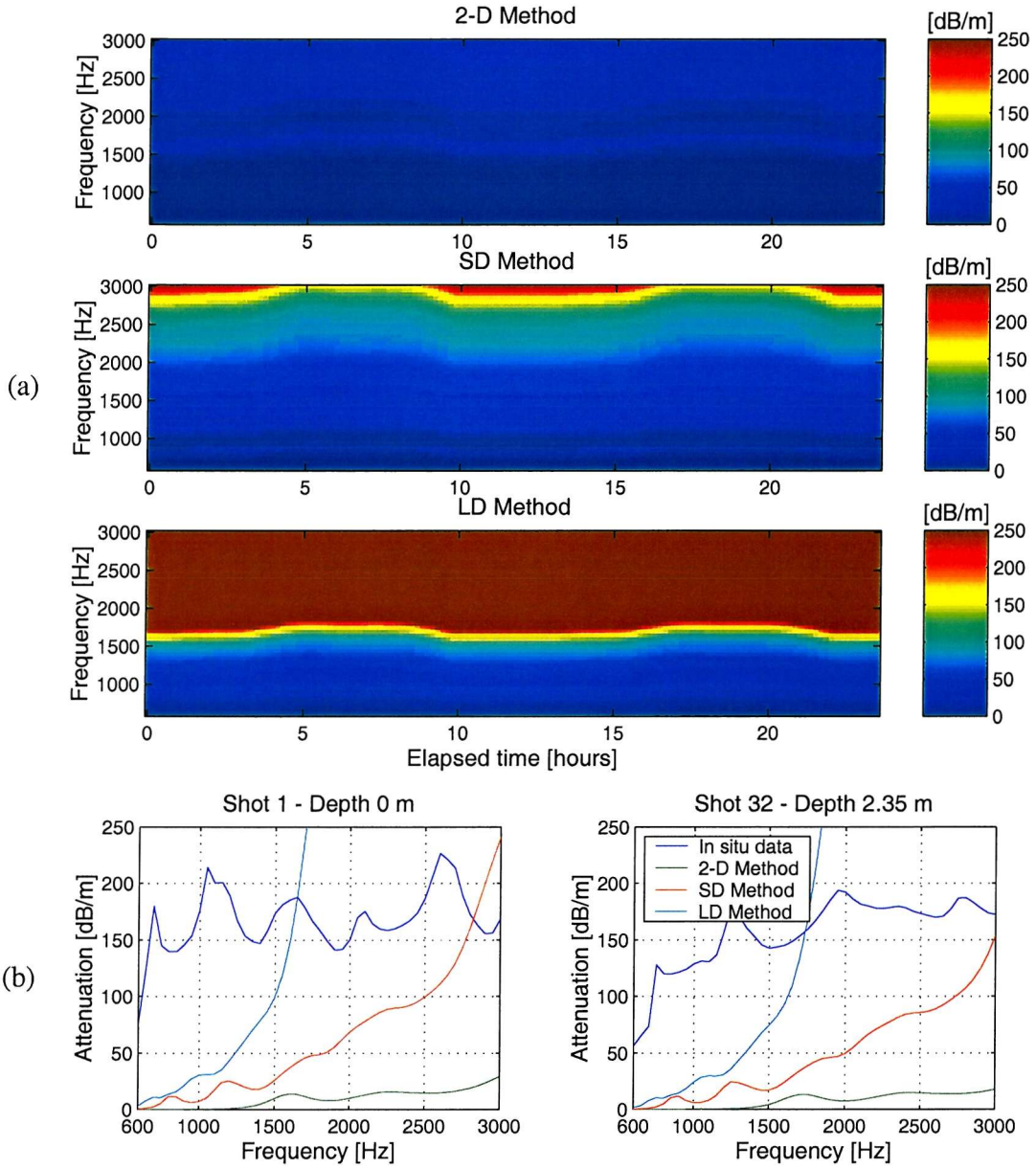

Figure 7.6. (a) Time- and frequency-dependent attenuation coefficients, calculated for the three bubbles size methods and (b) comparison of attenuation profiles of in situ (receivers 2 and 3) and model data at low and high tide.

The model derived attenuation coefficients are very different from those measured *in situ*. All three distributions underestimate the attenuation coefficients at low frequency. At approximately 1500 Hz, the LD distribution attenuation coefficients increase dramatically. This increase is also observed in the SD distribution attenuation

coefficients at approximately 2500 Hz. The 2-D distribution is consistently low. There is, however, still evidence for tidal-dependent variation of the attenuation (Figure 7.6a).

7.5.3 Phase velocity

The calculated phase velocity for the three distributions (2-D, SD and LD methods) are shown in Figure 7.7.

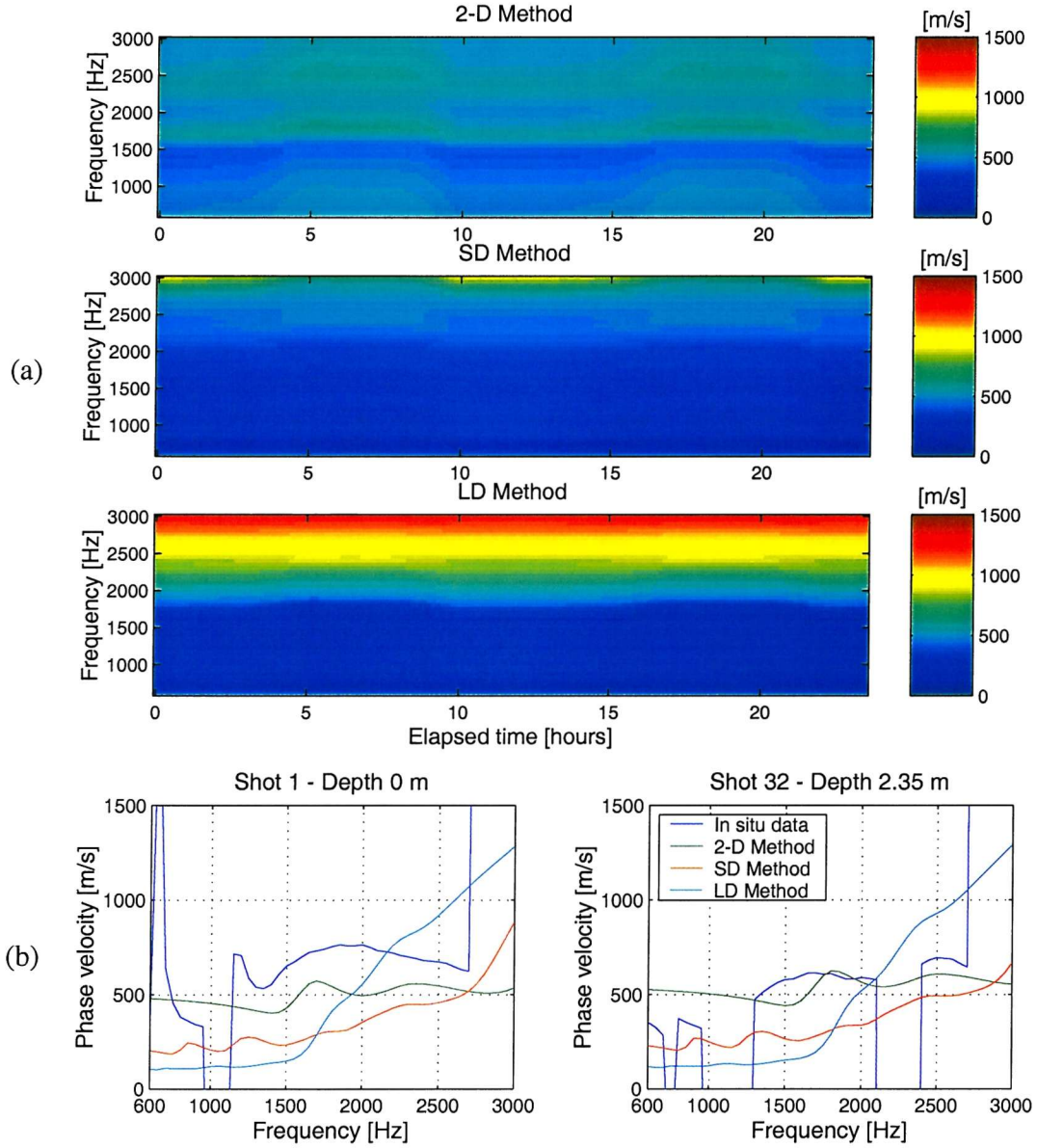

Figure 7.7. (a) Time- and frequency-dependent velocity, calculated for the three bubbles size methods and (b) comparison of phase velocity profiles of in situ (receivers 2 and 3) and model data at low and high tide.

At low tide, the model generally underestimates the phase velocity for each of the three distributions. The exceptions are the 2-D distribution below approximately

1100 Hz and the LD distribution above 2200 Hz. In both cases, the phase velocity is over estimated. At high tide and above 1750 Hz, the 2-D distribution appears to give a reasonable approximation of the *in situ* data. Again, it should be noted that the *in situ* data may be giving false results due to the high attenuation of the sediment / bubble system.

7.6 Discussion

The model adaptations cause the frequency of the peaks in attenuation to increase with increasing hydrostatic pressure, as observed *in situ*. In addition, the magnitude of the attenuation coefficients are broadly in agreement with the *in situ* data over the full range of tidal heights. It is clear that it is possible to fit a bubble size distribution to match *in situ* attenuation data. However, there are some differences between the model and the *in situ* data, most notably the change in frequency of the attenuation peaks. These changes are summarised in Table 7.6.

	In situ data		Fitted model data	
	Frequency [Hz]	Attenuation [dB/m]	Frequency [Hz]	Attenuation [dB/m]
Peak 1	50	-52	50	-4
Peak 2	200	-32	100	-6
Peak 3	300	6	100	-7
Peak 4	250	5	150	-8
Peak 5	200	-40	150	-10

Table 7.6. Changes in frequency and magnitude data for in situ and fitted model attenuation profiles of shots 1 and 32

There are a number of reasons for the discrepancies between the *in situ* data and the model output. The first is that the bubble radii, and associated gas porosities, are modelled to be affected by pressure only. As discussed in Section 7.2.2, there may also be a diffusive effect, dependent on the local rate of methanogenesis and the concentration of methane in the bubbles and surrounding pore water. However, a lack of detailed geochemical information precludes the calculation of the bubble adjustment due to this mechanism. The model also assumes that the bubbles are spherical. X-ray CT data show that this is not the case, and further evidence suggests that gas bubbles often form penny-shaped cavities with one of the long axes vertical or near-vertical (Abegg and Anderson, 1997). Furthermore, due to their irregular shape, a large bubble may also split into two or three smaller bubbles as it shrinks with increasing tide, and coalesce as it grows once more. For example, the increase in the magnitude of peaks 3

and 4 (Table 7.7) could be due to several large bubbles dividing and increasing the gas porosity at the radii of the newly formed bubbles and increasing the attenuation. Increases in bubbles size can occur from the effects of rectified diffusion, but investigations indicate that these effects are negligible when generated by tides (Boudreau *et al.*, 2001).

Clearly, attenuation coefficients generated using the X-ray CT generated distributions do not fit the *in situ* attenuation data. This could be due to the methods used to estimate the vertical extent of the bubbles as well as the assumption that the distribution is representative of the sediment through which the *in situ* experiment was conducted. However, by scaling the X-ray CT generated distributions so that the numbers of bubbles present are related to a 1 m^3 volume of sediment (as done for the fitted distribution in Figure 7.3b), it is possible to compare all four bubble size distributions and see that they are not dissimilar in their overall character (Figure 7.8).

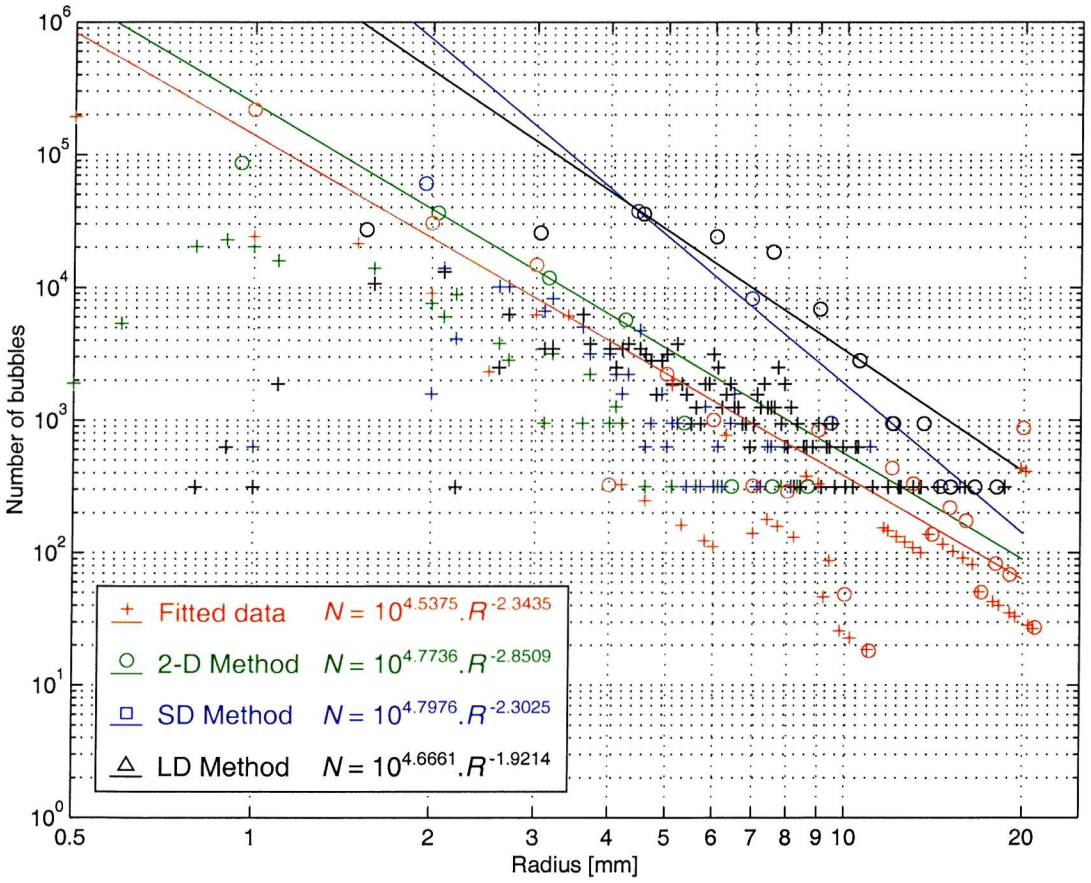

Figure 7.8. Final bubble size distributions based on a 1 m^3 volume of sediment. Note that numbers of bubbles smaller than 2 mm for the CT distributions have been matched to the best-fit line to compensate for under-sampling due to measurement resolution. The regression lines relate numbers of bubbles to the radius in mm.

It should be noted that there is only a limited range of scale used in the bubble size distribution, determined by the internal diameter of the core (approximately 100 mm) and the resolution of the measurement techniques, will result in some uncertainty over the validity of the relationship, although it should be noted that similar relationships have been observed in other studies (Anderson *et al.*, 1998). The major difference between the fitted distribution and the CT distributions is the fine detail. Due to the small amount of gassy sediment contained in the core, it is impossible to sample the full range of bubbles that may be present in the sediment, especially when they occur in small numbers (e.g., those with radii between 10 mm and 20 mm). As can be seen in Figure 7.8, the least number of bubbles present at any radius in the CT derived distributions is 312. This is an artefact of factoring up the distribution, but it shows that relying on such a small sample to generate a bubble size distribution can give undue influence to bubbles that occur only rarely, resulting in an over-estimation of the gas porosity of these bubbles. In addition, there is no information about bubbles smaller than 0.5 mm, and it is known that small bubbles can affect the attenuation characteristics of a bubble system at frequencies below their resonance (Figure 7.2).

The gradients of each of the distributions are similar (see Table 7.4), with the exception of the SD method, as are the magnitudes, indicating that the fitted distribution is, indeed, similar to that found *in situ*. This indicates that a power law may govern the distribution of bubbles in sediments. Further investigation of the actual *in situ* conditions (i.e., those through which the *in situ* acoustic data were collected) would be required to confirm this hypothesis. Extensions of this work to cover other types of sediment, such as sand and clay (Dibden Bay is generally clayey silt), may indicate that different distributions exist for different sediment types, possibly providing a route by which bubble distributions may be predicted.

7.7 Summary

The model adaptations cause the frequency of the peaks in attenuation to increase with increasing hydrostatic pressure, as observed *in situ*. In addition, the magnitude of the attenuation coefficients are broadly in agreement with the *in situ* data over the full range of tidal heights. However, the adaptations underestimate the magnitude of the changes experienced by the bubbles over the experimental period, and it is probable that diffusion is occurring, at least on the smaller bubbles. Other

differences can be attributed to the non-spherical nature of most of the bubbles, and the unknown manner in which the shrinkage occurs in a non-spherical bubble.

Attenuation coefficients calculated using X-ray CT derived bubble size distributions do not match the *in situ* data. Phase velocity computations match the *in situ* data more closely, but, in this case, uncertainty surrounds the *in situ* data due to the highly attenuating nature of the sediment. The X-ray CT data are deficient in that little is known about bubbles smaller than approximately 0.5 mm and very little quantitative information is known about the vertical axis of the bubbles. Finally, it was assumed that the bubble distributions measured from the CT data were representative of the distributions shallower in the sediment column, where different environmental conditions exist.

All four distributions (fitted and CT-derived) show similar relationships between numbers of bubbles present and radius (Figure 7.8), and it is possible that these relationships depend on sediment type. If this is true, it may provide a method by which bubble size distributions may be predicted.

Chapter 8. Conclusions and future work

8.1 Conclusions

The initial aims of this project were to: (a) to characterise the acoustic response of gassy sediments found at Dibden Bay at both high (300 – 700 kHz) and low (600 – 3000 Hz) frequencies; (b) to measure the physical characteristics of the sediment and the bubble size distribution; (c) to examine the veracity of an acoustic model of gassy sediments by comparison with *in situ* acoustic data; and (d) to provide a framework for future work aimed at predicting bubble size distributions from acoustic measurements. It has been proven that:

- Free, Type III gas bubbles are present in the sediments at Dibden Bay (Section 6.4.5)
- there is a noticeable effect on the radius of the bubbles over a tidal cycle resulting in a change in the acoustic character of the gassy sediment (Section 5.9.2)
- the changes in the bubbles are not due only to pressure equilibrium, but probably also to diffusive exchanges (Section 7.2.2)
- acoustic modelling of the gassy sediment provides a realistic bubble size distribution (Section 7.4)
- the bubble size distribution may conform to a power law (Section 6.4.5)

8.1.1 Aim A

In situ acoustic experiments were carried out at Dibden Bay using a chirp (2 - 8 kHz) sub-bottom profiler and a mini-boomer system. The sub-bottom profiling revealed acoustic turbidity throughout the region, estimated to occur between 0.75 and 1.5 m below the seafloor. A refraction / transmission experiment conducted using the mini-boomer with a horizontal array of four hydrophones show an offset dependent group velocity. At short offsets, the velocity is approximately 900 m/s, a similar value to that measured in soft, gassy clays found in the Gulf of Mexico (Edrington and Calloway, 1984). At longer offsets, the velocity increases and it is thought this is due to a waveguide effect produced by a non-gassy, surficial shell layer, resulting in the transmission of a headwave. The area surveyed is one of constant phase velocity, with frequency dependent Q and frequency independent attenuation. Values of attenuation

are at least an order of magnitude higher than other, fully saturated sediments of a similar composition (Kibblewhite, 1989).

A transmission / monitoring experiment was carried out using the mini-boomer system with a vertical array of four hydrophones in an attempt to localise the gas horizon and to measure the change in acoustic character with variable hydrostatic pressure. Hydrophones were placed strategically to ensure that there was at least one above and one below the gas horizon, and shots were fired at ten-minute intervals over approximately two tidal cycles. High attenuation was seen to occur between hydrophones placed at 80 cm and 120 cm, in agreement with data provided by the sub-bottom profiling. Measured attenuation coefficients are extremely high, above 200 dB/m in places, and this is thought to be the result of gas bubble scattering and resonance. In addition, the results clearly show that there is a variation in attenuation with hydrostatic pressure. The frequency at which various peaks in attenuation occur increases with increasing hydrostatic pressure. In addition, the magnitude of these peaks changes. This is believed to be the result of pore pressure variations causing bubbles to shrink and expand, and it is known that, in the same environmental conditions, a smaller bubble has a higher resonant frequency. This variation in acoustic character is a previously unobserved phenomenon. Gas expulsion has been observed (e.g. Jackson *et al.*, 1998) to occur in response to pressure changes on the seafloor, but this study, for the first time, provides concrete evidence for bubble size changes due to tidal variation.

The high frequency acoustic character generally conforms to the assumption that attenuation is proportional to the first power of frequency (Hamilton, 1972; Section 3.2.2) in the absence of Rayleigh scattering, when it is expected to be close to four (Busby and Richardson, 1957). At two depth regions, values of the exponent of frequency are above 2 but less than 3.5. The first, at approximately 100 cm depth, is in the region where the *in situ* acoustic experiments indicate that the gas horizon exists. The second, at approximately 130 cm depth, is where significant numbers of bubbles were observed in the X-ray CT scans (scan 13). It is thought that this may be due to the presence of the gas bubbles, but subsequent calculations indicate that the insonifying frequency is far above the resonant frequency of the bubbles.

8.1.2 Aim B

A number of laboratory tests were conducted on core material retrieved from the site. Two 150 mm square Kastenlot cores were collected, one 2 m long and one 3 m long, and two 3 m pressurised cores were collected, using specially designed end caps inserted on the seafloor by divers to maintain the *in situ* pressure. The tests were conducted to: characterise the sedimentary units and their physical properties for input to the gassy sediment model; verify the existence of bubbles at depth and to quantify the bubble size distribution with depth for input to the model; and measure the high frequency (300 – 700 kHz) acoustic response of the gassy sediment. The tests indicate that the sediment at Dibden Bay is typical of a clayey-silt with a porosity of 63 %. High frequency compressional wave velocity is very similar to that measured by Shumway (1960) in a similar porosity sediment, and the bulk modulus is in agreement with data presented by Hamilton (1971a). X-ray computed tomography was used to measure the bubble size distribution and it was observed that the bubbles take many forms, from long cavities filled with gas (e.g. Scan 8), to a great number of small, nearly spherical bubbles (e.g. Scan 13).

However, comparisons between the X-ray CT distributions and the fitted distribution indicate that they may follow a similar power law. It is hypothesised that particular sediment types may exert control on this power law and that bubble size distributions may be predicted using a similar approach to that described for the fitted bubble distribution.

8.1.3 Aim C

The Anderson and Hampton (1980a, b) model was adapted to account for the effect of varying hydrostatic pressure on the radii of the gas bubbles. This adjustment was based on the theory that, in equilibrium, the pressure inside the bubble must equal the pressure outside the bubble. An increase in pore pressure, due to an increase in water depth, must be accompanied by an increase in the internal pressure of the bubble. This can only be achieved by bubble shrinkage. In addition, it was shown that there must be some diffusive change related to the increase in concentration of gas in the bubble, but a lack of the chemical data required to calculate this change precluded this effect being included. Initially, a bubble size distribution was generated to fit the resultant attenuation coefficient profile at low tide to that measured in the twenty-four hour experiment. The model was then run for the whole period of the experiment, with

adjustments to the bubble radii, and their associated gas porosities, being based on the known tidal heights. The output showed that the model underestimated the changes to both the magnitude of the attenuation peaks and their frequencies. This was attributed to the diffusive component and the fact that the model assumes that the bubbles are spherical. The X-ray CT data show that the bubbles are often far from spherical, and other evidence (e.g. Abegg and Anderson, 1997) state that bubbles tend to form penny shaped cavities with one long axis in a vertical, or near-vertical, orientation. Also, if an irregularly shaped bubble were to shrink it is feasible that, due to its irregularities, it may split into two, or maybe three, separate bubbles thus affecting the gas porosity of the resultant bubble radii.

Bubble size distributions generated from the X-ray CT data do not fit the *in situ* attenuation data when applied to the model. This is due to a number of reasons. The X-ray CT scans were not recorded at the depth where the gas horizon occurred (between receivers 2 and 3), so it was assumed that the data obtained were representative of the sediment column. The scans were not continuous and the reproduced slices were not at consecutive positions, or at regular intervals, within the scans, with the result that estimations had to be made for the vertical extent of the bubbles. Finally the resolution of the X-ray CT data and the measurement technique meant that bubbles below 1 mm radius were under-sampled.

8.1.4 Aim D

It has been shown in the course of this thesis that it may be possible to predict the bubble size distribution of a gassy sediment using a similarly conducted series of tests: a twenty-four hour monitoring experiment to measure the attenuation changes due to bubble size variation over a tidal period and measurement of suitable parameters for entry into the Anderson and Hampton model, amended to account for bubble shrinkage due to pressure and diffusion (assuming sufficient chemical data can be obtained).

8.2 Future work

This project has provided evidence that gas bubbles are subject to changes over a tidal cycle. In order to increase the accuracy of the modelling approach to predict these changes, it is recommended that a chemical study be undertaken to measure the

local rate of methanogenesis and the concentration of methane in the pore water so that accurate adjustments to the bubble radius may be calculated.

In addition, detailed study of a large number of X-ray CT scans should be undertaken to accurately measure the bubble size distribution at the site of acoustic measurements and avoid the sampling effects described in Section 7.6. In this way, a more accurate comparison between the fitted and real distributions may be made. Similar studies should then be made of other types of sediment containing gas to determine whether this power law is dependent on sediment type.

Finally, it is not clear what the actual mechanisms of bubble resonance are. Conceptually, a bubble resonating in water is simple to understand, but what happens to a bubble inside a rigid frame? How does it resonate? What are the implications of a resonant bubble on local fluid flow? These questions, and others like them, must be answered before the acoustic character of gassy sediments can be further understood, and gassy sediment modelling can become more accurate.

References

Abegg, F., and A.L. Anderson, The acoustic turbid layer in muddy sediments of Eckernförde Bay, Western Baltic: methane concentration, saturation and bubble characteristics, *Marine Geology*, *137* (1/2), 137-147, 1997.

Aki, K., and P.G. Richards, *Quantitative Seismology*, W. H. Freeman and Co., New York, 1980.

Anderson, A.L., and L.D. Hampton, Acoustics of gas bearing sediments I. Background, *Journal of the Acoustical Society of America*, *67* (6), 1865-1889, 1980a.

Anderson, A.L., and L.D. Hampton, Acoustics of gas bearing sediments II. Measurements and models, *Journal of the Acoustical Society of America*, *67* (6), 1890-1903, 1980b.

Anderson, A.L., and W.R. Bryant, Acoustic properties of shallow seafloor gas, in *21st Annual Offshore Technology Conference*, pp. 669-676, Houston, Texas, 1989.

Anderson, A.L., and W.R. Bryant, Gassy sediment occurrence and properties: Northern Gulf of Mexico, *Geo-Marine Letters*, *10* (4), 209-220, 1990.

Anderson, A.L., F. Abegg, J.A. Hawkins, M.E. Duncan, and A.P. Lyons, Bubble populations and acoustic interaction with the gassy floor of Eckernförde Bay, *Continental Shelf Research*, *18* (14-15), 1807-1838, 1998.

Andreeva, I.B., Scattering of sound by air bladders of fish in deep sound-scattering ocean layers, *Soviet Physics - Acoustics*, *10*, 17-20, 1964.

Barnes, R.O., and E.D. Goldberg, Methane production and consumption in anoxic marine sediments, *Geology*, 297-300, 1976.

Bernard, B.B., Methane in marine sediments, *Deep-Sea Research*, *26A*, 427-443, 1979.

Best, A.I., and C. McCann, Seismic attenuation and pore-fluid viscosity in clay-rich reservoir sandstones, *Geophysics*, *60* (5), 1386-1397, 1995.

Best, A.I., and D.E. Gunn, Calibration of marine sediment core loggers for quantitative

acoustic impedance studies, *Marine Geology*, *160* (137-146), 137-146, 1999.

Best, A.I., Q.J. Huggett, and A.J.K. Harris, Comparison of *in situ* and laboratory acoustic measurements on Lough Hyne marine sediments, *Journal of the Acoustical Society of America*, *110* (2), 695-709, 2001.

Biot, M.A., Theory of propagation of elastic waves in a fluid-saturated porous solid. I. Low-frequency range, *Journal of the Acoustical Society of America*, *28* (2), 168-178, 1956a.

Biot, M.A., Theory of propagation of elastic waves in a fluid-saturated porous solid. II. Higher-frequency range, *Journal of the Acoustical Society of America*, *28* (2), 179-191, 1956b.

Boudreau, B.P., B.S. Gardiner, and B.D. Johnson, Rate of growth of isolated bubbles in sediments with a diagenetic source of methane, *Limnology and Oceanography*, *46* (3), 616-622, 2001.

Bowles, F.A., Observations on attenuation and shear-wave velocity in fine-grained, marine sediments, *Journal of the Acoustical Society of America*, *101* (6), 3385-3397, 1997.

Brennan, B.J., Pulse propagation in media with frequency-dependent *Q*, *Geophysical Research Letters*, *7* (3), 211-213, 1980.

Busby, J., and E.G. Richardson, The absorption of sound in sediments, *Geophysics*, *22* (4), 821-828, 1957.

Carlson, P.R., M. Golan-Bac, H.A. Karl, and K.A. Kvenvolden, Seismic and geochemical evidence for shallow gas in sediment on Navarin Continental Margin, Bering Sea, *American Association of Petroleum Geologists Bulletin*, *69* (3), 422-436, 1985.

Claypool, G.E., and I.R. Kaplan, The origin and distribution of methane in marine sediments, in *Natural Gases in Marine Sediments*, edited by I.R. Kaplan, pp. 99-139, Plenum, New York, 1974.

Clayton, C., Source volumetrics of biogenic gas generation, in *Bacterial Gas*, edited by

R. Vially, pp. 191-204, Éditions Technip, Paris, 1992.

Cline, J.D., and M.L. Holmes, Submarine seepage of natural gas in Norton Sound, Alaska, *Science*, *198*, 1149-1153, 1977.

Courtney, R.C., and L.A. Mayer, Calculation of acoustic parameters by a filter-correlation method, *Journal of the Acoustical Society of America*, *93* (2), 1145-1154, 1993.

Craig, R.F., *Soil Mechanics*, 427 pp., Chapman and Hall, London, 1992.

Davis, A.M., J.D. Bennell, and D. Taylor Smith, Dynamic-static implications from seismic observations of sediment geotechnical properties, in *Society of Exploration Geophysicists, 51st annual meeting*, SEG, Tulsa, Oklahoma, 1981.

Deuser, W.G., E.T. Degens, and G.R. Harvey, Methane in Lake Kivu: New data bearing on its origin, *Science*, *181*, 51-53, 1973.

Devin, C., Survey of thermal, radiation, and viscous damping of pulsating air bubbles in water, *Journal of the Acoustical Society of America*, *31* (12), 1654-1667, 1959.

Domenico, S.N., Elastic properties of unconsolidated porous sand reservoirs, *Geophysics*, *42* (7), 1339-1368, 1977.

Doose, P.R., M.W. Sandstrom, R.Z. Jodele, and I.R. Kaplan, Interstitial gas analysis of sediment samples from site 368 and hole 369A, *Initial Report, Deep Sea Drilling Project*, *41*, 861-863, 1978.

Dyer, K.R., Sedimentation and sediment transport, in *The Solent Estuarine System: An assessment of present knowledge*, edited by J.D. Burton, pp. 20-24, NERC Publications Series C, 1980.

Edrington, T.S., and T.M. Calloway, Sound speed and attenuation measurements in gassy sediments in the Gulf of Mexico, *Geophysics*, *49* (3), 297-299, 1984.

Eller, A.I., Damping constants of pulsating bubbles, *Journal of the Acoustical Society of America*, *47* (5), 1469-1471, 1970.

Emery, K.O., and D. Hoggan, Gases in marine sediments, *Bulletin of the American*

Association of Petroleum Geologists, *42* (9), 2174-2188, 1958.

Engleman, E.E., L.L. Jackson, and D.R. Norton, Determination of carbonate carbon in geological materials by coulometric titration, *Chemical Geology*, *53*, 125-128, 1985.

Farmer, D.M., and S. Vagle, Waveguide propagation of ambient sound in the ocean-surface bubble layer, *Journal of the Acoustical Society of America*, *86* (5), 1897-1908, 1989.

Flood, R.D., Distribution, morphology and origin of sedimentary furrows in cohesive sediments, Southampton Water, *Sedimentology*, *28* (4), 511-529, 1981.

Floodgate, G.D., and A.G. Judd, The origins of shallow gas, *Continental Shelf Research*, *12* (10), 1145-1156, 1992.

Fox, F.E., S.R. Curley, and G.S. Larson, Phase velocity and absorption in water containing air bubbles, *Journal of the Acoustical Society of America*, *27* (3), 534-539, 1955.

Futterman, W.I., Dispersive body waves, *Journal of Geophysical Research*, *67*, 5279-5291, 1962.

Gardner, T.N., and M.J. Goringe, The measurement of gas bubble size distributions in a three-phase laboratory gassy soil, *Geotechnical Testing Journal*, *11* (1), 49-55, 1988.

Gardner, T.N., An acoustic study of soils that model seabed sediments containing gas bubbles, *Journal of the Acoustical Society of America*, *107* (1), 163-176, 2000.

Gassmann, F., Elastic waves through a packing of spheres, *Geophysics*, *16*, 673-685, 1951.

Geertsma, J., and D.C. Smit, Some aspects of elastic wave propagation in fluid-saturated porous solids, *Geophysics*, *26* (2), 169-181, 1961.

Gunn, D.E., and A.I. Best, A new automated nondestructive system for high resolution multi-sensor core logging of open sediment cores, *Geo-Marine Letters*, *18* (1), 70-77, 1998.

Hamilton, E.L., Sound velocity and related properties of marine sediments, North

Pacific, *Journal of Geophysical Research, 75* (23), 4423-4446, 1970.

Hamilton, E.L., Elastic properties of marine sediments, *Journal of Geophysical Research, 76* (2), 579-604, 1971a.

Hamilton, E.L., Prediction of in-situ acoustic and elastic properties of marine sediments, *Geophysics, 36* (2), 266-284, 1971b.

Hamilton, E.L., Compressional-wave attenuation in marine sediments, *Geophysics, 37* (4), 620-646, 1972.

Hamilton, E.L., Sound velocity gradients in marine sediments, *Journal of the Acoustical Society of America, 65* (4), 909-922, 1979.

Hamilton, E.L., Acoustic properties of sediments, in *Acoustics and Ocean Bottom*, edited by A. Lara-Sáenz, C. Ranz-Guerra, and C. Carbó-Fité, pp. 3-58, Consejo Superior de Investigaciones Científicas (CSIC), Madrid, 1987.

Head, K.H., *Manual of Soil Laboratory Testing. Volume 3: Effective Stress Tests*, Pentech, London, 1986.

Head, K.H., *Manual of Soil Laboratory Testing. Volume 2: Permeability, Shear Strength and Compressibility Tests*, John Wiley & Sons, Inc., New York, 1994.

Hempel, P., V. Spieß, and R. Schreiber, Expulsion of shallow gas in the Skagerrak - Evidence from sub-bottom profiling, seismic, hydroacoustical and geochemical data, *Estuarine, Coastal and Shelf Science, 38* (6), 583-601, 1994.

Hill, R., A self-consistent mechanics of composite materials, *Journal of the Mechanics and Physics of Solids, 13*, 213-222, 1965.

Hill, J.M., J.P. Halka, R. Conkwright, K. Koczot, and S. Coleman, Distribution and effects of shallow gas on bulk estuarine sediment properties, *Continental Shelf Research, 12* (10), 1219-1229, 1992.

Hovem, J.M., and G.D. Ingram, Viscous attenuation of sound in saturated sand, *Journal of the Acoustical Society of America, 66* (6), 1807-1812, 1979.

Hovland, M., and J.H. Sommerville, Characteristics of two natural gas seepages in the

North Sea, *Marine and Petroleum Geology*, *2* (4), 319-326, 1985.

Hovland, M., and A.G. Judd, *Seabed pockmarks and seepages: impact on geology, biology and the marine environment*, 293 pp., Graham and Trotman, London, 1988.

Hovland, M., Large pockmarks, gas-charged sediments and possible clay diapirs in the Skagerrak, *Marine and Petroleum Geology*, *8* (3), 311-316, 1991.

Hunt, J.M., *Petroleum geochemistry and geology*, 617 pp., W.H. Freeman and Co., San Francisco, 1979.

Jackson, D.R., K.L. Williams, T.F. Wever, C.T. Friedrichs and L.D. Wright, Sonar evidence for methane ebullition in Eckernförde Bay, *Continental Shelf Research, 12* (10), 1893-1915, 1998.

Jones, J.L., C.B. Leslie, and L.E. Barton, Acoustic characteristics of underwater bottoms, *Journal of the Acoustical Society of America*, *36* (1), 154-157, 1964.

Jones, G.B., G.D. Floodgate, and J.D. Bennell, Chemical and microbiological aspects of acoustically turbid sediments: preliminary investigations, *Marine Geotechnology*, *6* (3), 315-322, 1986.

Judd, A.G., and M. Hovland, The evidence of shallow gas in marine sediments, *Continental Shelf Research*, *12* (10), 1081-1095, 1992.

Kaye, G.W.C., and T.H. Laby, *Tables of Physical and Chemical Constants*, Longman, 1995.

Kibblewhite, A.C., Attenuation of sound in marine sediments: A review with emphasis on new low-frequency data, *Journal of the Acoustical Society of America*, *86* (2), 716-738, 1989.

Kjatansson, E., Constant Q-wave propagation and attenuation, *Journal of Geophysical Research*, *84*, 4737-4748, 1979.

Kolsky, H., The propagation of stress pulses in viscoelastic solids, *Philosophical Magazine*, *8*, 693-710, 1956.

Kvenvolden, K.A., C.H. Nelson, D.R. Thor, M.C. Larson, G.D. Redden, J.B. Rapp, and

D.J. Des Marais, Biogenic and thermogenic gas in gas-charged sediment of Norton Sound, Alaska, in *11th Annual Offshore Technology Conference*, pp. 479-483, Houston, Texas, 1979.

Laier, T., N.O. Jørgensen, B. Buchardt, T. Cederberg, and A. Kuijpers, Accumulation and seepages of biogenic gas in Northern Denmark, *Continental Shelf Research, 12* (10), 1173-1186, 1992.

Laird, D.T., and P.M. Kendig, Attenuation of sound in water containing air bubbles, *Journal of the Acoustical Society of America, 24* (1), 29-32, 1952.

Lenham, J.W., High resolution seismology, archaeology and submerged landscapes - an interdisciplinary study, PhD thesis, School of Ocean and Earth Sciences, University of Southampton, 2000.

Malagnini, L., Velocity and attenuation structure of very shallow soils: Evidence for a frequency-dependant *Q*, *Bulletin of the Seismological Society of America, 86* (5), 1471-1486, 1996.

Martens, C.S., and R.A. Berner, Methane production in the interstitial waters of sulphate-depleted marine sediments, *Science, 185*, 1167-1169, 1974.

Martens, C.S., and R.A. Berner, Interstitial water chemistry of anoxic Long Island Sound sediments. 1. Dissolved gases, *Limnology and Oceanography, 22*, 10-25, 1977.

Martens, C.S., Methane production, consumption, and transport in the interstitial waters of coastal marine sediments, in *The Dynamic Environment of the Ocean Floor*, edited by K.A. Fanning, and F.T. Manheim, pp. 187-202, Lexington Books, Lexington, 1982.

Max, M.D., R. Schreiber, and N.Z. Cherkis, Geological control of shallow gas and pockmarks in the Norwegian Channel; High resolution shallow sub-bottom profiling of small scale features, *Marine Geophysical Researches, 14*, 77-85, 1992.

McCann, C., and D.M. McCann, A theory of compressional wave attenuation in non-cohesive sediments, *Geophysics, 50* (8), 1311-1317, 1985.

McQuillin, R., and N. Fannin, Explaining the North Sea's lunar floor, *New Scientist, 83*

(1163), 90-92, 1979.

Meyer, E., K. Brendel, and K. Tamm, Pulsation oscillations of cavities in rubber, *Journal of the Acoustical Society of America, 30* (12), 1116-1124, 1958.

Mienert, J., and J. Posewang, Evidence of shallow- and deep-water gas hydrate destabilizations in North Atlantic polar continental margin sediments, *Geo-Marine Letters, 19,* 143-149, 1999.

Minnaert, M., On musical air bubbles and the sounds of running water, *Philosophical Magazine, 16,* 235-248, 1933.

Muir, T.G., Experimental capabilities of the ARL sediment tank facility in the study of buried object detection, Applied Research Laboratories Technical Memorandum No. 72-32 (ARL_TM_72_32), The University of Texas, Austin, 1972.

Nageswaran, S., Effect of gas bubbles on the sea bed behaviour, D.Phil. thesis, University of Oxford, 1983.

Orsi, T.H., C.M. Edwards, and A.L. Anderson, X-ray computed tomography: A non-destructive method for quantitative analysis of sediment cores, *Journal of Sedimentary Research, A64,* 690-693, 1994.

Premchitt, J., N.S. Rad, P. To, R. Shaw, and J.W.C. James, A study of gas in marine sediments in Hong Kong, *Continental Shelf Research, 12* (10), 1251-1264, 1992.

Quinn, R., Marine high-resolution reflection seismology: acquisition, processing and applications, PhD thesis, Department of Geology, University of Southampton, 1997.

Quinn, R., J.M. Bull, and J.K. Dix, Optimal processing of marine high resolution seismic reflection (chirp) data, *Marine Geophysical Researches, 20,* 13-20, 1998.

Rashid, M.A., and G. Vilks, Environmental controls of methane production in Holocene basins in eastern Canada, *Organic Geochemistry, 1,* 53-59, 1977.

Rau, G., and R.C. Chaney, Triaxial testing of marine sediments with high gas contents, in *Advanced Triaxial Testing of Soil and Rock, ASTM STP 977,* edited by R.T. Donaghe, R.C. Chaney, and M.L. Silver, pp. 338-352, American Society for Testing

and Materials, Philadelphia, 1988.

Rice, D.D., and G.E. Claypool, Generation, accumulation, and resource potential of biogenic gas, *American Association of Petroleum Geologists Bulletin, 65*, 5-25, 1981.

Rice, D.D., Controls, habitat, and resource potential of ancient bacterial gas, in *Bacterial Gas*, edited by R. Vially, pp. 91-118, Éditions Technip, Paris, 1992.

Robb, G.B.O., A multitechnical analysis of the shallow gas blanket in Southampton Water, MSc thesis, School of Ocean and Earth Sciences, University of Southampton, 2000.

Schubel, J.R., Gas bubbles and the acoustically impenetrable, or turbid, character of some estuarine sediments, in *Natural Gases in Marine Sediments*, edited by I.R. Kaplan, pp. 275-298, Plenum, New York, 1974.

Shepard, F.P., Nomenclature based on silt-sand-clay ratios, *Journal of Sedimetary Petrology*, 24, 151-158, 1954.

Shirley, D.J., and L.D. Hampton, Shear-wave measurements in laboratory sediments, *Journal of the Acoustical Society of America, 63* (2), 607-613, 1978.

Shumway, G., Sound velocity versus temperature in water-saturated sediments, *Geophysics, 23* (3), 494-505, 1958.

Shumway, G., Sound speed and absorption studies of marine sediments by a resonance method: Part I, *Geophysics, 25* (2), 451-467, 1960.

Siddiquie, H.N., D. Gopala Rao, K.H. Vora, and R.S. Topgi, Acoustic masking in sediments due to gases on the western continental shelf of India, *Marine Geology, 39*, M27-M37, 1981.

Silberman, E., Sound velocity and attenuation in bubbly mixtures measured in standing wave tubes, *Journal of the Acoustical Society of America, 29* (6), 925-933, 1957.

Sills, G.C., S.J. Wheeler, S.D. Thomas, and T.N. Gardner, Behaviour of offshore soils containing gas bubbles, *Géotechnique, 41* (2), 227-241, 1991.

Sills, G.C., and S.J. Wheeler, The significance of gas for offshore operations,

Continental Shelf Research, 12 (10), 1239-1250, 1992.

Smith, G.C., and G.D. Floodgate, A chemical method for estimating methanogenic biomass, *Continental Shelf Research, 12* (10), 1187-1196, 1992.

Spitzer, L., NDRC Report No. 6, 1-sr20-918, 1943.

Stahl, W., Carbon isotope fractionations in natural gases, *Nature, 241*, 134-135, 1974.

Stein, R., Rapid grain-size analysis of clay and silt fraction by SediGraph 5000D: comparison with Coulter counter and Atterberg methods, *Journal of Sedimentary Petrology, 55* (4), 590-593, 1985.

Stoll, R.D., and G.M. Bryan, Wave attenuation in saturated sediments, *Journal of the Acoustical Society of America, 5* (2), 1440-1447, 1970.

Stoll, R.D., Acoustic waves in saturated sediments, in *Physics of Sound in Marine Sediments*, edited by L. Hampton, pp. 19-39, Plenum, New York, 1974.

Stoll, R.D., Theoretical Aspects of sound transmission in sediments, *Journal of the Acoustical Society of America, 68* (5), 1341-1350, 1980.

Stoll, R.D., Marine sediment acoustics, *Journal of the Acoustical Society of America, 77* (5), 1789-1799, 1985.

Stoll, R.D., Acoustic waves in marine sediments, in *Ocean Seismo-acoustics*, edited by T. Akal, and J.M. Berkson, pp. 417-434, Plenum, New York, 1986.

Taylor, D.I., Nearshore shallow gas around the U.K. coast, *Continental Shelf Research, 12* (10), 1135-1144, 1992.

Tinkle, A.R., K.R. Wener, C.A. Meeder, J.F. Huff, D.M. Johns, and J.A. May, Seismic No-Data Zone, Offshore Mississippi Delta: Part 1 – Acoustic Characterisation, in *20th Annual Offshore Technology Conference*, pp. 65-74, Houston, Texas, 1988.

Tissot, B.P., and D.H. Welte, *Petroleum formation and occurrence*, 699 pp., Springer-Verlag, Berlin, 1984.

Tittmann, B.R., Lunar rock Q in 3000-5000 range achieved in laboratory,

Philosophical Transactions of the Royal Society of London, Series A, 285, 475-479, 1977.

Toksoz, M.N., D.H. Johnston, and A. Timur, Attenuation of seismic waves in dry and saturated rocks: I. Laboratory measurements, *Geophysics, 44* (4), 681-690, 1979.

Tuffin, M.D.J., A.I. Best, J.K. Dix and J.M. Bull, Acoustic characterisation of gassy marine sediments in Dibden Bay, Southampton Water (U.K.), in *Proc. Fifth European Conference on Underwater Acoustics 2000*, Lyon, France, pp. 825-830, 2000.

Tuffin, M.D.J., A.I. Best, J.K. Dix and J.M. Bull, Temporal variability of P-wave attenuation due to gas bubbles in a marine sediment, in T. G. Leighton et al. (eds.), 'Acoustical Oceanography', Proc. Institute of Acoustics Vol. 23 Part 2, pp. 291-298, 2001.

Wang, Z., and A. Nur, Dispersion analysis of acoustic velocities in rocks, *Journal of the Acoustical Society of America, 87* (6), 2384-2395, 1990.

Wang, K., E.E. Davis, and G. van der Kamp, Theory for the effects of free gas in subsea formations on tidal pore pressure variations and seafloor displacements, *Journal of Geophysical Research, 103* (B6), 12339-12353, 1998.

Webber, N.B., Hydrography and water circulation in the Solent, in *The Solent Estuarine System: An assessment of present knowledge*, edited by J.D. Burton, pp. 25-35, NERC Publications Series C, 1980.

Wessex Archaeology, Dibden Terminal: Archaeology Impact Assessment, 2000.

Weston, D.E., Sound propagation in the presence of bladder fish, in *Underwater Acoustics*, edited by V.M. Albers, pp. 55-88, Plenum Press, New York, 1967.

Wever, T.F., F. Abegg, H.M. Fielder, G. Fechner, and I.H. Stender, Shallow Gas in the muddy sediments of Eckernförde Bay, Germany, *Continental Shelf Research, 18* (14-15), 1715-1740, 1998.

Wheeler, S.J., A conceptual model for soils containing large gas bubbles, *Géotechnique, 38* (3), 389-397, 1988a.

Wheeler, S.J., The undrained shear strength of soils containing large gas bubbles, *Géotechnique, 38* (3), 399-413, 1988b.

Wheeler, S.J., and T.N. Gardner, Elastic moduli of soils containing large gas bubbles, *Géotechnique, 39* (2), 333-342, 1989.

Wheeler, S.J., Movement of large gas bubbles in unsaturated fine-grained sediments, *Marine Geotechnology, 9* (2), 113-129, 1990.

Wheeler, S.J., W.K. Sham, and S.D. Thomas, Gas pressure in unsaturated offshore soils, *Canadian Geotechnical Journal, 27*, 79-89, 1990.

Whelan III, T., J.M. Coleman, H.H. Roberts, and J.N. Suhayda, The occurrence of methane in recent deltaic sediments and its effect on soil stability, *Bulletin of the International Association of Engineering Geology, 14*, 55-64, 1976.

Whiticar, M.J., The presence of methane bubbles in the acoustically turbid sediments of Eckernförde Bay, Baltic Sea, in *The Dynamic Environment of the Sea Floor*, edited by K.A. Fanning, and F.T. Manheim, pp. 219-235, Lexington Books, Lexington, 1982.

Whiticar, M.J., and E. Faber, Methane oxidation in sediment and water column environments - Isotope evidence, *Advances in Organic Geochemistry, 10*, 759-768, 1986.

Wilkens, R.H., and M.D. Richardson, The influence of gas bubbles on sediment acoustic properties: *in situ*, laboratory and theoretical results from Eckernförde Bay, Baltic Sea, *Continental Shelf Research, 18* (14/15), 1859-1892, 1998.

Winkler, K., A. Nur, and M. Gladwin, Friction and seismic attenuation in rocks, *Nature, 277*, 528-531, 1979.

Wood, A.B., *A Textbook of Sound*, McGraw-Hill, New York, 1955.

Wood, A.B., and D.E. Weston, The propagation of sound in mud, *Acustica, 14*, 156-162, 1964.

Wood, W.T., W.S. Holbrook, and H. Hoskins, In situ measurements of P-wave attenuation in the methane hydrate- and gas-bearing sediments of the Blake Ridge,

Proceedings of the Ocean Drilling Program, Scientific Results, *164*, 265-272, 2000.

Yuan, F., J.D. Bennell, and A.M. Davis, Acoustic and physical properties of gassy sediments in the western Irish Sea, *Continental Shelf Research*, *12* (10), 1121-1134, 1992.

Glossary

A	Gas polytropic coefficient
A_0	Initial signal amplitude
$A(t)$	Time-dependent signal amplitdue
$A_{ref}(f)$	Frequency-dependent amplitude of reference signal
$A_{sig}(f)$	Frequency-dependent amplitude of attenuated signal
$A_s(f)$	Spectral amplitude of signal through sediment-filled core
$A_w(f)$	Spectral amplitude of signal through water-filled core
a	Limiting value of radius of curvature of menisci
$A(f)$	Frequency-dependent attenuation in dB/m
C_g	Thermal conductivity of gas
c	Gassy compressional wave velocity
$c(f)$	Phase velocity
c_0	Gas-free compressional wave velocity
d	Outside diameter of core
d	Thickness of material in MSCL calibration
d	Total damping
d_{al}	Thickness of aluminium
d_f	Frictional damping component
d_r	Radiation damping component
d_t	Thermal damping component
d_v	Viscous damping component
d_w	Thickess of water
dx	x_{ref}-x_{sig}
f	Insonifying frequency
f_0	Resonant frequency
G	Dynamic shear modulus
G'	Imaginary component of complex dynamic shear modulus
G_m	Saturated sediment dynamic shear modulus
I	Measured gamma ray intensity
I_0	Gamma ray source intensity
K	Bulk modulus

K_f	Bulk modulus of sediment frame
K_m	Bulk modulus of saturated sediment matrix (Type III elastic model)
K_s	Bulk modulus of solid fraction of sediment
K_{sat}	Bulk modulus of saturated sediment
K_w	Bulk modulus of water
K_{wg}	Bulk modulus of pore water modified by the gas
k	Constant of proportionality (attenuation vs frequency)
k	Wave number at frequency f
k_0	Wavenumber at resonance
N	Number of bubbles
n	Number of cycles in signal amplitude calculation
n	Porosity
n'	Exponent of frequency
n_g	Gas porosity
P_0	Ambient hydrostatic pressure
P_I	Initial pressure
P_F	Final pressure
Q	Quality factor
Q_g	Gassmann parameter
R	Radius of bubbles in distribution
R	Radius of curvature of menisci
R_c	Critical value of radius of curvature of menisci
r_0	Bubble radius
s_p	Specific heat of gas at constant pressure
T	Surface tension
T_{ref}	Start time of window of reference signal
T_{sig}	Start time of window of attenuated signal
T_s	Start time of window of signal through sediment
T_w	Start time of window of signal through water
t	travel time
t_{sig}	Signal first arrival time
u_g	Internal gas pressure
u_w	Pore water pressure

V_g	Group velocity
V_p	Compressional wave velocity
V_s	Shear wave velocity
V_w	Compressional wave velocity in water
v_g	Volume concentration of bubbles in water
x_{int}	Internal diameter of core
x_{ref}	Source-receiver separation of reference signal
x_{sig}	Source-receiver separation of attenuated signal
α	Attenuation in nepers / m
α_w	Compressional wave attenuation in water
γ	Ratio of the specific heats of the gas
$\delta t(f)$	Frequency-dependent time delay
μ	Compton mass attenuation
μ	Viscocity of water
ρ	General density
ρ	Gamma-ray density
ρ	Total bulk density
ρ_{al}	Aluminium density
ρ_{ave}	Average calibration density
ρ_g	Gas density
ρ_m	Mineral grain density
ρ_s	Solid material density
ρ_{sat}	Saturated sediment density
ρ_w	Water density
ϕ_s	Phase spectrum of signal through sediment-filled core
ϕ_w	Phase spectrum of signal through water-filled core
ω	Angular frequency
ω_0	Angular frequency at resonance

Appendix A. X-Ray Computed Tomography Scans

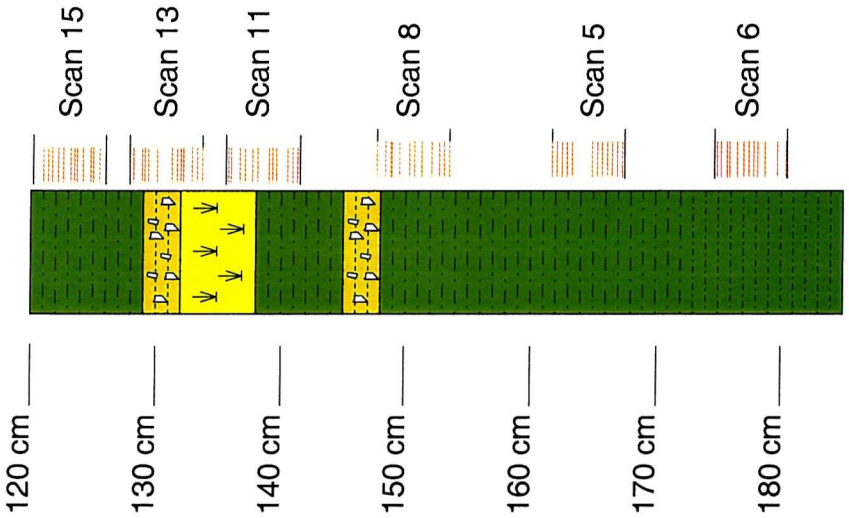

Figure A.1. Scan locations. Black lines mark the limits of the scans, red lines mark the positions of the individual slices.

Scan 5: 161.7 – 167.5 cm		Scan 6: 174.7 – 180.5 cm		Scan 8: 147.7 – 153.5 cm	
Slice	Depth in core [cm]	Slice	Depth in core [cm]	Slice	Depth in core [cm]
6	161.7	404	174.9	126	147.7
10	162.1	407	175.2	133	148.4
14	162.5	412	175.7	137	148.8
18	162.9	414	175.9	138	148.9
22	163.3	420	176.5	144	149.5
38	164.9	425	177.0	152	150.3
42	165.3	429	177.4	156	150.7
46	165.7	433	177.8	162	151.3
50	166.1	436	178.1	170	152.1
54	166.5	442	178.7	176	152.7
58	166.9	452	179.7	180	153.1
62	167.3	459	180.4	184	153.5

Scan 11: 141.5 – 135.6 cm		Scan 13: 133.7 – 127.9 cm		Scan 15: 126.0 – 120.2 cm	
Slice	Depth in core [cm]	Slice	Depth in core [cm]	Slice	Depth in core [cm]
189	141.3	265	133.7	331	125.5
193	140.9	269	133.3	336	125.0
197	140.5	273	132.9	338	124.8
206	139.6	280	132.2	344	124.2
209	139.3	282	132.0	349	123.7
212	139.0	285	131.7	351	123.5
221	138.1	289	131.3	354	123.2
225	137.7	301	130.1	360	122.6
231	137.1	308	129.4	364	122.2
235	136.7	311	129.1	369	121.7
242	136.0	313	128.9	372	121.4
244	135.8	320	128.2	376	121.0

Table A.1. CT Scan and slice positions.

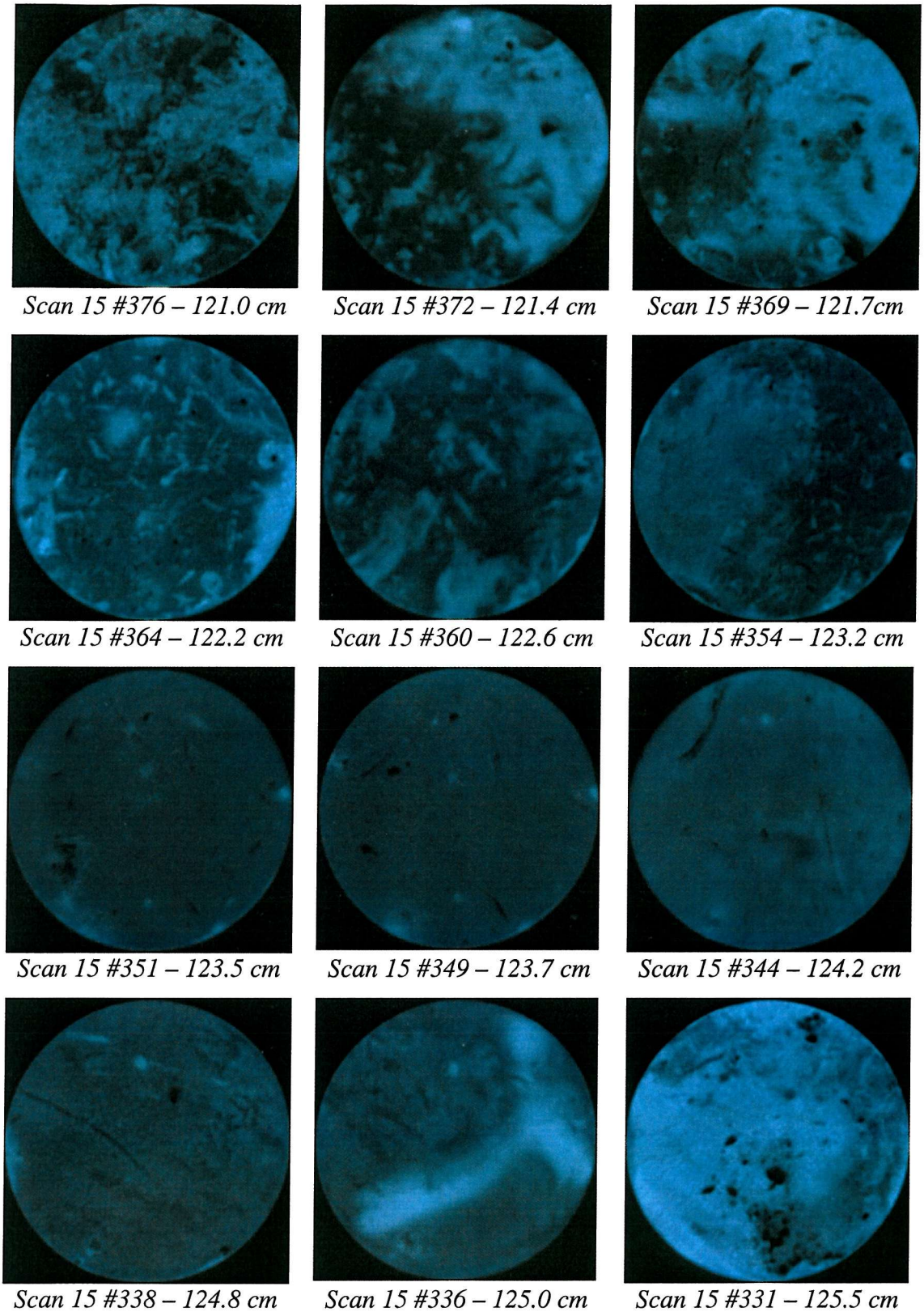

Figure A.2. X-Ray CT slices from Scan 15 (120.2 – 126.0 cm)

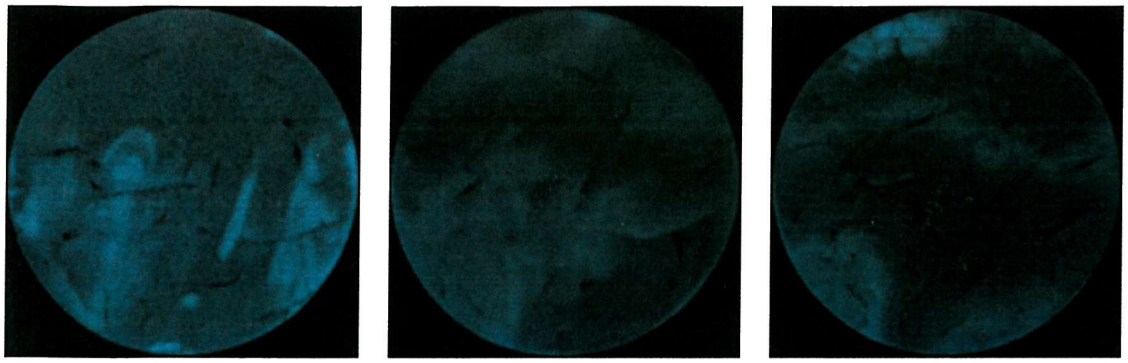

Scan 13 #320 – 128.2 cm | Scan 13 #313 – 128.9 cm | Scan 13 #311 – 129.1 cm

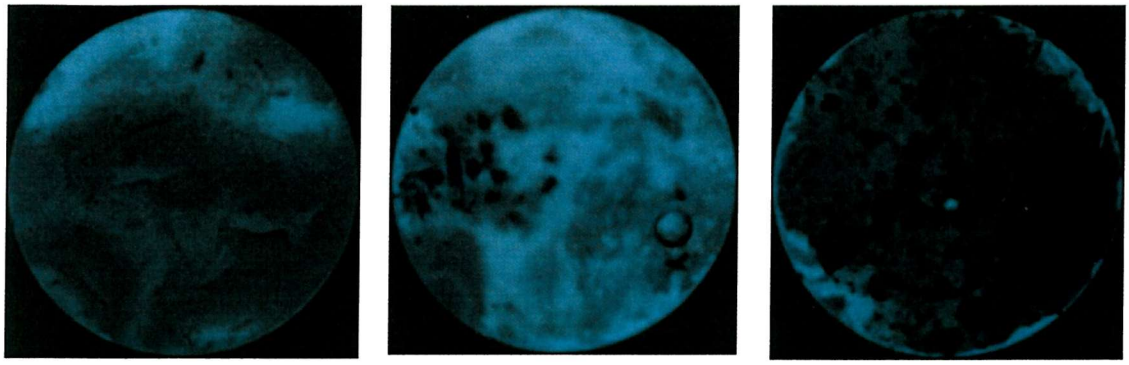

Scan 13 #308 – 129.4 cm | Scan 13 #301 – 130.1 cm | Scan 13 #289 – 131.3 cm

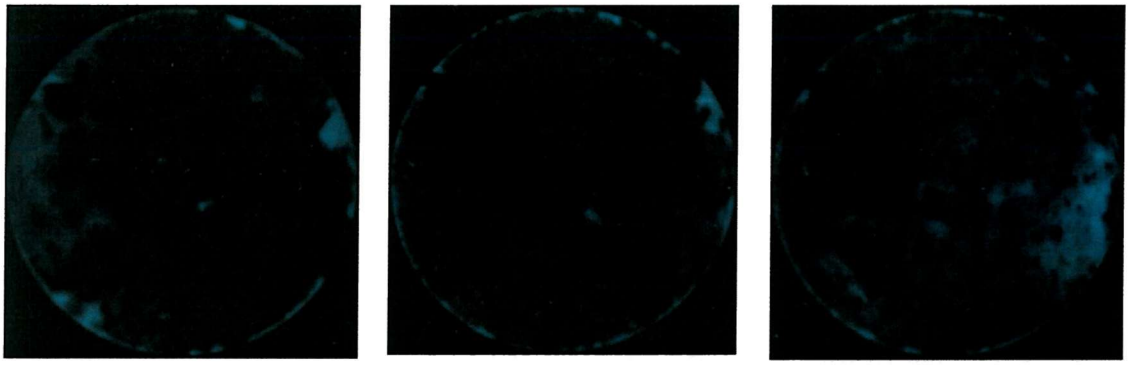

Scan 13 #285 – 131.7 cm | Scan 13 #282 – 132.0 cm | Scan 13 #280 – 132.2 cm

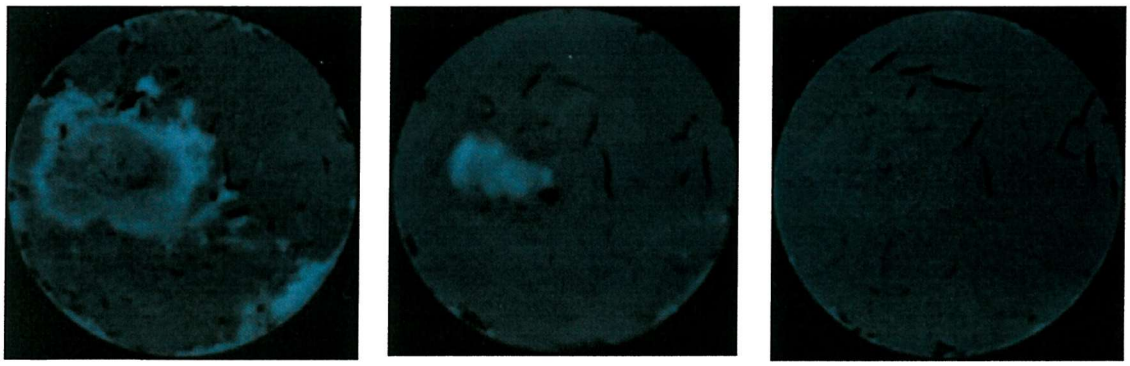

Scan 13 #273 – 132.9 cm | Scan 13 #269 – 133.3 cm | Scan 13 #265 – 133.7 cm

Figure A.3. . X-Ray CT slices from Scan 13 (127.9 – 133.7 cm)

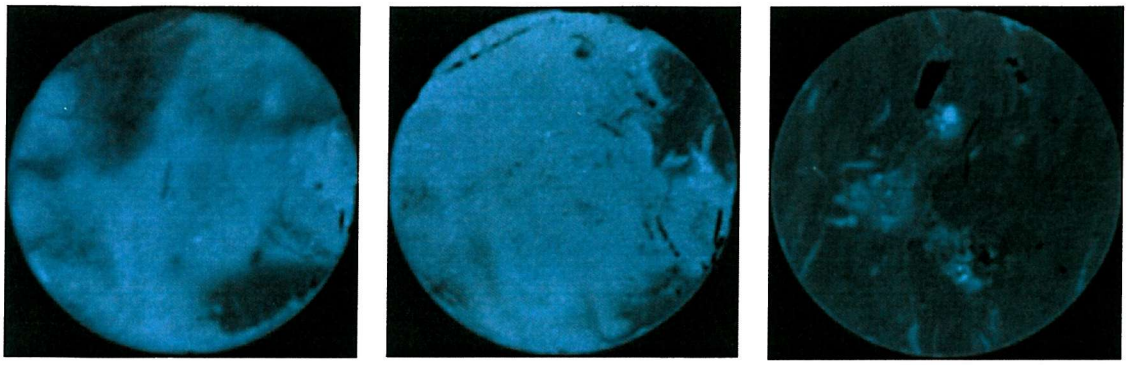

Scan 11 #244 – 135.8 cm | Scan 11 #242 – 136.0 cm | Scan 11 #235 – 136.7 cm

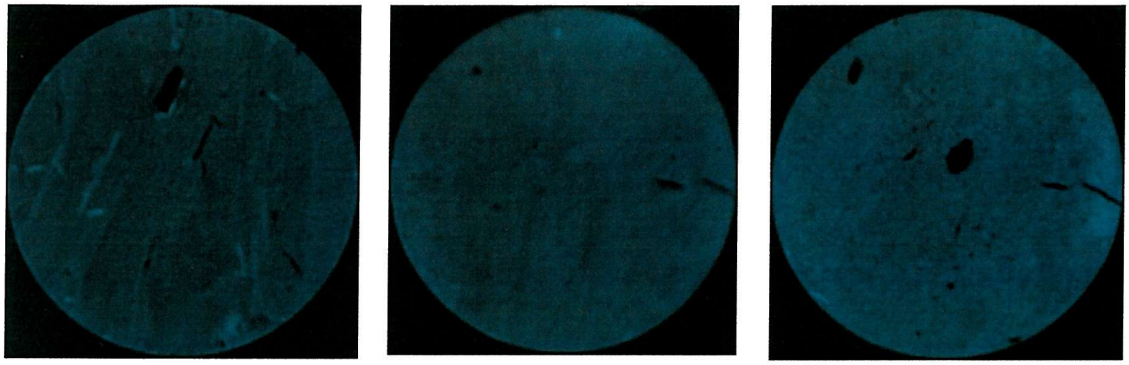

Scan 11 #231 – 137.1 cm | Scan 11 #225 – 137.7 cm | Scan 11 #221 – 138.1 cm

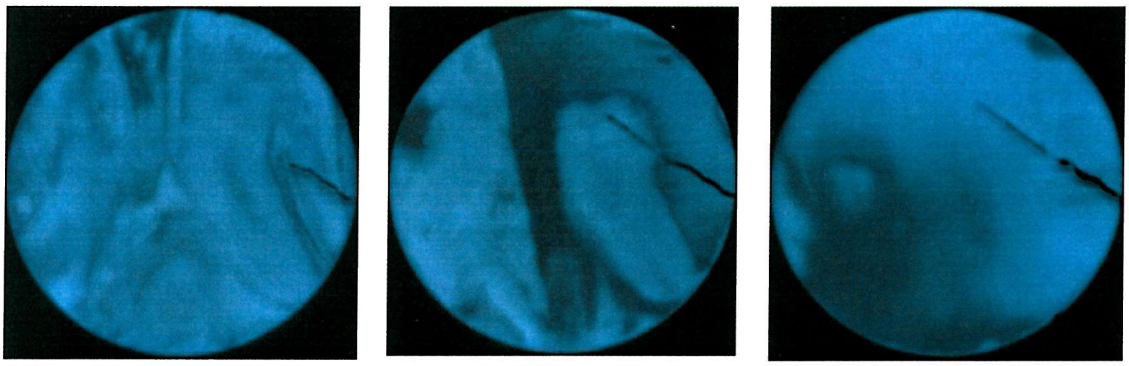

Scan 11 #212 – 139.0 cm | Scan 11 #209 – 139.3 cm | Scan 11 #206 – 139.6 cm

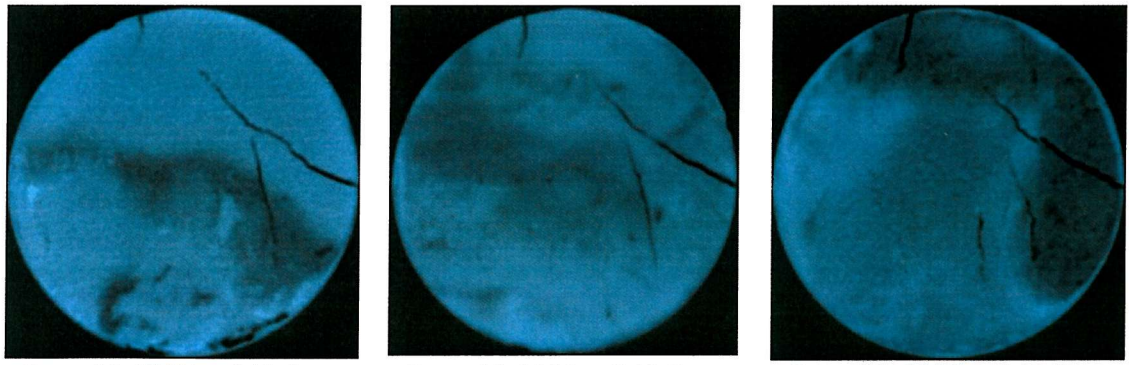

Scan 11 #197 – 140.5 cm | Scan 11 #193 – 140.9 cm | Scan 11 #189 – 141.3 cm

Figure A.4. X-Ray CT slices from Scan 11 (135.6 cm – 141.5 cm)

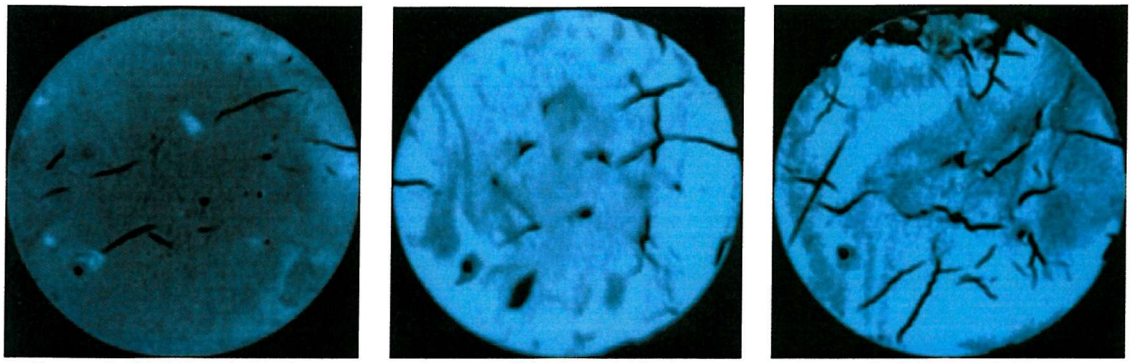

Scan 8 #126 – 147.7 cm *Scan 8 #133 – 148.4 cm* *Scan 8 #137 – 148.8 cm*

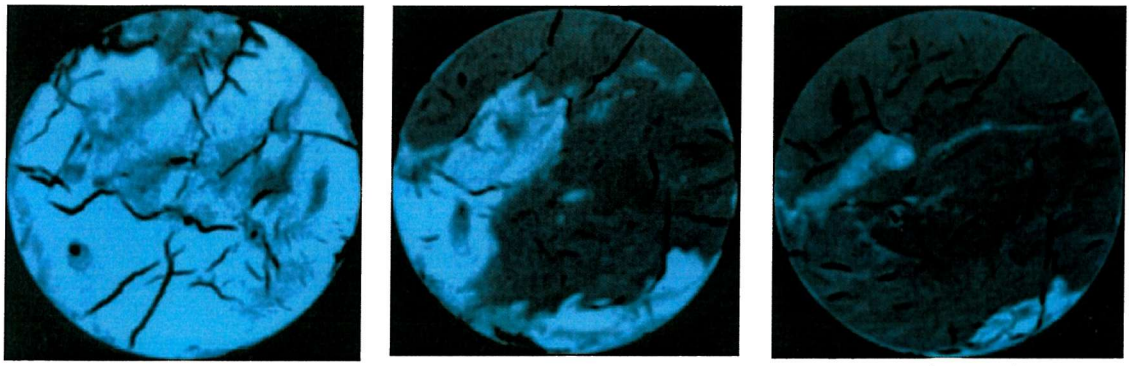

Scan 8 #138 – 148.9 cm Scan 8 #144 – 149.5 cm Scan 8 #152 – 150.3 cm

Scan 8 #156 – 150.7 cm *Scan 8 #162 – 151.3 cm* *Scan 8 #170 – 152.1 cm*

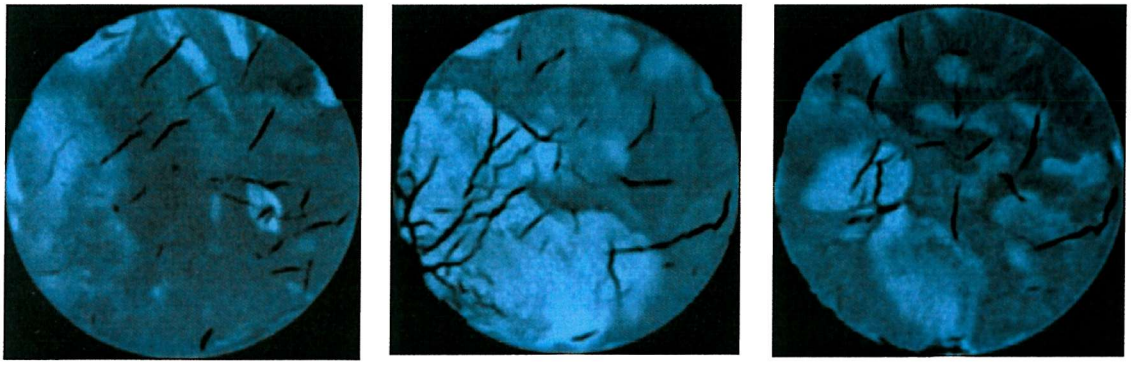

Scan 8 #176 – 152.7 cm *Scan 8 #180 – 153.1 cm* *Scan 8 #185 – 153.5 cm*

Figure A.5. X-Ray CT slices from Scan 8 (147.7 cm – 153.5 cm)

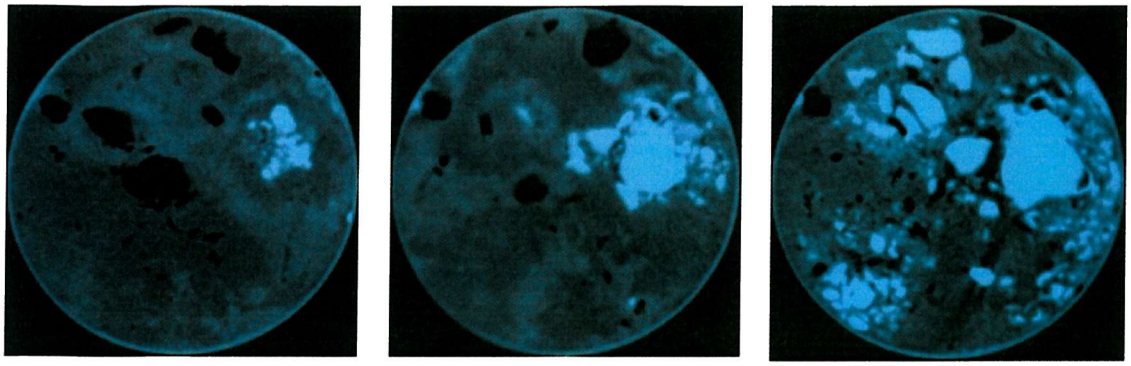

Scan 5 #06 – 161.7 cm | Scan 5 #10 – 162.1 cm | Scan 5 #14 – 162.5 cm

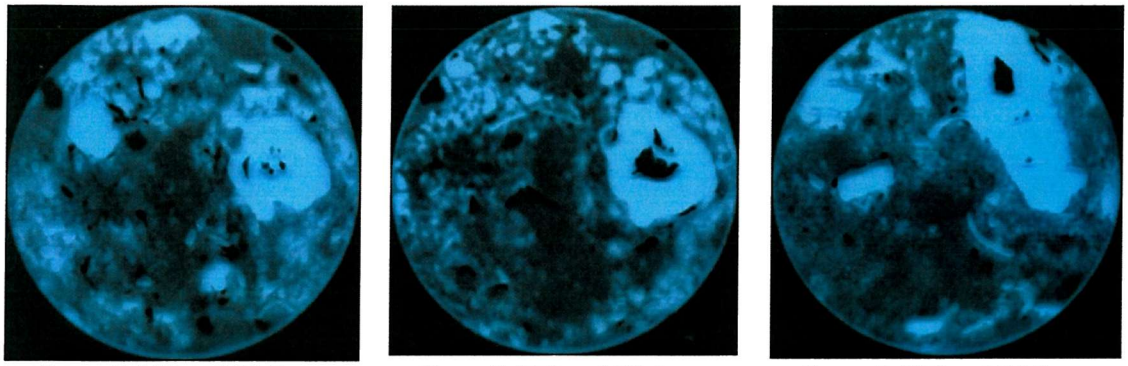

Scan 5 #18 – 162.9 cm | Scan 5 #22 – 163.3 cm | Scan 5 #38 – 164.9 cm

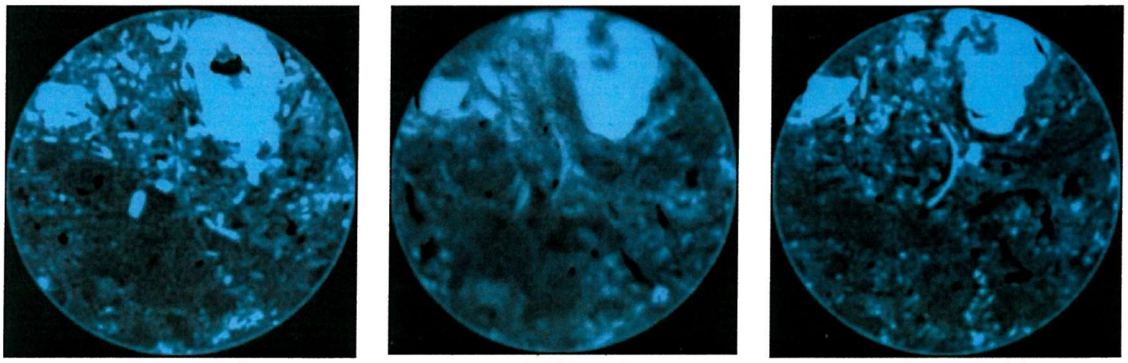

Scan 5 #42 – 165.3 cm | Scan 5 #46 – 165.7 cm | Scan 5 #50 – 166.1 cm

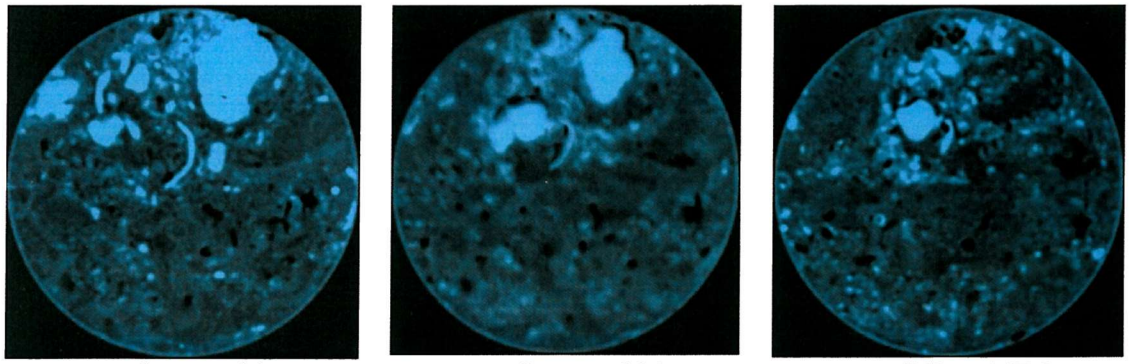

Scan 5 #54 – 166.5 cm | Scan 5 #58 – 166.9 cm | Scan 5 #62 – 167.3 cm

Figure A.6. X-Ray CT slices from Scan 5 (161.7 cm – 167.5 cm)

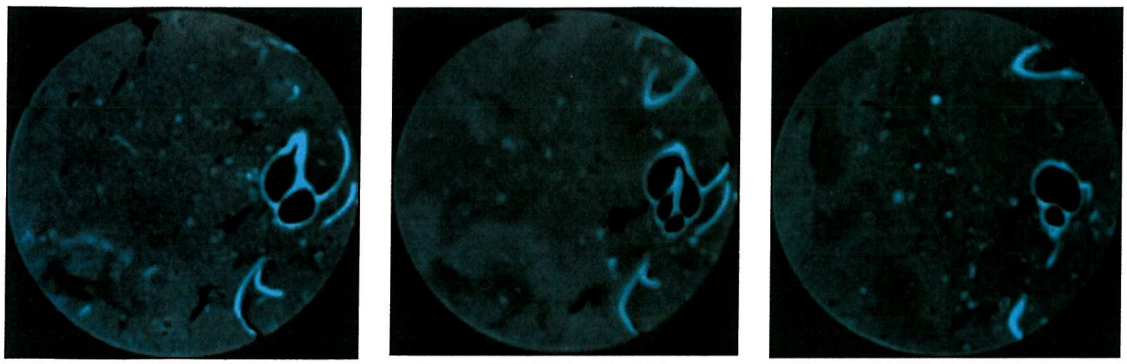

Scan 6 #404 – 174.9 cm | Scan 6 #407 – 175.2 cm | Scan 6 #412 – 175.7 cm

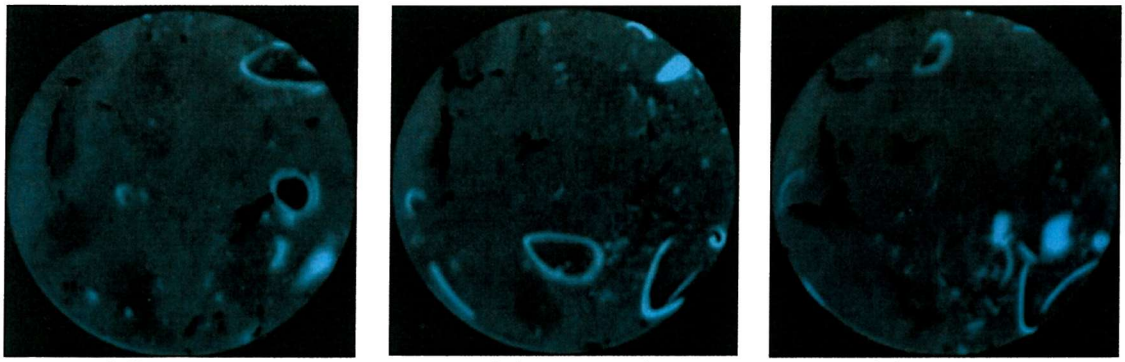

Scan 6 #414 – 175.9 cm | Scan 6 #420 – 176.5 cm | Scan 6 #425 – 177.0 cm

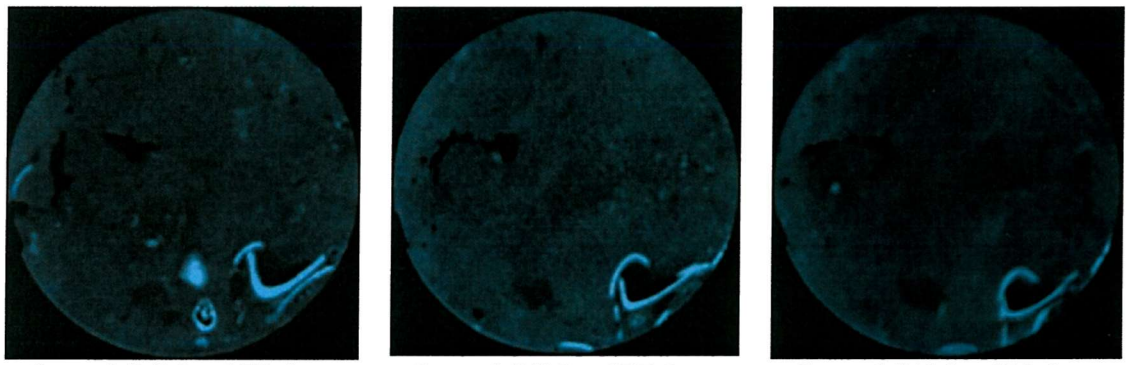

Scan 6 #429 – 177.4 cm | Scan 6 #433 – 177.8 cm | Scan 6 #436 – 178.1 cm

Scan 6 #442 – 178.7 cm | Scan 6 #452 – 179.7 cm | Scan 6 #459 – 180.4 cm

Figure A.7. X-Ray CT slices from Scan 6 (174.7 cm – 180.5 cm)

Appendix B. Broadband transmission data

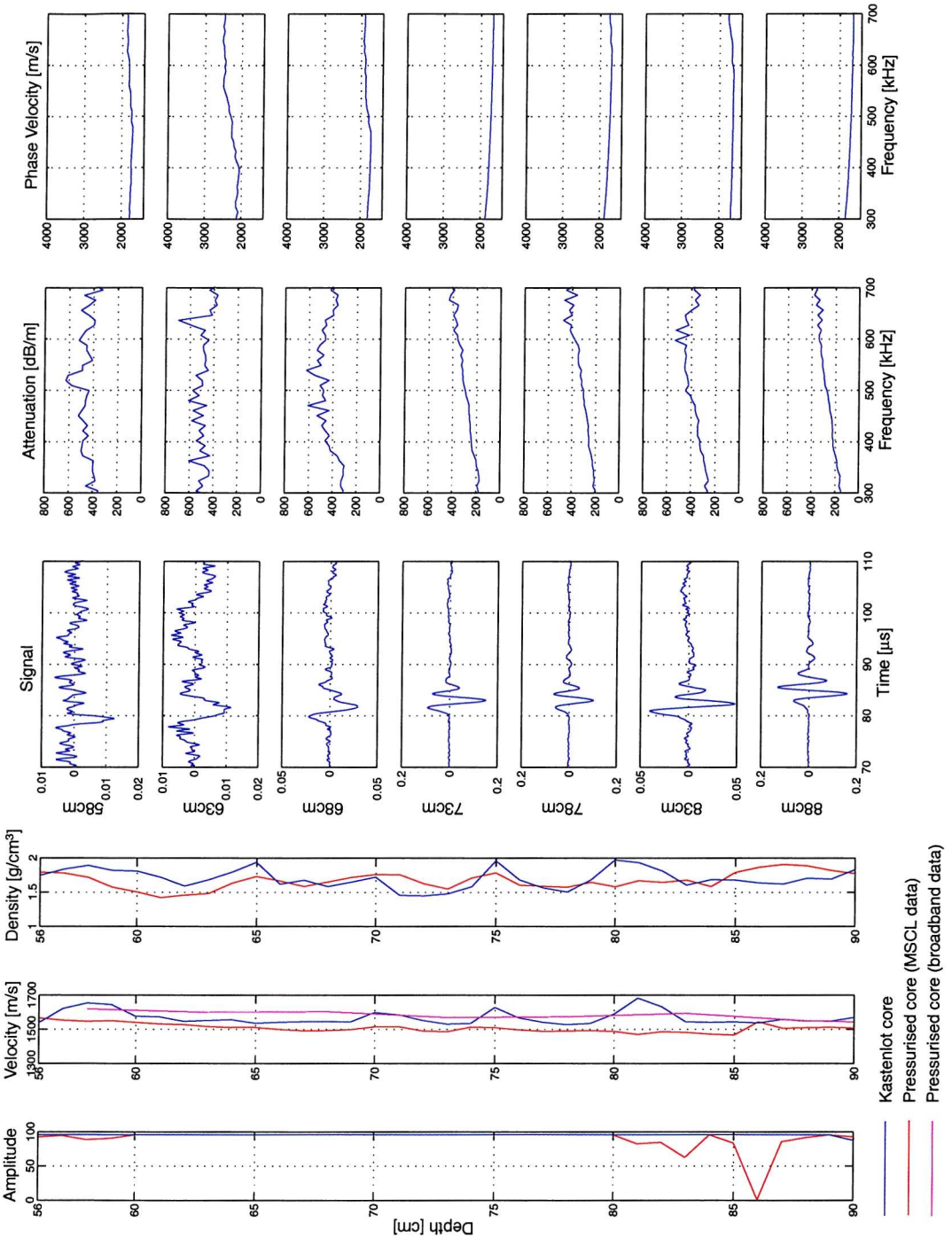

Figure B.1. Broadband transmission and related MSCL data – 58 to 88 cm

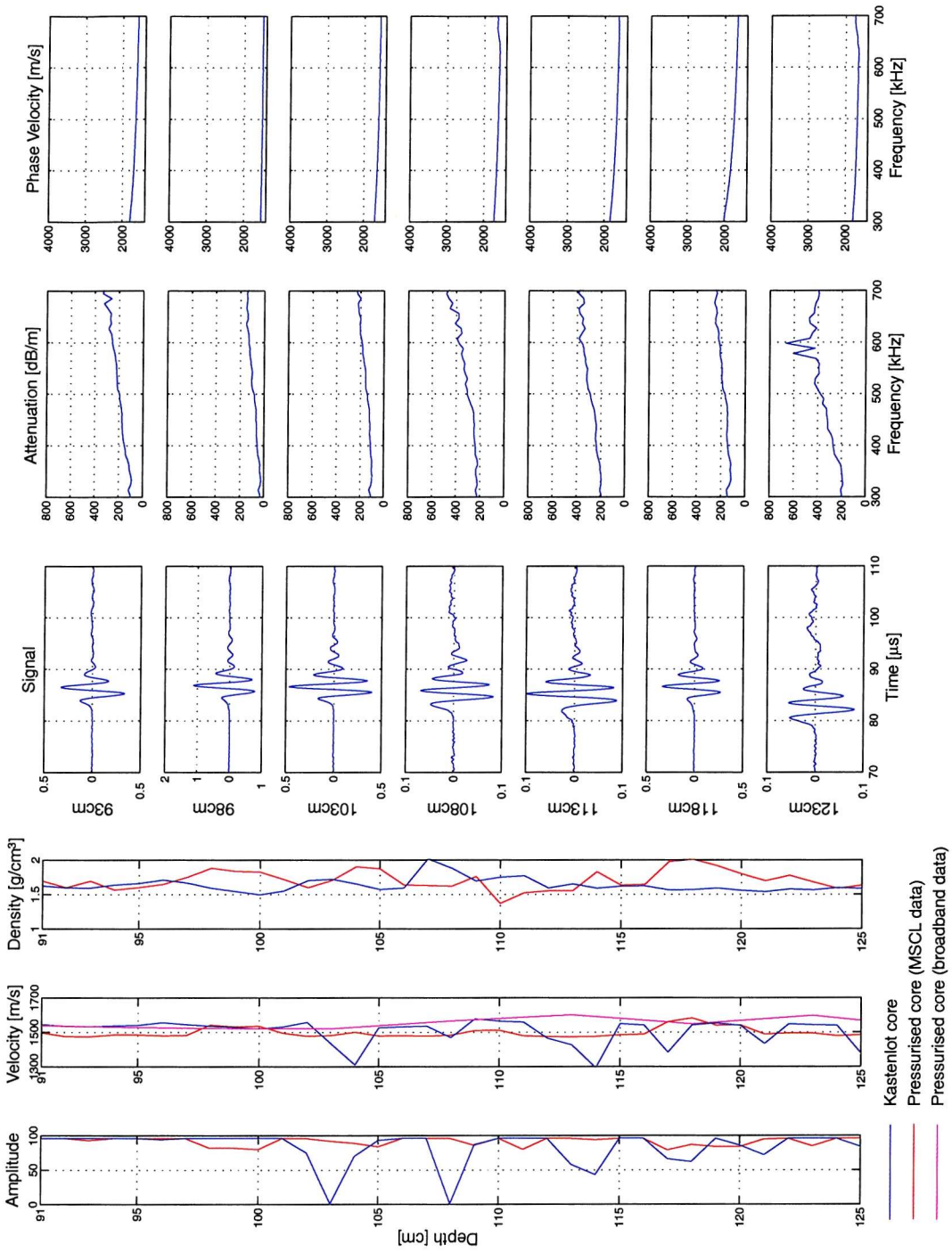

Figure B.2. Broadband transmission and related MSCL data – 93 to 123 cm

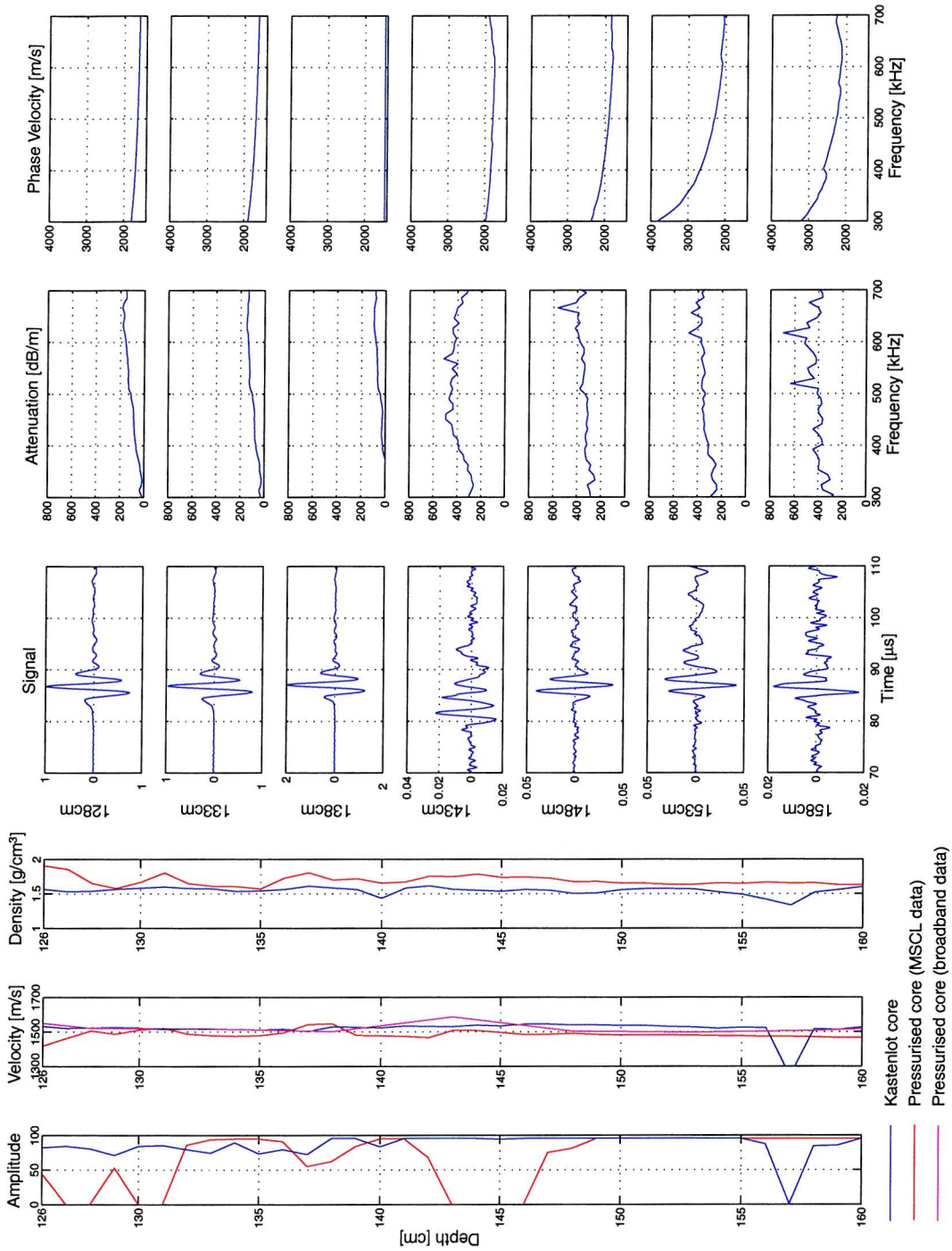

Figure B.3. Broadband transmission and related MSCL data – 128 to 158 cm

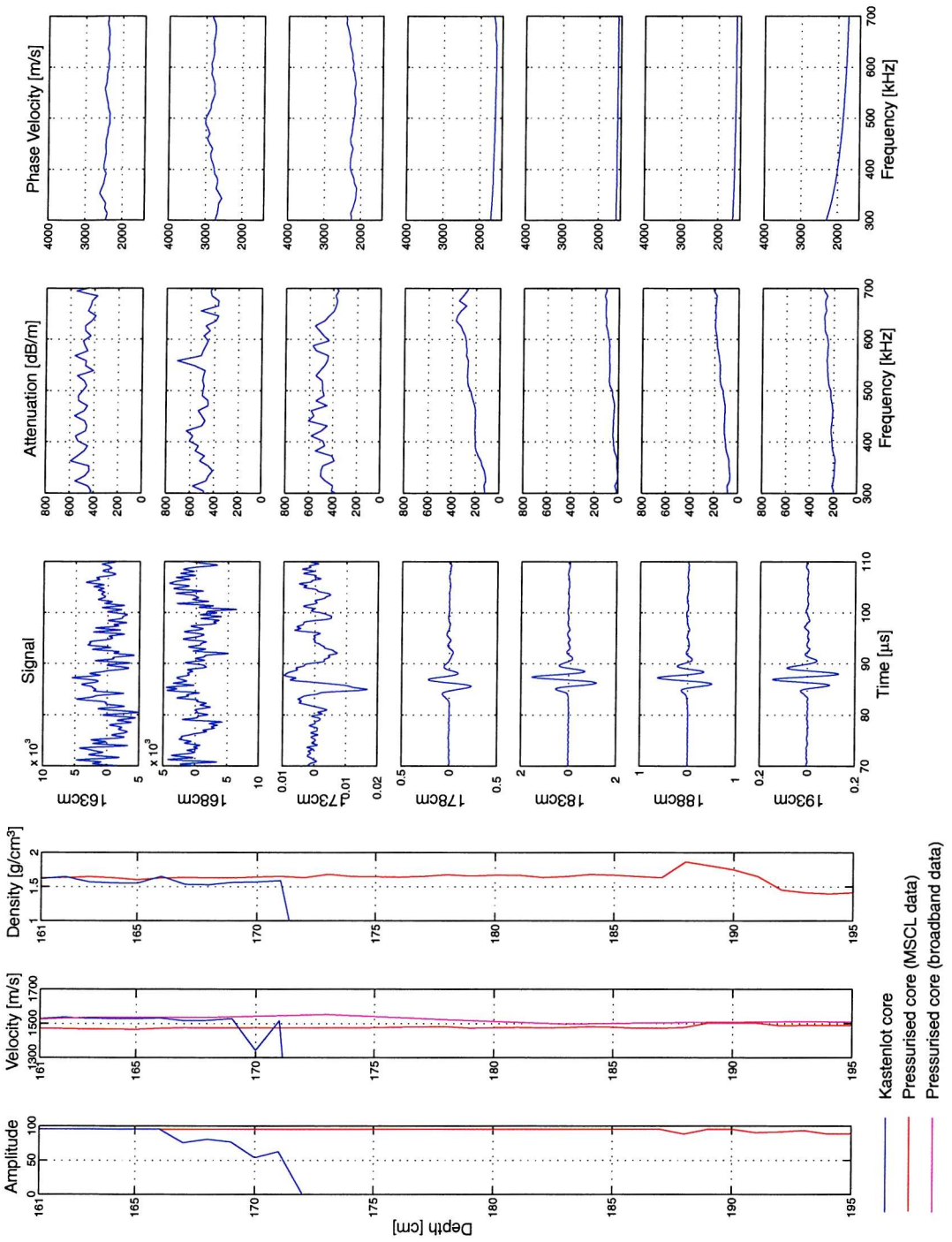

Figure B.4. Broadband transmission and related MSCL data – 163 to 193 cm

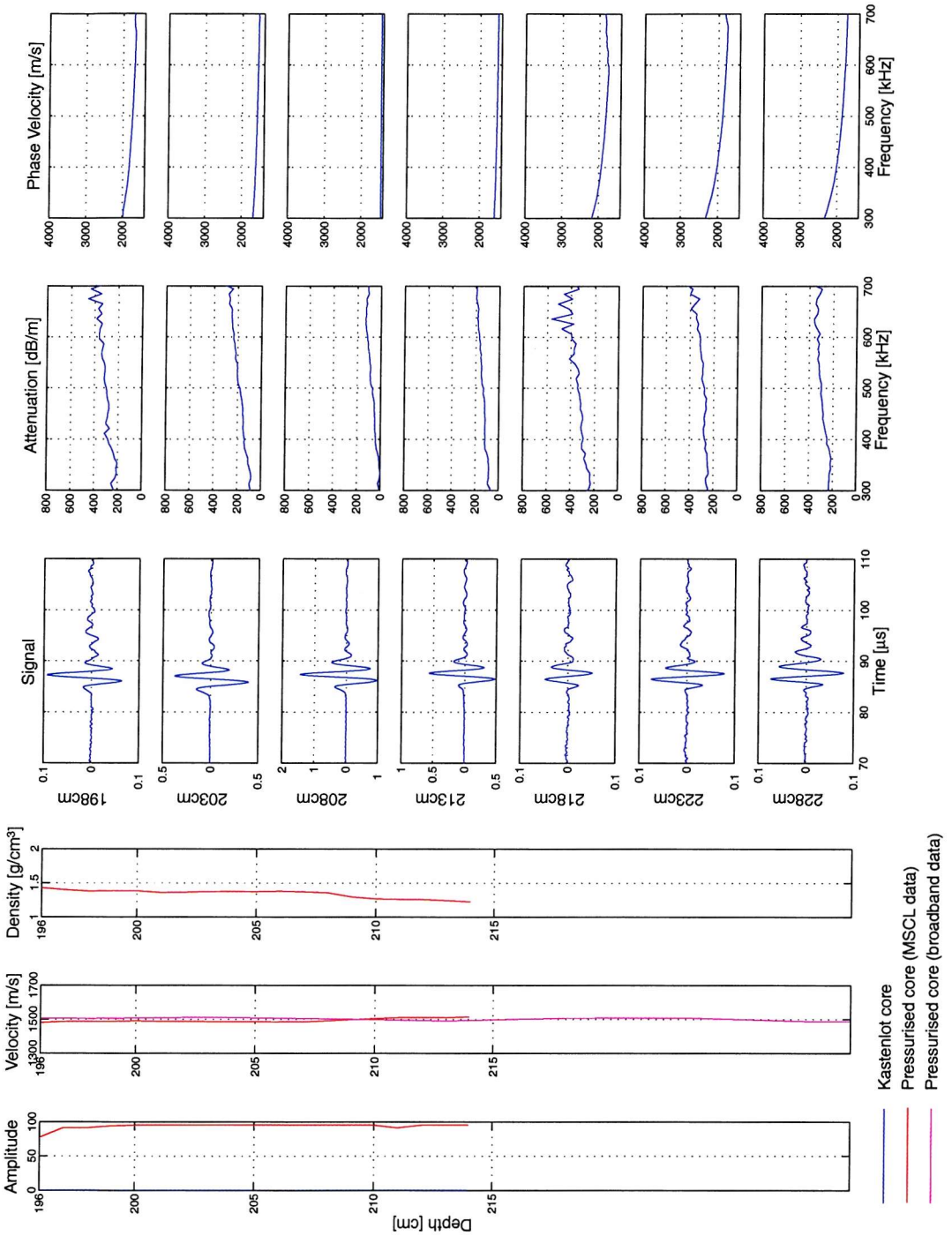

Figure B.5. Broadband transmission and related MSCL data – 198 to 228 cm

Appendix C. Geotechnical testing

Attempts were made to measure the frame bulk modulus of the sediment, using an isotropic compression test. However, measuring elastic moduli at high strain amplitudes (i.e. higher than acoustic strains) is known to underestimate the value of the modulus appropriate for acoustic strains (e.g. Davis *et al.*, 1981). Values of geotechnically measured frame bulk moduli will be compared to values obtained from acoustic methods. Knowledge of the density, bulk modulus of the saturated sediment and dynamic shear modulus of the saturated sediment, obtained acoustically, enables a calculation of the frame bulk modulus to be made. This is done by measuring the porosity and assuming values for the bulk moduli of the sediment grains and pore fluid and rearranging Gassmann's (1951) equations (Equations 3.2 and 3.3), as described in Hamilton (1971a). An oedometer test was performed to measure the 90 % consolidation time for the sediment. This time was used as a guide in calculating how long drainage would take in the isotropic consolidation test.

These values were then compared to calculated values. Frame bulk modulus may be calculated in two different ways. The first method uses Hamilton's (1971a) regression equations. The second uses Gassmann's (1951) equation (Equations 3.2 and 3.3) which can be solved for K_f, as described by Hamilton (1971a):

$$K_f = \frac{K[n(K_s - K_w) + K_w] - K_s K_w}{n(K_s - K_w) + K_w\left(\frac{K}{K_s} - 1\right)} \qquad \text{C.1}$$

Therefore, by acoustically deriving a value for the bulk modulus, K, measuring density (to obtain porosity) and assuming values for the bulk moduli of the pore water and mineral grains, a value of the frame bulk modulus may be calculated.

C.1 Oedometer test

One-dimensional consolidation of sediment is tested using an oedometer (Figure C.1). Consolidation is the gradual reduction of the total sediment volume due to drainage of some of the pore water and is complete when all of the stress of the applied load is carried by the sediment structure and not the pore water. An oedometer test was performed on a sample in order to calculate a rough value for the 90% consolidation time using the square-root-time method as described by Head (1994).

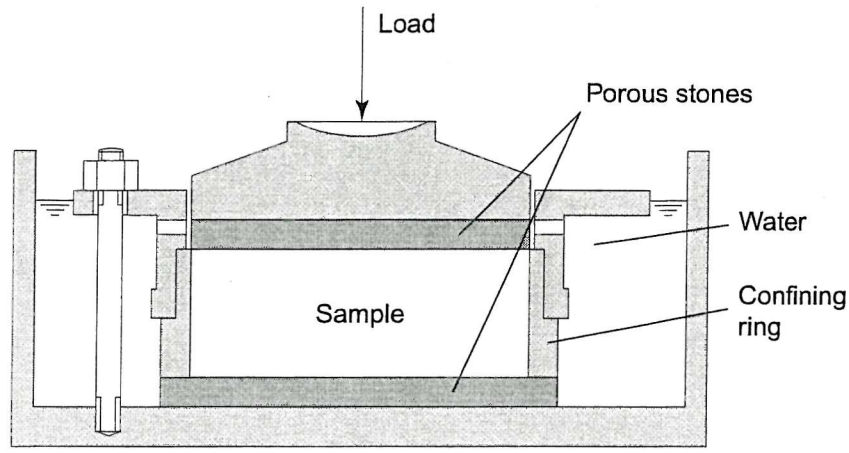

Figure C.1. The oedometer. From Craig (1992).

C.2 Isotropic compression testing

The shorter of the Kastenlot cores was cut into a series of slabs, each ten centimetres thick. Each slab was sub-sampled to obtain two cylinders of sediment, 38 mm in diameter and 75 mm long, using a soil lathe. The samples were placed in a rubber membrane with a de-aired porous disk at one end and a plastic cap at the other. The sample was mounted in a Bishop-Wesley geotechnical testing cell (Figure C.2) attached to two GDS controllers.

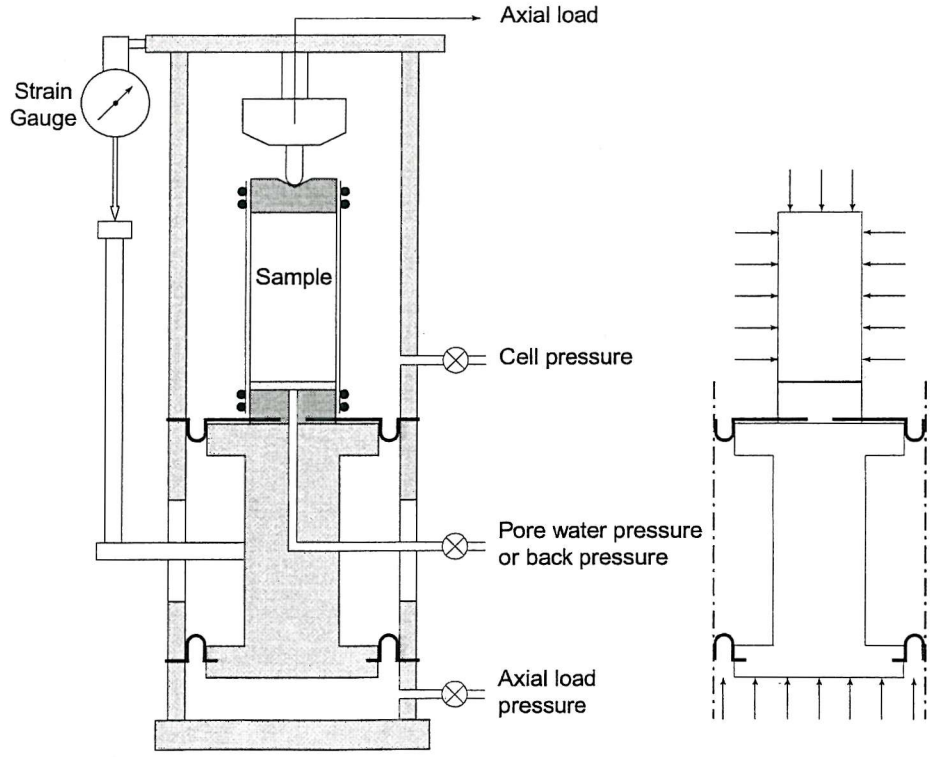

Figure C.2. The principle of the Bishop-Wesley cell. From Head (1986).

The GDS controller is a computer controlled hydraulic actuator for the precise regulation and measurement of liquid pressure and liquid volume change. The hydraulic fluid in this case was de-aired water. De-aired water in a cylinder is pressurised and displaced by a piston moving in the cylinder. The piston is activated by a ball screw turned by a stepper motor in a captive ball nut. Pressure is detected by an integrated solid-state pressure transducer. The system may be programmed to cause the motor to seek a target pressure or step to a target volume change. Volume change is detected by counting the steps of the motor.

In the experiment, one GDS controller was connected to the cell pressure (i.e., the isotropic pressure) and another was connected to the sample to provide a back pressure in the sample (i.e. increase the sample pore pressure) or to measure the pore pressure. An initial effective stress of 20 kN/m^2, equivalent to 2 m of water, was applied to the sample to keep it in position by increasing the cell pressure to 25 kN/m^2 and the back pressure to 5 kN/m^2, since effective stress equals the difference between the total stress (cell pressure) and the pore water pressure (applied back pressure). To ensure that the sample was fully saturated, the cell pressure and back pressure were ramped from their initial values of 25 kN/m^2 and 5 kN/m^2 to 500 kN/m^2 and 480 kN/m^2, respectively, over a period of 12 hours ensuing that the effective stress on the sample remained at approximately 20 kN/m^2. To test whether the sample was saturated, the cell pressure was increased by 50 kN/m^2 and the other controller was left in pore pressure measurement mode. If the sample was saturated, the increase in the cell pressure should be mirrored by an equal increase in the pore pressure of the sample. This is known as a B test, where:

$$B = \frac{\Delta\sigma_3}{\Delta u} \qquad \text{C.2}$$

where $\Delta\sigma_3$ is the change in total stress; and Δu is the change in pore pressure. A fully saturated sample will have a B value of 1, although in practice that is very difficult to obtain. The GDS controllers were then set such that the cell pressure was ramped from 550 kN/m^2 to 600 kN/m^2 over a period of 24 hours to apply an increase in effective stress, while the back pressure was kept constant at 530 kN/m^2. This increase in effective stress causes a volume change in the sample, which is measured by the GDS controller. Finally, the frame bulk modulus, K_f, of the sample may be calculated from:

$$K_f = \frac{\Delta\sigma_3'}{\varepsilon_{vol}} \qquad \text{C.3}$$

where $\Delta\sigma_3'$ is the change in effective stress and ε_{vol} is the volumetric strain of the sample, $\varepsilon_{vol} = \frac{\Delta V}{V}$ where ΔV is the volume change and V is the initial volume of the sample.

The results of the frame bulk modulus comparison are shown in Figure C.3. Data are presented for both types of core for Hamilton's regression equation (calculations based on porosity) and the inversion of Gassmann's equation. The two methods give very different results with the Gassmann results spread around the Hamilton results, generally remaining between 200 and 500 MN/m^2 for all porosities.

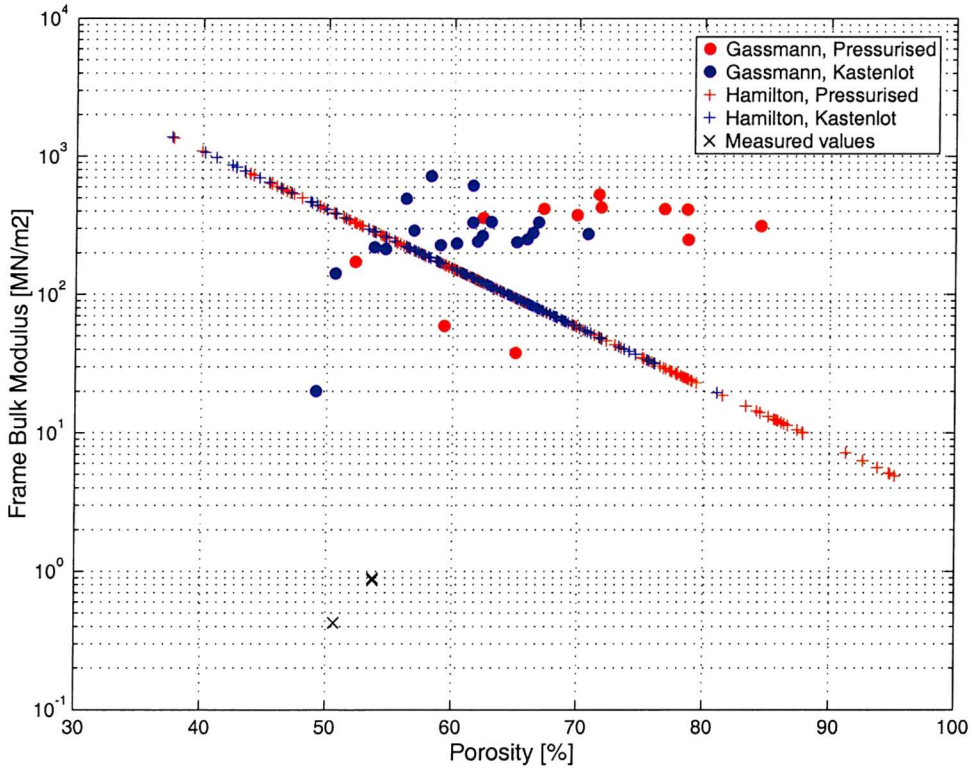

Figure C.3. Frame bulk moduli comparisons

The data displayed above clearly indicate that the geotechnically measured frame modulus values are significantly lower than those derived from the results of Hamilton (1971a) and Gassmann (1951).

Appendix D. Publications

Publication 1:

Tuffin, M. D. J., A. I. Best, J. K. Dix and J. M. Bull, Acoustic characterisation of gassy marine sediments, in Proc. Fifth European Conference on Underwater Acoustics 2000, Lyon, France, pp. 825-830, 2000.

Publication 2:

Tuffin, M. D. J., A. I. Best, J. K. Dix and J. M. Bull, Temporal variability of P-wave attenuation due to gas bubbles in a marine sediment, in T. G. Leighton et al., (eds.), 'Acoustical Oceanography', Proc. Institute of Acoustics Vol. 23 Part 2, pp. 291-298, 2001.

Poster:

Tuffin, M. D. J., A. I. Best, J. K. Dix and J. M. Bull, Temporal variability of P-wave attenuation due to gas bubbles in a marine sediment, presented at Acoustical Oceanography conference, Southampton 9 – 13 April, 2000

ACOUSTIC CHARACTERISATION OF GASSY MARINE SEDIMENTS IN DIBDEN BAY, SOUTHAMPTON WATER (U.K.).

M.D.J. Tuffin[1], A.I. Best[2], J.K. Dix[1], J.M. Bull[1]

[1]School of Ocean and Earth Sciences, University of Southampton, Southampton Oceanography Centre, Southampton, U.K., SO14 3ZH.
[2]Challenger Division for Seafloor Processes, Southampton Oceanography Centre, Southampton, U.K., SO14 3ZH.
Email: Michael.Tuffin@soc.soton.ac.uk

Gassy sediments can exhibit different velocity- and attenuation-frequency responses to their fully saturated counterparts. Gassy sediments found in Dibden Bay, Southampton Water (U.K.) were studied using a high-resolution (chirp) acoustic reflection profiler, a mini-boomer system and laboratory core measurements. Results from the chirp profiles at high tide and refraction lines at low tide indicate the presence of free gas. The sediment exhibits high attenuation coefficients (4 – 6 dB/m at 1.5 kHz) and low group velocity (~1400 m/s). High frequency (500 kHz) core measurements show attenuation coefficients of 200 - 450 dB/m, which are higher than values normally found in fully saturated silty sediments. The system is modelled to show how free gas could affect the geoacoustic properties of the sediment and explain the low velocities and high attenuation coefficients observed.

1. INTRODUCTION

It has been observed that many shallow sediments (within 20 metres of the seafloor) appear to be almost acoustically impenetrable to sub-bottom profiling systems. This 'acoustic turbidity' is caused by the presence of free gas in the sediment, which also causes increased attenuation and decreased P-wave velocity [1]. These areas are widely distributed and one example is Dibden Bay, Southampton Water (U.K.), which is ideal for experimentation because it is exposed at low tide, thus enabling both marine and terrestrially based experiments to be completed. The area is composed of very soft mud with a surficial shell layer in some areas (including the mini-boomer site).

The presence of methane, and smaller amounts of other gases, in shallow sediments is thought to be the result of anaerobic bacterial decomposition of organic matter [2]. In the marine environment sediment pore water is rich in sulphates allowing sulphate reducing bacteria to dominate and produce hydrogen sulphide. Once the sulphates have been depleted, carbonate reducing bacteria can compete more efficiently and begin methane production [3] (Fig. 1).

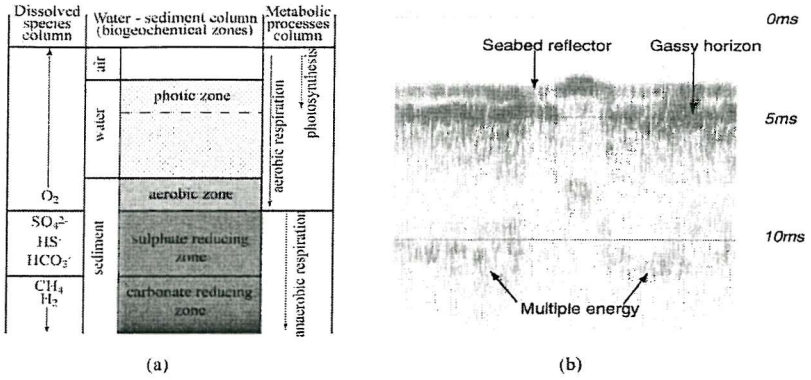

Fig. 1: (a) Diagrammatic cross-section of a typical sediment/water column (from [3]) and (b) a chirp normal incidence sub-bottom profile over the mini-boomer site at Dibden Bay.

The odour of hydrogen sulphide was detected at the Dibden Bay site and chirp sub-bottom profiles (Fig. 1) show only acoustic turbidity, both of which strongly indicate the presence of: a) anaerobic conditions within the sediment and b) free gas within the sediment.

The aims of this ongoing study are to determine what effect the presence of free gas has on the geotechnical and geoacoustic properties of a sediment and to explore links with the acoustic signature and sediment loading conditions. The in-situ measurements will be accompanied by laboratory experiments on pressurised cores collected by SCUBA divers. Core measurements will include acoustic velocity, attenuation, bulk density and resistivity over a range of P-T conditions typical of shallow water (< 30m) sediments. X-ray computed tomography will be used to image the gas bubbles and volumetric analysis will allow the gas fraction to be quantified. Comparison of in-situ and laboratory results should give insight into the undisturbed state of gassy marine sediments.

2. DATA COLLECTION

The mini-boomer system uses a high voltage inverter to drive a magneto propulsive plate, 20 cm in diameter, and a set of four hydrophones to receive the transmitted signal. Tests have shown that the mini-boomer produces a repeatable signal, a spherical radiation pattern and a spectral content between 0 – 11 kHz notched at about 2.5 kHz; the hydrophones show a flat frequency response up to 10 kHz [4]. The mini-boomer and the hydrophone array were buried below the shell layer at 0.3 m and 0.6 m, respectively. The experiment configuration may be seen in Fig. 2.

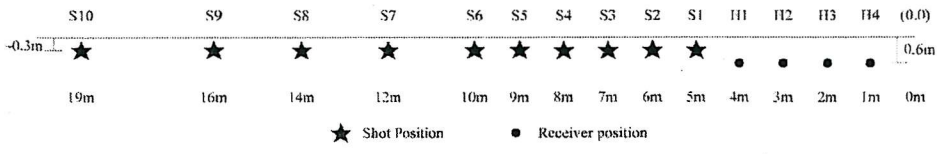

Fig. 2: Shot points and receiver positions

Additionally, three cores have been taken at the site. Two are short (1 m) push cores, one capped using specially designed pressure sealed end caps. The other was left uncapped. The third core is a 3 m long auger core used for describing the sediment.

3. IN-SITU DATA PROCESSING

Group velocity was calculated using first arrival times; phase velocity, attenuation coefficient and quality factor, Q, were calculated using a filter correlation technique [5]. This technique involves filtering the selected data and a reference signal into a series of frequency bands, each of 100 Hz, from a minimum central frequency of 100 Hz, to an arbitrarily determined maximum frequency of 3 kHz. The reference signal was taken to be the signal at the closest source-receiver separation. A cross correlation between the filtered signal and the filtered reference is calculated and the time delay that corresponds to the cross correlation maximum is used to calculated the phase velocity at that frequency band (Equation (1)). The attenuation coefficient is then calculated using Equation (2). Finally, quality factor, Q, is calculated using Equation (3).

$$c(f)=\frac{x_{sig}-x_{ref}}{(t_{sig}-t_{ref})+timedelay} \tag{1}$$

$$a(f)=\frac{8.686}{\delta x}\ln\left|\frac{A_{ref}}{A_{sig}}.\frac{x_{ref}}{x_{sig}}\right| \tag{2}$$

$$Q(f)=\frac{\pi.f}{\alpha(f).c(f)} \tag{3}$$

where $c(f)$ = phase velocity; $a(f)$ = attenuation coefficient in dB/m; $Q(f)$ = quality factor; $A_{ref,\ sig}$ = root mean square energies of the reference and signal series, respectively; $x_{ref,\ sig}$ = source-receiver separations for reference and signal series, respectively; $t_{ref,\ sig}$ = first arrival time of pulse for reference and signal series, respectively; $\delta x = x_{sig} - x_{ref}$; f = central frequency of the current pass band.

4. LABORATORY DATA PROCESSING

Transmission tests were carried out across the diameter of the sealed core and a calibration core filled with distilled water. Phase velocity, attenuation coefficient and Quality factor were computed using Equations (4), (5) and (3) respectively.

$$c(f)=\frac{x_d}{t_c-2t_L-\left(\frac{\phi(f)}{2\pi f}\right)} \tag{4}$$

$$a(f)=\frac{8.686}{x_d}\left[\ln\left|\frac{A_w(f)}{A_{sed}(f)}\right|+f^2.\alpha_w.x_d\right] \tag{5}$$

where x_d = internal diameter of the core; $t_{c,L}$ = first arrival time of pulse through whole core barrel and liner, respectively; $\phi(f)$ = phase of signal transmitted through the core barrel; $A_{w,sed}(f)$ = spectral amplitude of the water and sediment signals,

respectively; α_w = attenuation coefficient of distilled water (36×10^{-15} N.m.$^{-1}$.Hz^{-2} at 10°C).

Group velocity, V, was calculated using Equation (6).

$$V = x_{sed}/(t_c - t_L) \tag{6}$$

The uncapped core was split and sampled for density and porosity. A miniature shear vane was used to gain an estimate of the shear strength of the sediment.

5. MODELLING

The Anderson and Hampton model [6], later used by Wilkens and Richardson [7], was implemented in an attempt to gain an understanding of a range gas fractions may produce high attenuation coefficients and low P-wave velocities for the Dibden Bay sediment, assuming free gas is present. The following equations were used predict gassy sediment sound speed and attenuation due to the bubbles:

$$\left(\frac{c_0}{c}\right)^2 = \frac{1}{2}\left(1+\frac{K.X_1}{\gamma P_0 + \frac{4}{3}.G}\right)\left\{1 \pm \left[1+\left(\frac{K.Y_1/\left(\gamma P_0 + \frac{4}{3}.G\right)}{1+K.X_1/\left(\gamma P_0 + \frac{4}{3}.G\right)}\right)^2\right]^{1/2}\right\} \tag{7}$$

$$a = 8.686.\left(\frac{\pi.f}{c_0}\right)\left(\frac{c}{c_0}\right)\left[\frac{K.Y_1}{\gamma.P_0 + \frac{4}{3}.G}\right] \tag{8}$$

where c, c_0 = sound speed in gassy and non-gassy sediments, respectively; K = saturated sediment bulk modulus; γ = ratio of the specific heats of the gas (methane); P_0 = the ambient hydrostatic pressure; G = sediment shear modulus; f = measurement frequency; X_1, Y_1 = values depending on gas fraction, damping, bubble resonance frequency and measurement frequency.

See Table 1 for a list of parameters, and their values, input to model.

Sediment porosity	0.61
Saturated sediment density, ρ_{sat}	1475 kg.m^{-3}
Mineral bulk modulus, K_m	3.6×10^{10} N.m^{-2} †
Frame bulk modulus, K_f	1.389×10^{8} N.m^{-2} ‡
Interstitial water bulk modulus, K_w	2.24×10^{9} N.m^{-2}
Dynamic shear modulus, G	2.813×10^{5} N.m^{-2} †
Imaginary part of shear modulus, G'	1×10^{4} N.m^{-2}
Bubble radius, r	0.01-10 $\times 10^{-3}$ m
Gas porosity, n_g	0.0001, 0.001, 0.01
Gas density, ρ_g	0.717 kg.m^{-3} at STP
Specific heat at constant pressure of gas, S_p	2.19 J.kg^{-1}.°C^{-1}
Thermal conductivity of gas, C_g	3.11×10^{-2} J.s^{-1}.m^{-1}.°C^{-1}
Ratio of the specific heats of the gas, γ	1.31

† Value from [7], ‡ Calculated from results in [8]

Table 1: Values of parameters used in model

Other values for the model (for example, c_0) can be calculated using [6], [7] and [9].

6. RESULTS

The auger core revealed layers of dark grey silty clay interspersed with smaller layers of sandier and more organic material. At about 2.3 m there is a layer of organic rich silty clay containing extensive wood fragments. This layer extends to the core's maximum depth of three metres. The silty clay had a saturated density of 1475 kg/m^3, a porosity of 0.61 (Table 1) and shear strengths in the region of 9 kN/m^2.

Group velocity calculated from the mini-boomer data varies from 889 m/s to 1405 m/s at the shortest and longest offsets, respectively; group velocity calculated from the core is 1472 m/s. Both of these values are lower than the theoretical saturated sediment velocity value calculated in the model at 1572 m/s. Phase velocity (see Fig. 3) at the lower frequency range is always less than 1500 m/s; at the higher frequency range it appears to vary between 1500 and 2000 m/s.

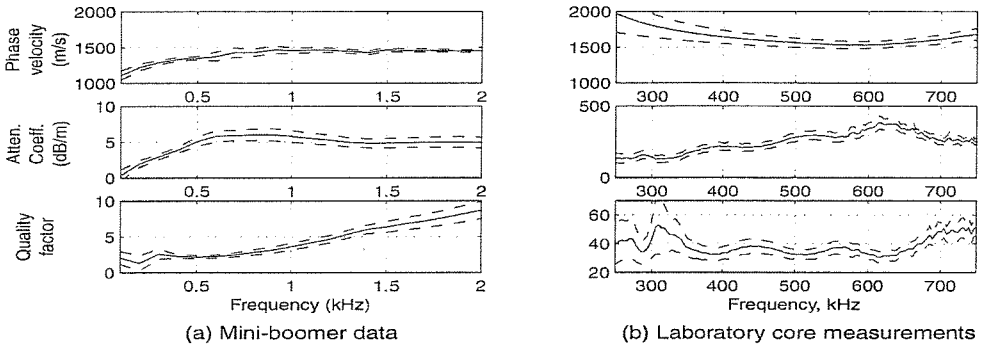

Fig. 3: Phase velocity, attenuation and quality factor within 95% confidence intervals.

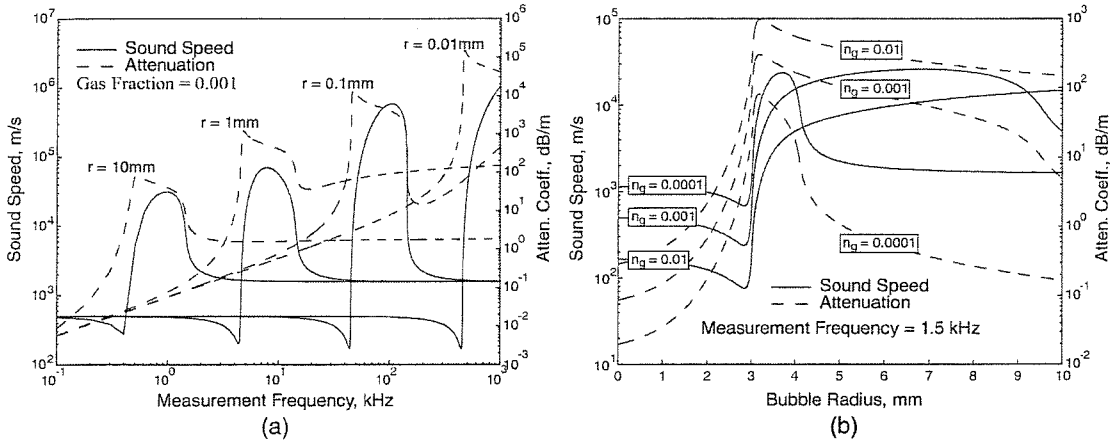

Fig. 4: Model results of sound speed and attenuation for (a) constant bubble radius and gas fraction versus measurement frequency and (b) constant measurement frequency and gas fraction versus bubble radius

High attenuation is seen in both frequency ranges (Fig. 3). The mini-boomer data show attenuation coefficients from 4 - 6 dB/m in the frequency range 0.5 - 2 kHz while data from Lough Hyne [4] indicate attenuation coefficients of 1 - 3 dB/m for a frequency range of 0.2 - 1.2 kHz. The high frequency core data also shows attenuation

coefficients greater than 100 dB/m. Previous studies [10] show that, for this frequency range, attenuation in silts and clays is generally less than 100 dB/m.

A value for Q between 3 and 10 for the frequency range 0.1 - 2 kHz is also an indicator of the attenuating nature of the sediments found in Dibden Bay. Q values between about 10 and 20 were found in Lough Hyne for a frequency range of 0.2 - 1.2 kHz.

The model (Fig. 4) shows that very large variations in seismic velocity may be seen in gassy sediments. Below resonance the velocity is below that found in saturated sediments and above resonance the velocity is approximately that seen in saturated sediments. The attenuation due to the bubbles can be seen to vary with bubble radius.

7. DISCUSSION

The sediments in Dibden Bay exhibit many of the characteristics of gassy sediments, including acoustic turbidity and high attenuation coefficients. The presence of hydrogen sulphide indicates that conditions are likely to favour methane production deeper in the sediment column. High attenuation coefficients and low P-wave velocities encountered in the mini-boomer tests could be accounted for by free gas affecting the geoacoustic properties of the sediment, but it is unlikely that resonance conditions themselves have been met at these frequencies as bubbles would have to be very large (r = 10 mm). A new acoustic source is being developed that will enable the emitted frequency to be through the ranges described here in an effort to explore the effects of in-situ resonance more closely. Pressurised cores and transmission studies over a 24 hour period will also help to determine the effect of sediment loading (due to tides) on the bubble population and, hence, the geoacoustic properties of the sediment.

8. ACKNOWLEDGEMENTS

We gratefully acknowledge the work of Andy Harris, from the Ocean Technology Division at S.O.C., for the design and construction of the mini-boomer system. This work was supported by N.E.R.C. grant number GT04/98/272/ES.

9. REFERENCES

[1] Schubel, J.R., Natural Gases in Marine Sediments, edited by I.R. Kaplan, pp. 275-298, Plenum, 1974.

[2] Floodgate, G.D., and A.G. Judd, The origins of shallow gas, Continental Shelf Research, Vol. 12 (10), pp. 1145-1156, 1992.

[3] Rice, D.D., and G.E. Claypool, Generation, accumulation, and resource potential of biogenic gas, Amer. Assoc. Petrol. Geol. Bull., Vol. 65, pp. 5-25, 1981.

[4] Best, A.I., Q.J. Huggett, and A.J.K. Harris, Comparison of in-situ and laboratory acoustic measurements on Lough Hyne marine sediments, submitted to J. Acoust. Soc. Am.

[5] Courtney, R.C., and L.A. Mayer, Calculation of acoustic parameters by a filter-correlation method, J. Acoust. Soc. Am., Vol. 93 (2), pp. 1145-1154, 1993.

[6] Anderson, A.L., and L.D. Hampton, Acoustics of gas bearing sediments I. Background, II. Measurements and models, J. Acoust. Soc. Am., Vol. 67 (6), pp. 1865-1903, 1980.
[7] Wilkens, R.H., and M.D. Richardson, The influence of gas bubbles on sediment acoustic properties: in situ, laboratory and theoretical results from Eckernförde Bay, Baltic Sea, Continental Shelf Research, Vol. 18 (14/15), pp. 1859-1892, 1998.
[8] Hamilton, E.L., Elastic properties of marine sediments, J. Geophys. Res., Vol. 76 (2), pp. 579-604, 1971.
[9] Gassmann, F., Elastic waves through a packing of spheres, Geophysics, Vol. 16, pp. 673-685, 1951.
[10] Kibblewhite, A.C., Attenuation of sound in marine sediments: A review with emphasis on new low-frequency data, J. Acoust. Soc. Am., Vol. 86 (2), pp. 716-738, 1989.

Temporal variability of P-wave attenuation due to gas bubbles in a marine sediment

Michael D. J. Tuffin[1], Angus I. Best[2], Justin K. Dix[1], Jonathan M. Bull[1]
[1] School of Ocean and Earth Sciences, University of Southampton, Southampton Oceanography Centre, Southampton, SO14 3ZH, UK. mdjt@soc.soton.ac.uk
[2] Challenger Division for Seafloor Processes, Southampton Oceanography Centre, Southampton, SO14 3ZH, UK. aib@soc.soton.ac.uk

Abstract

Acoustic attenuation measurements in gassy intertidal sediments in Dibden Bay, Southampton Water (UK) show significant and systematic changes over a tidal cycle. Modelling of the attenuation-frequency response curves, based on extant theory with modifications for hydrostatic pressure/gas bubble size relations and bubble size distributions, reproduces the observations over the tidal cycle. However, more work is needed to constrain the model input parameters to verify the theory more completely, particularly bubble size distribution and morphology.

1. Introduction

Zones of poor acoustic penetration and high reflection/backscatter amplitudes are observed in many shallow marine sediments, that is those less than 20 m sub-seafloor depth. This "acoustic turbidity" is caused by the presence of free gas bubbles, principally methane, that result in high attenuation and low velocity of transmitted signals relative to those transmitted through fully water saturated sediments [1].

The presence of methane, and smaller amounts of other gases, in shallow sediments is thought to be the result of anaerobic bacterial decomposition of organic matter [2]. In the marine environment, sediment pore water is rich in sulphates, allowing sulphate-reducing bacteria to dominate and produce hydrogen sulphide. Once the sulphates have been depleted, carbonate-reducing bacteria can compete more efficiently, and begin methane production [3].

Knowledge of gassy sediment properties is of interest to a number of offshore activities, including drilling operations and the siting of seafloor structures [4]. Slope stability is an area of concern to offshore operators who are working increasingly in the deep waters of the continental slope (water depths 200 – 2000 m). Evidence for gassy sediments (e.g. pockmarks [5]) and gas hydrates are commonly found adjacent to large, historical, submarine landslides [6], and, although the causes of submarine landslides are poorly understood at present, it is known that the presence of gas bubbles lowers the shear strength of a marine sediment [7]. Remote sensing of the seabed and sub-seabed using high-resolution acoustic methods promotes the possibility of inverting acoustic data for the geotechnical parameters needed in the above applications. However, a better understanding of acoustic propagation mechanisms in both fully saturated and gassy marine sediments is required to achieve this goal.

Acoustic turbidity was observed on chirp (2 – 8 kHz) sub-bottom profiles of the intertidal zone at Dibden Bay, Southampton Water (UK), and this site was subsequently chosen for a series of more detailed experiments [8]. This paper presents the preliminary results of an *in situ* acoustic transmission experiment conducted on the gassy sediments found at this site and provides a basis for validating existing models. The experiment used a vertical hydrophone array and a mini-boomer sound source to monitor acoustic attenuation over one complete tidal cycle. The effect of hydrostatic pressure on bubble size and the associated acoustic response was modelled using the theory of Anderson and Hampton [9, 10] with some enhancements. These were introduced to account for both the effects of variable bubble size and bubble size distribution. The outputs from the model were compared to the *in situ* P-wave transmission data.

The results show that *in situ* acoustic attenuation is sensitive to hydrostatic pressure and is broadly well described by the model. However, further work is needed to constrain the model input parameters, especially bubble size distribution, total gas volume and sediment shear strength. This will

be achieved by collecting pressurised sediment cores at the site in the near future and by subsequent laboratory analyses.

2. The Anderson and Hampton model

Anderson and Hampton [9, 10] developed a model to predict the effects of shallow gas on the attenuation and velocity characteristics of gassy sediments, based on the theory of gas bubble resonance in water. They concluded that bubble resonance frequency depends upon the bubble radius, the thermal properties of the gas, the dynamic shear modulus and bulk density of the sediment, and the ambient hydrostatic pressure. Therefore, knowledge of a bubble resonance frequency, for example, could be used to derive information on the radius of the bubble or the dynamic shear modulus of the saturated sediment. Bubble resonance has a significant effect on acoustic propagation and three distinct states may be identified: the insonifying frequency may be below, at/near or above the resonance frequency. Each state has its own characteristic sound speed, c, and attenuation, a, predicted by the model. A typical set of input parameters and their values, either measured from samples recovered from the Dibden Bay site or taken from the literature, are given in Table 1. Values of the remaining parameters required by the model not mentioned in the table (A, the gas polytropic coefficient; P_0, the ambient hydrostatic pressure; K, the bulk modulus of the saturated sediment; c_0, the P-wave velocity in the gas free sediment; ρ_w, water density; damping coefficients δ_r, δ_t, δ_f) may be measured, calculated or estimated from the literature [9, 10, 11, 12].

Sediment porosity, n	0.61
Saturated sediment density, ρ_{sat}	1475 kg / m^3
Mineral bulk modulus, K_m	3.6×10^{10} N / m^2 †
Frame bulk modulus, K_f	1.389×10^9 N / m^2 ‡
Interstitial water bulk modulus, K_w	2.24×10^9 N / m^2
Dynamic shear modulus, G	2.813×10^5 N / m^2 †
Imaginary part of dynamic shear modulus, G'	1×10^4 N / m^2
Bubble radius, r	$0.01 - 10 \times 10^{-3}$ m
Gas porosity, n_g	0.0001, 0.001, 0.01
Gas density, ρ_g	0.717 kg / m^3 at STP
Specific heat at constant pressure of gas, S_p	2.19 J / kg.°C
Thermal conductivity of gas, C_g	3.11×10^{-2} J / s.m.°C
Ratio of the specific heats of the gas, γ	1.31

† from [11]
‡ from [13]

Table 1. Values of parameters used in the model.

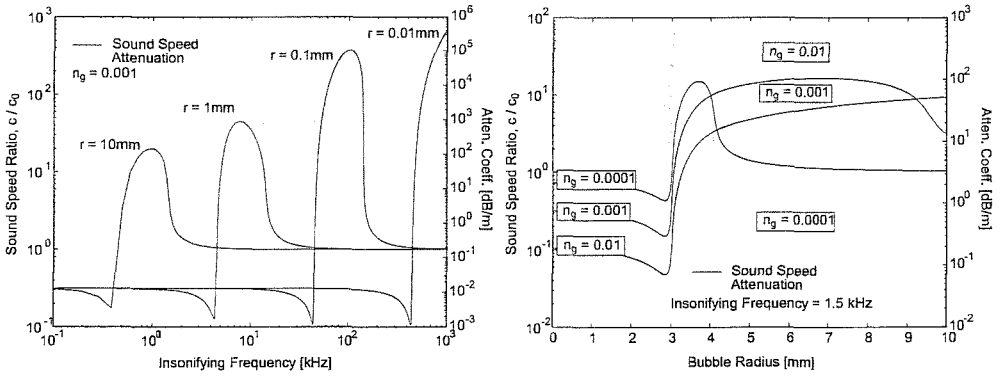

(a) (b)

Figure 1. Model results of sound speed ratio, c/c_0, and attenuation, a, for (a) constant bubble radius, r, and gas porosity, n_g, versus insonifying frequency, f, and (b) constant insonifying frequency, f, and gas porosity, n_g, versus bubble radius, r.

The model results in Figure 1 show that if the insonifying frequency is lower than the resonance frequency then the sound speed ratio, c/c_0, is less than unity. This would indicate a gassy sediment sound speed less than its gas free equivalent. A transition zone is seen at frequencies near resonance: the sound

speed ratio dramatically increases before gradually approaching a value of 1.0 when the resonance zone is exceeded. The bubbles also cause a dramatic increase in attenuation at frequencies near resonance. This is thought to be a result of the large increase in scattering cross section of the bubble at resonance [9]. Note that the attenuation calculated here does not include contributions from the intrinsic attenuation (absorption) of the sediment. Smaller bubbles require a higher insonifying frequency to make them resonate (Figure 1a) and a single insonifying frequency will cause resonance only in a narrow range of bubble radii (Figure 1b). In a real sediment there will be a variety of bubble sizes present. Hence, bubble resonances might be detected across a broad frequency range.

3. *In situ* measurements

3.1 Experimental set-up

In situ transmission measurements were obtained during March 2000 at Dibden Bay, an intertidal mudflat situated on the eastern shore of the upper reaches of Southampton Water (UK). The site is composed of very soft mud with a surficial shell layer in some areas. Evidence of free gas may be inferred from acoustic turbidity on chirp reflection profiles (Figure 2a) and the odour of hydrogen sulphide in the mud – an indicator of the anoxic conditions required by methanogenic bacteria. The site chosen for the experiment, an area with a surficial shell layer, may be seen in the chirp reflection profile (Figure 2a) as the domed area of high amplitude reflections. It is assumed that the gas layer, seen as the reflector about 1 ms below the seabed, extends under this shelly zone. The experiment used a mini-boomer acoustic source and a vertical array of four hydrophones placed at strategic depths within the sediment 1m from the source (Figure 2b). The mini-boomer uses a high-voltage inverter to drive a magneto-propulsive plate 20 cm in diameter and tests have shown that it produces a repeatable signal, a spherical radiation pattern and a spectral content between 0-11 kHz notched at about 2.5 kHz; the hydrophones show a flat frequency response up to 10 kHz [14]. The depths were chosen to ensure that there was at least one hydrophone above the gas horizon and at least one below, as inferred from chirp reflection profile data (Figure 2b). The mini-boomer was fired at ten-minute intervals over the period of a tidal cycle. The data were recorded using a digital storage oscilloscope and tidal height was calculated from tide gauge data collected routinely around the port of Southampton.

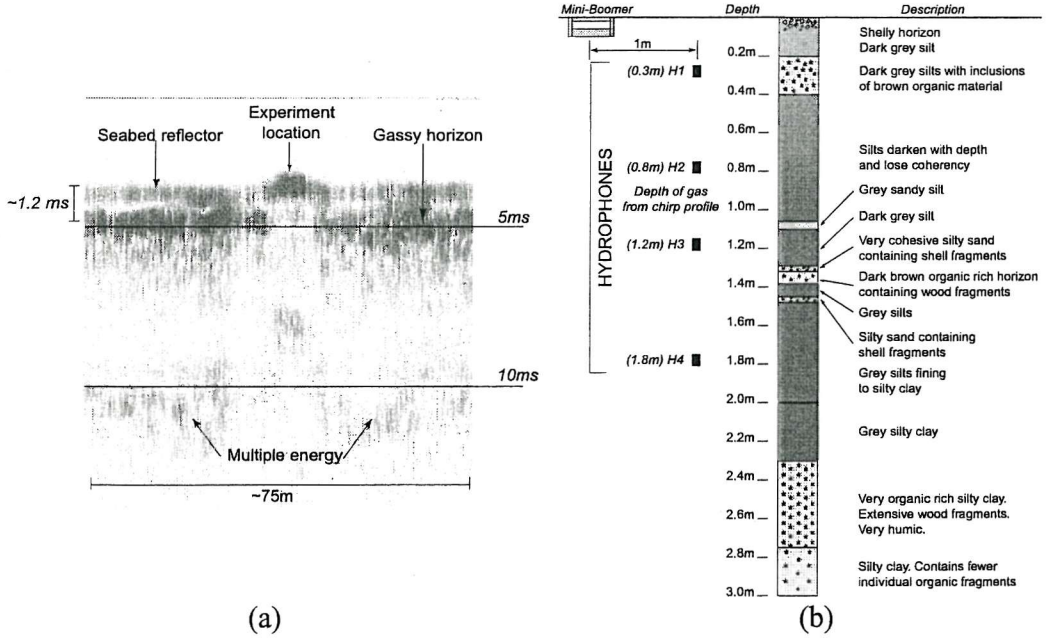

Figure 2. (a) Chirp reflection profile showing experiment location, seabed reflector and gassy horizon, and (b) positions of hydrophones within the sediment column.

3.2 Data processing

The data were processed using a filter correlation technique [15], which involves filtering the signal and a reference with a series of band pass filters, each with a width of 100 Hz, from a minimum central frequency of 100 Hz to an arbitrarily determined maximum central frequency of 2 kHz. Attenuation coefficients for each frequency band were calculated using the log spectral ratio method (Equation 1) with a spherical spreading law. Two reference signals were used, those signals received at hydrophones H1 and H2. Each shot was processed in the same manner.

$$a(f) = \frac{8.686}{\delta x} \ln \left| \frac{A_{ref}}{A_{sig}} \cdot \frac{x_{ref}}{x_{sig}} \right| \tag{1}$$

Where $a(f)$ is the attenuation coefficient [dB/m]; $A_{ref,sig}$ are the root mean square energies of the filtered reference and signal time series, respectively; $x_{ref,sig}$ are the source receiver separations in metres for the reference and signal time series, respectively; and δx is the $x_{sig} - x_{ref}$.

3.3 Results

Shot gathers for low and high water (Figure 3a,b) indicate a change in the character of the received signal both with tidal height and hydrophone depth.

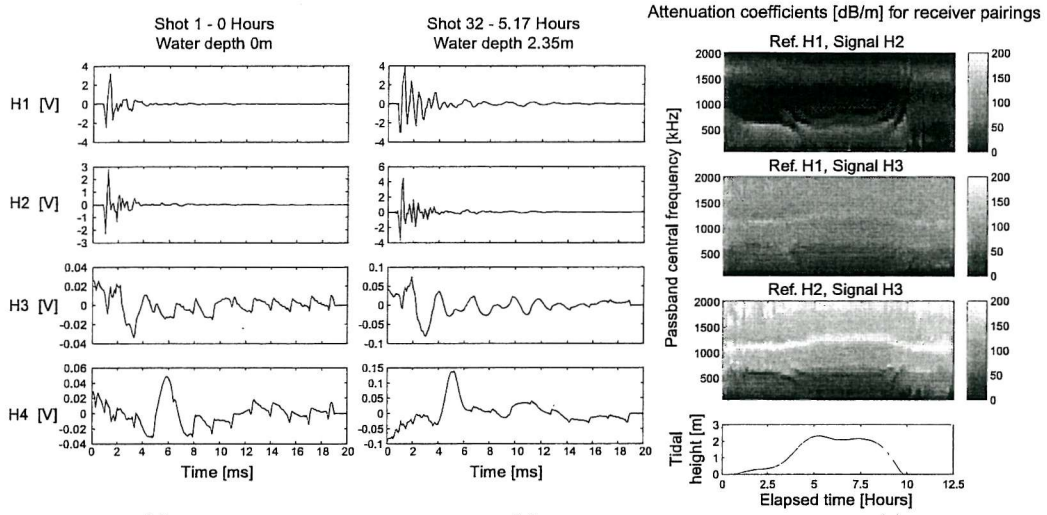

(a) (b) (c)

Figure 3. Self normalised shot gathers at (a) the start of the experiment and (b) the highest tide during the experiment. (c) Calculated attenuation coefficients for various reference/signal pairings.

A deterioration in the signal to noise ratio (SNR) with increasing depth of receiver is evident in both shot gathers. The spikes occurring at approximately 2 ms intervals on H3 and H4 in Figure 3a are thought to be the results of interference from the oscilloscope power supply. There is a clear drop in signal amplitude between receivers H2 and H3 in both gathers, indicating the presence of a highly attenuating zone between the two. There is little difference in amplitude of the signals received at H1 and H2. An improvement in SNR with increasing tidal height is evident from H3 and H4 in both shot gathers. The signals show less influence from the electrical noise due to the oscilloscope power supply with deeper water (Figure 3b) and the highest voltage recorded for each hydrophone is in excess of those seen for shallow water (Figure 3a), indicating lower attenuation of the signal. Problems with the data from hydrophone H4 meant that these data were excluded from the analysis.

Calculated attenuation coefficients for receiver reference/signal pairs, plotted against frequency and time in Figure 3c, show an influence of tidal height on attenuation. Attenuation coefficients calculated using H2 as the reference and H3 as the source (i.e. those receivers either side of the gassy/non-gassy sediment boundary) show a comparatively low attenuation zone below 600 Hz and a high attenuation zone above, peaking at approximately 1.1 – 1.4 kHz. The values of attenuation are very high (greater than 200 dB/m at 1 kHz) suggesting that attenuation caused by bubble resonance and scattering is

occurring at these frequencies. This attenuation peak increases in frequency in response to an increase in tidal height.

4. The effects of hydrostatic pressure on a gassy sediment

A comparison of the experimental and model results in Sections 2 and 3 suggest the increase in resonance frequency with tidal height is due to a decrease in bubble radius. The driving mechanism for this bubble radius decrease is a change in hydrostatic pressure, which will affect the internal bubble pressure as the system equilibrates, and hence, bubble radius.

4.1 Pressure equilibrium

Direct measurement of the pressure inside each individual bubble is not practical so an estimate must be made by considering the conditions in the surrounding saturated sediment matrix. The following limits on the internal pressure, u_g, were proposed by Wheeler *et al.* [16].

$$u_w + \frac{2T}{R_{\max}} \le u_g \le u_w + \frac{2T}{R_{\min}}, \tag{2}$$

where u_w is the pore water pressure; T is the surface tension; R_{max}, R_{min} are the limiting values of radius of curvature of meniscus (see [16] for details). The pore pressure at the depth of interest (approximately 1m) is taken as hydrostatic for simplicity [17], although it is important to note that a more accurate model of tidally induced pore pressure is available [18]. Surface tension effects are small compared to the pore pressure depending on the bubble radius: for a bubble radius of 0.1 mm and a surface tension coefficient of 0.073 N/m (the value for an air/water mixture), surface tension amounts to 1.46 kN/m^2; for a bubble radius of 1 mm the surface tension amounts to 146 N/m^2. The available evidence suggests that bubble radii are generally in excess of 0.1 mm [19], [20] and the frequency range of the processed data will be restricted to below 2 kHz, well below the resonance frequency of a 0.1mm bubble, so surface tension effects will be ignored here.

It is also assumed that the increase in pore pressure at the depth of the gas is instantaneous with the increase in hydrostatic pressure. Since the pressure inside the bubble equilibrates with the surrounding conditions there must be a similar increase in the internal pressure of the bubble. In the absence of any mass transfer into the bubble there is a decrease in bubble volume, and hence bubble radius. This change in bubble radius will result in a change in resonance frequency of the system. Assuming the gas conforms to the Ideal Gas Law and there is no temperature within the sediment change during the adjustment, the final bubble radius, r_1, may be calculated from:

$$r_1^3 = \frac{P_0}{P_1} . r_0^3, \tag{3}$$

where r_0 is the initial bubble radius; and P_0, P_1 are the initial and final pressures respectively. A decrease in hydrostatic pressure will result in an increase in bubble radius using the same argument.

4.2Gas diffusion

The following model for predicting the radius $R(t)$ of a growing bubble was proposed by Boudreau *et al.* [21]:

$$R(t) = \left[\frac{nD}{2c_g} \left\{ \frac{SR_1^{\,2}}{3D} + (c_1 - c_0) \right\} t + R_0^{\,2} \right]^{1/2}, \tag{4}$$

Where n is the porosity; D is the tortuosity-corrected diffusivity; c_g is the concentration of gas in the bubble; S is the local rate of methanogenesis; R_1 is the separation distance between bubbles ($R_1 \gg R$); c_1 is the ambient concentration of the gas; c_0 is the pore water concentration of the gas at R and is a function of c_g; t is the time; R_0 is the initial radius of the bubble. Consider a gas bubble at equilibrium with the surrounding water saturated sediment. A small reduction in bubble volume, such as that caused by an increase in hydrostatic pressure, will lead to a small increase in c_g (small enough that $c_0 \le c_1$); diffusion will act to slow down the rate of bubble growth. However, a large reduction in bubble volume (and associated increase in c_g) will lead to sediment undersaturation ($c_0 > c_1$) that may outweigh the local

rate of gas production (methanogenesis); this will result in a net reduction in bubble volume and radius. If there in insufficient undersaturation the bubble will continue to grow, albeit at a slower rate.

With sufficient chemical data it should be possible, using this model, to calculate the effect of increasing c_g on the radius of the bubble, but in the absence of this data in this study it has been decided to assume that there is no net change of the bubble radius due to diffusion.

4.3 Bubble size distribution

X-ray computed tomography (CT) scans of gassy sediment cores [20] show that a range of bubble sizes is the norm, with each bubble size population having its own associated gas porosity. Sediment coring at Dibden Bay and X-ray CT scans are planned for the near future, but for the purposes of this work a series of gas porosities were assigned to a set of arbitrarily determined bubble radii. Attenuation coefficients were calculated for each bubble radius using (1) to (9) and the input parameters in Table 1. The total attenuation due to the bubble size distribution is found by summing the individual bubble size attenuation coefficients at each insonifying frequency.

4.4 Model implementation

The model was implemented as a function of hydrostatic pressure using the tidal height curve obtained during the acoustic transmission experiment at Dibden Bay. The increment in hydrostatic pressure caused by the tide was used to calculate the bubble shrinkage/expansion due to pressure equilibrium and this new radius was used to calculate the attenuation coefficients over an arbitrarily defined frequency range (100 – 2000 Hz). The sequence was repeated for each subsequent tidal increment, equivalent to one sample interval of 10 minutes. The attenuation contribution from each bubble size was calculated in this manner for the whole tidal cycle, and then these single bubble size components were summed to give the total attenuation of the arbitrary bubble size distribution, according to Section 4.3. The arbitrary bubble size distribution was adjusted to obtain the best fit to the *in situ* data, the final distribution shown in Figure 4.

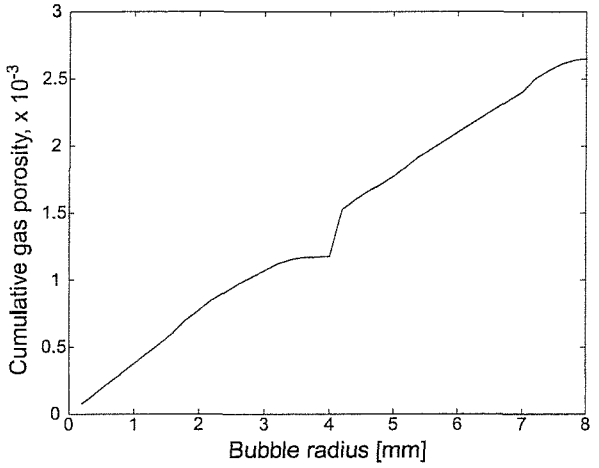

Figure 4. Cumulative gas porosity versus bubble radius.

5. Results and Discussion

It can be seen from the *in situ* results and the model results shown in Figure 5a that hydrostatic pressure (expressed here as tidal height) has a marked effect on dominant resonance frequency, because the only compressible components of the sediment at these pressures are the gas bubbles. The *in situ* data show an increase in resonance frequency from approximately 1150 Hz to approximately 1250 Hz as the tidal height over the site increases. Our model reproduces this observation, and although the dominant resonance frequencies predicted are slightly lower than those seen in the *in situ* data, the increase seen is of a similar size (Figure 5b). The model results match the magnitude and shape of the attenuation profiles adequately in the 600 – 1400 Hz range, especially for the 0.38 m tidal height. The model varies from the *in situ* data by less than 10% in this region with the exception of the points at 700 Hz and 1150 Hz, the attenuation peaks in the *in situ* data.

Differences between the model results and the *in situ* data can be explained by a number of factors. A lack of quantitative geotechnical measurements, except for some basic porosity and density measurements, means that several of the input values had to be estimated or calculated from other sources. Most importantly, there was no data available for the bubble size distribution within the sediment, so a series of values, as shown in Figure 4, were hypothesised and adjusted to best approximate the *in situ* data.

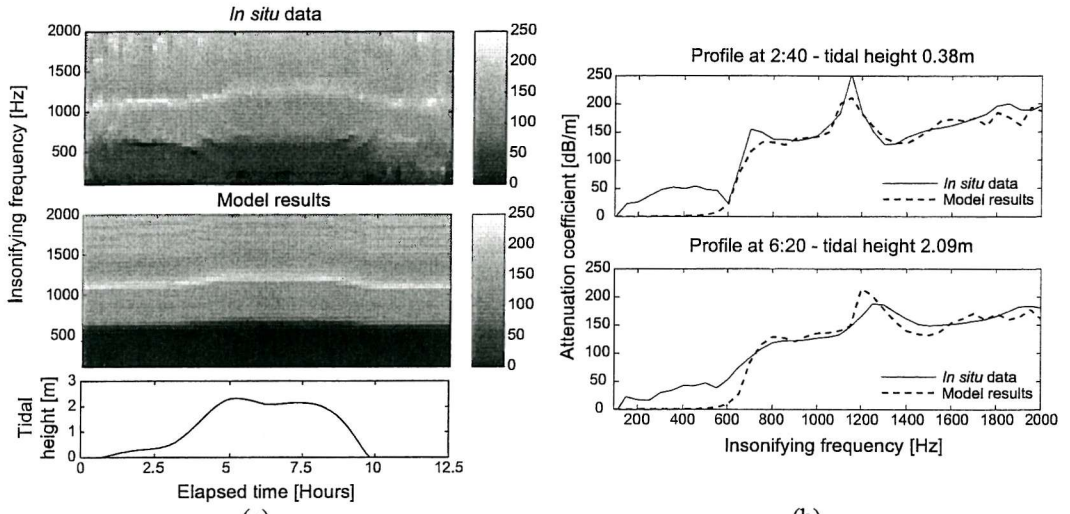

(a) (b)

Figure 5. Attenuation coefficients (a) over a whole tidal cycle for the *in situ* data and the model, and (b) for tidal heights of 0.38 m and 2.09 m.

The various assumptions made will have an effect on the final model result with the most important being the internal bubble pressure. The lack of any information concerning the local rate of methanogenesis and concentrations of methane in the pore water and bubbles means that any diffusive component is impossible to estimate. The impracticality of measuring the pressure inside an individual gas bubble buried in sediment without disturbing the bubble means that other methods to establish an internal pressure must be made. Calculations based on indirect measurements have been undertaken [22], but the problem of sediment disturbance remain and relating gas pressure to pore pressure, as presented here, also introduces problems. Pore pressure has been assumed to be the hydrostatic pressure at the gas horizon. This is clearly a simplification of the problem, and further improvements could be made to the model by calculating the tidally induced pore pressure more accurately and accounting for the effect of the presence of gas, as has been described in [18]. Despite these assumptions, the model shows good correlation with the *in situ* data in terms of the time at which the dominant resonance frequency changes and the shape of the curve. It should be noted, however, that the attenuation coefficients calculated in the model do not include the intrinsic attenuation due to the fully saturated sediment.

The model results indicate that, by matching model output to *in situ* acoustic data and using accurate geotechnical data, an estimation of the bubble size distribution within the sediment may be made. Further constraining the gas pressure could make improvements, although results here show a reasonable estimate. This bubble size distribution may be used to calculate the bulk gassy sediment geotechnical properties using relationships such as those presented in [23].

6. Conclusions

The Anderson and Hampton model [9], [10] was used to predict the change in the attenuation-frequency response of the gassy marine sediments in Dibden Bay due to changes in tidal height. The effect of changing hydrostatic pressure on gas bubbles contained within the sediment was modelled by considering pressure equilibrium between the bubble and the surrounding pore water. A bubble size distribution was estimated, the attenuation due to each bubble size/gas porosity pair was calculated and the total attenuation was obtained from the sum of the individual components. The model output shows good correlation with the *in situ* data, although improvements could be made by further constraining methods for assessing the internal bubble pressure. The agreement seen suggests that bubble size

distributions may be estimated with knowledge of water saturated sediment geotechnical properties and *in situ* acoustic measurements. Further work is planned to constrain these parameters.

7. Acknowledgements

This work is supported by Natural Environment Research Council studentship number GT04/98/272/ES. Thanks are extended to Gary Robb and Simon Dean for their assistance in collecting the *in situ* data, to Andy Harris for the design and construction of the mini-boomer system and to Bernie Boudreau for his advice. Finally, thanks go to Associated British Ports (Southampton) for granting access to the field site and for the tide data.

8. References

[1] Schubel JR. Natural Gases in Marine Sediments. Plenum, New York, 1974, pp. 275-298
[2] Floodgate GD and Judd AG. The origins of shallow gas. *Cont. Shelf Res.* 1992; **12**: 1145-1156
[3] Rice DD and Claypool GE. Generation, accumulation, and resource potential of biogenic gas. *AAPG Bull.* 1981; **65**: 5-25
[4] Sills GC and Wheeler SJ. The significance of gas for offshore operations. *Cont. Shelf Res.* 1992; **12**: 1239-1250
[5] McQuillin R and Fannin N. Explaining the North Sea's lunar floor. *New Scientist* 1979; **83**: 90-92
[6] Mienert J and Posewang J. Evidence of shallow- and deep-water gas hydrate destabilizations in North Atlantic polar continental margin sediments. *Geo-Marine Letters* 1999; **19**: 143-149
[7] Whelan III T, Coleman JM, Roberts HH and Suhayda JN. The occurrence of methane in recent deltaic sediments and its effect on soil stability. *Bull. Int. Assoc. Eng. Geol.* 1976; **14**: 55-64
[8] Tuffin MDJ, Best AI, Dix JK and Bull JM. Acoustic characterisation of gassy marine sediments in Dibden Bay, Southampton Water (UK), in *Proc. 5th European Conference on Underwater Acoustics,* 2000, pp. 825-830
[9] Anderson AL and Hampton LD. Acoustics of gas bearing sediments I. Background. *J. Acoust. Soc. Am.* 1980; **67**: 1865-1889
[10] Anderson AL and Hampton LD. Acoustics of gas bearing sediments II. Measurements and models. *J. Acoust. Soc. Am.* 1980; **67**: 1890-1903
[11] Wilkens RH and Richardson MD. The influence of gas bubbles on sediment acoustic properties: *in situ*, laboratory and theoretical results from Eckernförde Bay, Baltic Sea. *Cont. Shelf Res.* 1998; **18**: 1859-1892
[12] Gassmann F. Elastic waves through a packing of spheres. *Geophys.* 1951; **16**: 673-685
[13] Hamilton EL. Elastic properties of marine sediments. *J. Geophys. Res.* 1971; **76**: 579-604
[14] Best AI, Huggett QJ and Harris AJK. Comparison of *in situ* and laboratory acoustic measurements on Lough Hyne marine sediments. Submitted to *J. Acoust. Soc. Am.*.
[15] Courtney RC and Mayer LA. Calculation of acoustic parameters by a filter-correlation method. *J. Acoust. Soc. Am.* 1993; **93**: 1145-1154
[16] Wheeler SJ, Sham WK and Thomas SD. Gas pressure in unsaturated offshore soils. *Can. Geotech. J.* 1990; **27**: 79-89
[17] Craig RF. Soil Mechanics. Chapman and Hall, London, 1992, pp 80-85.
[18] Wang K, Davis EE and van der Kamp G. Theory for the effects of free gas in subsea formations on tidal pore pressure variations and seafloor displacements. *J. Geophys. Res.* 1998; **103**: 12339-12353
[19] Gardner TN and Goringe MJ. The measurement of gas bubble size distributions in a three phase laboratory gassy soil. *Geotech. Test. J.* 1988; **11**: 49-55
[20] Anderson AL, Abegg F, Hawkins JA, Duncan ME and Lyons AP. Bubble populations and acoustic interaction with the gassy floor of Eckernförde Bay. *Cont. Shelf Res.* 1998; **18**: 1807-1838
[21] Boudreau BP, Gardiner B, Johnson, B. Rate of growth of isolated bubbles in sediments with a distributed diagenetic source of methane. Submitted to *Limnol. Oceanogr.*.
[22] Whelan III T, Ishmael JT and Rainey GB. Gas-sediment interactions in Mississippi Delta sediments, in *Proc. 10th Annual Offshore Technology Conference* 1978, pp. 1029-1036.
[23] Wheeler SJ and Gardner TN. Elastic moduli of soils containing large gas bubbles. *Géotech.* 1989; **39**: 333-342

Temporal variability of P-wave attenuation due to gas bubbles in a marine sediment

Michael Tufin, Angus Best, Justin Dix and Jon Bull

Southampton Oceanography Centre, Southampton, SO14 3ZH, U.K.

Southampton Oceanography Centre

Abstract

Acoustic attenuation measurements in gassy intertidal sediments in Dibden Bay, Southampton Water (UK) (Figure 1) show significant and systematic changes over a tidal cycle. Modelling of the attenuation-frequency response curves, based on extant theory with modifications for hydrostatic pressure/gas bubble size relations and bubble size distributions, reproduces the observations over the tidal cycle. However, more work is needed to constrain the model input parameters to verify the theory more completely, particularly bubble size distribution and morphology.

Figure 1. Dibden Bay at low tide

Chirp profiling

- 2 - 8 kHz chirp sub-bottom reflection profiles shot parallel to shore
- Very little penetration of energy
- Acoustic turbidity dominates across entire survey area
- Figure 2 shows data from terrestrial experiment location
- Domed structure corresponds to a shell bed

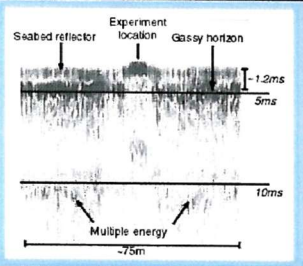

Figure 2. Chirp sub-bottom profile over experiment location

Modelling

- Anderson and Hampton (1980) model implemented
- Calculates:
  - attenuation due to gas bubble resonance
  - sound speed ratio (gassy / saturated speed)
- Typical model results for a single depth / bubble size shown in Figure 3
- Model extended to account for:
  - variable water depth (known tidal curve)
  - variable bubble radius (due to pressure variation)
  - bubble size distribution - arbitrary bubble size distribution used (Figure 4)

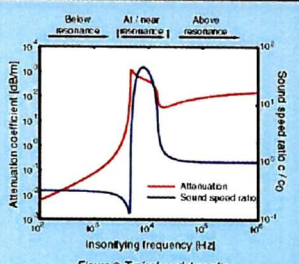

Figure 3. Typical model results

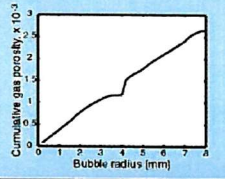

Figure 4. Assumed bubble size distribution

- Model predicts 3 states for the insonifying frequency:
  - Below resonance
  - At / near resonance
  - Above resonance
- Attenuation peaks when the bubble resonates

The Experiment

- Acoustic transmission experiment
- Mini-boomer acoustic source
- Vertical array of four hydrophones
- Shots fired every ten minutes
- Data filtered into separate frequency bands
- Attenuation coefficients calculated for each frequency band using spectral analysis techniques
- Source level is estimated to be 215 dB re. 1 mPa @ 1m
- Maximum strains of ~ 10^{-5} induced - non-linear effects may be ignored

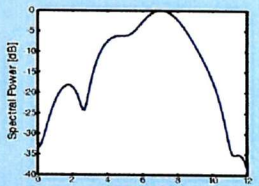

Figure 5. Mini-boomer spectral content in water

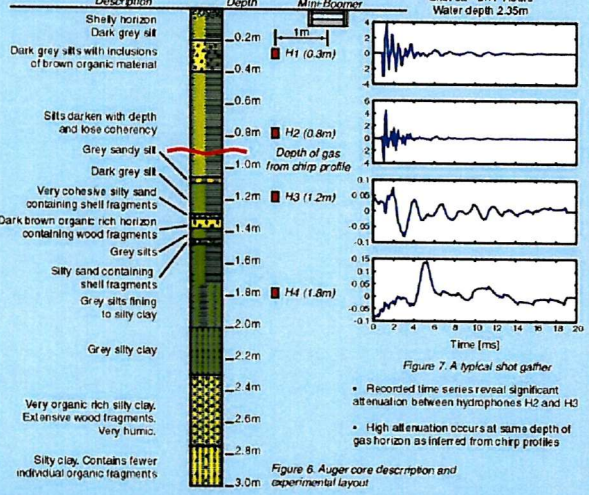

Figure 7. A typical shot gather

- Recorded time series reveal significant attenuation between hydrophones H2 and H3
- High attenuation occurs at same depth of gas horizon as inferred from chirp profiles

Figure 6. Auger core description and experimental layout

Results and Conclusions

- Direct evidence for tidal influence on bubble size and attenuation
- *In situ* results show that hydrostatic pressure has an effect on the dominant resonance frequency
- Increasing water depth correlates with an increase in frequency of maximum attenuation, caused by decrease in dominant bubble radius
- Model shows good correlation to *in situ* data
  - Time of resonant frequency change
  - Attenuation profile at discrete times
- Potential for bubble size distribution prediction using attenuation frequency change over known tidal variation
- Further work required to verify model
  - Accurate geotechnical measurements
  - Validation using known bubble size distributions

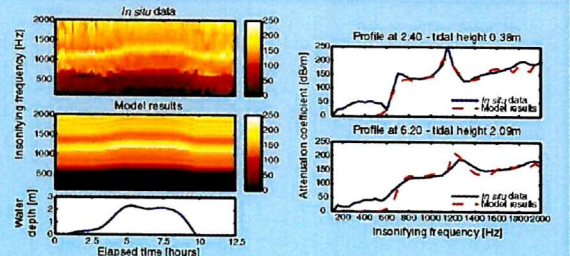

Figure 8. In situ and model attenuation results

Acknowledgements

This work was supported by Natural Environment Research Council Studentship GT04/97/272/ES. Thanks are extended to Gary Robb and Simon Dean for their assistance in the field and to Andy Harris for the design and construction of the mini-boomer system. Finally, thanks go to Associated British Ports (Southampton) for granting access to the field site.